ABSTRACT

Title of Dissertation:	Z-PINNING TECHNIQUES AND MODELING IN COMPOSITE LAMINATES AND X-COR SANDWICH STRUCTURES
	Ananth Kumar Musurapakam Virakthi, Doctor of Philosophy, 2018
Dissertation directed by:	Professor, Sung W. Lee, Department of Aerospace Engineering

Z-pinning is a technique where composite laminates are typically reinforced with metal or composite fiber pins inserted vertically into the laminate. The strength and fracture toughness of a Z-pinned laminate is directly dependent on the mechanical interlocking of the pin and the laminate. In the present work, novel approaches to the current Z-pinning technology are investigated to increase mechanical interlocking of the pins. Towards this end, we study pin insertion at an angle to the vertical unlike the traditional vertical pin insertion. In addition, a novel variety of pin, namely the threaded pin, is studied as a candidate for reinforcement. Using threaded pins for reinforcement increases mechanical interlocking between the pin and the laminate as well as the epoxy-pin contact area thus delaying delamination. When smooth metal pins are used for reinforcement, anchoring their ends on to the surface of the laminate before curing delays delamination through pin gripping.. Experiments performed show increase in

pullout strengths and fracture toughness when angled, threaded or anchored pins were used.

This research also looks at developing a computational-analytical model to represent the behavior of Z-pin reinforced X-Cor composite sandwich panels under out-of-plane compression and shear loading. Parameters important in representing the behavior of the individual components of the sandwich are identified. The softening of Z-pins under compression from geometric and material imperfections, densification of the foam and pin-facesheet interface strengths are incorporated into the model. For validation, the values of the parameters are obtained from experiments performed at UMD, and then for comparison, they are used to estimate the stiffness and strength of the specimens with experimentally obtained results reported in an open literature. Good correlation using these parameters across different specimens has implications on development of a predictive methodology for the behavior of Z-pin reinforced sandwich materials under compression and shear.

Cohesive Zone Modeling (CZM) is a numerical technique used to model composite delamination in conjunction with FE models, A material damping based approach is proposed to encounter the typical convergence issues faced by CZM and is implemented on FE models to analyze composite delamination and Z-pin pullout.

Z-PINNING TECHNIQUES AND MODELING IN COMPOSITE LAMINATES AND X-COR SANDWICH STRUCTURES

by

Ananth Kumar Musurapakam Virakthi

Dissertation submitted to the Faculty of the Graduate School of the
University of Maryland, College Park, in partial fulfillment
of the requirements for the degree of
Doctor of Philosophy
2018

Advisory Committee:
Professor Sung W. Lee, Chair
James Baeder
Hugh Bruck
Inderjit Chopra
Norman M. Wereley

Dedicated to Amma and Appa

for their unconditional love and support

Acknowledgements

First and foremost, I would like to express my immense gratitude and thanks to my doctoral advisor, Dr. Sung Lee. Over the years, Dr. Lee has been a mentor to me not only in my research but also in my life in general. Through his guidance, I have learnt to appreciate the virtues of perseverance, kindness and empathy. I wholeheartedly thank him for his encouragement, and availability to assist me throughout my graduate school. I'm also very thankful to Dr. Hugh Bruck who has generously guided me with the experimental aspect of my research and has provided access to experimental facility. I also acknowledge my dissertation committee for their suggestions, encouragement and motivation.

I must acknowledge the support of my fellow lab-mates and graduate students, Erick, James, Arianne, Dr. Kwon, Jack, Sandip, Prakhar, Joe, Nelson, Ganesh and Andrew who worked alongside me and have provided useful inputs at times. Sandip, and Dr. Kwon in particular have helped me brainstorm certain ideas pertaining to my research and I thank them for that. I thank my students from courses that I instructed and assisted for keeping me motivated and excited about my field of research through their inquisitiveness and inspiration.

The Aerospace staff, Tom, Erika, LaVita, Deborah, Otto, Becky and Laura deserve all the credit for guiding me through paperwork and helping me with the appropriate support I needed towards meeting important deadlines, financial support and travel assistance.

I have been extremely fortunate to have an excellent support network in my friends, Chris, Vikas, Aishwarya, and Ryan, who have helped me through difficult times in

graduate school. In particular, I would like to thank Chris who has been on my side and a great source of support in the past few years. My ex-dog, Lucy was a lovely companion and a best friend of sorts providing unintentional support as well. Erica and her co-leaders have counseled me on a great variety of issues pertaining to graduate school and I am greatly indebted to them.

Last, but not the least, I would like to thank my parents, my sister and my entire close-knit extended family for their dependable support at any time despite any adversity. My parents in particular have made numerous sacrifices throughout their lives and that is directly the reason for my success in any aspect of life.

Table of Contents

Chapter 1: Introduction and Literature Review……1
1.1 Background……1
1.2 Techniques to improve delamination resistance of composites……..3
1.2.1 3d Weaving……..4
1.2.2 3d Stitching……..6
1.2.3 3d Tufting……...……..7
1.2.4 Matrix Toughening……...8
1.2.5 Interleaving……10
1.26 Z-pinning……..11
1.3 Z-pinning in composite laminates……...……...12
1.3.1 Manufacture of Z-pin composite laminates……12
1.3.2 Influence of Z-pin material……18
1.3.3 Influence of Z-pin insertion on laminate properties……...22
1.4 Z-pinning in sandwich panels……26
1.5 Numerical methods to model composite delamination……28
1.6 Motivation and objectives of this research……29
1.6.1 Novel techniques for Z-pinning in composite laminates ...……29
1.6.2 Computational-Analytical modeling of Z-pinned Sandwich Structures …….……...31
1.6.3 1.6.3 Numerical Techniques to Model Composite Delamination……....33

Chapter 2: Novel Z-pinning in Composite Laminated Structures…….……35
2.1 Introduction……35
2.2 Specimen preparation and pullout tests…….……....35
2.3 Angled pin insertion…….…….....40
2.3.1 Linear FE Analysis……. ...……40
2.3.2 Experiments for tensile pullout strengths……...49
2.3.3 Non-linear FE analysis for tensile pullout strengths……..53
2.3.4 Experiments for pullout under shear loading……55
2.3.5 Effect of pin material on tensile pullout strengths…….58
2.4 Threaded pin insertion…….…….…….....61
2.4.1 Tensile pullout strengths of T1 pins..……. ...……61
2.4.2 Shear pullout strengths of threaded pins ……...66
2.4.3 Effect of insertion angle on pullout strengths of threaded pins……..67
2.3.4 Pullout tests on specimens with S1 pins……69
2.3.5 Optimal contouring of threaded pins…..……70
2.5 Anchored pin ……..…….…….....72

2.5.1 Pullout tests of AS1 pins..……..72
2.5.2 Pullout tests of AS2 pins and non-linear FE models……..…...76
2.6 DCB Experiments…..……..…….....79
2.7 Galvanic Corrosion Tests…….…….....91
2.8 Conclusions…….…….…….....92

Chapter 3: Modeling of Z-pinning in X-Cor Sandwich Structures……..…94
3.1 Introduction……...….94
3.2 Sandwich Geometry, Nomenclature..……...….94
3.2.1 Sandwich Geometry and Physics……94
3.2.2 Experimental specimen samples at UMD……...96
3.3 Preliminary Model of X-Cor Sandwich…..……...….98
3.3.1 Pin spring constants……98
3.3.2 Model 1: A perfect-bonding model……..101
3.4 Improvements to X-Cor model…….……...…104
3.4.1 Motivation……104
3.4.2 Bending Axial Coupling…….……..104
3.4.3 Pin Boundary Conditions……109
3.4.4 Eccentric loading of sandwich under compression……..114
3.4.5 Effect of geometric imperfections of the pin……117
3.4.6 Effective imperfection and effective interface modulus……...121
3.4.7 Stiffness and strength of the T-pin under shear loading……...121
3.4.8 Contribution from foam……123
3.5 Model 2 for X-Cor sandwich…….……...…..128
3.5.1 Compressive Stiffness.……129
3.5.2 Compressive Strength…….……129
3.5.3 Shear Stiffness…….130
3.5.3 Shear Strength…….130
3.6 Experimental Correlations with UMD and CU Specimens……..…132
3.6.1 Compressive stiffness and strength.……134
3.6.2 Shear stiffness and strength …….……..139
3.7 Conclusions……143

Chapter 4: Numerical tools to model composite delamination- Cohesive Zone Modeling……...…145
4.1 Introduction…….....145
4.2 Cohesive separation law and modeling……...….146
4.2.1 Constitutive law for cohesive zone……..146
4.2.2 Development of user-based cohesive element……148
4.2.3 Verification of Cohesive Zone Model…….151
4.3 Convergence issues in CZM……...….154
4.3.1 Viscous Regularization……..……..154
4.3.2 Single Degree of Freedom model attached to a softening spring……..…….156
4.3.3 Cantilever beam on a softening non-linear spring ……..159
4.3.4 Effect of beam inertia and transient response of the beam …..164

4.3.5 Material damping and quasi-static solutions ……166
4.4 UMD experiments for mixed-mode crack propagation…...……...….167

Chapter 5: Conclusions and Future Work……...…….175
5.1 Summary and contributions of this research…….....175
5.2 Applications of this research and recommendations for future work……...….177
5.2.1 Optimal Contouring of Pins ……177
5.2.2 Application to tapered and curved tapered laminates …….178
5.2.3 Application to T-joints…… …….178
5.2.4 Modeling of DCB beams with cohesive springs…….179
5.2.5. Anchored pin for sandwich panels……..179

Appendix: Stress Analysis of Tapered and Curved Laminates under Tensile Loading**……**……...…….181

List of Tables

Table 2.1: Material and geometric properties of pin and laminate used in FE models ……..42
Table 2.2. Comparison of stiffness before delamination for tensile and shear loading conditions…….44
Table 2.3. Comparison of stiffness after delamination for tensile and shear loading conditions…….44
Table 2.4. Pin diameters and %weight increase for various pin inserts……..49
Table 2.5. Pin density and %weight increase for carbon fiber (C2) pins……51
Table 2.6. Pin density and %weight increase for steel (S2) pins……51
Table 2.7: Coefficient of thermal expansion for some materials……59
Table 2.8. Pin density and %weight increase for vertical pin of different materials……..60
Table 3.1: Geometric properties of X-Cor sandwiches tested at UMD……...97
Table 3.2: Material properties of pin, foam-core and facesheets of the X-Cor sandwiches tested at UMD……..97
Table 3.3: Experimental values for compressive and stiffness and strengths of UMD specimens……98
Table 3.4: Comparison of Experimental and Model-1 estimates for compressive stiffness and strengths of UMD specimens……104
Table 3.5: Sandwich properties for X-Cor UMD and CU specimens tested for compression……...134
Table 3.6: Mean values for compressive stiffness and strengths of UMD and CU specimens……...135
Table 3.7: κ and α values for UMD and CU specimens……...137
Table 3.8: Mean values for shear stiffness and strengths of specimens from UMD and CU……..141
Table 4.1: Lamina and cohesive properties used in the model, obtained from the paper by Landry and Laplante…….153
Table 4.2: Lamina properties of the composite used as the test specimen, obtained experimentally……173

List of Figures

Figure 1.1 (a) A sketch of the outer skin of the Boeing 787 Dreamliner (b) A graph of the different materials used over time in Boeing planes……2
Figure 1.2: Examples of 3D woven preforms in the shape of a cylinder and flange, egg crates and turbine engine rotors……..5
Figure 1.3: Weaving mechanism showing through-the-thickness yarns woven into a composite structure …...……5
Figure 1.4: An illustration of stitching mechanism for a composite laminate …….7
Figure 1.5: (a) Schematic of tufting mechanism (b) Partial and full penetration of tufted yarns……8
Figure 1.6: Schematic of different toughening mechanisms playing a role in thermoplastic-modified epoxy including crack bridging, particle bridging and crack deflection ….……9
Figure 1.7: Schematic of lamination of composites and interleaving layers ….…….11
Figure 1.8: SEM micrographs of ENF fracture surfaces on both sides of a laminate interleaved with CTBN epoxy ……11
Figure 1.9 (a) Photograph showing the size of a typical Z-pin (b) close-up of Z-pins inside composite prepregs……12
Figure 1.10: Z-pin automation technique using UAZ method ….……...14
Figure 1.11: Z-pins inserted into a soft collapsible foam ready for insertion into composite laminate……..15
Figure 1.12: Z-pin insertion mechanism developed by Choi et. al…..……...15
Figure 1.13: Schematic of insertion head for multiple Z-pin insertion developed by Qinghua et. al……...16
Figure 1.14: Device for feeding multiple straight pins into the director plate for Z-pin for multiple Z-pin insertion …...……..17
Figure 1.15: Z-pinned foam blocks inserted by multi-pin insertion technique …..…18
Figure 1.16: Test equipment to compare tensile pullout strengths of metal versus composite fiber Z-pins embedded in laminates……...19
Figure 1.17: Crack growth curves for laminates reinforced with metal and composite fiber pins …...……..20
Figure 1.18: Tensile load versus displacement of Z-pinned specimens comparing pullout strengths of composite and titanium Z-pins …..…….21
Figure 1.19: Deformed Z-pins and plastic indentation of substrate in composite laminate under shear loading for (a) Titanium pins (b) Composite fiber pins……22
Figure 1.20: Fiber waviness in the composite laminate caused from Z-pin insertion……..23
Figure 1.21: Resin-rich zones around Z-pin in composite laminate……...23

Figure 1.22: Finite element mesh for a Z-pin-laminate interface showing resin-rich pockets ……..……..25
Figure 1.23: Schematic of X-Cor and K-Cor composites……...27
Figure 1.24 A Z-pinned sandwich specimen (left) as received, (right) with top face sheet removed…… 27
Figure. 1.35: Bi-linear traction separation law for a CZM…….29
Figure 1.36: Z-pin pullout under DCB tests for mode-I crack propagation……...30
Figure 2.1: A single pin inserted through acrylic guides showing the varying degrees of pin insertion angle……..37
Figure 2.2: Top view of laminate geometry for specimens tested for influence of pin insertion angle…….37
Figure 2.3: Reveal lengths of pin flattened on the laminate surface to anchor pin37
Figure 2.4(a) A batch of reinforced specimens before curing, (b) Cured laminate trimmed into smaller specimens…….38
Figure 2.5: IMADA load frame used for testing of reinforced laminate strengths under tensile loading……..39
Figure 2.6: IMADA load frame used for testing of reinforced laminate strengths under shear loading……... 40
Figure 2.7: ABAQUS models of a single pin embedded in a composite laminate at 0^o, 15^o, 30^o and 45^o to the vertical……41
Fig 2.8: Schematic for Mode-I opening condition on a laminate reinforced with a single pin before and after delamination……..42
Fig 2.9: Schematic for Mode-II sliding condition on a laminate reinforced with a single pin before and after delamination……..43
Figure 2.10: Pin reinforcement for tensile loading condition of a laminate before and after delamination for different pin insertion angles……46
Figure 2.11 : Pin reinforcement for shear loading condition of a laminate before and after delamination for different pin insertion angles……46
Figure 2.12: Pin reinforcement density for tensile loading condition of a laminate before and after delamination for different pin insertion angles……..47
Figure 2.13 : Pin reinforcement density for shear loading condition of a laminate before delamination for different pin insertion angles…….47
Figure 2.14: Average Von-Mises stress per unit tensile or shear force in the interface layer for models with varying pin angles…….48
Figure 2.15.Top view of laminate geometry for specimens with 16 composite pins…… 50
Figure 2.16: Pullout strengths for laminates with vertical and oblique (30^o) carbon-fiber pins…….50
Figure 2.17: Plot of tensile pullout strengths versus pin insertion angles for S2 pins52

Figure 2.18.:Typical force vs. displacement plots for tensile pullout tests conducted on specimens with different pin angles……52
Figure 2.19: Bilinear traction separation law for cohesive layer modeling…….54
Figure 2.20: Plot of tensile pullout strengths versus pin insertion angle for S2 pin inserts with estimates from non-linear FE model…….…..55
Figure 2.21: Plot of shear pullout strengths versus pin insertion angle for S2 pin inserts……..56
Figure 2.22: Typical force vs. displacement plots for shear pullout tests conducted on specimens with different pin angles……....57
Figure 2.23: Sketch showing angled pins under tension (T-pin) and compression (C-pin) under shear loading……..57
Figure 2.24: Nonlinear FE model-generated force-displacement plots for C-pin under shear loading for various pin insertion angles…….58
Figure 2.25: Schematic showing the opposing forces in laminate and Z-pin during cooling phase of the laminate due to varying level of thermal expansion coefficients…….. 59
Figure 2.25. Tensile pullout strengths of laminates reinforced with pins of different materials……...61
Figure 2.26. : (a) Threaded steel pin used to reinforce laminate (b) Forces on the external surfaces of smooth steel pin and threaded steel pin under tensile loading…….62
Figure 2.27: Contact forces on smooth pin and threaded pin…….62
Figure 2.28: Tensile pullout strengths of laminates reinforced with C2, S2 and T1 pins of standard diameters……...63
Figure 2.29: Typical force-displacement curves for specimens with C2, S2 and T1 pins……..64
Figure 2.30(a) Finite element model of a single threaded pin embedded in a laminate. (b) Cohesive damage contour map on a deformed threaded pin post failure……..65
Fig 2.31: Tensile force vs. displacement plot obtained from non-linear FE analysis of a laminate reinforced with threaded pin (T1)……..65
Figure 2.32: Tensile pullout strengths of laminates reinforced with C2. S2 and T1 pins (b) smooth and threaded pins of different thicknesses…….66
Figure 2.33: Tensile pullout strengths of laminates reinforced with smooth and threaded pins of different thicknesses……..67
Figure 2.34: Plot of tensile and shear pullout strengths versus pin insertion angle for T1 pins…….69
Figure 2.35: Plot of pullout strengths versus pin insertion angles under tensile and shear loading conditions for laminate reinforced with S1 pins……70
Figure 2.36: Isometric and cross-sectional views of threaded pins with sharp edges (left) and smoothened edges (right)…….71

Figure 2.37: Displacements applied to outer surface of epoxy layer surrounding the threaded pins……72
Figure 2.38: Plot comparing average von-Mises stress in critical locations of threaded pins with sharp and smooth edges for non-zero helix angles……..72
Figure 2.39(a): Pin anchored to the laminate by flattening reveal lengths on the laminate surface (b) Sketches showing direction of flattening of the reveal lengths……..73
Figure 2.40 (a) FE model of anchored pin reinforcement (b) Effect of anchoring on boundary conditions on pin ends……74
Figure 2.41: Plot of pullout strengths versus pin insertion angles under tensile loading conditions for laminate reinforced with anchored and non-anchored pins (AS1)…..74
Figure 2.42: Plot of pullout strengths versus pin insertion angles under shear loading conditions for laminate reinforced with anchored and non-anchored pins (AS1)…..75
Figure 2.43: Bending of pins apparent in specimens reinforced with anchored pins post-failure under tensile and shear loading respectively……75
Figure 2.44: Typical force vs. displacement plots for shear pullout tests conducted on specimens with anchored and non-anchored S1 pins inserted at 30……76
Figure 2.45: Tensile pullout strengths of the laminate under tensile loading conditions with AS2 and S2 pins…….. 77
Figure 2.46: Typical force vs. displacement plots for tensile pullout tests conducted on specimens with anchored and non-anchored S2 pins…….78
Figure 2.47: Shear pullout strengths of the laminate under tensile loading conditions with AS2 and S2 pins…….78
Figure 2.48: Schematic for the Double Cantilever Beam (DCB) test (not drawn to scale)……80
Figure 2.49: Top view of the laminate showing positions of pins on the top surface as well as the direction of pin insertions……..80
Figure 2.50: Vertical markings on laminate cross-section to identify position of crack-tip as a function of time and applied displacement……..81
Figure 2.51. Force vs. displacement plot and progression of crack length in DCB specimens with smooth pins of different thicknesses inserted vertically……82
Figure 2.52. Force vs. displacement plot and progression of crack length in DCB specimens with S2 pins inserted at different angles……83
Figure 2.53. Critical strain energy release rate at the onset of crack propagation for DCB specimens with S2 pin inserted at different angles…….83
Figure 2.54. Force vs. displacement plot and progression of crack length in DCB specimens with threaded pins of different thicknesses……85
Figure 2.55. Force vs. displacement plot and progression of crack length in DCB specimens with anchored pins of different thicknesses……...85

Figure 2.56. Critical strain energy release rate at the onset of crack propagation for DCB specimens with different pin reinforcements…….86
Figure 2.57: Top view of the laminate showing positions of pins on the top surface and the direction of pin insertions…… 87
Figure 2.58: FE models created in ABAQUS for a single pin inserted at 30^{o} to the vertical in the x-direction (top) and y-direction (bottom) ……88
Figure 2.59: Force vs. displacement and progression of crack length in DCB specimens with pins inserted in the x-direction at different angles to the vertical……89
Figure 2.60: Force vs. displacement and progression of crack length in DCB specimens with pins inserted in the y-direction at different angles to the vertical……89
Figure 2.61: Plots showing progression of crack length in DCB specimens with pins inserted at the same angle to vertical but at different orientations…….90
Figure 2.62: Top view of laminate geometry for specimens used to investigate the effect of galvanic corrosion……91
Figure 2.63: Mean tensile pullout strengths of specimens tested after various degrees of exposure to saline solution…….92
Figure 3.1(a) An isometric view of the pyramid geometry of the Z-pin reinforced sandwich structure (b) Top view of the arrangement…….95
Figure 3.2 Sketch of the sandwich panel in its side view showing the geometric parameters……..96
Figure 3.3: An oblique pin isolated from the sandwich structure under compression or shear loading represented as a slender body with guided boundary condition……..99
Figure 3.4: Oblique pin under compression isolated on the right showing boundary forces and moments acting……..105
Figure 3.5: Compressive Force vs. displacement obtained by including bending-axial coupling compared with linear decoupled analysis……...108
Figure 3.6: Shear Force vs. displacement obtained by including bending-axial coupling compared with linear decoupled analysis……...109
Figure 3.7: An oblique C-pin isolated from the sandwich structure under compression or shear loading represented as a slender body with rotational springs at its boundaries……..110
Figure 3.8: Resin rick area around a Z-pin inserted into aI composite laminate showing the crack around the z-pin, taken from [1]…….110
Figure 3.9 (a) FE model of a single pin embedded in a facesheet with a central load (b) Pin-facesheet interface showing adhesive layer surrounding the pin inside the facesheet (c) Interface layer isolated from rest of the model……112
Figure 3.10: Z-pin represented with rotational spring constant at its ends……112

Figure 3.11: Plot showing relationship between α and non-dimensional spring constant κ ...……...114
Figure 3.12 (a) An oblique pin subjected under axial loads at a distance away from the centroidal axis of the pin (b) Moments resulting at pin ends from eccentric loading……115
Figure 3.13: Compressive Force vs. displacement for an oblique T300 pin of 0.28 mm diameter with simply supported ends under eccentric axial loading with varying degrees of eccentricity……...117
Figure 3.14: : A slender beam with geometric imperfections under compressive loading…….……..118
Figure 3.15: Axial force vs. displacement plots for a T300 pin with and without geometric imperfection……..120
Figure 3.16: Variation of parameter, λ with pin axial displacement for a pin with geometric imperfections……120
Figure 3.17: T-pin under shear loading being pulled though the pin-facesheet interface123
Figure 3.18: Vertical and horizontal springs on an X-cor pin (concept taken from [21])……124
Figure 3.19: Foundation springs on pin due to foam with effective foundation modulus as a result of vertical and horizontal springs (concept taken from [21])……124
Figure 3.20: Variation of buckling force with foundation stiffness shown for a pin with pinned and clamped ends……...127
Figure 3.21: Experimental setup for compression testing of sandwich specimens on INSTRON 8841 machine……...135
Figure 3.22: Comparison of experimental and model strengths for UMD specimens (top) and CU specimens (bottom) under compression loading…….138
Figure 3.23: Comparison of experimental and model stiffness for UMD specimens (top) and CU specimens (bottom) under shear loading…….139
Figure 3.24: Experimental setup for shear testing of sandwich specimens on IMADA load frame……..141
Figure 3.25: Comparison of experimental and model strengths for UMD specimens (top) and CU specimens (bottom) under shear loading…….142
Figure 3.26: Comparison of experimental and model stiffness for CU specimens under shear loading……143
Figure. 4.1: Bi-linear traction separation law for a CZM……..147
Figure 4.2: A representative cohesive element connecting the two arms of a laminate ……148
Fig 4.3: Cohesive element and its degrees of freedom. The midplane of the cohesive element is isolated on the right……..149

Figure 4.4: Double cantilever beam (DCB) configuration for crack opening of a composite laminate. a_0 is the initial crack length. P is the loading force, and δ is the loading point opening displacement. Total length of the beam is 150 mm……..152
Figure 4.5: Meshing used for the FE model of composite beam in ABAQUS152
Figure 4.6: Comparing force-displacement curves between experiment and ABAQUS' computational model……...153
Figure 4.7: Delamination length versus load point displacement…….154
Figure 4.8: Load displacement curves obtained from computational models with different values of viscous regularization coefficients……..156
Figure 4.9: SDOF system with a non-linear (softening) spring……..…..157
Figure 4.10: Force-displacement relationship for the non-linear spring…….157
Figure 4.11: Solution for equilibrium positions as a function of the steady state values of applied displacements, for a system with m = k = 1, $k_1$158
Figure 4.12: A cantilever beam on a spring model……159
Figure 4.13: Force-displacement relationship for the non-linear spring……160
Figure 4.14: Analytical solution for w_2 as a function of w_1 when $\tilde{k}_2 < \frac{768}{7}$(left) and $\tilde{k}_2 > \frac{768}{7}$(right)……...161
Figure 4.15: Analytical solution for load F_1 as a function of w_1 when $\tilde{k}_2 < \frac{768}{7}$(left) and when $\tilde{k}_2 > \frac{768}{7}$(right)…….162
Figure 4.16: Newton-Raphson method fails for this case……163
Figure 4.17 a) Steady solutions for w_2 obtained as a function of applied displacement, w_1 b) Corresponding load vs. displacement plot……..164
Figure 4.18 a) Steady solutions for w_2 obtained dynamically with inertia included, for two different rates of increase of applied displacement, w_1 b) Corresponding load vs. displacement plot…….……165
Figure 4.19 a) Transient solutions for w_2 obtained for different values of damping coefficient and neglecting the inertia of the beam b) Corresponding load vs. displacement plot…….166
Figure 4.20: Wyoming Test Fixture used at FGM Lab, UMD to perform mix-mode crack propagation test on composite laminate……..……168
Figure 4.21: Mixed-mode bending test schematic …..……169
Figure 4.22: Illustration of the model constructed in Abaqus……...169
Figure 4.23: The test specimen model with meshing……170
Figure 4.24: Close up of meshing of composite laminate around the crack-tip…...171
Figure 4.25: Deformed state of FE models corresponding to mode-I and 22% mode-mix bending conditions…….172
Figure 4.26: Global load displacement results for delamination of a carbon-fiber/epoxy laminate under mode-I loading……..173

Figure 4.27: Global load displacement results for delamination of a carbon-fiber/epoxy laminate under 22% mode-mix conditions…….174
Figure 4.28: Global load displacement results for delamination of a carbon-fiber/epoxy laminate under mode-II loading…….174
Figure 5.1: Z-pinning in T-joints to increase delamination resistance…….178
Figure 5.2: DCB specimens of Z-pinned laminates modeled with cohesive layers acting as spring between two arms of the laminate……...179
Figure 5.3: Sketch of an anchored Z-pin in a sandwich panel……180
Fig A1: Ply layup and geometry for flat tapered laminate taken from [27]……..181
Fig A2: Curved tapered laminate with same layup and ply-dimensions as the flat laminate…….182
Figure A3: Planform view of plies 11-14 for curved laminate showing the fiber angles different from longitudinal direction…….182
Figure A4 (a) Sketch of the tapered laminate with appropriate boundary conditions at its ends. (b) Location of resin-rich layers above ply 4 and below ply 11 extending across the length of the laminate. (c) Resin-rich layers shown on cross-sectional view……... 184
Figure A5: Von-Mises stresses along the length of the laminate in regions R_A for curved and flat specimens of ply configuration A…….185
Figure A6: Von-Mises stresses along the length of the laminate in regions R_B for curved and flat specimens of ply configuration A……186
Figure A7: Von-Mises stresses along the length of the laminate in regions R_A for curved and flat specimens of ply configuration B…….187
Figure A8: Von-Mises stresses along the length of the laminate in regions R_B for curved and flat specimens of ply configuration B…….188

Chapter 1: Introduction and Literature Review

1.1 Background

Composite materials are attractive in engineering design because of their advanced properties like high stiffness, versatility and their ability to tailor their anisotropy to specific needs of the structure. The high specific stiffness and strength properties of composites are extremely valuable in aerospace applications. In addition to weight savings, composite materials such as Kevlar have high impact resistance which may be used to shield sensitive parts of the airplane skin with composites. For example, accidental damage to engine pylons that carry engine controls and fuel lines can be reduced with usage of composites. Composites are also thermally stable, corrosion resistant and have low electric conductivity when compared to metals.

Owing to these superior properties, laminated composites are increasingly being used as replacements for metals in many practical structures that include aerospace structures. Composites have been increasingly found a wide scale use in the airplane industry today, which is very well elaborated by its use in Boeing 787 Dreamliner as shown in Figure 1.1(a). Figure 1.1(b) shows how composites have overtaken metals such as steel, titanium and aluminum in their usage on the Boeing aircraft. In fact, half of the weight of Boeing's 787 Dreamliner comes from composites. Composite applications on aircraft include fairings, flight control surfaces, landing gear doors, leading and trailing edge panels on the wing and stabilizer, floor beams and floor boards, vertical and horizontal stabilizer primary structure, primary wing and fuselage structure, turbine engine fan blades and propellers.

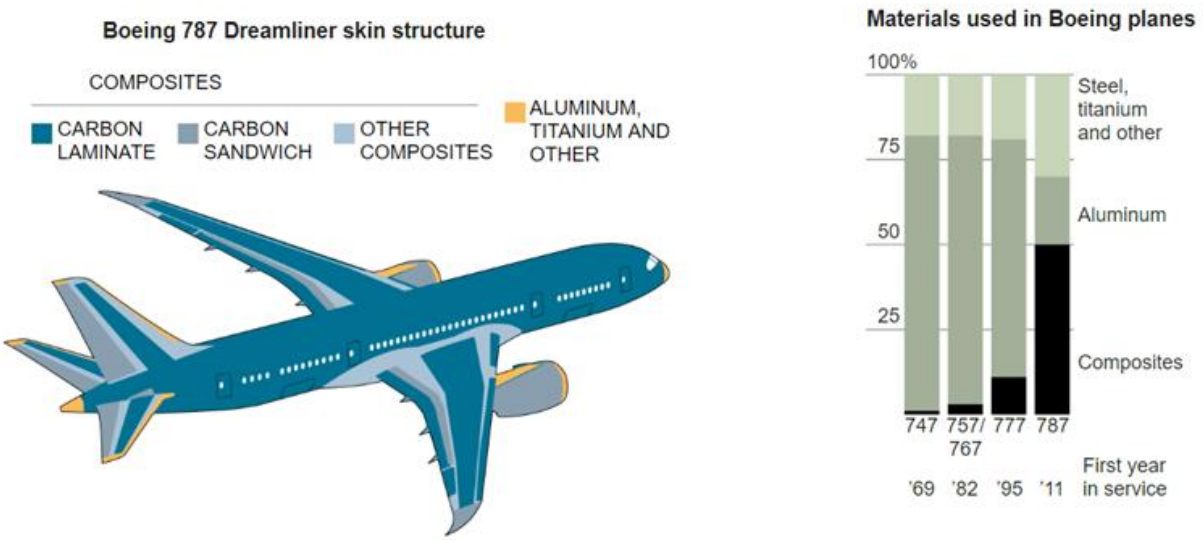

Figure 1.1 (a) A sketch of the outer skin of the Boeing 787 Dreamliner (b) A graph of the different materials used over time in Boeing planes [source: boeing.com]

Composites like any other kind of materials are prone to deterioration and damage. Delamination is the most important mode of failure that occurs in laminated composites as it can result from several different sources. Locations of geometric and material discontinuities are ripe locations for onset of composite delamination. For instance, tapering of composites is common where a change in thickness of the composite laminate is required. An example is the increased thickness at the root of helicopter blades where they connect to the hub. The manufacture of tapered sections in composite structures involve the inclusion of ply terminations that can be a source of stress concentrations.

In addition to tapering, composites may also be in the shape of curved geometries as observed in many engineering structures including pressure vessels, submarine hulls, wings and fuselages of airplanes, rocket fuselage, rotor blades and shafts etc. The taper

and curve of laminated composite not only allows the structure to comply with a desired shape but also permits structural tailoring by modulating the stiffness through its length. The sites of ply drop-offs have geometrical and material discontinuities which produces out-of-plane stresses potentially causing damage via delamination of the composite structure. Curved laminates in particular can generate high interlaminar normal stresses under bending. Bending will also arise in curved composites owing to temperature changes as a result of the difference in expansion coefficients in the plane and through the thickness of the composite. This will produce interlaminar normal stresses if the laminate is not free to deform

Geometrical and material discontinues are also produced in composite structures when two different segments of the structure have to be bonded together. Delamination is especially likely in co-bonded or secondary-bonded joints as the adhesive typically has a higher toughness than the matrix resin, driving the failure into the composite when the structure is subjected to external loads. A notch in a composite structure acts like an external crack resulting in high stresses in that region. Interlaminar normal and shear stresses are also produced at free edges where there are differences in Poisson's ratio between plies owing to different ply orientations. In addition to the geometry of the composite structure, external loads, in particular out-of-plane loading and impact loading on the composite laminate can trigger delamination.

1.2 Techniques to improve delamination resistance of composites

Several technologies have been proposed in literature to enhance composite delamination resistance. Some of the techniques are detailed below.

1.2.1 3D Weaving

3d weaving is a process of creating a special kind of 3D composites in which yarns from two sources are individually fed into a mechanism that weaves them together. Typically warp yarns are fed via an automated mechanism from one source into a container such that they can lifted at precise locations and angles for insertion of weft yarns. The automated mechanism of lifting the yarns can be controlled to create a specific pattern of interlinking to create several different components as complex as the ones shown in Figure 1.2 [1].

The mechanism of 3d-weaving can not only be automated to produce complex patterns, but it can also be manufactured to include through-thickness reinforcements that can be interlocked within the planar warp and weft weaves. Such a weaving mechanism is shown in Figure 1.3. [1]

While 3d weaving improve the delamination properties of the laminate, they have relatively weaker tension and shear properties that do not allow them to be extensively used in applications where 2d composites are utilized. Additionally, the in-plane properties and failure criteria of 3d woven composites are not clearly understood as there is a high degree of anisotropy from the nature of weaving.

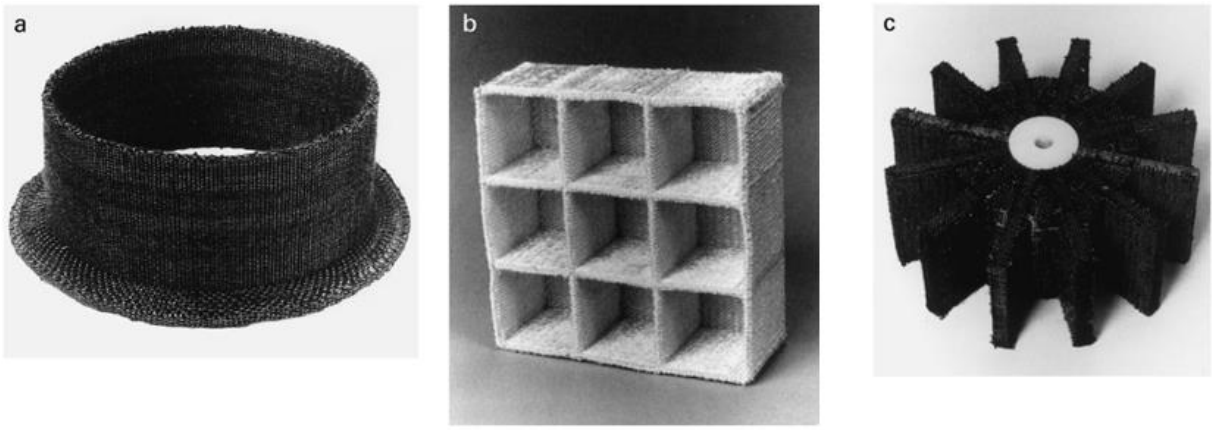

Figure 1.2: Examples of 3D woven preforms in the shape of a cylinder and flange, egg crates and turbine engine rotors [1]

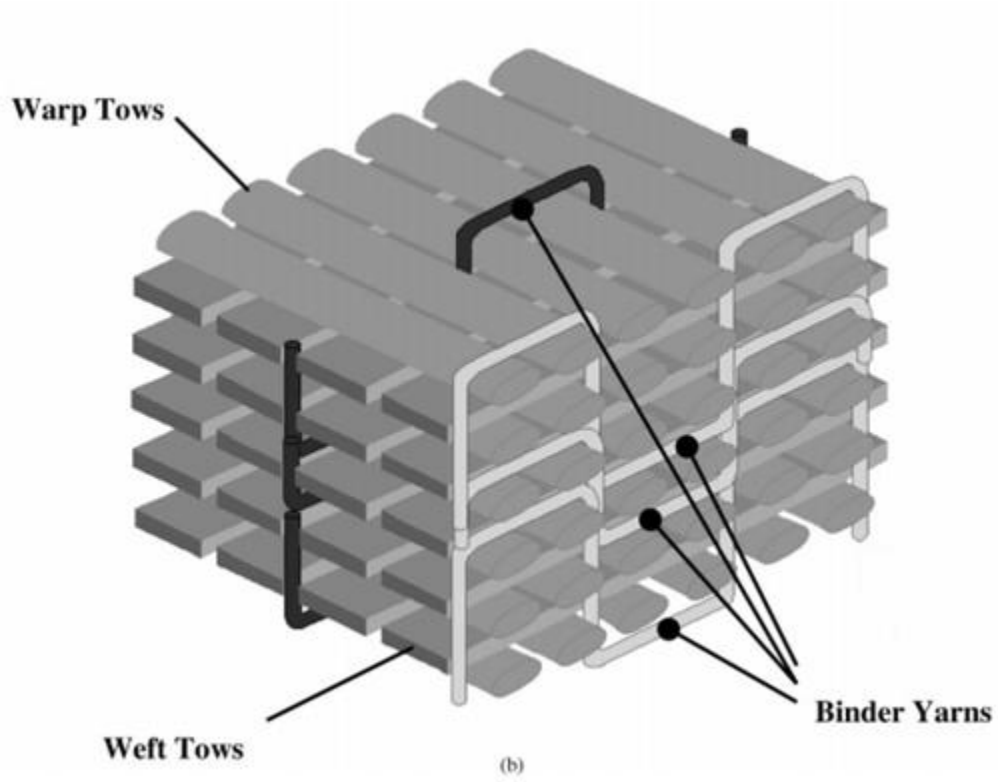

Figure 1.3: Weaving mechanism showing through-the-thickness yarns woven into a composite structure [1]

1.2.2 3d-Stitching

3d stitching is a technique in which yarns of a different fabric as the composite are inserted into a composite laminate in the through the thickness direction. The fibers inserted into the composite typically have high strength such as Kevlar, glass that can improve the through-the-thickness properties of the laminate. Judicious insertion of the stitching fabric can be used to increase the specific strength of the laminate by reducing the total weight of the composite laminate.

The stitching process can be automated via an industry sewing machine as shown in Figure 1.4 [2]. The automation process allows for variability in stitch density and stitch material based on the application. The advantage of stitching process is that it can be entirely automated with the ability to vary amount of stitching and the yarn material used for stitching to meet the application of the composite laminate. Stitching can also be locally performed on specific areas to repair a particular section of the composite laminate. However, the biggest disadvantage with the stitching process is that the process has to be performed only on dry, uncured composite preforms prior to resin infusion. If the composite fibers are infiltrated with matrix material, the stitching process can severely negatively affect the in-plane properties of the composite laminate. For the same reason, stitching cannot be used as a reinforcement technique on composite prepregs. In addition, the stitching technique is limited to planar or flat structures which can be fed into the sewing machine. With several of aerospace and other application requiring curved geometries, the automation process of stitching may not be viable in such cases.

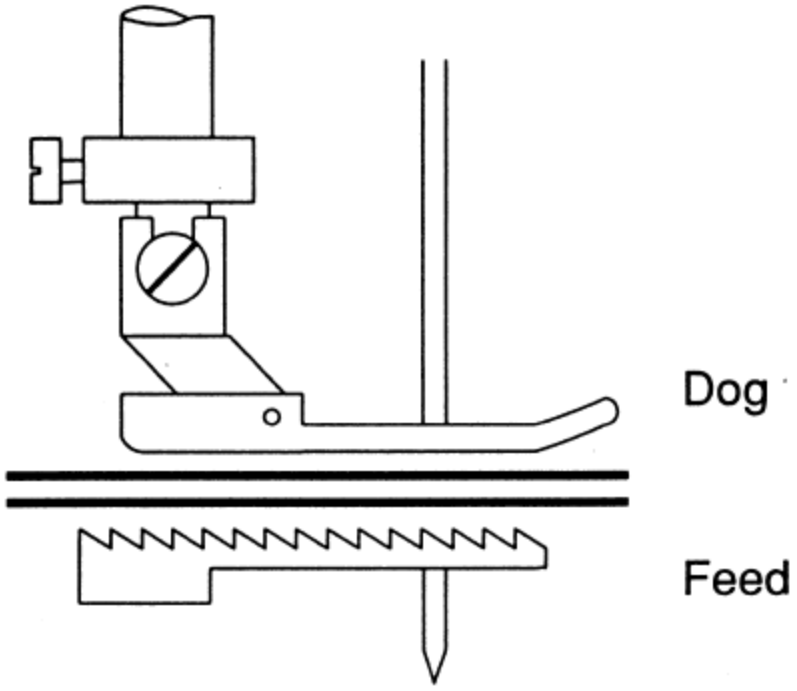

Figure 1.4: An illustration of stitching mechanism for a composite laminate [2]

1.2.3 Tufting

Tufting is a special version of stitching where the stitching yarn is only inserted into the dry preforms once. In this process, a dry preform is laid up and tows are inserted through a single needle through its layers as shown in Figure 1.5(a). Figure 1.5(b) shows how the depth and angle of tow insertion may be varied [3]. In tufted composite laminates, the yarn is not tied or interlocked with the adjacent loop, but the tuft is able to remain in place owing to frictional forces between the composite fibers and the tufting thread. Tufting is particularly ideal for applications where only a single side of the composite is accessible for repair or reinforcement.

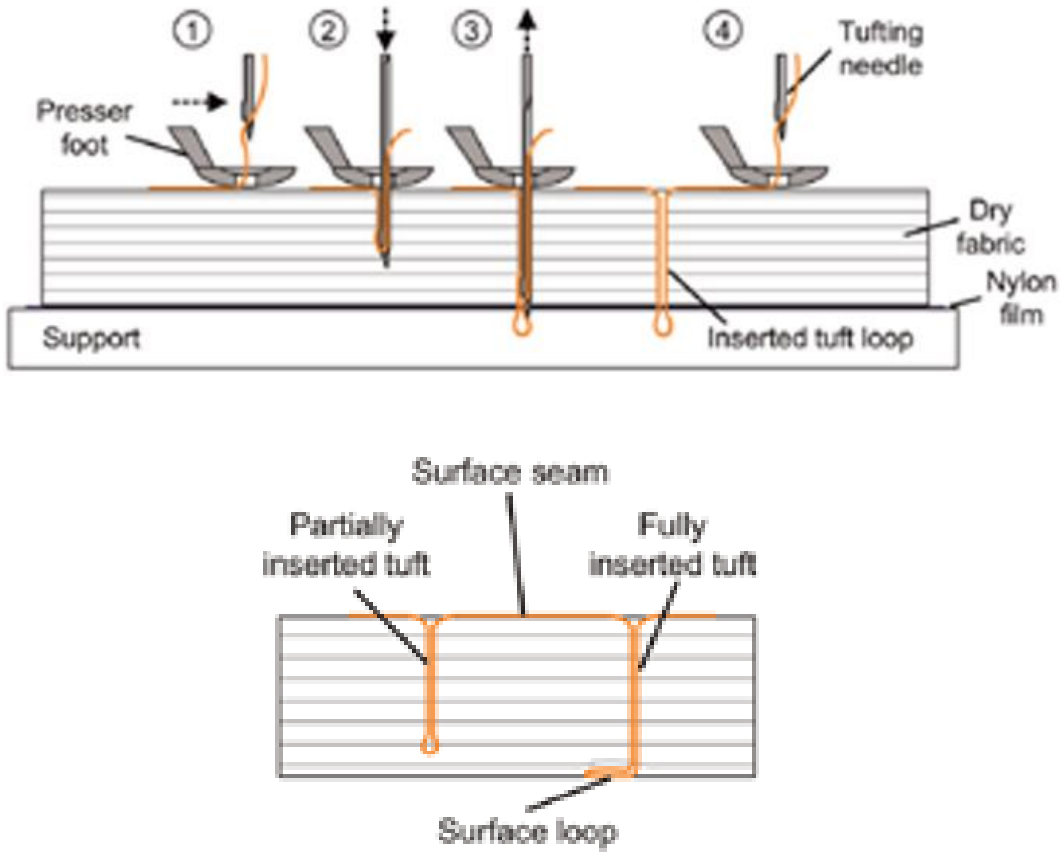

Figure 1.5: (a) Schematic of tufting mechanism (b) Partial and full penetration of tufted yarns [3]

1.2.4 Matrix Toughening

Matrix toughening is the process of adding foreign agents into the matrix of a composite laminate to strengthen the fracture properties of the matrix and thus the fracture toughness of the laminate. Rubber modification is an age-old technique of adding soft rubbery particles into the epoxy to improve its fracture toughness. The disadvantage of such a process is that it can diminish the elastic properties and yield strength of the matrix material.

A novel approach in matrix toughening is to use rigid, thermoplastic materials to toughen the matrix. Thermoplastic materials are able to increase fracture toughness of

the composite laminate through various mechanisms as shown in Figure 1.6 [4]. Thermoplastic materials at the interface of a crack tip can bind the two regions opposing the crack effectively reducing the magnitude of the load carried at the crack tip. Crack pinning is the phenomenon where the crack propagation is halted in the presence of thermoplastics in the matrix owing to their impenetrability. This allows for greater consumption of energy during crack propagation process. When the crack deflects from its original path, the surface area of the crack increases effectively increasing the energy required for crack propagation.

While matrix toughening can be an effective method to increase delamination toughness of the laminate, the understanding of the physics behind the toughening mechanisms is still incomplete. This limits the ability to effectively tailor the matrix since the relationship between particle density and fracture toughness is greatly variable across different specimens.

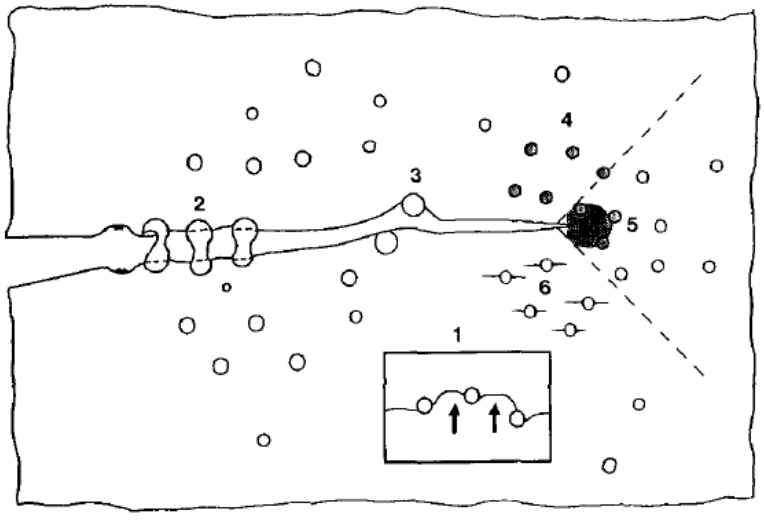

Figure 1.6: Schematic of different toughening mechanisms playing a role in thermoplastic-modified epoxy including crack bridging, particle bridging and crack deflection [4]

1.2.5 Interleaving

The matrix and fibers in a composite laminate are brittle and are unable to undergo any plastic deformation. This leads to transverse cracking under high interplay stresses and can be a major cause for delamination. Interleaving is the technique in which flexible layers are inserted into the composite between successive layers of composite preforms enhancing the damage tolerance of brittle composites. Figure 1.7 [5] shows a schematic of the interleaving technique. Modified epoxy resins such as carboxyl-terminated butadiene acrylonitrile (CTBN) and polyurethane (PU) have been shown to increase fracture toughness of the composite when added in thin layers as they are able to suppress inter-ply damage.

Figure 1.8 [6] shows SEM micrographs of fracture surfaces in interleaved composites. The figure shows presence of a large amount of interlayer residue at the interleaving film and fiber interface. Long hackles are observed at the interface causing a rough fracture surface and hence the ability for a high energy absorption during crack propagation process.

The biggest advantage of interleaving is that the increase fiber-matrix interfacial bonding forces crack propagation along interface between fiber and interleaf layer. The major source of concern for this technique, however, is that the success of the method depends on the compatibility of the interleaf material with the base matrix system. The wettability and solubility of interleaved particles in the resin solution is a deciding factor in the effectiveness of this technique in enhancing fracture toughness of the laminate.

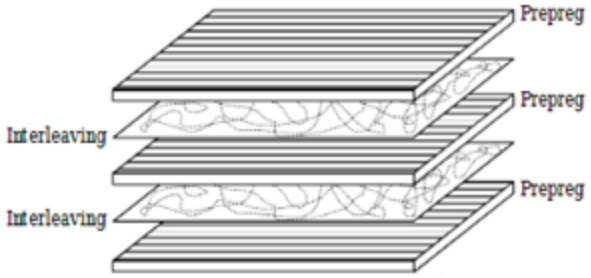

Figure 1.7: Schematic of lamination of composites and interleaving layers [5]

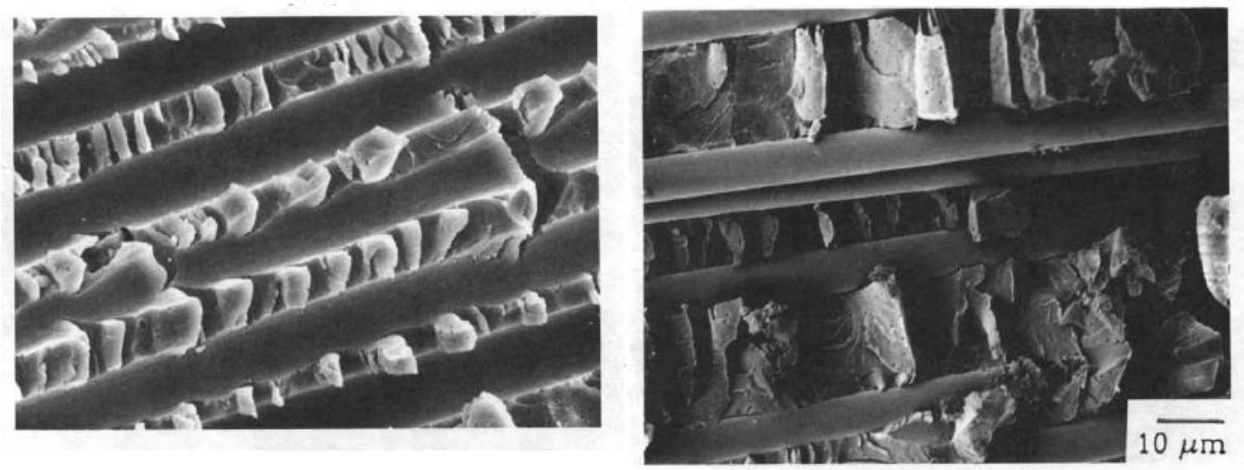

Figure 1.8: SEM micrographs of ENF fracture surfaces on both sides of a laminate interleaved with CTBN epoxy [6]

1.2.6 Z-pinning

Z-pinning is a technique in which reinforcing thin pins (called z-pins) of metal or composite fibers are inserted in the thickness or z-direction of the laminated composite structures to improve resistance to delamination. The z-pins comprise rods inserted serve to stitch the material together by a combination of friction and adhesion. Z-pins may be used across an entire panel or be applied locally on select areas where

reinforcement is desired. The typical size of a Z-pin is shown in Figure 1.9(a). Figure 1.9 (b) shows a close-up on Z-pins inserted into a composite laminate.

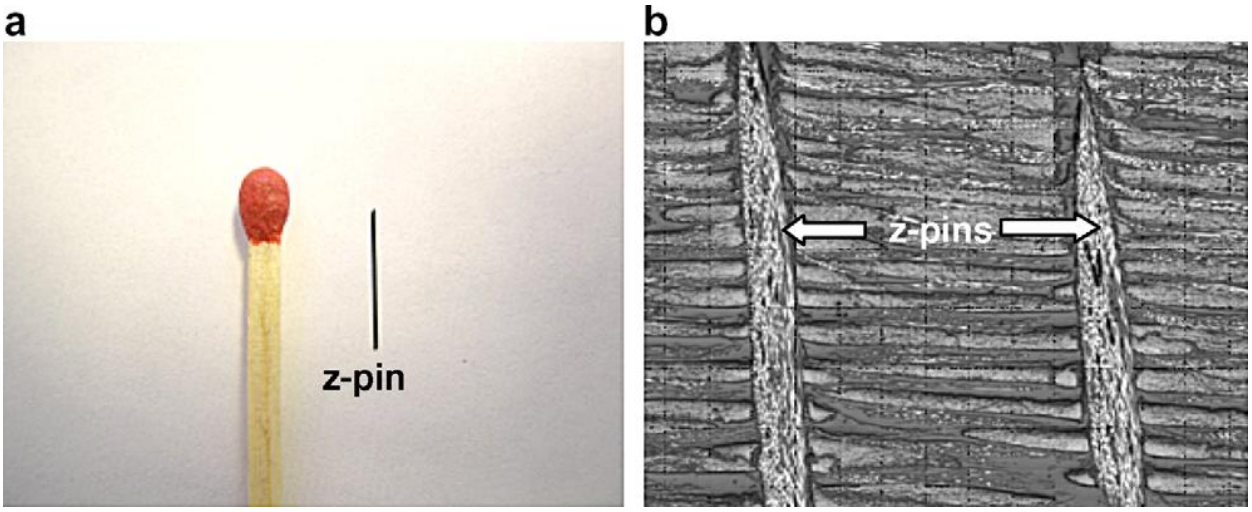

Figure 1.9 (a) Photograph showing the size of a typical Z-pin (b) close-up of Z-pins inside composite prepregs [8]

1.3 Z-pinning in composite laminates

Among the technical approaches to increase delamination resistance, z-pinning reinforcement appears attractive in that manufacturing process of z-pinned composite laminates is relatively simple and cost effective compared with other technologies. In this section, we take a closer look into the Z-pinning technology.

1.3.1 Manufacture of Z-pin composite laminates

Z-pinning of composite laminate is an extensive process that can be repetitive and time-consuming. Automatic insertion of z-pinning has been perfected thus reducing manufacturing cost and time needed for laminate reinforcement. A patented automation

called the UAZ insertion of Z-pins is shown in Figure 1.10 [7]. This technique of automated Z-pin insertion is performed by a special ultrasonic horn with a very high frequency in the range of 20 kHz. In this technique, Z-pins are initially inserted into a soft collapsible foam material as shown in Figure 1.11 in desired patterns based on required pin density and insertion angle. This pre-form is placed on a hard foam material which is laid on top of composite prepregs as shown in Figure 1.10. [8] The foam acts as a stabilizing medium for holding the pins during insertion process. Then, the high density ultrasonic horn is operated upon the low density foam effectively causing the foam to collapse. The compressive stress waves caused by the ultrasonic gun causes the prepregs to heat up locally at the point of pin insertion. This helps the pin insertion process by softening the matrix material. The collapse of the foam causes the Z-pins to penetrate into the composite prepregs underneath the foam. After pin insertion into the prepregs is complete, the foam layer is removed and excess pin ends are sheared away. The composite laminate is then cured via a conventional curing procedure.

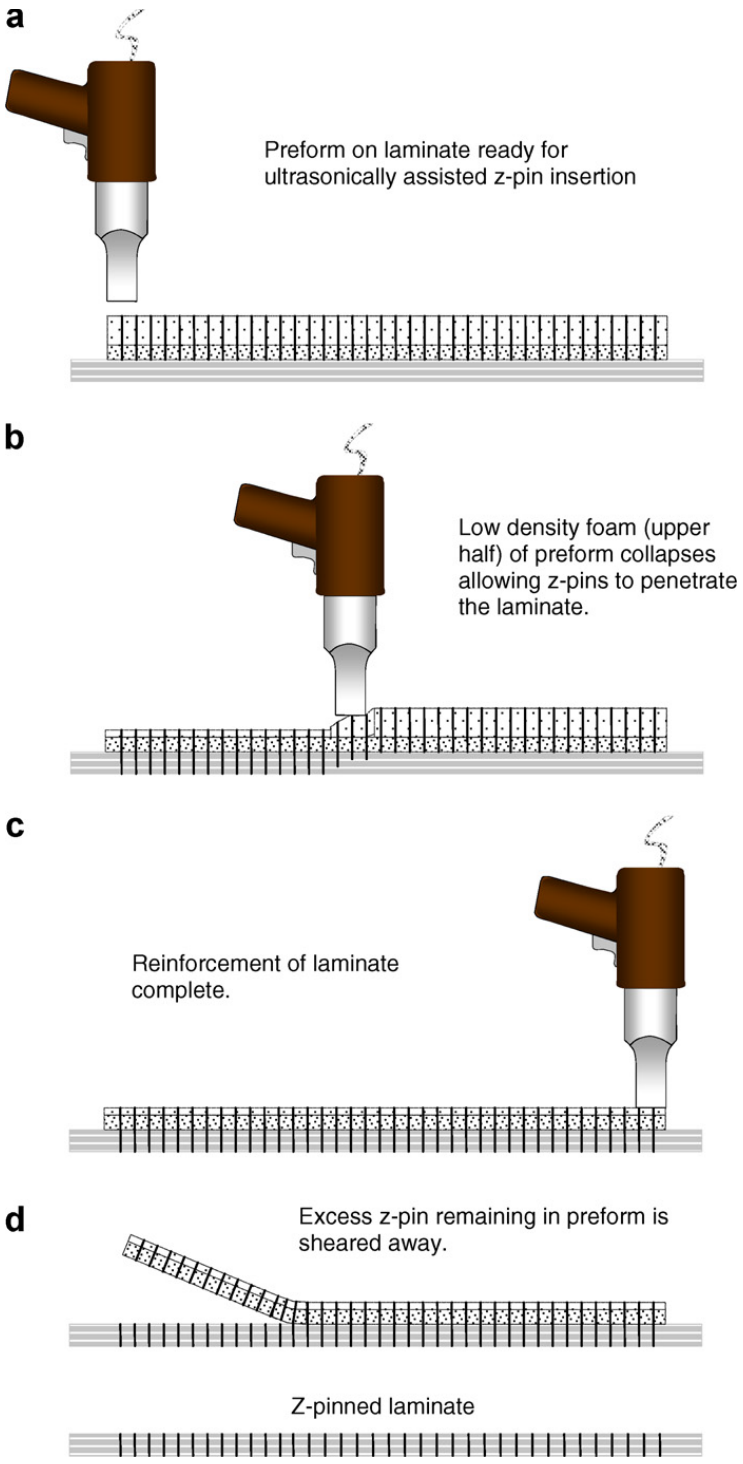

Figure 1.10: Z-pin automation technique using UAZ method [7]

Figure 1.11: Z-pins inserted into a soft collapsible foam ready for insertion into composite laminate [8]

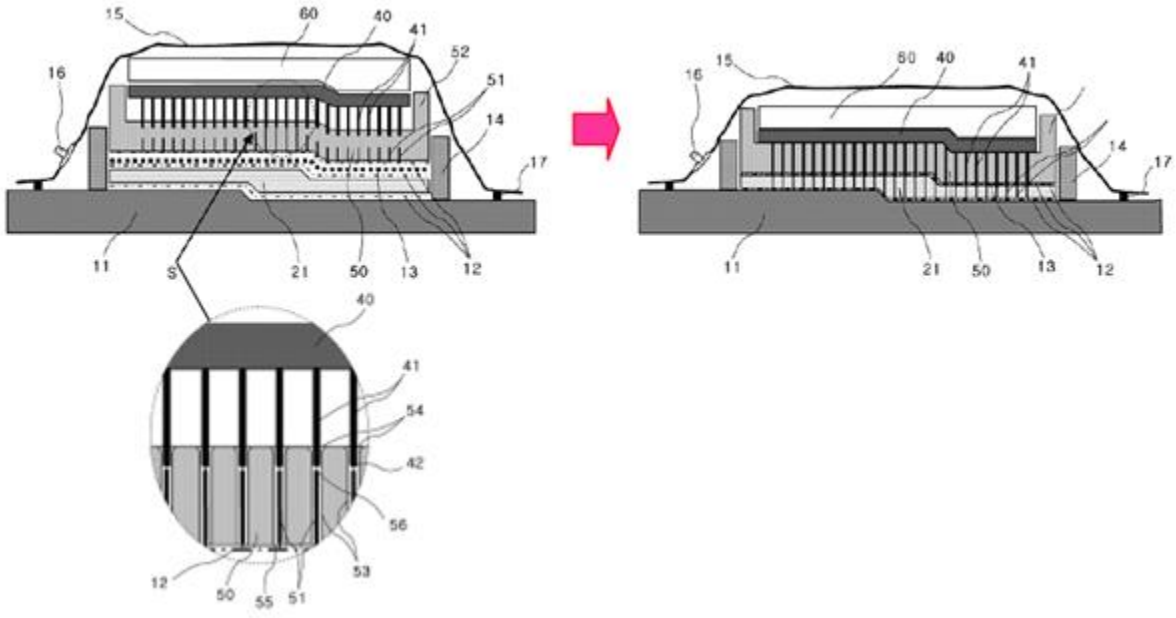

Figure 1.12: Z-pin insertion mechanism developed by Choi et. al. [9]

Choi et. al. [9] have developed a new z-pinning technique illustrated in Figure 1.12. In this technique, Z-pins are placed into vertical holes of a rigid fixture which is placed

upon the composite prepregs. Another fixture is placed on top which protruding knobs at the exact location of the Z-pins in the lower fixture. When a pressure is applied in the autoclave, the upper fixture pushes the lower fixture forcing the Z-pins to penetrate into the prepregs. This technique does not require a separate insertion and curing process and the fixtures can be used repeatedly on prepregs for Z-pin insertion.

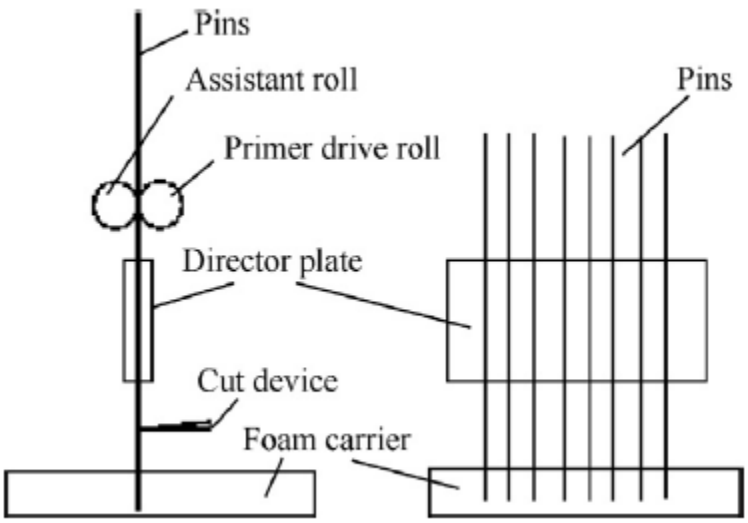

Figure 1.13: Schematic of insertion head for multiple Z-pin insertion developed by Qinghua et. al [10]

Qinghua et. al [10] have developed a new technology called the transitional insertion system which allows for insertion of multiple pins into the composite prepregs at the same time. Figure 1.13 shows a schematic diagram insertion heads where multiple pins are inserted into a foam carrier to a director plate. The pins are carefully directed into the plate by a feeding driver driven by a motor as shown in Figure 1.14. The compressive force between the drive rollers allows the pinto grip with the rollers via

friction and penetrate into the prepregs. During this process it is ensured that there is no relative sliding between the drive rollers and the pens to create perfect insertion angles into the composite prepregs. As soon as the pins are inserted at the required depth into the composite laminate, a cutter Cuts all the pins synchronously following which the foam is moved a unit step away from the rollers. This process is repeated for different regions of the foam carrier to create foam blocks as shown in Figure 1.15. The prototype device developed in the paper is able to insert 9 pins at the same time increasing the pin insertion efficiency greatly.

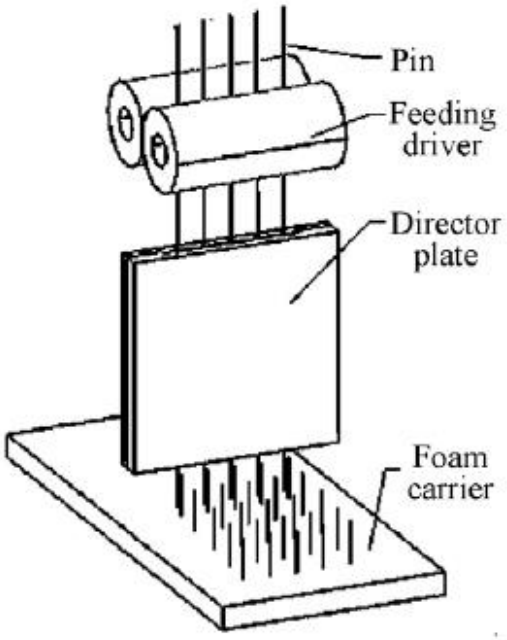

Figure 1.14: Device for feeding multiple straight pins into the director plate for Z-pin for multiple Z-pin insertion [10]

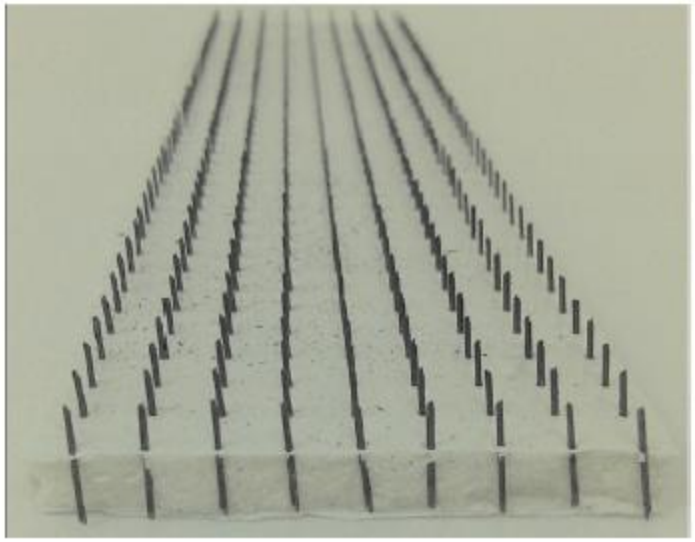

Figure 1.15: Z-pinned foam blocks inserted by multi-pin insertion technique [10]

1.3.2 Influence of Z-pin materials

Carbon fiber composites and metals are both good candidates for Z pinning of composite laminates. Pingkarawat et. al. [11] have presented a comparative study of Z-pins made of composite carbon fibers and metals in improving mode I fracture toughness and fatigue strength. Figure 1.16 shows the design of test equipment to measure pullout strengths of laminate reinforced with both metal and carbon fiber composite Z-pins. Based on the pullout tests, they observed that copper pans tend to fail via plastic deformations while stainless steel, titanium and carbon fiber have high strengths and pull out from the composite laminate instead.

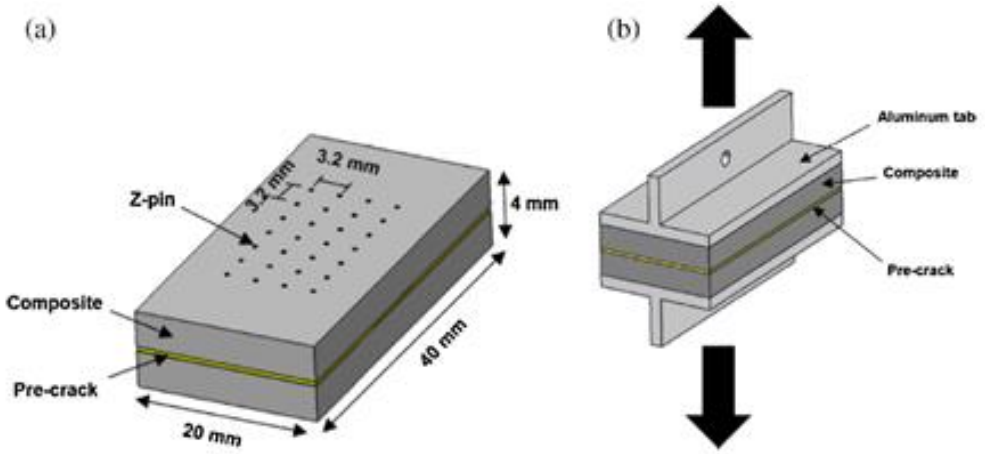

Figure 1.16: Test equipment to compare tensile pullout strengths of metal versus composite fiber Z-pins embedded in laminates [11]

The low tensile strength of copper also result in low delamination toughness of composite laminate to reinforce with copper pins. Figure 1.17 shows a plot of delamination fracture toughness versus crack length for laminates reinforced with various materials. The plot shows that the performance of titanium, steel and carbon fiber Z-Pins were comparable to each other. This is expected because since the pins pull out from the composite laminate, the pull out strengths are not dependent on the tensile strength of the Z-pins, but instead they depend on the strength of the pin-laminate interface.

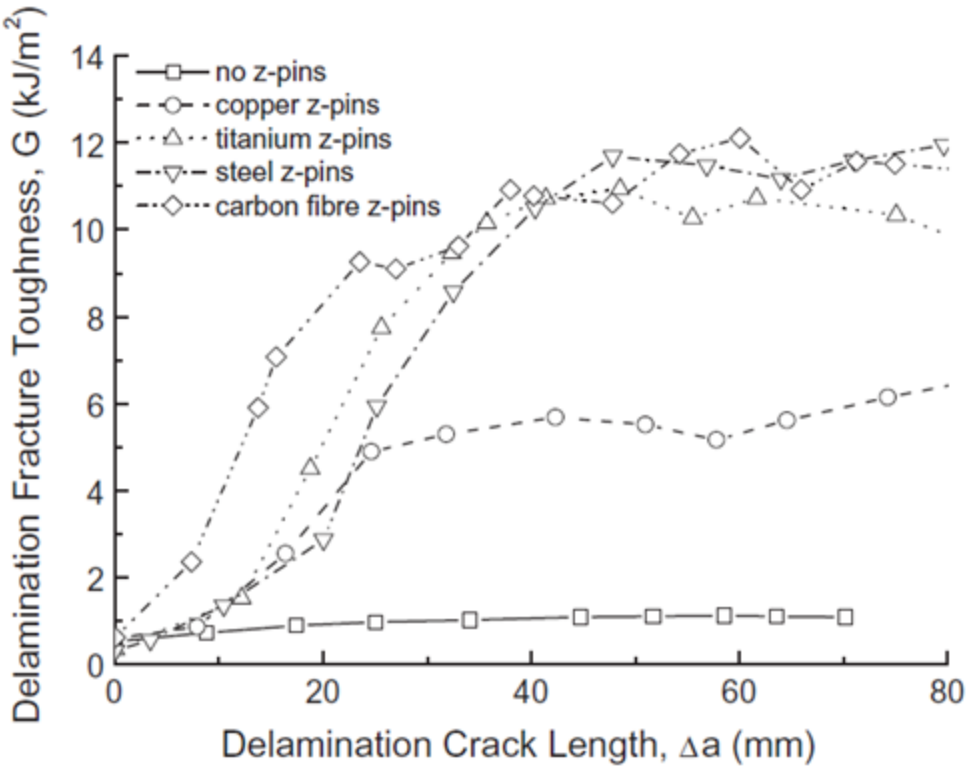

Figure 1.17: Crack growth curves for laminates reinforced with metal and composite fiber pins [11]

Tensile pullout strengths extracted for Titanium and Carbon fiber pins inserted in UD IMS Carbon-924 epoxy laminates through experiments performed by Cartie et. al. provided similar conclusions as shown in Figure 1.18. [12] The tensile strength of both pins were nearly similar since the weakest link in the composite was the pin-laminate interface.

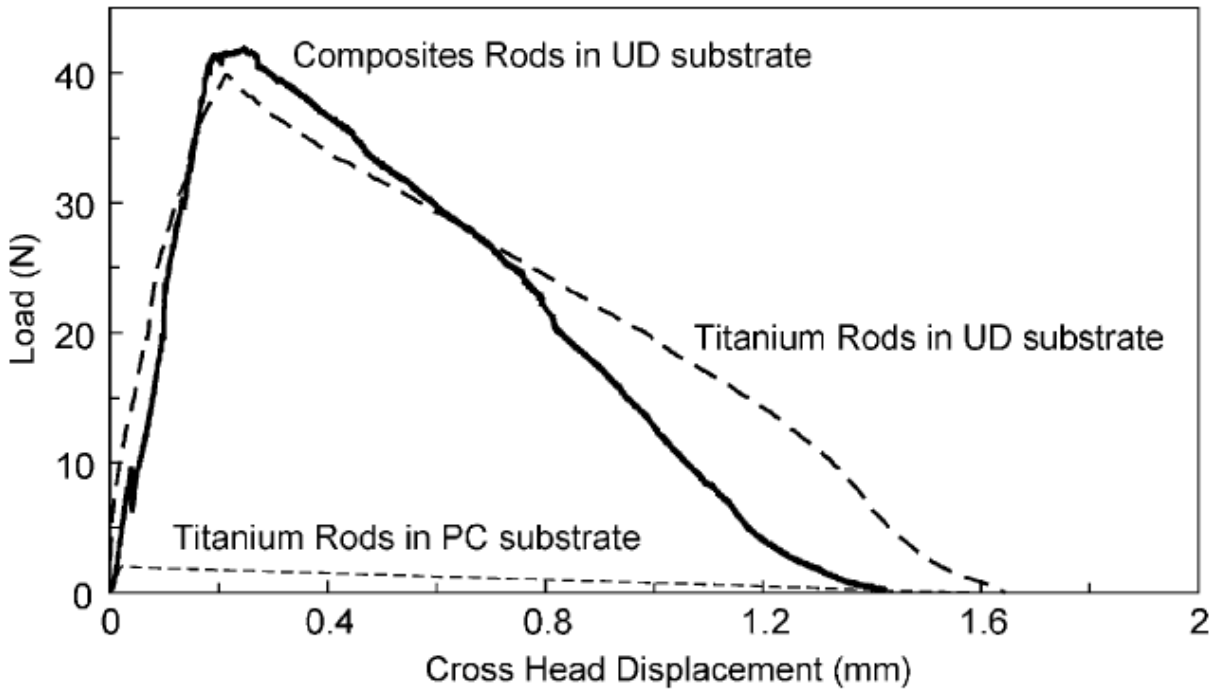

Figure 1.18: Tensile load versus displacement of Z-pinned specimens comparing pullout strengths of composite and titanium Z-pins [12]

For shear tests of single pin embedded in the laminate however, the pins showed different behavior based on pin material. For both carbon fiber inserts and Titanium pins, the laminate when examined in the pin-laminate interface showed substrate indentation as shown in Figures 1.19(a) and (b). The substrate indents plastically to accommodate lateral movement of the Z-pin at the interface. However, the plastic deformations with carbon fiber pins were much smaller compared to that of Titanium pins. This is explained due to the face that carbon fiber pins are brittle while the Titanium pins are more ductile. Titanium pin reinforced composites showed noticeable bending at two locations under shear loading- at the location of the pin-laminate interface and near the middle of the freestanding rod segment. In addition, for carbon

fiber reinforced laminates, numerous splits appeared in the Z-pin. Micrographs of the laminate specimens showed accumulation of debris in front of the composite pin.

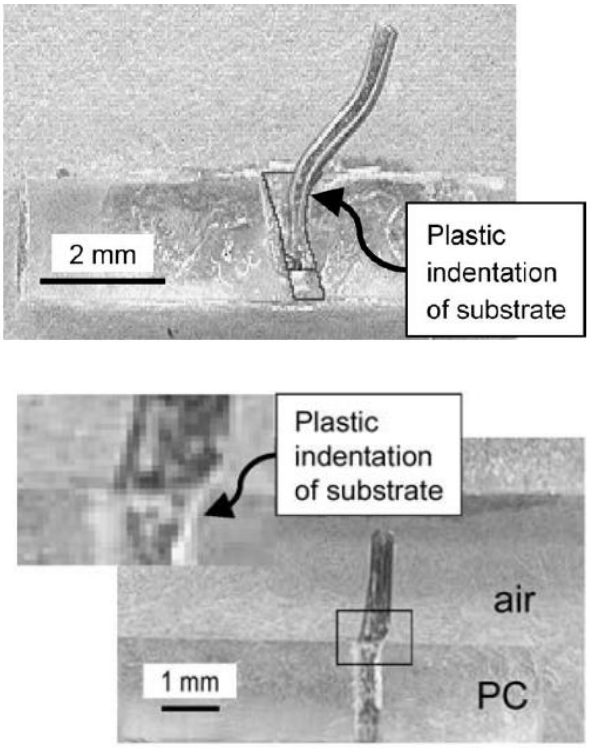

Figure 1.19: Deformed Z-pins and plastic indentation of substrate in composite laminate under shear loading for (a) Titanium pins (b) Composite fiber pins [12]

1.3.3 Influence of Z-pin insertion on laminate properties

The biggest disadvantage in the technique of z-pinning is the reduction of in-plane mechanical properties of the laminate due to the pins. The insertion of Z-pins into composite laminate changes the microstructure of the composite laminate and thus the properties of the laminate as well. SEM micrographs of Z-pin insertion in laminate show that when Z-pins are inserted into the laminate, the fibers of the laminate experience waviness around the region of Z-pins as they are forced aside. This

phenomenon is shown in Figure 1.20 [8]. The waviness angle is the angle subtended by the fiberes around the Z-pins and can vary across different types of laminate.

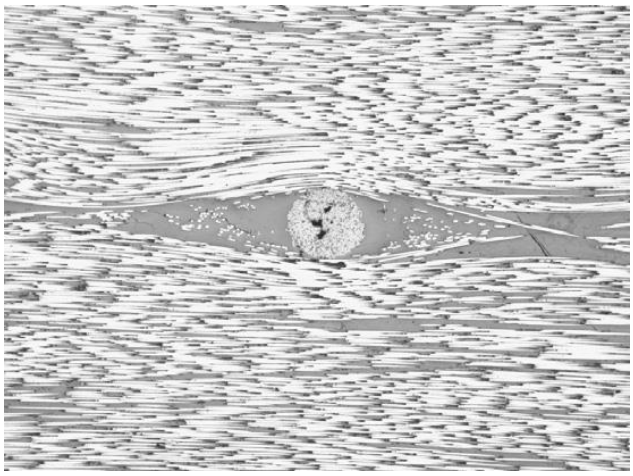

Figure 1.20: Fiber waviness in the composite laminate caused from Z-pin insertion [8]

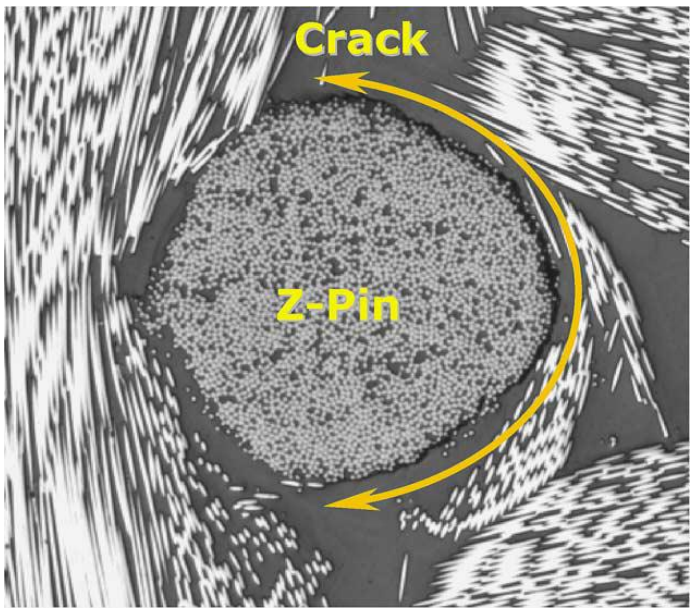

Figure 1.21: Resin-rich zones around Z-pin in composite laminate [13]

In addition to fiber waviness, the insertion of Z-pin creates resin rich zones around the Z-pin as shown in the SEM photo in Figure 1.21 [13]. Steeves and Fleck [14] performed a finite element simulation to quantify the applied stress versus axial strain response and the evolution of fibre waviness with load as shown in Figure 1.22. They observed tensile strength of the unidirectional composites is reduced by approximately 27% while the compressive strength is reduced by at least 30% due to the presence of the z-pins. Research by Sweeting and Thompson [13] showed that the predicted stress levels in the resin pocket around the Z-pin was much greater than the failure stress of the epoxy.

Owing to the mismatch of the thermal expansion coefficients of the Z-pins and the composite laminate, thermal stresses develop at the interface during the cure cycle. The axial thermal expansion of carbon pins is much lower than that of the laminate. Accordingly, Z-pins experience little change in their length, while the laminate undergoes a large contraction during the cooling process in the thickness direction. This induces axial compressive stress in the Z-pins and tensile stress in the laminate. FE modeling of the pin-laminate interface from the research of Sweeting and Thompson [13] predicted that the thermal residual stresses were higher than the failure stress of the resin, indicating that the interface was the weakest link in the Z-pin laminate.

.

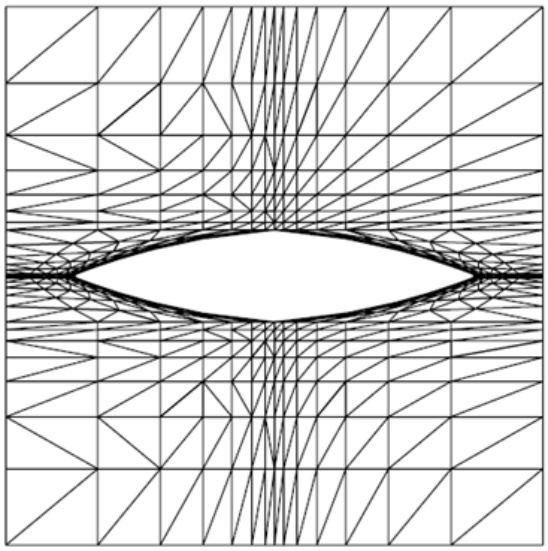

Figure 1.22: Finite element mesh for a Z-pin-laminate interface showing resin-rich pockets [14]

While Z-pinning can affect the in-plane properties of the composite, benefits to the properties in the through-the-thickness direction often outweigh any in-plane property reduction, especially in cases where delamination is of primary concern. For example, according to the data from Mouritz [8], the reduction in the in-plane stiffness properties caused by z-pinning is usually modest (typically under 5~15%) compared with the very large improvements in delamination toughness (up to nearly 500%). There is a trade-off between improving the through-thickness properties of the laminate and loss of in-plane stiffness and strength properties of the z-pinned laminate. The in-plane losses are proportional to the z-pin density in the laminate [9]. In order to limit the loss of in-plane properties of the laminate, it is imperative to extract the maximum potential in increasing delamination strength for a single z-pin. Then, z-pins can be selectively applied only to the delamination prone area instead of the entire laminate and the pin

density at the applied region can be tailored to minimize the reduction of in-plane properties caused by z-pins.

1.4 Z-pinning in sandwich panels

Composite sandwich structures are constructed using thin and stiff facesheets made of composite laminates, attached to a thick core composed of a light weight compliant material like foam or honeycomb .The stiff facesheets separated by the thick core allows for a high bending stiffness and an overall low density for the structure. The facesheets are the major load bearing components while the lightweight core supports the facesheets and provides shear strength and energy absorbing capability. Due to the high stiffness to weight ratio and tailorable properties, sandwich structures have proven to be a favorite in various engineering applications including aerospace, marine, automotive, windmills, building and consumer industries. For instance, the structural sandwich with PMI foam core has been successfully used in the fuselage of helicopter Ecureil EC120 as early as 1971 [15].

Due to the increased use of sandwich composites as structural members, their mechanical performance has been extensively investigated under various loading conditions. The low-density foam core, being a very soft material, may not provide enough out-of-plane stiffness and strength to the sandwich structure rendering it prone to damage when subject to local loading. Z-pinning provides a means of reinforcement in which composite or metal pins are inserted into the foam core at specific angles at regular intervals to strengthen the sandwich structure. Z-pin reinforcement can be implemented via a K-Cor or X-Cor pin bonding with the facesheets. When the

protrusions of the pins outside the foam core are folded on either sides of the pin and bonded to the facesheet using an adhesive layer, it is known as K-Cor. In an X-Cor type of construction the reinforcing pins penetrate into the facesheets. Therefore, the connection between facesheet and pins provide the core-facesheet interface strength in X-Cor, whereas, in K-Cor sandwich, the reinforced core and facesheets are glued by adhesive. The length of the pin beyond the facesheet either anchoring into the facesheet or laid over the facesheet is called reveal length. This is illustrated in Figure 1.23. Figure 1.24 shows a Z-pinned sandwich specimen and the core of the specimen.

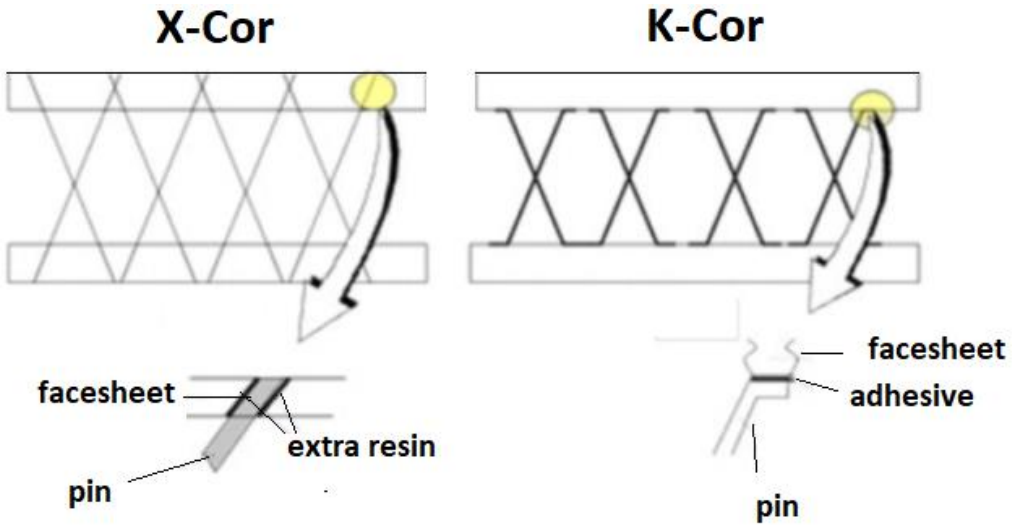

Figure 1.23: Schematic of X-Cor and K-Cor composites

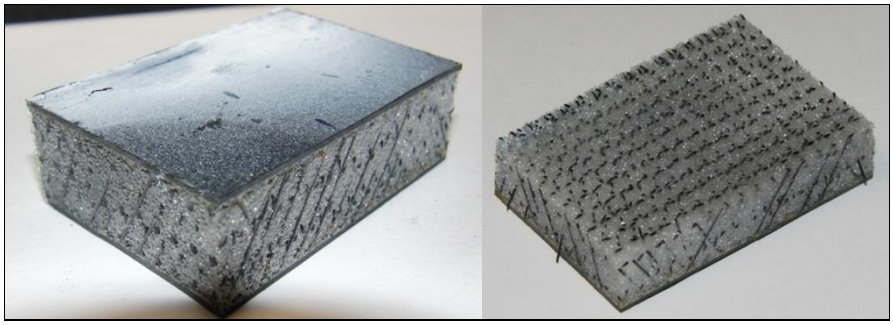

Figure 1.24 A Z-pinned sandwich specimen (left) as received, (right) with top face sheet removed

1.5 Numerical methods to model composite delamination

The understanding of the physics of Z-pinned composite laminates, sandwiches and composite delamination can be attained by accurate computational models. Accordingly, there is a strong need for development of predictive models for damage initiation, propagation and failure of composite structures. The requirement for these models is not only to predict the rate of delamination growth accurately but also that they apply to realistic composite geometries.

Cohesive zone models (CZM) serve as good methodologies in conjunction with FEM to simulate damage in real composite structures. The CZM technique is a unique combination of the concept of strain energy release rate as a criterion used in fracture mechanics for crack propagation and the damage mechanics of a non-linear process zone ahead of the crack tip described in terms of stiffness degradation. In a cohesive zone model (CZM), cohesive elements are placed in the path of potential crack path and they are governed by a prescribed traction-separation displacement law to simulate delamination.

The idea of a cohesive zone model can be traced back to the 1960's although its use in crack propagation grew vastly only recently. It is implemented into FEM as one of the two following ways- by either inserting interface elements in the potential crack path of the laminate [16] or by specifying a cohesive property as a traction-separation law between two plies of the composite laminate [17]. The latter is the limiting case of the former approach as the interface element thickness approaches zero. A variety of traction-separation curves are present in literature [18], but the simplest and the most common form is the bi-linear traction law where the relationship between contact stress

and displacements consists of a linear elastic region of a high stiffness followed by a linear softening region. A typical bilinear traction-separation law is shown in Figure 1.25. A dimensionless damage coefficient, D is associated to the cohesive region when the contact stresses reach a critical value. At this point, D is equal to 0 and damage is initiated. The value of the damage coefficient linearly increases to a value of 1 at the maximum separation displacement.

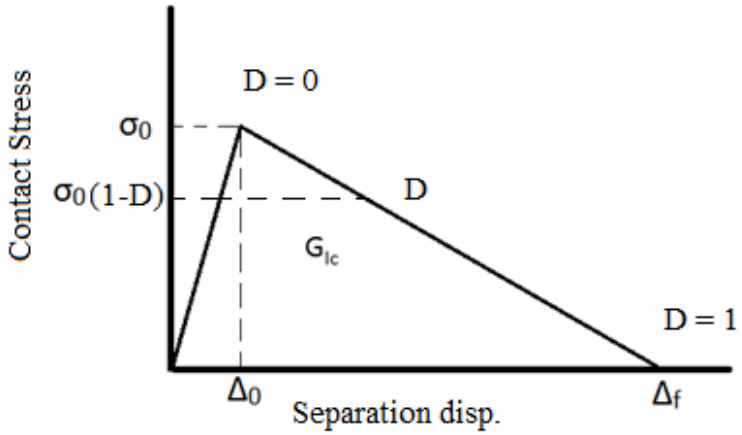

Figure. 1.25: Bi-linear traction separation law for a CZM

1.6 Motivation and Objectives of this research

1.6.1: Novel techniques for Z-pinning in composite laminates

Literature survey of Z-pinned laminates detailed above show that the pin-facesheet interface is the weakest link in the composite laminate. Typical DCB tests for Z-pinned laminates show that under mode-I delamination of the composite, Z-pins pull out from the laminate as shown in Figure 1.26 [19].

Accordingly, improving the pullout strength increases the delamination strength of the laminate. In the study presented in this research, we attempt to achieve significant

enhancement over the currently available z-pinning technology by increasing mechanical interlocking of the pins in the laminate. Z-pin reinforced laminates are traditionally manufactured by inserting the pins vertically into the laminate. However, in the present work, a method is considered in which pins are inserted at an angle to the vertical to enhance delamination resistance under tensile loading. When the z-pin is inserted with an angle, not only the contact area of the z-pin with laminate, but also mechanical interlocking in the loading direction can significantly increase. Angled z-pin have been considered for composite sandwich structures to increase shear and compressive properties of the foam. In addition, a novel variety of pin, namely the threaded pin is examined as a candidate for reinforcement of composite laminates via increase in mechanical interlocking.

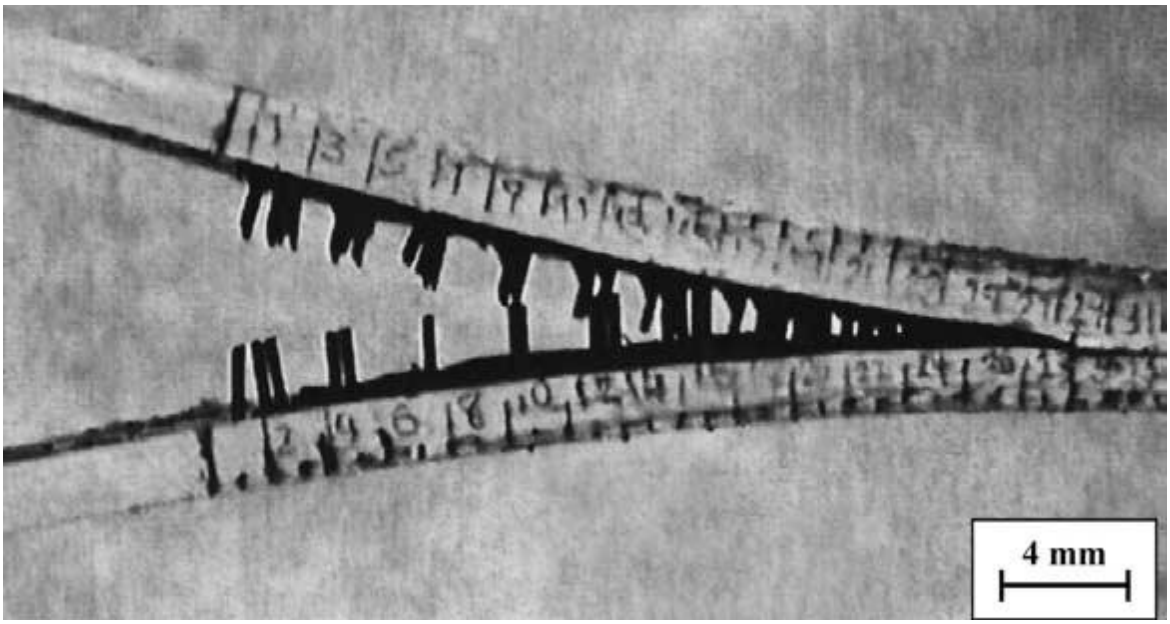

Figure 1.26: Z-pin pullout under DCB tests for mode-I crack propagation [19]

Threaded pins are commercially available in different sizes. These pins have ridges and grooves on the outer surface which increase pin-epoxy contact area. During curing of the laminate, the epoxy occupies the pockets between these ridges and increases the mechanical interlocking of the pin with the laminate. In addition, a simple modification to the current technique of z-pinning is to use pins of longer lengths and anchor the reveal lengths of the pins on to the laminate surface. These reveal lengths are flattened onto the laminate before curing allowing for a greater resistance to pin pullout under delamination conditions. Both threaded pins and anchored pins are expected to arrest crack growth across the laminate more effectively than conventional pin inserts.

Research by Sweeting and Thompson [13] indicates that residual stresses in the pin-laminate interface can be a limiting factor under out-of-plane loading. Accordingly, we investigate the effect of different pin materials in pullout strengths. The research related to Z-pinning techniques is presented in Chapter 2 of this dissertation.

1.6.2 Computational-Analytical modeling of Z-pinned Sandwich Structures

In conventional sandwich structures, the interface between the face sheet and the core is considered to be the weak link as disbonding may occur at this interface. In the sandwich composite with Z-pin truss structure in the core, or X-Cor/K-Cor sandwich, the pins produce pin-facesheet interaction that affect the behavior of the sandwich. For a Z-pinned sandwich structure, the pin truss geometry is an important part of the design and different kinds of pin geometries have been studied in the literature. However, bulk of the studies on sandwich structures with pin-reinforced foam cores are based on

experimental measurements and analytical and computational studies on the performance of Z-pin sandwich structures have been limited.

Analytical models have been proposed in a few studies in which the effect of the foam is included by modeling the foam as a spring (Winkler) foundation on the pins. Cartie et al. [20] provided empirical relations for spring constant of the foundation and verified it by experiments involving pulling of the pin through a foam material. This was corroborated by Tao Liu et al. [21], by modeling the foundation springs in both in-plane out-of-plane directions. In these studies, it was reported that the foam had little effect on the stiffness of the structure, but it stabilizes the structure by increasing its strength by delaying pin buckling. Tao Liu et al [21] developed a micromechanics-based model to calculate the effective properties of pin-reinforced foam cores and derived analytical formulae for the effective elastic–plastic properties of pin-reinforced foam cores with either a pyramidal or tetrahedral arrangement of pin reinforcements.

In the present research, we focus on modeling the out-of-plane compressive and shear stiffness and strength of X-Cor sandwich structures where pins are aligned in a pyramidal geometry. A model based on the assumptions of a perfect pin geometry with rigid connection to the facesheet overestimates the stiffness and strength values. Accordingly, the study presented in this paper has been motivated in recognition of the need for a comprehensive analytical and computational model to understand the physics of the sandwich structure and to estimate its performance with particular focus on individual components of the structure and the interaction between them. The current paper is focused on developing appropriate macro-mechanical models that account for the meso-structural details unique to X-Cor composite sandwich panels.

The new modeling approach proposed accounts for geometric and material imperfections of the pin under compression and imperfect bonding between the pin and the facesheet through interface. The pin boundary conditions are extracted through finite element (FE) models constructed via ABAQUS. Pin-foam interaction is studied and incorporated in estimating sandwich strengths. The pin-facesheet interface strength determines the pin pullout under tension and is appropriately incorporated into the model. The research related to modeling of sandwich structures is presented in Chapter 3 of this dissertation.

1.6.3 Numerical Techniques to Model Composite Delamination

Cohesive Zone Modeling (CZM) has been shown to be an effective tool in modeling composite delamination. Finite element analyses of laminate models using CZM typically has severe convergence issues. This results as a consequence of the softening part of the cohesive zone law that leads to a negative value for tangential stiffness and hence failure of the Newton-Raphson method when it comes to solving the FE problem. Various approaches have been used to solve convergence issues in literature, but these schemes require some significant effort to implement and can give unrealistic results. Viscous regularization is one common numerical technique used to combat the convergence problem, but the solution obtained heavily depends on the viscous regularization parameter used in the model. In Chapter 4 of this dissertation, we explore the approach of solving the FE problem dynamically with material damping included in the model to dissipate energy during element separation under cohesive law. This approach is used in models for Z-pinned laminates to model Z-pin separation from the

laminate. Experimental specimens tested in Chapter 2 of this dissertation have been validated by computational model using the dynamic CZM approach presented in Chapter 4.

Chapter 2: Novel Z-pinning in Composite Laminated Structures

2.1 Introduction

Experiments on Z-pinned laminates under mode-I crack propagation show that the Z-pins are typically pulled out through the laminate. This indicates lack of exploiting the full potential of the Z-pin capabilities in enhancing the delamination strength of the laminate. Accordingly, our research in this chapter is focused in developing novel techniques for Z-pinning based on improving the mechanical interlocking of the Z-pins with the composite laminate. Towards this end, three kinds of Z-pinning are studied- angled pin insertion, threaded pin insertion and anchoring of Z-pins on the outer surface of the laminate. We study the bridging properties and delamination resistance of Z-pins under these novel techniques through computational modeling and experiments. Additionally, we also investigate the effect of galvanic corrosion on the properties of laminates reinforced with steel Z-pins.

2.2 Specimen preparation and pullout tests

Laminates reinforced with various Z-pin insertions studied in this chapter were compared for their reinforcement properties through pullout tests under tensile and shear loading conditions. For this purpose, composite laminates were manufactured

from IM8/8552-epoxy prepregs through which Z-pins were manually inserted. Three types of improvements for z-pinning are investigated in this work: angled pin insertion, threaded pin insertion and anchoring pins. For angled pin insertions, four different pin insertion angles of 0^o, 15^o, 30^o, 45^o were used in the test specimens. To manufacture composite laminates with angled pin insertions, guides were made from acrylic plastic material by punching holes through plastic blocks at precise angles in a laser cutting machine. The machine precisely measures the dimension of the guide before firing laser at the intended locations for the cuts. Guides manufactured thus with corresponding pin insertion angles are shown in Figure 2.1.

To test the pullout strengths of the laminates reinforced with Z-pins, we manufacture composite specimens with a pre-crack in the center of the laminate. The Z-pins inserted into the laminate then act as bridging components between the two halves of the specimen. For our specimens, prepregs were stacked according to the ply configuration, $[0/90/90/0]_{2S}$ with Teflon at mid layer to represent a pre-crack. A Teflon layer was also laid out on the top surface of the topmost ply after which the guides were placed on them. The Teflon layer allows for easy disengaging of the guides after curing of the laminate. Pins were then manually, and carefully inserted by punching them through the guides into the prepregs according to the geometric configuration shown in Figure 2.2. This figure also shows the direction of insertion for angled pin insertions. The pins are separated by 8 mm apart in a square configuration such that for angled pin insertions, the direction of the pin is cyclically consistent.

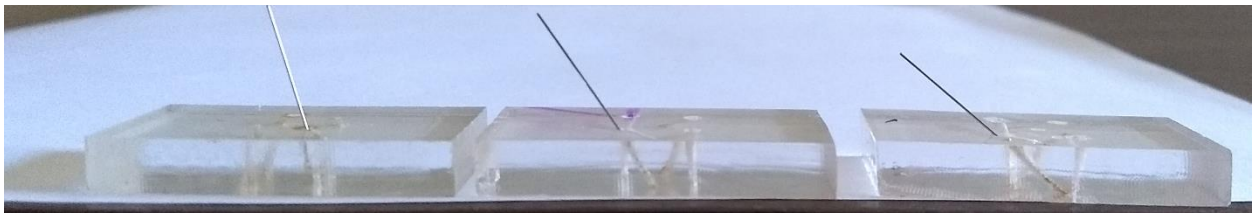

Figure 2.1: A single pin inserted through acrylic guides showing the varying degrees of pin insertion angle

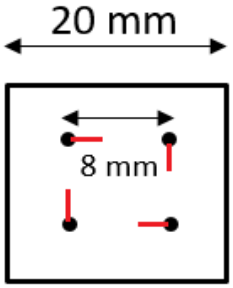

Figure 2.2: Top view of laminate geometry for specimens tested for influence of pin insertion angle

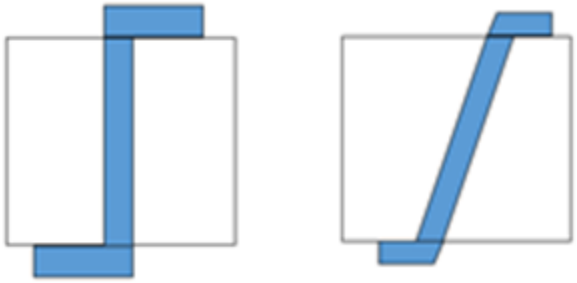

Figure 2.3: Reveal lengths of pin flattened on the laminate surface to anchor pin

For threaded pin insertions, the prepregs were first pierced with smooth pins of diameter smaller than the outer diameter of the threaded pin. The threaded pins were then inserted into the grooves created inside the prepreg layers. For laminates with anchored pin inserts, pins were flattened on the outer surface of the laminate as shown in Figure 2.3 such that the flattened segments of the pins is equal to 3 mm. Anchored pin specimens with angled pin insertions were flattened so that the reveal lengths

formed an obtuse angle with the inserted portion of the pins as shown in Figure 2.3. The laminate surfaces of anchored pin specimens were covered with two layers of 0^o plies on top and bottom to allow for uniform bonding with loading plates. Specimens were prepared initially in batches on a single stack of prepregs as shown in Figure 2.4(a). The excess pin ends were then trimmed off with a shear cutter and placed in the oven with a heavy metal plate on top to apply pressure. The laminate was then cured in the oven at 130^o C after which it was trimmed and cut into smaller specimens, ready for testing as shown in Figure 2.4(b).

Figure 2.4(a) A batch of reinforced specimens before curing, (b) Cured laminate trimmed into smaller specimens

Test specimens with various pin inserts were manufactured according to geometric configuration shown in Figure 2.2 for evaluating pin pullout strengths. The specimens were tested for their tensile and shear pullout strengths by loading it on an IMADA load frame (model MX 500) equipped with Z2H-440 2 kN load cell with a resolution of 1 N and displacement gauge with a resolution of 0.01 mm. as shown in Figures 2.5 and 2.6. Laminate specimens were bonded to the plates which were attached to the

fixture through a ball and socket connector for tensile testing and a hinged connection for shear testing as shown in the figures. The ball and socket connectors ensure that the load on the blocks and thus on the specimens is purely vertical thus simulating a mode-I type loading condition. Particular attention was given toward attaching of the specimens to the plate symmetrically to avoid any rotational effects during loading. For shear testing, in accordance to the guidelines provided by ASTM (C273 manual), the plate length was chosen so that the line of action of the direct tensile or compressive force passes through the specimen tested as shown in the Figure. 2.6.

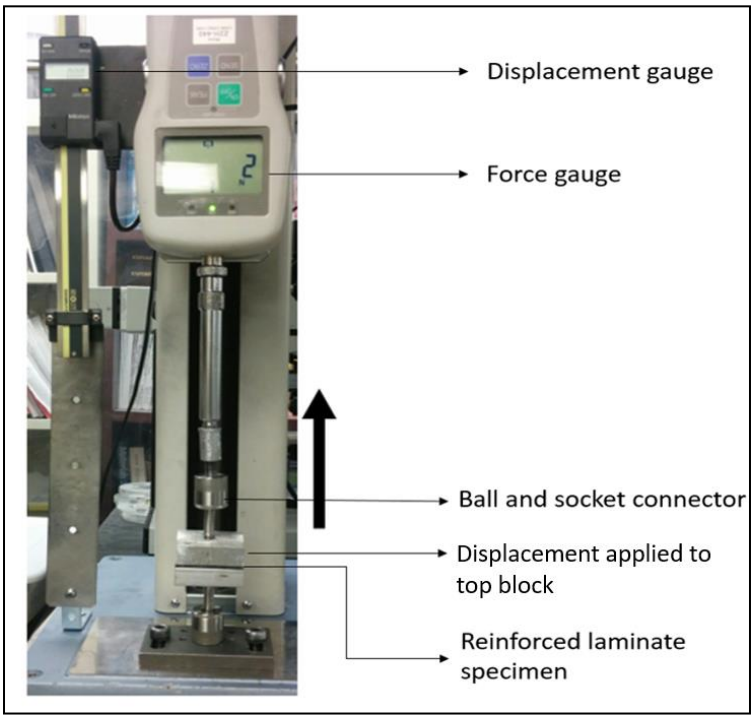

Figure 2.5: IMADA load frame used for testing of reinforced laminate strengths under tensile loading

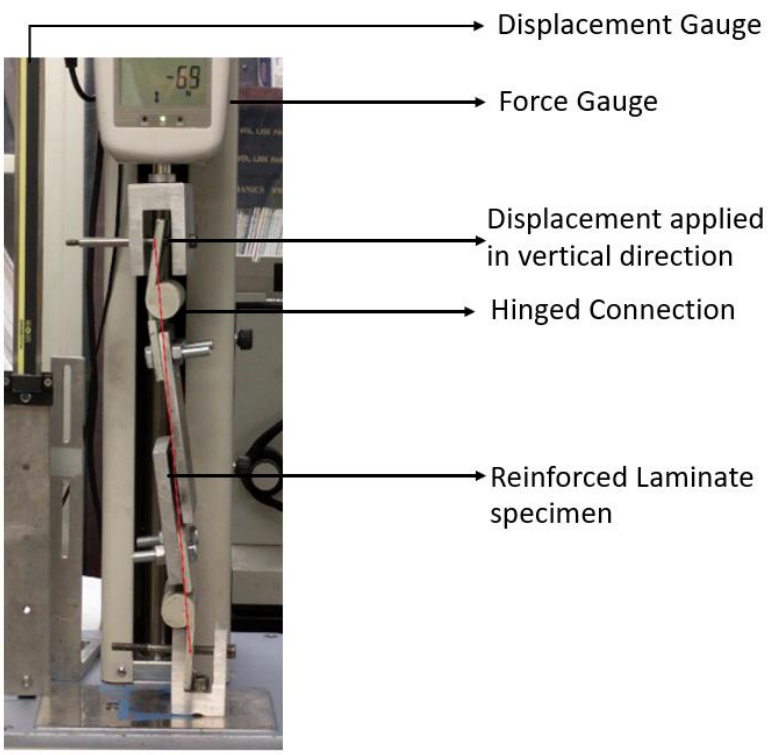

Figure 2.6: IMADA load frame used for testing of reinforced laminate strengths under shear loading

2.3 Angled pin insertion

2.3.1 Linear FE Analysis

A composite laminate reinforced with Z-pins shows an increase in the delamination resistance in Mode I (opening), Mode II (sliding) and mixed mode (opening and sliding). The pin bridging strengths under tensile and shear loading conditions may be tested out by performing pullout tests in corresponding loading directions. In this section, the performance of a single pin reinforcement embedded in a laminate is analyzed for different loading conditions and angles of the pin. Towards this end,

finite element models were constructed in ABAQUS as shown below in Figure 2.7. Four different pin insertion angles are considered for this analysis- 0^o, 15^o, 30^o, 45^o.

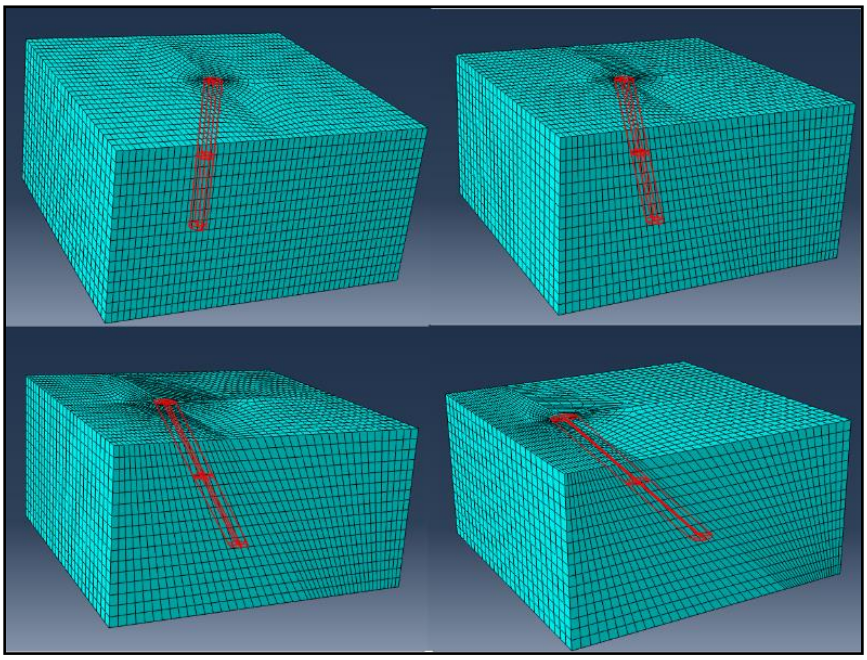

Figure 2.7: ABAQUS models of a single pin embedded in a composite laminate at 0^o, 15^o, 30^o and 45^o to the vertical

The geometrical and material properties of the laminate and the pin used in the model are given in Table 2.1. The stiffness of the Z-pin reinforced laminate could serve as a measure of its delamination resistance. Accordingly, the stiffness of the laminate was obtained from the FE model for each insertion angle under two different conditions- a) before delamination of the laminate, b) after delamination with a pre-crack at the mid-plane of the laminate. Figures 2.8 and 2.9 show the schematic for these two conditions on a pin reinforced laminate for tensile and shear loading conditions respectively. Two types of bonding between the pin and the laminate were considered. For perfect bonding the pin and the laminate will move

together at the interface. A more realistic kind of bonding with adhesive material at the interface of the pin-laminate was also considered with thickness of the adhesive layer equal to 10% that of the radius of the pin. The modulus of the adhesive was assumed to be E = 4.7 GPa, which is epoxy modulus.

Table 2.1: Material and geometric properties of pin and laminate used in FE models

Property	**Value**
Pin Material	Steel with E = 200 GPa and $\nu = 0.3$
Pin diameter	0.51 mm
Pin angle with vertical	0^o, 15^o, 30^o, 45^o
Laminate material	IM8 with E_L = 163 GPa, E_T = 10.7 GPa ν_{LT} = 0.36 ν_{TT}=0.3 G_{LT}= 5.93 GPa, G_{TT} = 5.15 GPa
Laminate ply configuration	$[0/90/90/0/0/90/90/0]_s$
Laminate size	5 mm x 5 mm x 1.5 mm (total thickness)

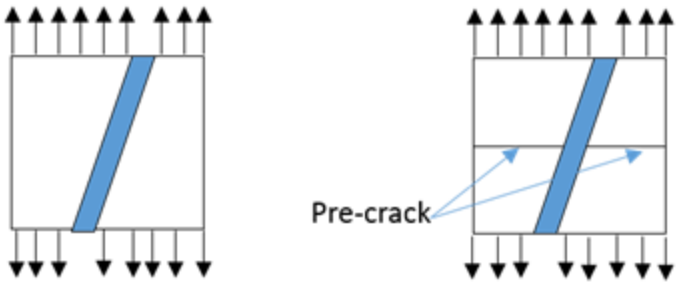

Fig 2.8: Schematic for Mode-I opening condition on a laminate reinforced with a single pin before and after delamination

Fig 2.9: Schematic for Mode-II sliding condition on a laminate reinforced with a single pin before and after delamination

A unit vertical displacement is applied on the top and bottom surfaces of the laminate in opposite directions to simulate mode-I delamination conditions. To simulate shear loading conditions, a unit horizontal displacement is applied on the top and bottom surfaces of the laminate in opposite shear directions. . The tensile or shear stiffness is then obtained as the total vertical or horizontal force needed to produce a unit displacement in the respective directions. The effect of the z-pin toward increasing the stiffness of the laminate is measured in each case. For the laminate before delamination, reinforcement stiffness is defined as the difference in the stiffness values of the laminate with and without the z-pins. For the models with a pre-crack, the reinforcement stiffness is simply the stiffness of the laminate with the z-pins.

Table 2.2. Comparison of stiffness before delamination for tensile and shear loading conditions

	Tensile Stiffness (x 10^6 N/m)		**Shear Stiffness (x 10^6 N/m)**	
	Bonding through adhesive	Perfect bonding, no adhesive	Bonding through adhesive	Perfect bonding, no adhesive
No Pin	361.6		173.85	
0º	370.4	377.3	175.6	177.5
15º	370.2	376.8	176.1	178.2
30º	369.6	375.6	177.4	180.0
45º	368.4	370.4	179.1	182.3

Table 2.3. Comparison of stiffness after delamination for tensile and shear loading conditions

	Tensile Stiffness (x 10^6 N/m)		**Shear Stiffness (x 10^6 N/m)**	
	Bonding through adhesive	Perfect bonding, no adhesive	Bonding through adhesive	Perfect bonding, no adhesive
0º	25.13	33.19	23.72	28.12
15º	24.27	32.17	23.89	28.56
30º	23.42	30.40	25.47	30.54
45º	21.30	25.75	27.91	33.42

Tables 2.2 and 2.3 illustrate the stiffness values of the laminate with the pins before and after delamination respectively. The tensile and shear reinforcement stiffness provided by the pins is plotted in Figure 2.10 and 2.11 respectively. From the tables, we infer that the laminate has nearly the same tensile and shear stiffness with or without the z-pins before delamination. In addition, the models show that when the pin is bonded through the adhesive, the reinforcement stiffness does not show much variation with angle of the pin indicating that most of the deformation is taken by the compliant interface. This means that the z-pins do not have a significant effect on the laminate stiffness before delamination. However, the z-pins have a profound effect in preventing crack propagation and enhancing delamination resistance when there is a pre-crack in the laminate because the pins carry a significant portion of the applied load. In this case, the degree of pin-laminate bonding as well the pin angle determine the magnitude of reinforcement stiffness. The reinforcement stiffness under tensile loading decreases with pin angles and the 0^o pin provides the highest value. The trend is opposite for shear loading as seen in Figure 2.11.

When a composite laminate is reinforced with z-pins, there is a loss of volume in the laminate due to insertion of the pins. The volume occupied by the 45^o laminate is more than that occupied by the 0^o pin. This loss of volume comes at a cost of the in-plane properties of the laminate. To quantify the volume loss, we define reinforcement stiffness density as the reinforcement stiffness per volume of the pin. This is plotted in Figures 2.12 and 2.13 for pins of different angles before and after delamination. Under tensile loading, both reinforcement stiffness and the stiffness

density decrease with pin angles. Under shear loading, the reinforcement stiffness density decreases with increase in angle for the laminate with a pre-crack.

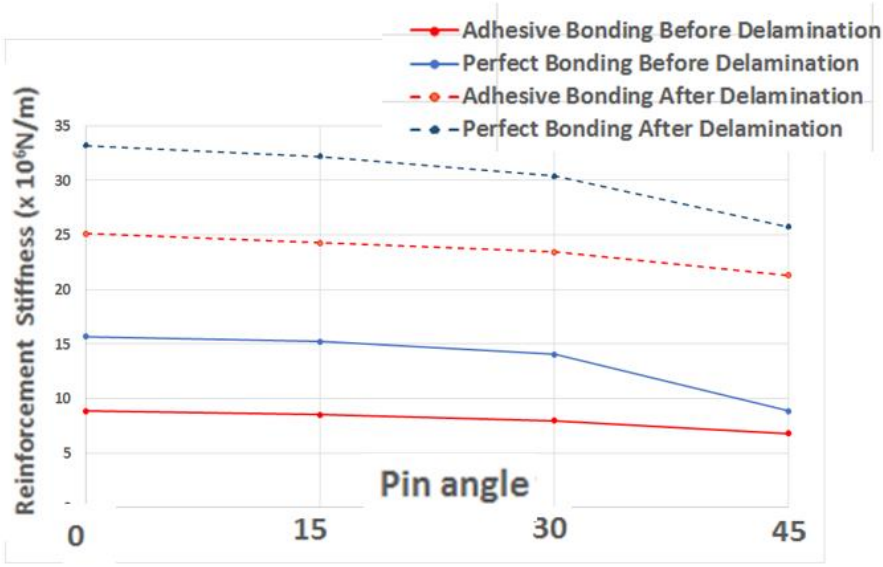

Figure 2.10: Pin reinforcement for tensile loading condition of a laminate before and after delamination for different pin insertion angles

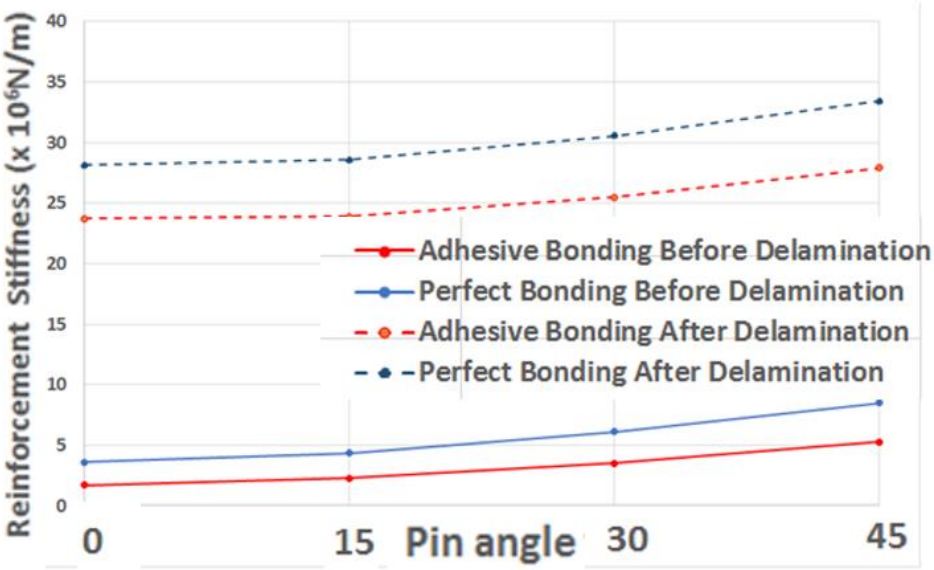

Figure 2.11 : Pin reinforcement for shear loading condition of a laminate before and after delamination for different pin insertion angles

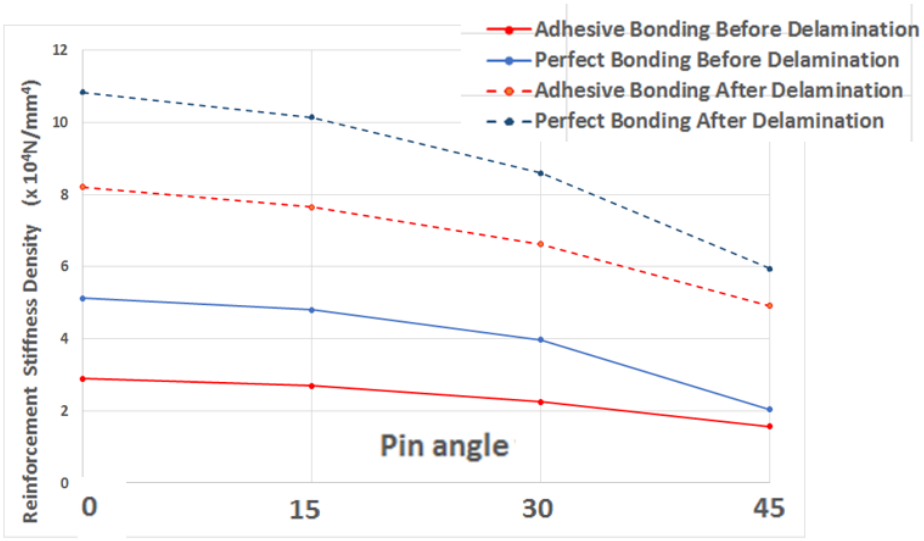

Figure 2.12: Pin reinforcement density for tensile loading condition of a laminate before and after delamination for different pin insertion angles

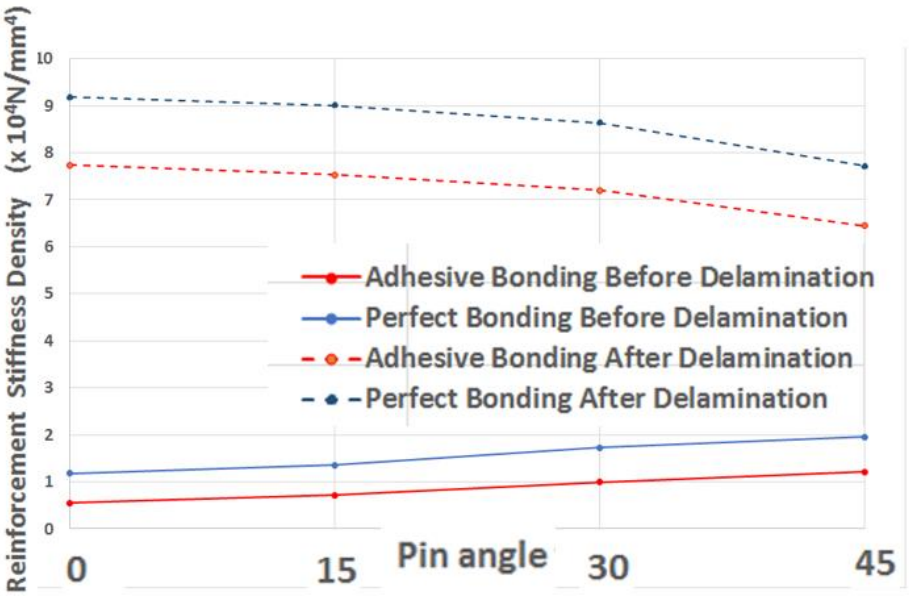

Figure 2.13 : Pin reinforcement density for shear loading condition of a laminate before delamination for different pin insertion angles

Since the interface region is the most compliant part of the laminate, the load capacity of the interface determines the traction bridging properties of the z-pin. . For a preliminary estimate of the load capacity of the laminate, average Von-Mises stress in the interface layer obtained from a linear FE analysis was used as a relative indicator for damage onset. The average Von-Mises stress in the interface for a unit tensile or shear force for different pin insertion angles is plotted in Figure 2.14. The figure shows that the average Von-Mises stresses decrease with increasing pin angles for tensile loading while the trend reverses for shear loading conditions. This would suggest that tensile force at which the onset of interface damage occurs increases with increasing pin angles. Similarly, the results would indicate that for shear loading conditions, the vertical pin may be best suited based on delayed onset of interface damage.

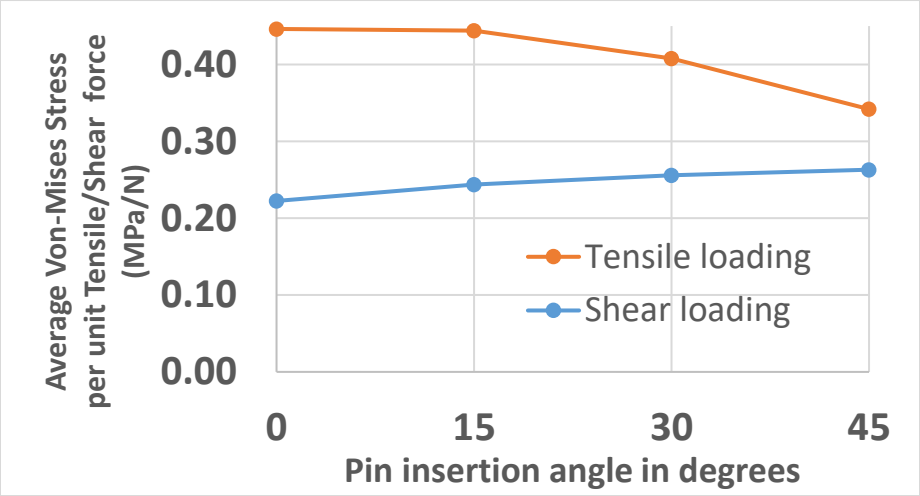

Figure 2.14: Average Von-Mises stress per unit tensile or shear force in the interface layer for models with varying pin angles

2.3.2 Experiments for tensile pullout strengths

In the following sections, we test the pullout strengths of laminates reinforced with several different types of pin. Table 2.4 lists the labels, diameters, material and the corresponding percent weight increase of the laminate for the pins used in the test specimens.

Table 2.4. Pin diameters and %weight increase for various pin inserts

Label	**Pin Material**	**Pin Texture**	**Diameter (mm)**	**% weight increase**
T1	Steel	Threaded	0.33, 0.53	0.90 %
T2	Steel	Threaded	0.59, 0.86	2.52 %
S1	Steel	Smooth	0.33	0.52 %
S2	Steel	Smooth	0.51	1.24 %
S3	Steel	Smooth	0.61	1.77 %
AS1	Steel	Smooth, anchored	0.33	1.17 %
AS2	Steel	Smooth, anchored	0.51	2.35 %
C2	Carbon fiber	Smooth	0.51	0.27%

A comparison of the reinforcement properties of the oblique and vertical pins was determined through pullout tests. For our first set of experiments, composite laminates with T700 carbon fiber pin inserts of diameter equal to 0.51 mm (labeled C2 pin) were manufactured according to the geometry shown in Figure 2.15. Ply configuration of the laminates is $[0/90/90/0]_s$ with Teflon at mid layer to simulate a

pre-crack. Oblique pins inserted at 30° to the vertical were compared with vertical pin reinforcements. The pin densities and the percent increase in laminate weight from the pin reinforcement is given in Tables 2.5 and 2.6. The strength of the z-pin laminate under tensile loading was measured on an IMADA frame and the results of the test are shown in Figure 2.16. The oblique pins showed, on an average, a 40% increase in pullout strengths from the vertical pin.

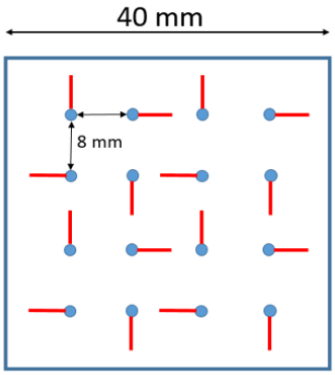

Figure 2.15.Top view of laminate geometry for specimens with 16 composite pins

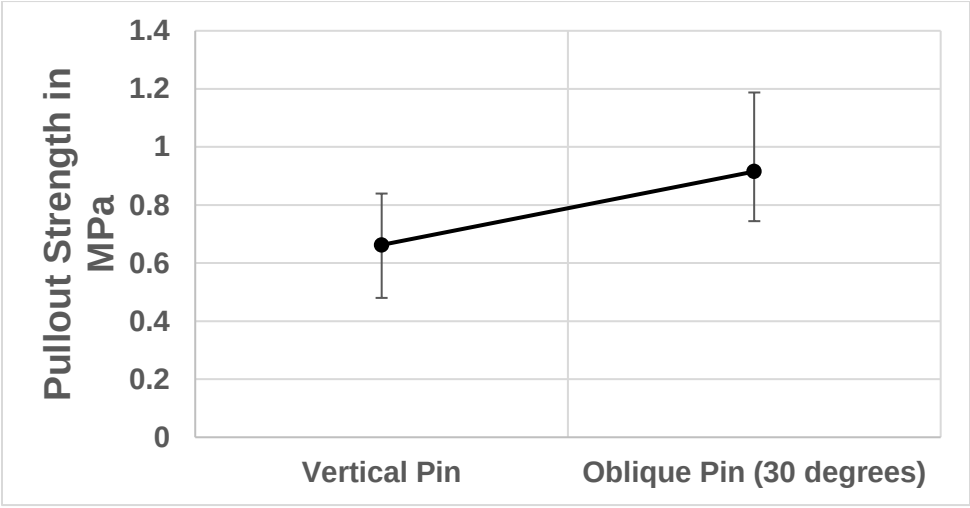

Figure 2.16: Pullout strengths for laminates with vertical and oblique (30°) carbon-fiber pins

Table 2.5. Pin density and %weight increase for carbon fiber (C2) pins

Pin angle (C2 pin)	**0º pin**	**30º pin**
Pin density (pcf)	0.22	0.25
% weight increase	0.27%	0.31%

Table 2.6. Pin density and %weight increase for steel (S2) pins

Pin angle (S2 pin)	**0º pin**	**15º pin**	**30º pin**	**45º pin**
Pin density (pcf)	0.89	0.92	1.03	1.26
% weight increase	1.24%	1.28%	1.43%	1.75%

A second set of experiments was performed with stainless steel pin inserts at four different insertion angles of 0º, 15º, 30º and 45º. The steel pins were identical in diameter to the carbon fiber pins and are labeled S2 pins. The specimens were manufactured according to the geometry shown in Figure 2.2 with a ply configuration, $[0/90/90/0]_{2S.}$ Results for tensile strengths of the specimens are shown in Figure 2.17. The 15º pin does not have a considerable difference in strengths from that of the 0º pin, but the 30º and 45º pins show an increase in pullout strengths by 38% and 75% respectively. Typical force-displacement curves for pins of different angles during pullout are given in Figure 2.18. The traction energy defined as the area under the graph consistently increases with pin insertion angles. The 45º pin shows a considerable increase in traction energy as compared to the 0º pin. This set of experiments confirms the advantage of the oblique pin over the vertical pin through the mechanism of interlocking induced by normal (contact) and friction-induced forces. The bending of the pins through normal contact forces on

the oblique pin during pullout was clearly visible on the damaged specimen with 45^{o} pins.

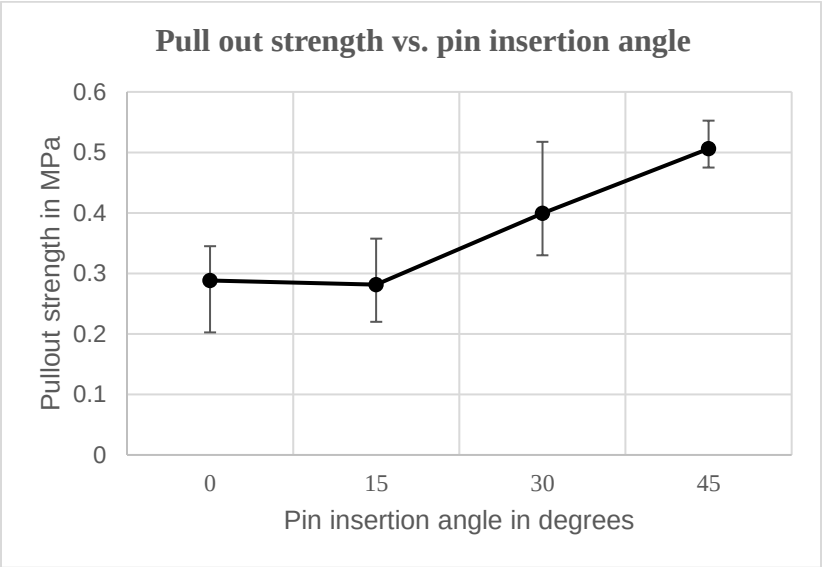

Figure 2.17: Plot of tensile pullout strengths versus pin insertion angles for S2 pins

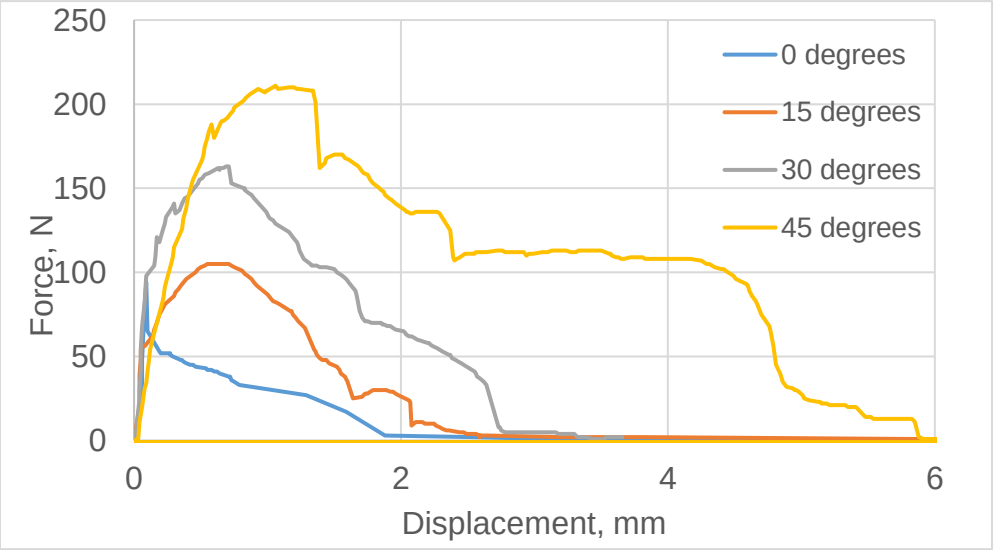

Figure 2.18.:Typical force vs. displacement plots for tensile pullout tests conducted on specimens with different pin angles.

2.3.3 Non-Linear FE Analysis for tensile pullout strengths

To simulate damage progression in the pin-laminate interface in the FE models of Figure 2.7, a cohesive layer is inserted in the interface governed by an uncoupled bi-linear traction separation law shown in Figure 2.19. This cohesive model assumes initial linear elastic behavior followed by damage onset at point A, and evolution of damage until total separation at point B. The cohesive layer links every node on the outer surface of the pin to the node on the laminate it is in contact with initially. This kind of modeling simulates the degradation and failure of the bond between pin and laminate under tensile loading condition. When the cohesive interface between two corresponding nodes reach point B depicted in Figure 2.19, there is complete separation of those two nodes. The traction separation law is governed by three properties labeled in Figure 2.19, namely the initial elastic stiffness K, maximum stress σ_0 that defines onset of damage and strain energy release rate G_c as a measure of fracture toughness. Note that G_c is equal to the area under the traction-separation curve shown in Figure 2.19. Cohesive damage D is a non-dimensional parameter indicating the magnitude of damage at the contact point increasing linearly from 0 at point A to 1 at point B. The model assumes uncoupled behavior in the normal and shear directions, and the same maximum stress for both shear and normal directions. A detailed analysis of the cohesive zone modeling and techniques developed for FE analysis of structures with cohesive zone is given in Chapter 4.

In addition to the cohesive zone between pin and laminate, our non-linear FE models also include the non-linear material properties of the pin. The ultimate tensile strength of 303 steel used in laminate reinforcement is equal to 2020 MPa, while the linear elastic limit is equal to 965 MPa. Properties, K, σ_0 and G_c for the cohesive zone are extracted from the FE model of the vertical pin by matching with pullout strengths obtained from experiments above. Accordingly the values for these parameters are obtained as $K = 1.5\ GPa/mm$, $\sigma_0 = 1.1\ MPa$ and $G_c = 5\ kJ/m^2$. Values for these parameters are then copied into the models for pins inserted at an angle. The tensile strengths obtained for the models thus are plotted and included in Figure 2.20. The figure shows that tensile pullout strengths obtained from the non-linear FE analysis are a close match to the experimental values. The FE models showed that the 0^o pin did not experience any plastic deformation before total pullout, while for the other pins, plastic deformation at pullout increased with increasing pin angles.

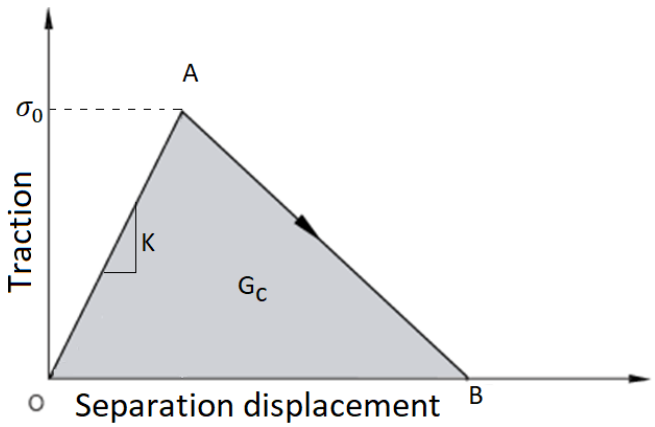

Figure 2.19: Bilinear traction separation law for cohesive layer modeling

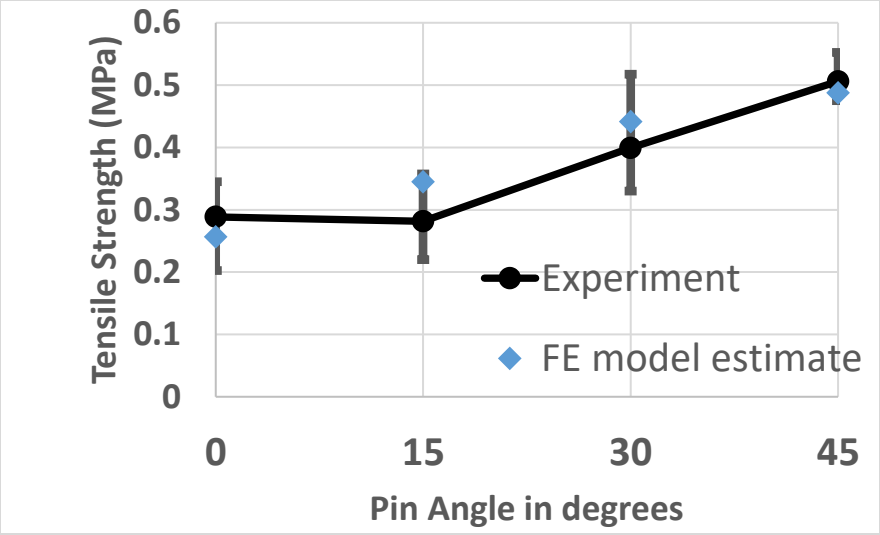

Figure 2.20: Plot of tensile pullout strengths versus pin insertion angle for S2 pin inserts with estimates from non-linear FE model

2.3.4 Experiments for pullout under shear loading

Figure 2.21 shows the experimental results for pullout strengths of test specimens reinforced with S2 pins under shear loading conditions. Typical Force-displacement relations for the specimens are shown in Figure 2.22. Pullout strengths increase with increase in pin angles, but the 15^o pin does not show a considerable improvement over the 0^o pin. The 30^o pin shows a modest increase of 16% while the 45^o pin improves pullout strengths by 77%. From the average Von-Mises stress obtained by a linear FE analysis plotted in Figure 2.14, it would be expected that the onset of damage occurs earlier for higher pin insertion angles. However, the experimental results show a reverse trend as predicted from linear FE analysis.

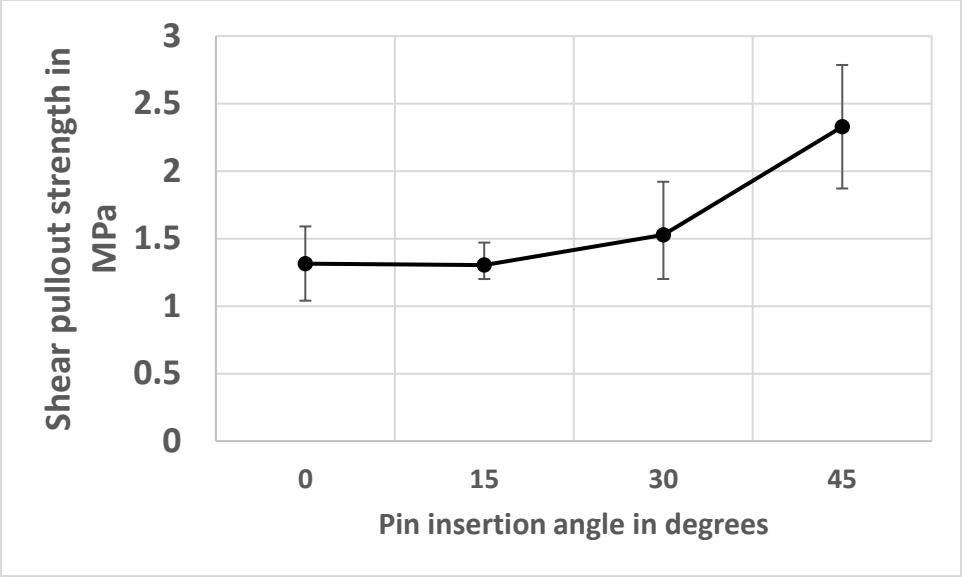

Figure 2.21: Plot of shear pullout strengths versus pin insertion angle for S2 pin inserts

Under shear loading, there are two pins in the specimen along the direction of loading. During the initial loading phase, one pin is under tension (T-pin) and the other under compression (C-pin)as shown in Figure 2.23. With increase in pin angles, the T-pin will begin to provide less reinforcement as the axial forces on the pin will weaken the interface around it causing interface failure as predicted by the Von-Mises stress plot in Figure 2.14. On the other hand, the C-pin experiences axial compression forces in the initial stages of loading and will not cause interface damage. Instead, for this pin, failure is predominantly caused by bending of the pin into its plastic phase and eventual pullout from the laminate. Increasing pin angles for the C-pin increases reinforcement because the pin must undergo more displacement before pullout. Non-linear FE analysis is carried out for models of Figure 2.7 under shear loading such that the pins are under compression. With a

perfect pin-laminate bonding, and non-material properties for the pin, force-displacement plots are extracted and plotted in Figure 2.24. This figure shows that shear strength of the C-pin increases with insertion angles. Experimental results in Figure 2.21 show an increase in shear strengths with pin angles indicating that the C-pin provides the most reinforcement for the laminate under shear loading.

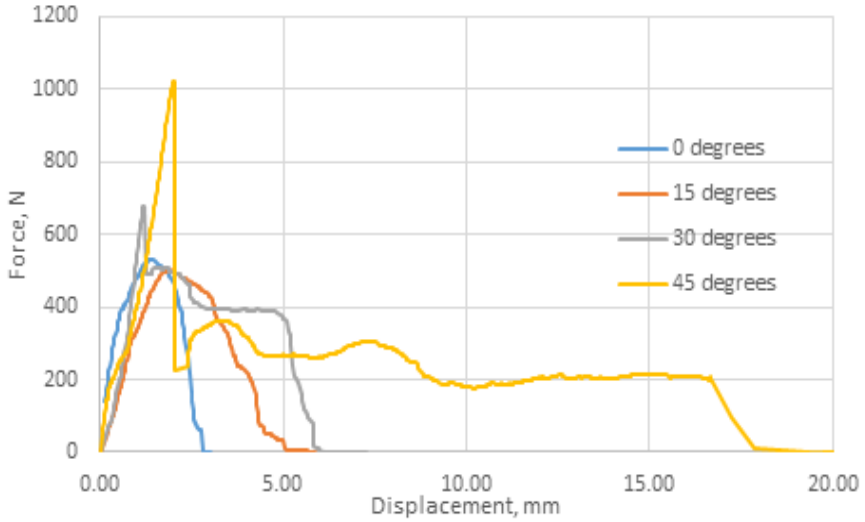

Figure 2.22: Typical force vs. displacement plots for shear pullout tests conducted on specimens with different pin angles.

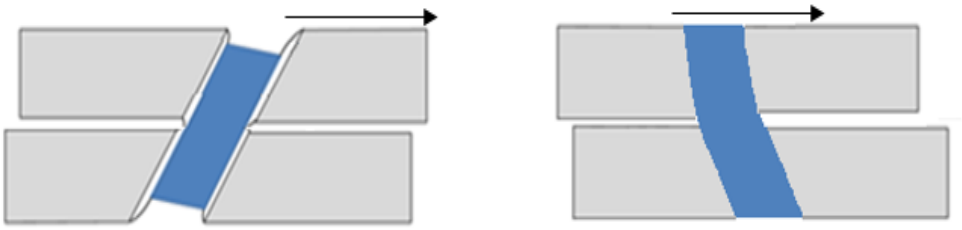

Figure 2.23: Sketch showing angled pins under tension (T-pin) and compression (C-pin) under shear loading

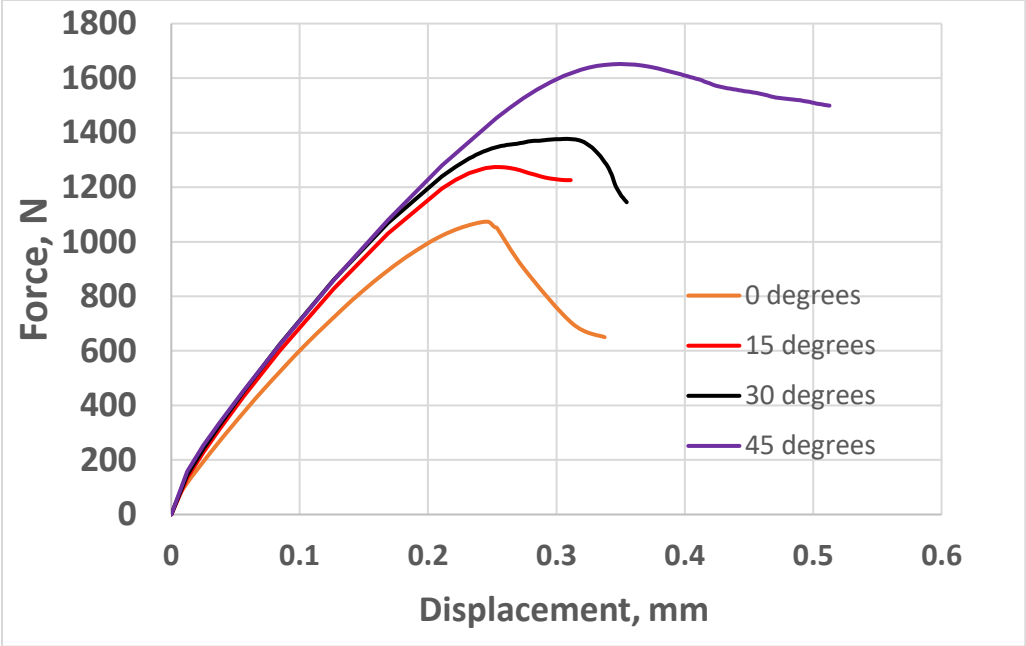

Figure 2.24: Nonlinear FE model-generated force-displacement plots for C-pin under shear loading for various pin insertion angles

2.3.5 Effect of pin material on tensile pullout strengths

During the cooling phase of curing, the laminate is subjected to opening stresses due to difference in thermal expansion coefficients (CTE) of the pin material and the epoxy as shown in Figure 2.25. To improve bonding between the Z-pin and the laminate, the thermal expansion mismatch between the z-pin and the laminate in the thickness direction need to be minimized to avoid debonding of the z-pin from the laminate.

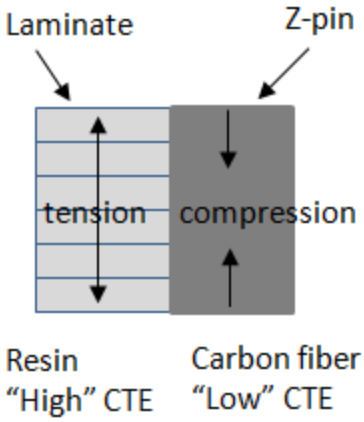

Figure 2.25: Schematic showing the opposing forces in laminate and Z-pin during cooling phase of the laminate due to varying level of thermal expansion coefficients

Table 2.7: Coefficient of thermal expansion for some materials

Material	**CTE (10^{-6} K^{-1})**
Resin (Epoxy)	45-65
Graphite (Carbon)	2-6
Titanium	8.6
Steel	13.0

Table 2.7 lists the coefficient of thermal expansion of various pin materials and epoxy. It is expected that based on the proximities of CTE of Steel or Titanium to that of epoxy, these pins may have stronger bonds with the laminate than the carbon fiber. The effect of pin material on the tensile pullout strengths was experimentally tested by inserting pins of different materials vertically through the laminate. Specimens were manufactured and tested in three different batches. The curing and cooling conditions

of the laminates were maintained same within each batch. These specimens were manufactured according to the geometry shown in Figure 2.2. Ply configuration of the laminates is $[0/90/90/0/0/90/90/0]_s$ with Teflon at mid layer. Table 2.8 shows the pin densities and the percent increase in laminate weight from the pin reinforcement with stainless steel, T700 carbon fiber and titanium pins.

The results of the experiments are shown in Figure 2.25. The carbon fiber pin provided the highest reinforcement strength, while the steel and titanium pin provided similar strengths. The reason for this could be the compatibility between carbon and epoxy material based on wettability of the epoxy at high temperatures. Metal pins such as steel or titanium pins may have to be treated chemically to improve the bonding compatibility with epoxy. This set of experiments showed that the CTE difference may not be a critical factor in bonding of the pins to the laminate.

Table 2.8. Pin density and %weight increase for vertical pin of different materials

Pin material	**Pin density**	**%weight increase**
Carbon fiber	0.22	0.27%
Stainless steel	0.89	1.24%
Titanium	0.55	0.69%
Threaded Steel	0.75	1.04%

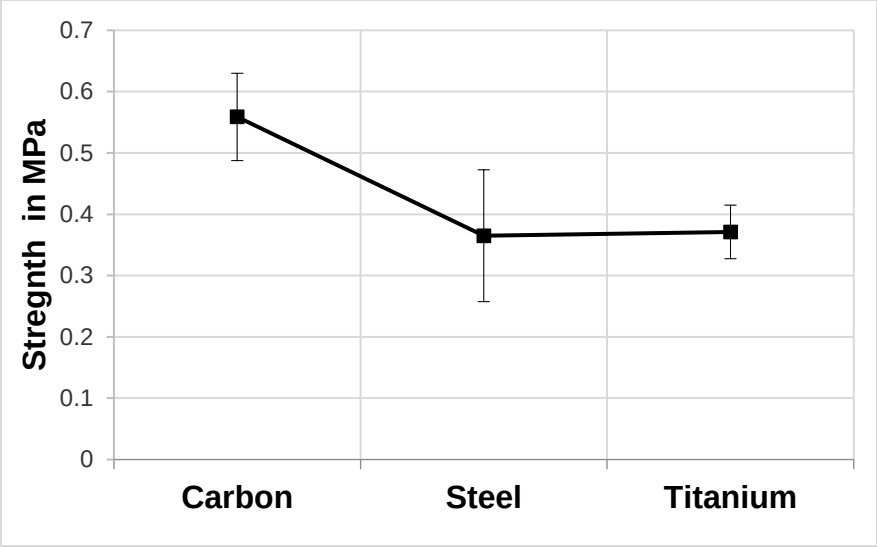

Figure 2.25. Tensile pullout strengths of laminates reinforced with pins of different materials

2.4.1 Threaded pin insertion

2.4.1 Tensile pullout strengths of T1 pins

Laminates reinforced with smooth pins, angled or otherwise, fail under both tension and shear loading via pin pullout suggesting that the pin-laminate interface is the weakest link in the laminate. One way to enhance the pin-laminate bonding is to use a threaded pin as shown in Figure 2.26(a) which increases mechanical interlocking as well as the epoxy-pin contact area through change in contact surface. Figure 2.27 compares the nature of forces acting on a smooth pin and a threaded pin under tensile loading. With smooth pins, only shear forces act on the surface of the pin while, with a threaded pin, the normal forces from epoxy increases mechanical interlocking. The additional normal forces on the threaded pin surface increases mechanical interlocking of the pins.

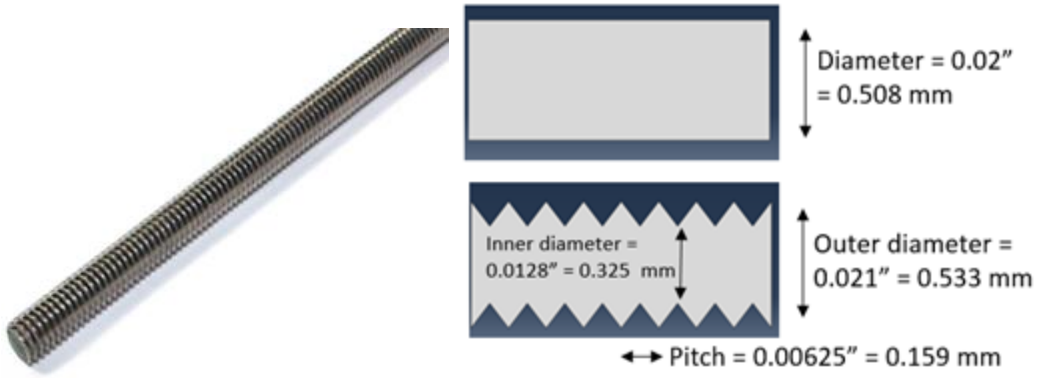

Figure 2.26. : (a) Threaded steel pin used to reinforce laminate (b) Forces on the external surfaces of smooth steel pin and threaded steel pin under tensile loading

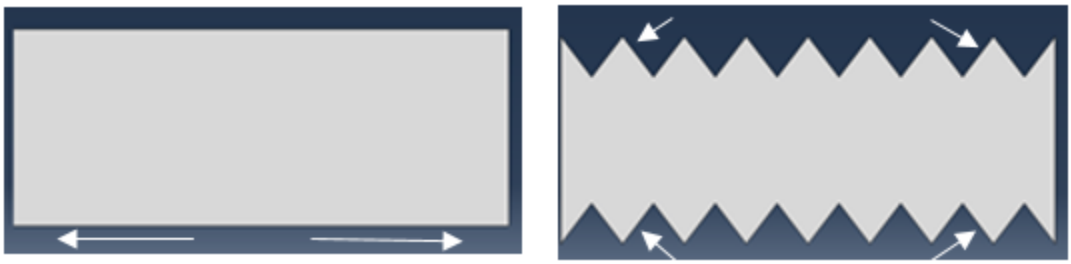

Figure 2.27: Contact forces on smooth pin and threaded pin

To examine the performance of threaded pin insertion, laminate specimens reinforced with threaded pins made of stainless steel were compared with the specimens with carbon fiber and smooth steel pin inserts. Pins were inserted vertically into the laminate. Commercially available threaded pin, T1 was chosen as a candidate as it has a comparable outer diameter as the S2 pin. Based on the geometry as shown in Figure 2.26(b), the T1 pin occupies only 72% volume as that of the S2 pin. Accordingly, for the threaded pins, the pin density and the percent weight increase are smaller than that for a smooth steel pin as shown in Table 2.4. C2 pins are T700-epoxy carbon fiber pins with similar diameter as S2 pins. Test specimens with T1, S2, and C2 pins inserted

vertically were tested for pullout strengths under tensile loading. The results of these tests are shown in Figure 2.28. Figure 2.28 shows that laminates with T1 pin inserts have much higher tensile pullout strengths, i.e, 3.5 times that of S2 pin and 2.8 times that of C2 pin inserts. Typical force-displacement curves during pullout are provided in Figure 2.29. Specimens with threaded pin inserts failed due to breaking of pins under tension while the smooth pins always pulled out from the composite laminate. This confirms the advantage of the threaded pin in increasing the bonding properties of the epoxy to the pin surface through mechanical interlocking.

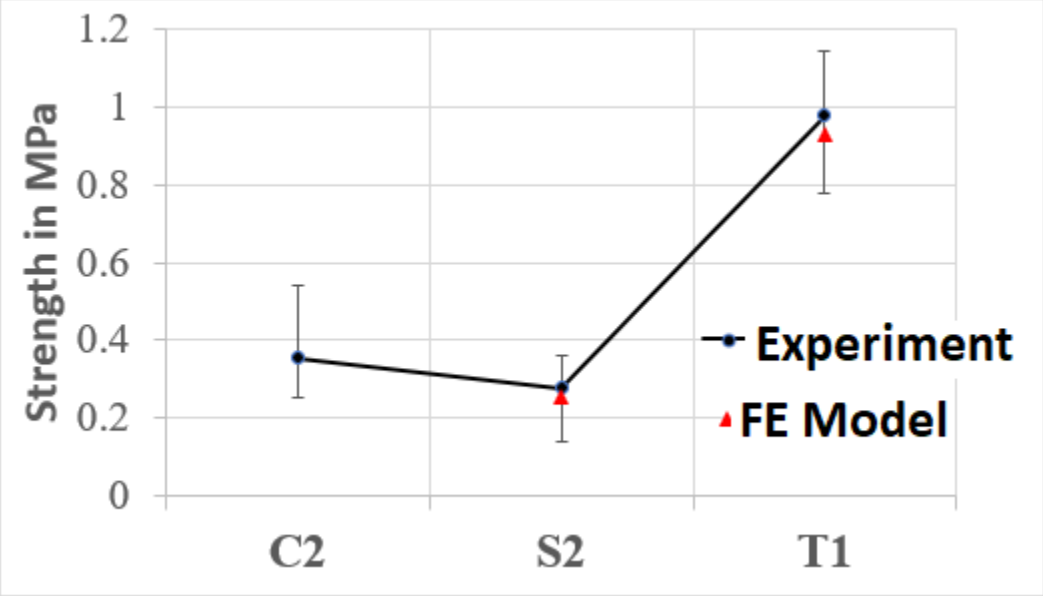

Figure 2.28: Tensile pullout strengths of laminates reinforced with C2, S2 and T1 pins of standard diameters

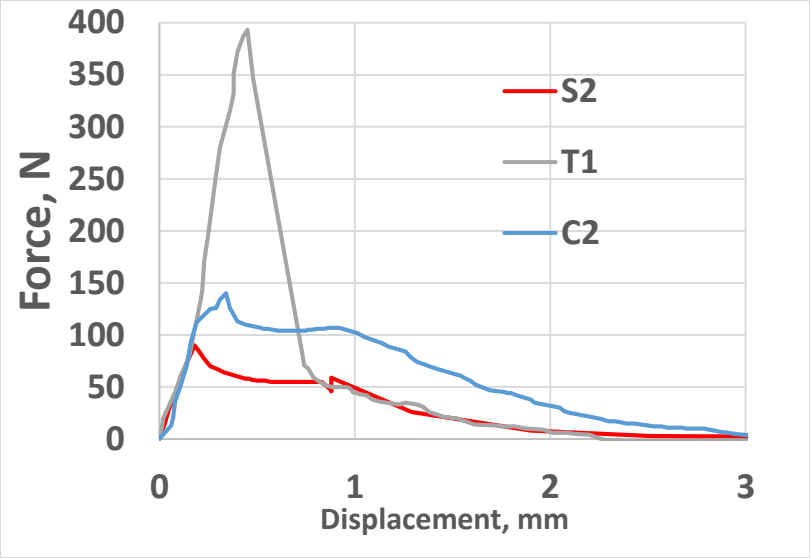

Figure 2.29: Typical force-displacement curves for specimens with C2, S2 and T1 pins

FE model for a single threaded pin, T1 embedded in the laminate is constructed in ABAQUS as shown in Figure 2.30(a). A cohesive layer is inserted in the pin-laminate interface with parameters, $K = 1.5\ GPa/mm$, $\sigma_0 = 1.1\ MPa$ and $G_c = 5\ kJ/m^2$ obtained from the analysis in the previous section. Non-linear material properties are assigned to the threaded pin to allow for plastic deformations. The threaded pin is made of 303 steel material with a yield strength of 424 MPa and an ultimate tensile strength equal to 804 MPa. The tensile strength of the laminate obtained from the model is included in Figure 2.28 which is a close match with the experimental values. Figure 2.31 shows the force-displacement plot of a threaded pin specimen obtained from the non-linear FE model. Figure 2.30(b) shows the deformation state of the threaded pin post damage overlaid with a contour map of cohesive damage parameter, D. The figure shows that failure of the threaded pin occurs through plastic deformation, and thus

eventual breakage at the middle section of the pin. Most of the pin-facesheet interface does not experience cohesive damage, thus corroborating experimental observations and the advantage of the threaded pin in increasing mechanical interlocking.

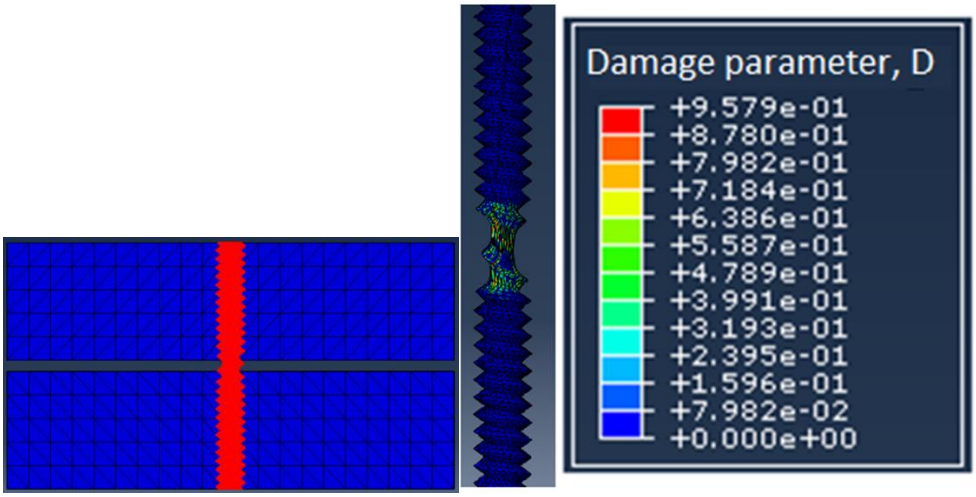

Figure 2.30(a) Finite element model of a single threaded pin embedded in a laminate.

(b) Cohesive damage contour map on a deformed threaded pin post failure.

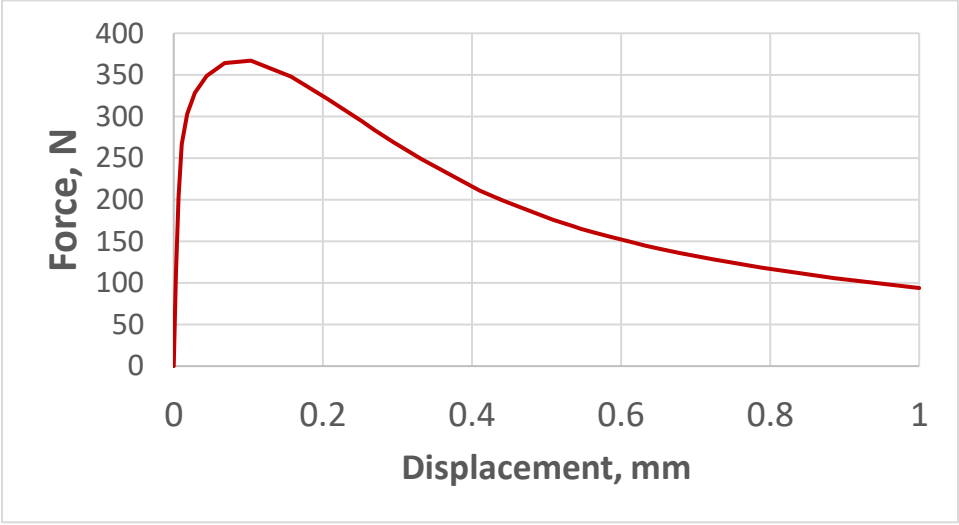

Fig 2.31: Tensile force vs. displacement plot obtained from non-linear FE analysis of a laminate reinforced with threaded pin (T1)

2.4.2 Shear pullout strengths of threaded pins

When the pullout tests were repeated for shear loading conditions, the T1 pin exhibited lower strength when compared with both C2 and S2 as shown in Figure 2.32. This is expected because the inner diameter of the T1 pin is much smaller than that of the S2 or C2 pins. Under shear loading, the pin is subjected to bending loads and the bending rigidity of the pin is inversely proportional to the fourth power of its radius. Hence at the location of its smallest radius, the T1 pin has a bending rigidity only 17% as that of the S2 pin. This means that the shear stresses from bending of the threaded pin will be nearly 6 times as the stresses in the smooth pin. In addition, the sharp edges on the threaded pin causes stress concentration that can lead to breakage of the pin.

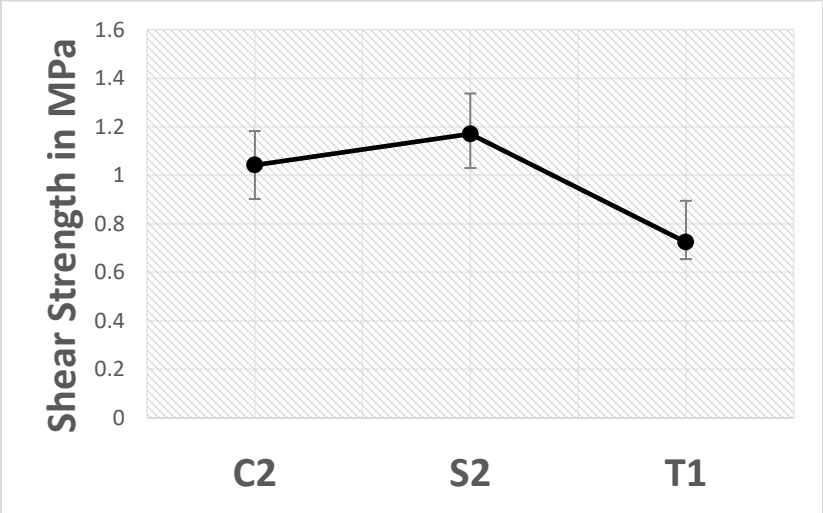

Figure 2.32: Tensile pullout strengths of laminates reinforced with C2. S2 and T1 pins (b) smooth and threaded pins of different thicknesses

For a fairer comparison of pullout strengths under shear loading, test specimens with S1, S3 and T2 pins were additionally manufactured. The mean pullout strengths of these specimens under shear loading in given in Figure 2.33. The T1 pin has 13% higher pullout strengths than the S1 pin which has a diameter comparable to the inner diameter of the T1 pin. A similar trend was observed between T2 and S3 pins which have comparable inner diameters. The T2 pin has marginally higher strengths than the S3 pin. Under shear loading, laminates with T1 and T2 pins failed due to breaking of the pins.

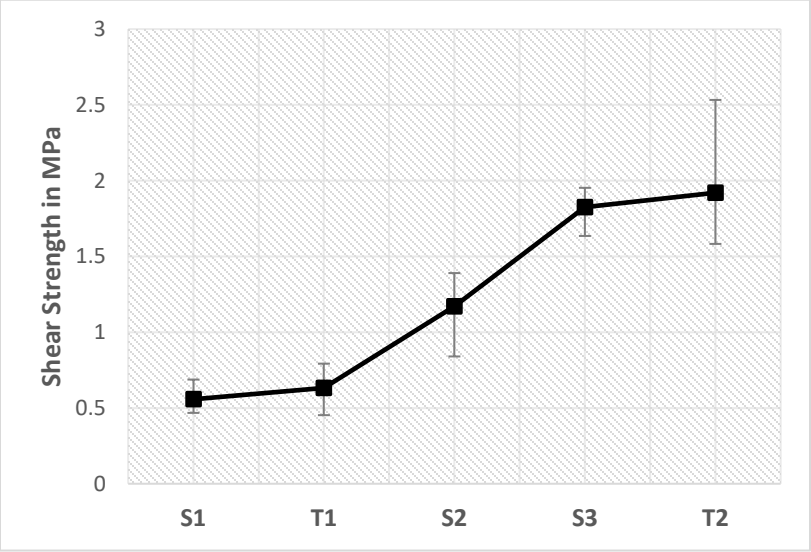

Figure 2.33: Tensile pullout strengths of laminates reinforced with smooth and threaded pins of different thicknesses

2.4.3 Effect of insertion angle on pullout strengths of threaded pins

The effect of insertion angle of the T1 pin on pullout strengths is also investigated for both tensile and shear loading conditions. The results are shown in Figure 2.34. The plot shows that tensile pullout strengths decrease with angle while the

trend reversed for shear pullout strengths. The advantage of the threaded pin is the ability of the epoxy interface to grip the pin around the ridges of the pin. Under shear loading, this advantage is lost as the primary load on the threaded pin is that of bending. A threaded pin inserted at an angle has a lower tensile pullout strength than that inserted vertically because of the bending loads on the pin. Similarly, the threaded pin performs better at high insertion angles under shear loading conditions because some of the load is distributed in the axial direction of the pin.

These results confirm that the threaded pin is a viable candidate for reinforcement particularly when the laminate is subject to delamination under mode-I type conditions. Even though the threaded pin does not offer a great deal of advantage under shear loading conditions, its performance is comparable to that of smooth pins of comparable inner diameter. In addition, since the insertion angle has opposite effects on tensile and shear pullout strengths, it may be tailored according to the typical loading conditions on the laminate.

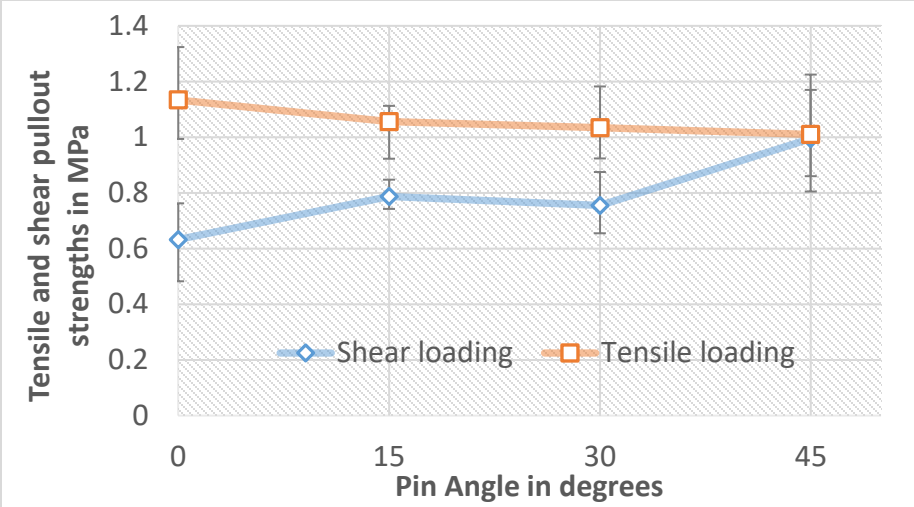

Figure 2.34: Plot of tensile and shear pullout strengths versus pin insertion angle for T1 pins

2.4.4 Pullout tests on specimens with S1 pins

Steel pins S1 and S3 were chosen with diameters equal to inner and outer diameters of commercially available T1 and T2 pins respectively. S1 pin has a diameter equal to 0.33 mm, equal to the inner diameter of the threaded pin while S3 pin has a diameter equal to 0.59 mm comparable to the inner diameter of T2 pins.. Results for pullout strengths under tensile and shear loading conditions with the S1 pin are shown in Figure 2.25. The plots indicate that, contrary to the S2 pin, the S1 pin does not have a significant advantage with increasing pin angles for either tensile and shear loading conditions. This can be explained by the fact that the S1 pin is susceptible to bending because of its small radius and the damage of the interface layer may be accelerated due to excessive bending of the pin. Under tensile loading conditions, the bending

forces on the pin are higher for larger pin insertion angles, thus reversing the positive effects of mechanical interlocking.

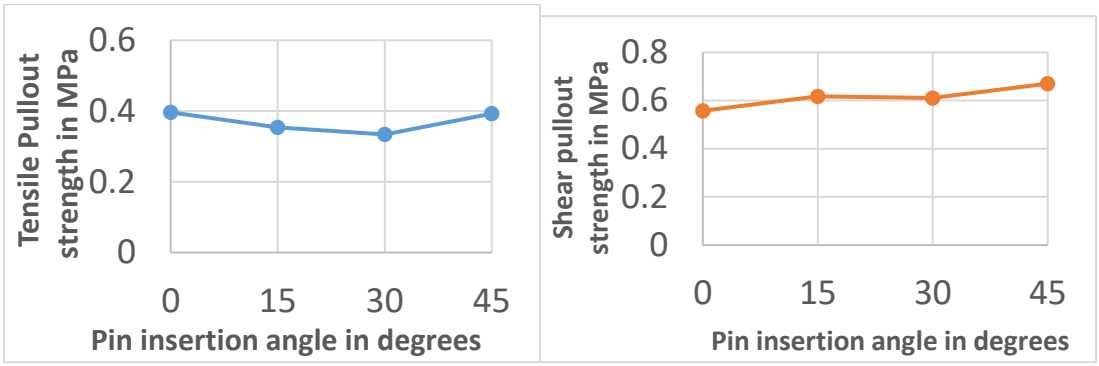

Figure 2.35: Plot of pullout strengths versus pin insertion angles under tensile and shear loading conditions for laminate reinforced with S1 pins

2.4.5 Optimal contouring of threaded pins

Pullout experiments performed thus far have confirmed that the threaded steel pin provides better reinforcement than smooth pins under both tensile and shear loading conditions. Threaded pins increase mechanical interlocking by allowing epoxy to occupy pockets between threads. Typically, threaded pins fail by breakage where as smooth pins fail from pullout from the laminate. The threaded pin used in the experiments have sharp edges at maximum and minimum diameter points which are prime locations for stress concentration. The stress concentration may be reduced by using a smoother contour on the threaded pin that may enable better performance through delayed breaking of the pins.

Towards this end, finite element models of threaded pins with both smooth and sharp edges are constructed in ABAQUS. The first set of models constructed are threaded pins with a helix angle equal to 0^o as shown in Figure 2.36. Threaded pins with sharp

edges are constructed according to the geometry given in Figure 2.26. Threaded pins with smooth edges are created by using the spline feature around the sharp edges in ABAQUS.

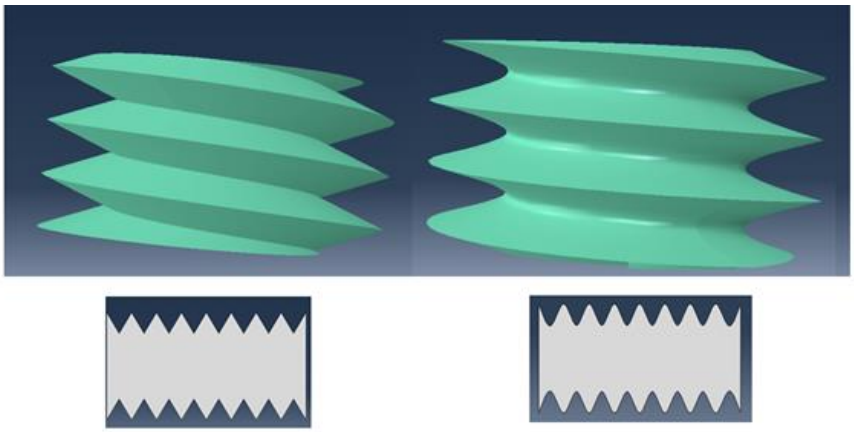

Figure 2.36: Isometric and cross-sectional views of threaded pins with sharp edges (left) and smoothened edges (right)

To simulate tensile pullout conditions, an epoxy interface layer of thickness equal to 17% of the outer radius of the threaded pin is attached to the pin as shown in Figure 2.37, and displacements are applied in the opposite directions on its top and bottom lateral surfaces. The average Von-Mises stress at the minimum and maximum diameter locations of the threaded pin may be used as an indicator for onset of pin breakage. Accordingly, the average Von-Mises stress at these locations for unit applied displacements are plotted and compared for the pins in Figure 2.38. This plot shows that there is a 15% drop in the average Von-Mises stress when threaded pins with sharp edges were replaced with ones with smooth edges indicating that thread contouring is an important consideration in delaying of pin breakage. Designing a threaded pin with optimum thread contour for delaying pin breakage is left for future work.

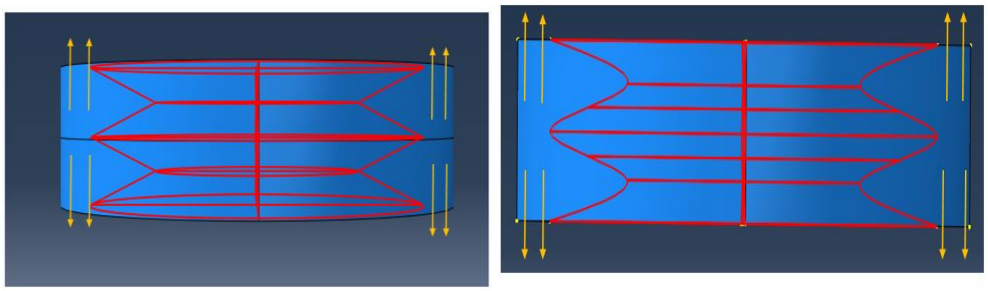

Figure 2.37: Displacements applied to outer surface of epoxy layer surrounding the threaded pins

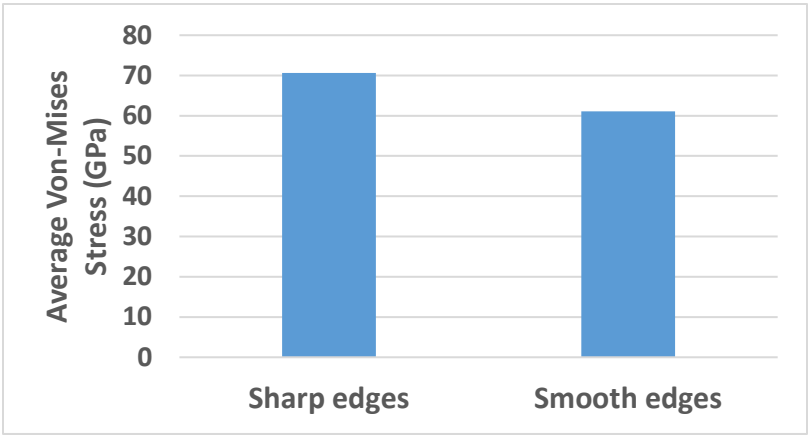

Figure 2.38: Plot comparing average von-Mises stress in critical locations of threaded pins with sharp and smooth edges for non-zero helix angles

2.5 Anchored pin

2.5.1 Pullout tests of AS1 pins

One way to improve the reinforcement strength of the Z-pin is to allow the pin to take the applied load to alleviate the load carried by the pin-laminate interface. This can be accomplished by anchoring the pin ends on to the outer surface of the laminate as shown in Figure 2.39. For a laminate reinforced with anchored pin, the pin ends undergo applied displacements as shown in Figure 2.40(b).

Specimens with AS1 pins (anchored S1 pins) are tested for strengths under shear and tensile loading conditions and are compared with those without anchor in Figures 2.41 and 2.42. Results show that anchoring of pins considerably increases the strengths of the reinforced laminate. The laminates with anchored pins also failed from pulling out the pins through considerable bending of the pins as shown in Figure 2.30. The 0^o pin had a much better gripping with the laminate than the 30^o pin and hence the improvement from anchoring is significant in the case of 0^o pin.

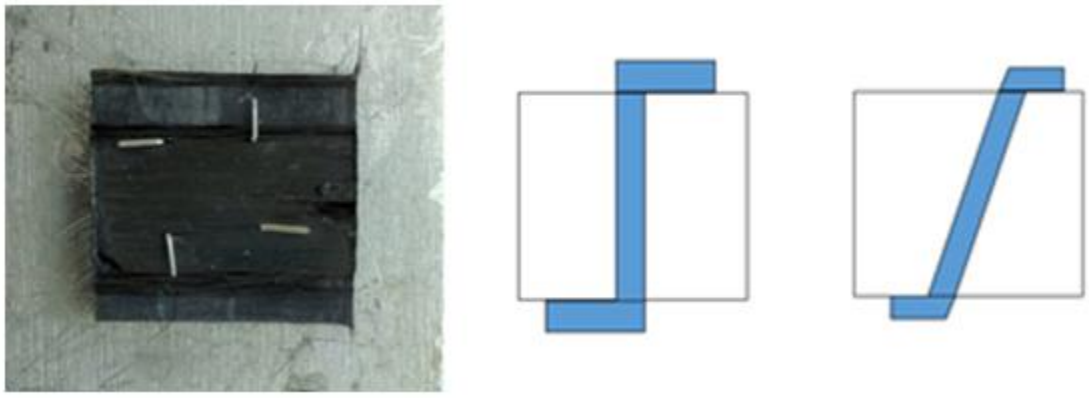

Figure 2.39(a): Pin anchored to the laminate by flattening reveal lengths on the laminate surface (b) Sketches showing direction of flattening of the reveal lengths

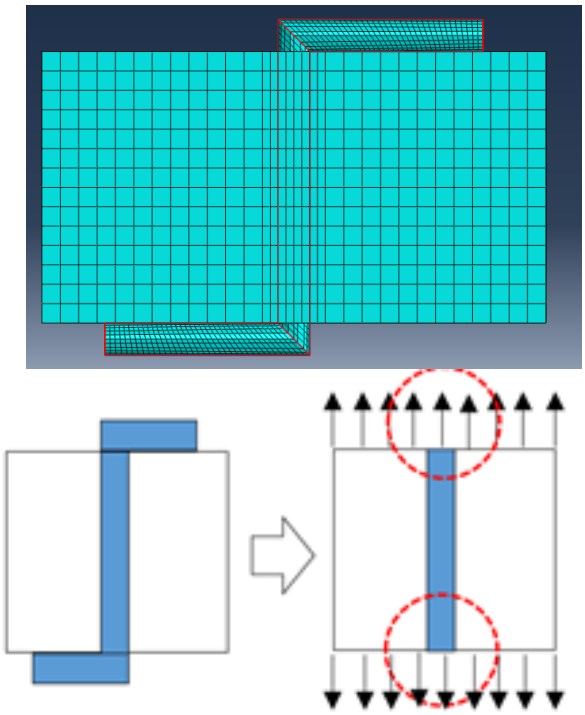

Figure 2.40 (a) FE model of anchored pin reinforcement (b) Effect of anchoring on boundary conditions on pin ends

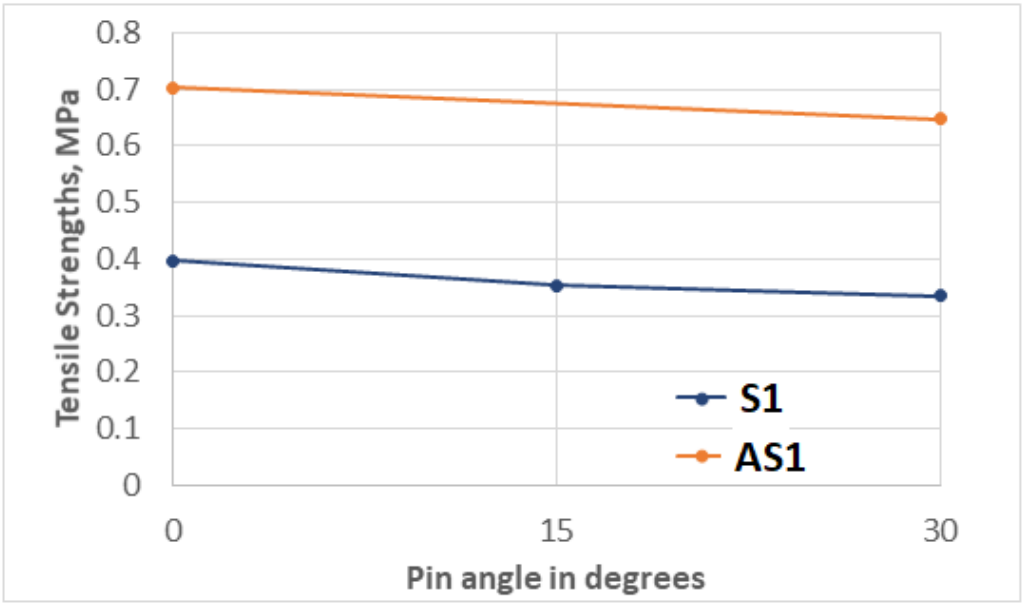

Figure 2.41: Plot of pullout strengths versus pin insertion angles under tensile loading conditions for laminate reinforced with anchored and non-anchored pins (AS1)

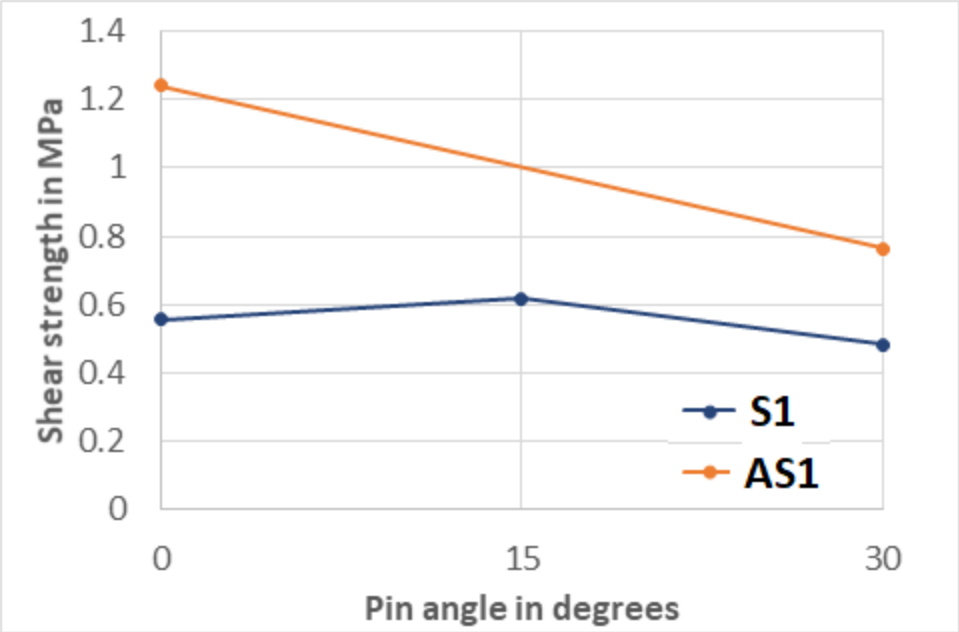

Figure 2.42: Plot of pullout strengths versus pin insertion angles under shear loading conditions for laminate reinforced with anchored and non-anchored pins (AS1)

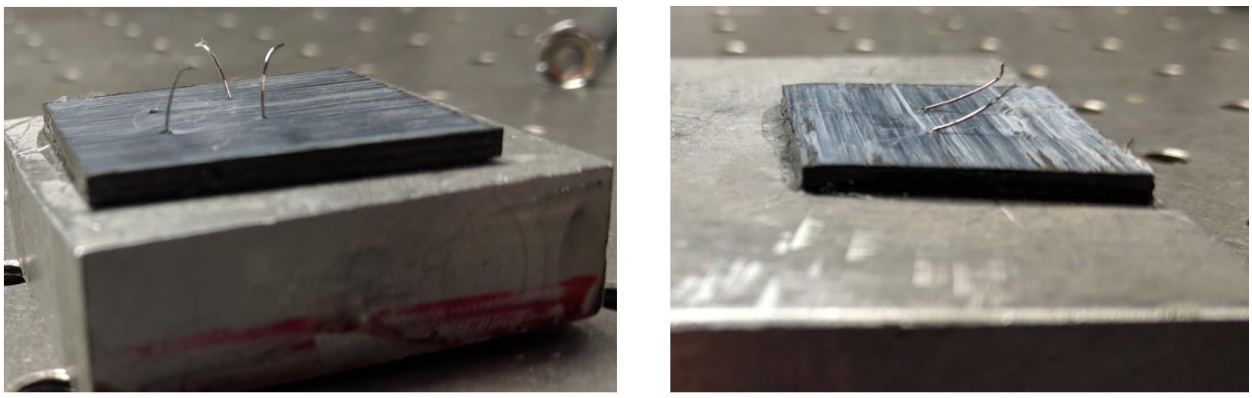

Figure 2.43: Bending of pins apparent in specimens reinforced with anchored pins post-failure under tensile and shear loading respectively

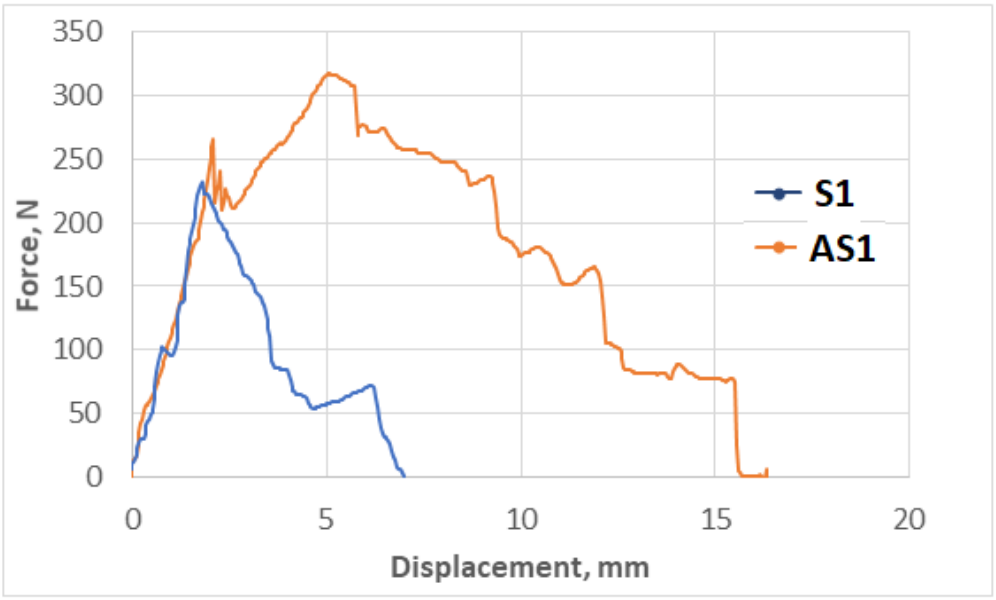

Figure 2.44: Typical force vs. displacement plots for shear pullout tests conducted on specimens with anchored and non-anchored S1 pins inserted at 30^{o}

Typical force-displacement curves during pullout for laminates with pins inserted at 30^{o} with and without anchored reveal lengths are provided in Figure 2.44. The plot for anchored pin shows that not only does the laminate strength increase with anchoring, but the traction energy defined as the area under the graph increases largely as well. This is because the anchored parts of the pin grips around the laminate exerting normal and frictional forces on the laminate thus delaying pullout. For the plot corresponding to anchored pins in Figure 2.44, the sequential pulling out of the pins one after another is apparent in the part with decreasing slope.

2.5.2 Pullout tests of AS2 pins and non-linear FE models

Specimens with anchored pin, AS2 were also tested for pullout strengths under shear and tensile loading conditions. The results were compared with the corresponding

strength of laminates reinforced with S2 pins that are not anchored. Figure 2.45 depicts the tensile pullout strengths of the specimens respectively which show a significant improvement in pullout strengths for anchored pins. The tensile pullout strength of the AS2 specimen inserted vertically is nearly 8 times that of an S2 pin. Figure 2.46 shows a typical force-displacement plot of an AS2 pin and an S2 pin under tensile loading. The traction energy is significantly higher in the case of anchored pin specimens. Figure 2.47 compares the shear pullout strengths of AS2 and S2 pins.

Figure 2.40 (a) shows a FE model of an anchored pin constructed in ABAQUS. Cohesive layer with properties, $K = 1.5\,GPa/mm$, $\sigma_0 = 1.1\,MPa$ and $G_c = 5\,kJ/m^2$is inserted at the pin-laminate contact surface. Non-linear material properties are assigned to the pin. The results from the simulations show that the model fails via plastic deformations of the pin. The tensile pullout strengths obtained from the model are included in Figure 2.45 and are reasonably close to experimental values.

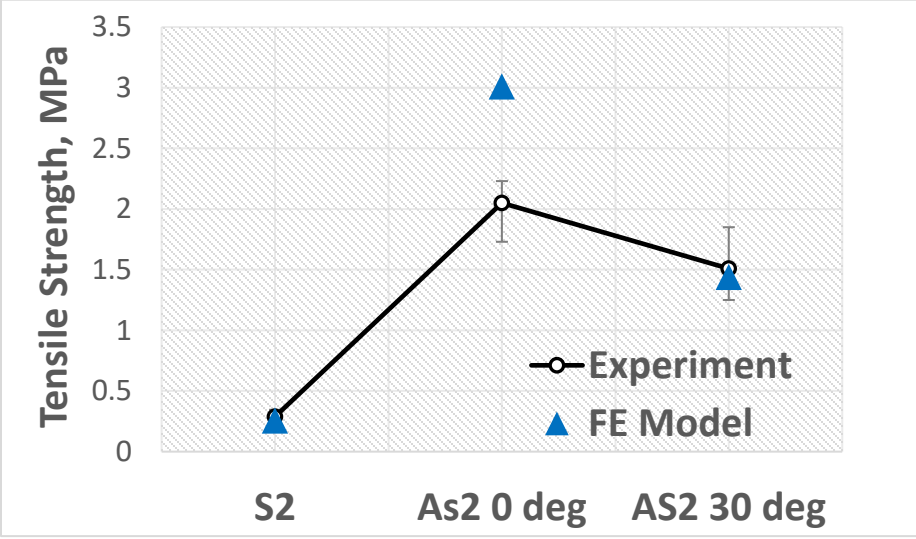

Figure 2.45: Tensile pullout strengths of the laminate under tensile loading conditions with AS2 and S2 pins

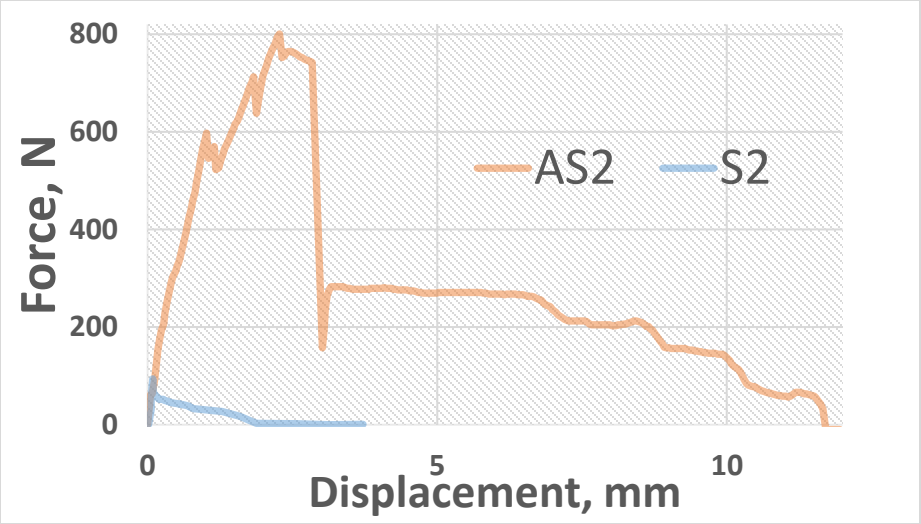

Figure 2.46: Typical force vs. displacement plots for tensile pullout tests conducted on specimens with anchored and non-anchored S2 pins

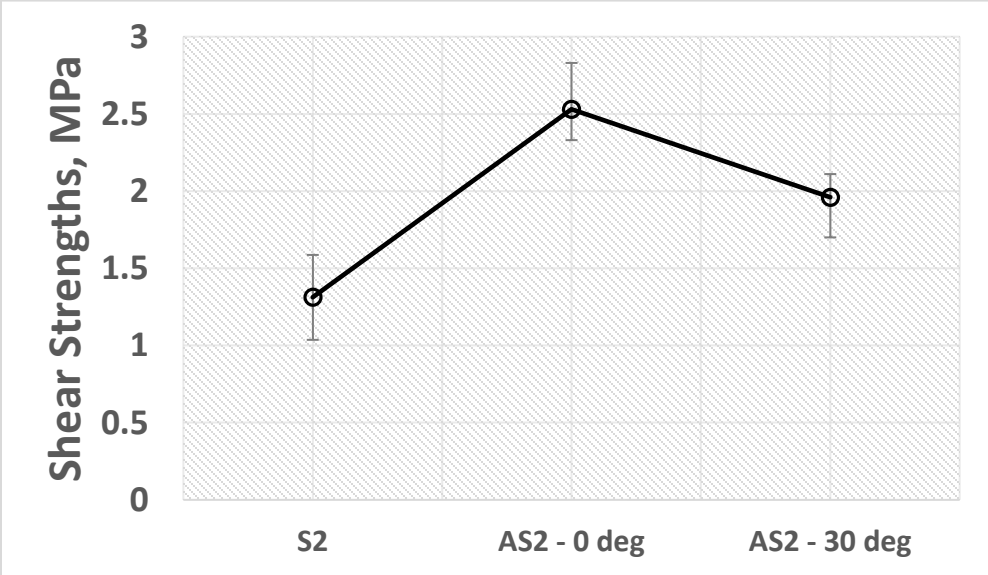

Figure 2.47: Shear pullout strengths of the laminate under tensile loading conditions with AS2 and S2 pins

2.6 DCB Experiments

The mode I delamination propagation properties of z-pin laminate for different kinds of pin inserts were experimentally obtained from tests on DCB specimens. The schematic for the DCB setup along with the geometric configuration of the specimens is given in Figure 2.48. Test specimens have a ply configuration $[0/90/90/0]_{2S}$ with Teflon at mid layer on a portion of its length as depicted. The configuration for z-pin insertions in the DCB specimens is shown in Figure 2.49. Two rows of eight pins are inserted behind the pre-crack region of the laminate. These pins are equidistant on the top surface of the laminate and the direction of insertion is systematically varied as shown in the figure, while keeping insertion angles constant for the entire specimen. The first pins behind the pre-crack is positioned such that the pin intersects the mid-layer of the laminate exactly at the boundary of the pre-crack. This implies that the position of the first pin behind the crack will depend on the insertion angle. Other pins are placed at a constant distance of 8 mm from the adjacent pins on the top surface.

The DCB test specimens were attached to metal plates which are then connected to the IMADA loading frame that measures vertical force and displacement. DCB test specimens with different pin inserts were then compared for force-displacement plots and rate of crack propagation. To measure the rate of crack propagation, vertical lines were marked on the cross-section of the laminate as shown in Figure 2.50. These markings are at constant distance of 5 mm from each other starting at the location of the pre-crack boundary. A camera was then used to capture the laminate motion during DCB tests to obtain the position of the crack-tip with time and applied displacement.

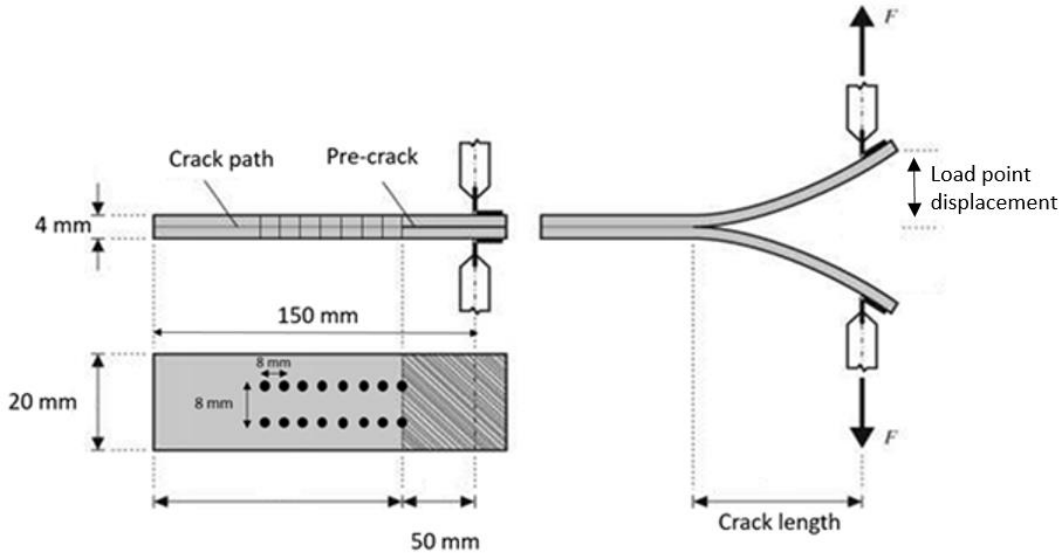

Figure 2.48: Schematic for the Double Cantilever Beam (DCB) test (not drawn to scale)

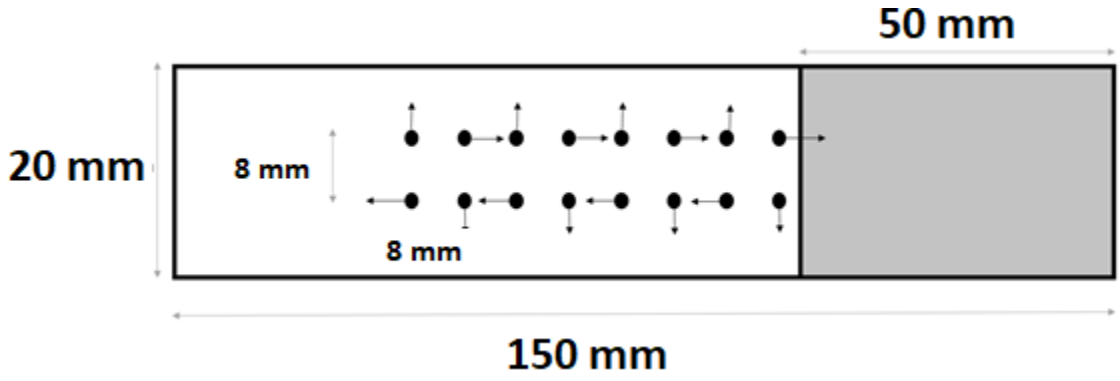

Figure 2.49: Top view of the laminate showing positions of pins on the top surface as well as the direction of pin insertions

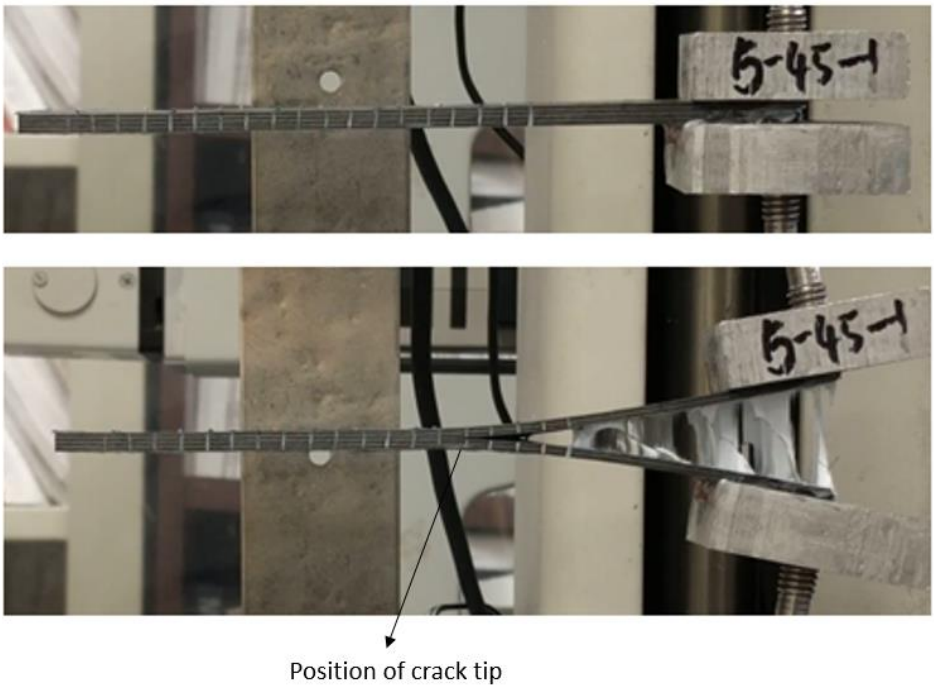

Figure 2.50: Vertical markings on laminate cross-section to identify position of crack-tip as a function of time and applied displacement

Figure 2.51 shows the load-displacement and crack propagation plots for laminates with smooth pin inserts of varying thicknesses inserted vertically. Figure 2.52 compares the delamination properties of laminates with S2 pin inserted at different angles. Ignoring rotations at the delamination front, beam theory gives the strain energy release rate of a DCB specimen as $G_I = \frac{3P\delta}{2ba}$ where P and δ are force and displacement at the load point, a is the delamination length, and b is the specimen width. Plugging values for the variables at onset of crack propagation, we obtain the critical strain energy release rate for the DCB specimens. Figure 2.53 compares the critical strain energy release rate at the onset of delamination for these specimens. The force needed for crack initiation as well as the critical strain energy release are higher for z-pinned laminates

and progressively increases with both pin thickness and insertion angle. Accordingly, the rate of crack propagation decreases with increase in pin diameter and pin angles. In fact, due to very high fracture toughness, specimens with insertion angles of 45° experienced bonding failure at the interface of loading plate and specimen before the crack propagated unto the last set of pins.

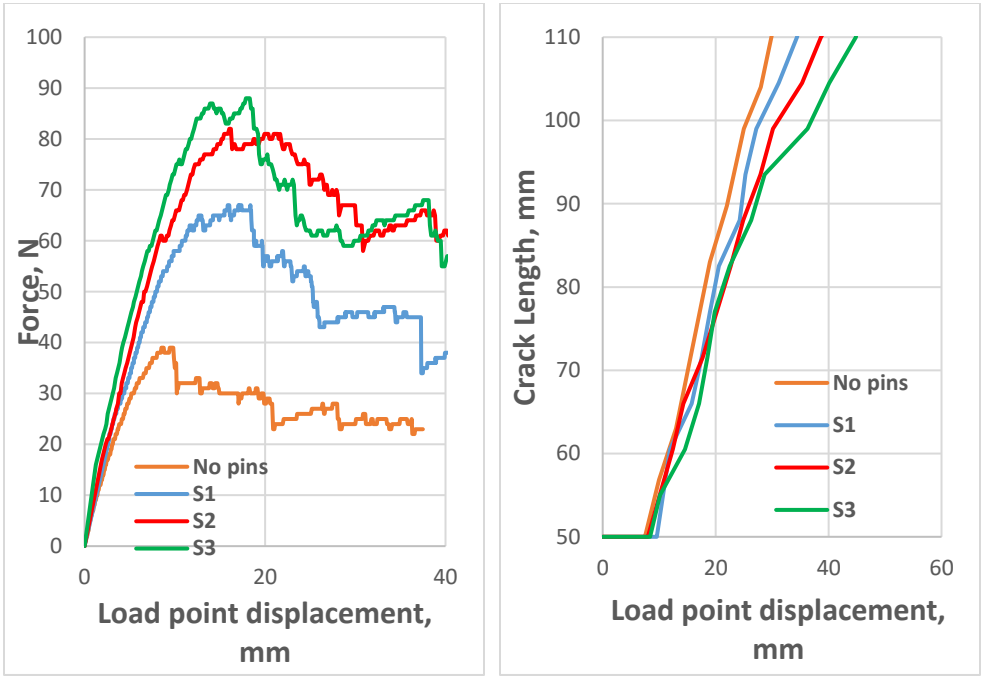

Figure 2.51. Force vs. displacement plot and progression of crack length in DCB specimens with smooth pins of different thicknesses inserted vertically

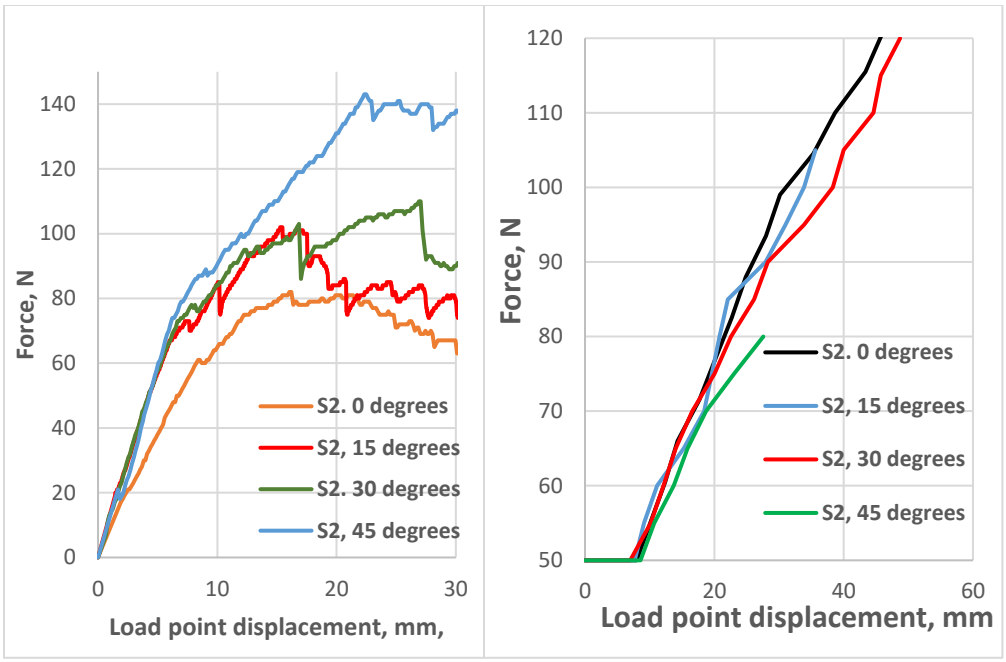

Figure 2.52. Force vs. displacement plot and progression of crack length in DCB specimens with S2 pins inserted at different angles

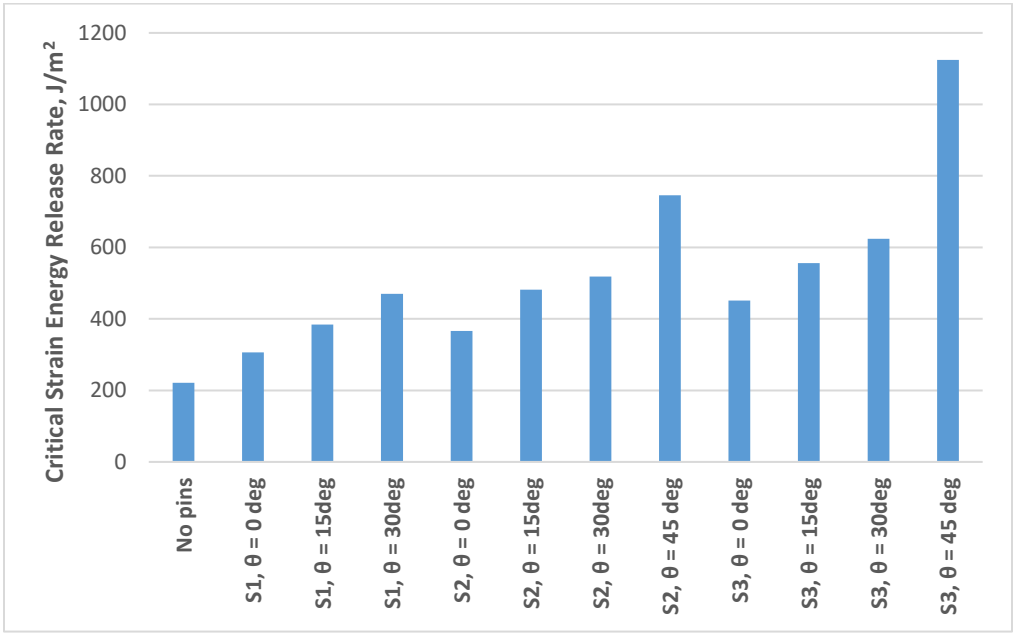

Figure 2.53. Critical strain energy release rate at the onset of crack propagation for DCB specimens with S2 pin inserted at different angles

Figures 2.54 and 2.55 show the load-displacement and crack propagation plots for laminates reinforced with threaded pins and anchored pins respectively. It can be inferred that threaded pins provide significantly higher resistance to crack propagation compared with smooth pins and that anchored pins outperformed threaded pins under mode-I loading.

Figure 2.56 compares the critical strain energy release rates at the onset of crack propagation for the laminates with different pin reinforcements. Threaded and anchored pins have significantly higher G values compared with smooth pins in that order. These results indicate that anchoring of pins can be highly effective in increasing fracture toughness and pin pullout properties. In situations where anchoring of the pins may not be acceptable due to exposure of the pins, threaded pins may be used as a viable alternative with excellent delamination resistance properties.

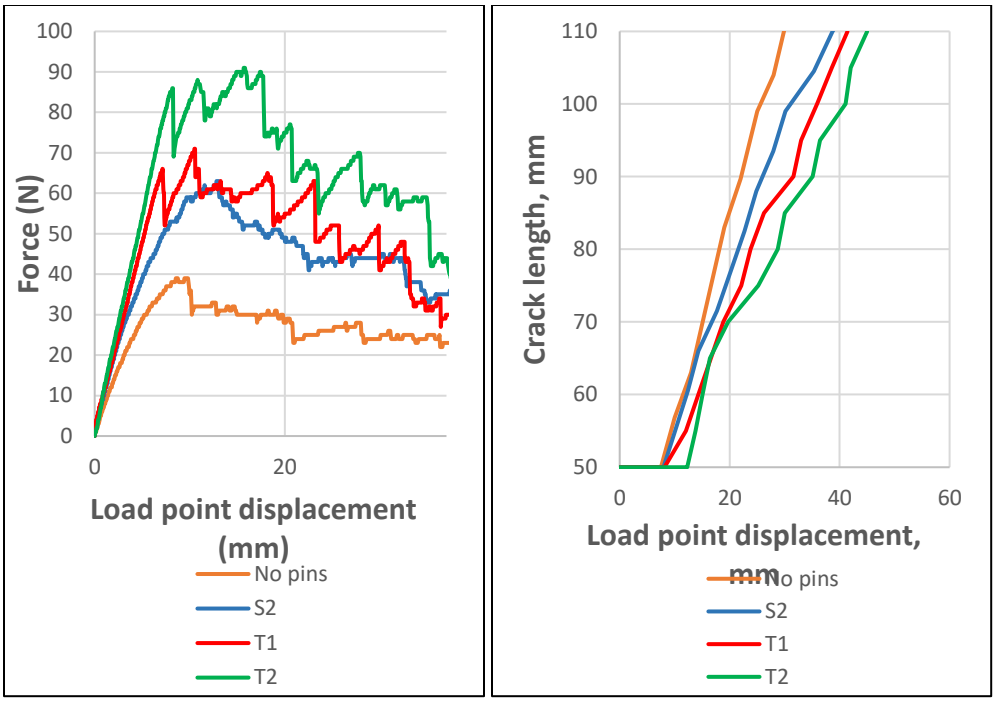

Figure 2.54. Force vs. displacement plot and progression of crack length in DCB specimens with threaded pins of different thicknesses

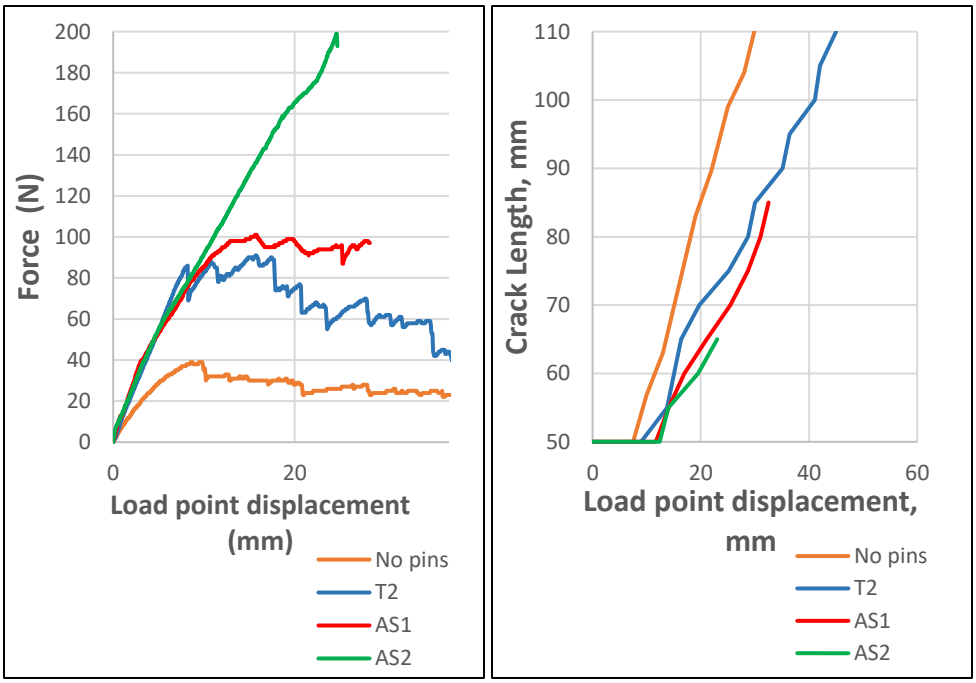

Figure 2.55. Force vs. displacement plot and progression of crack length in DCB specimens with anchored pins of different thicknesses

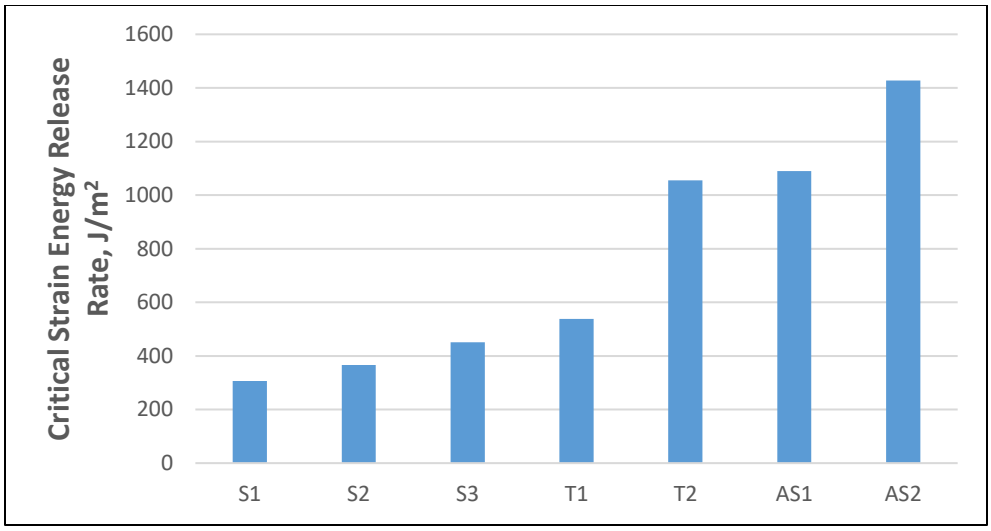

Figure 2.56. Critical strain energy release rate at the onset of crack propagation for DCB specimens with different pin reinforcements

In addition to the above tests, another set of tests were performed on DCB specimens to compare the performances of pins inserted at the same angle to the vertical, but in a different orientation. Towards this end, laminates with pin insertions according to configurations shown in Figure 2.57 are manufactured. One set of specimens have pins inserted at a 30^{o} to the vertical in the direction of length of the laminate (x-direction), and the other specimen set has pins inserted at the same angle in the direction of the width of the laminate (y-direction).

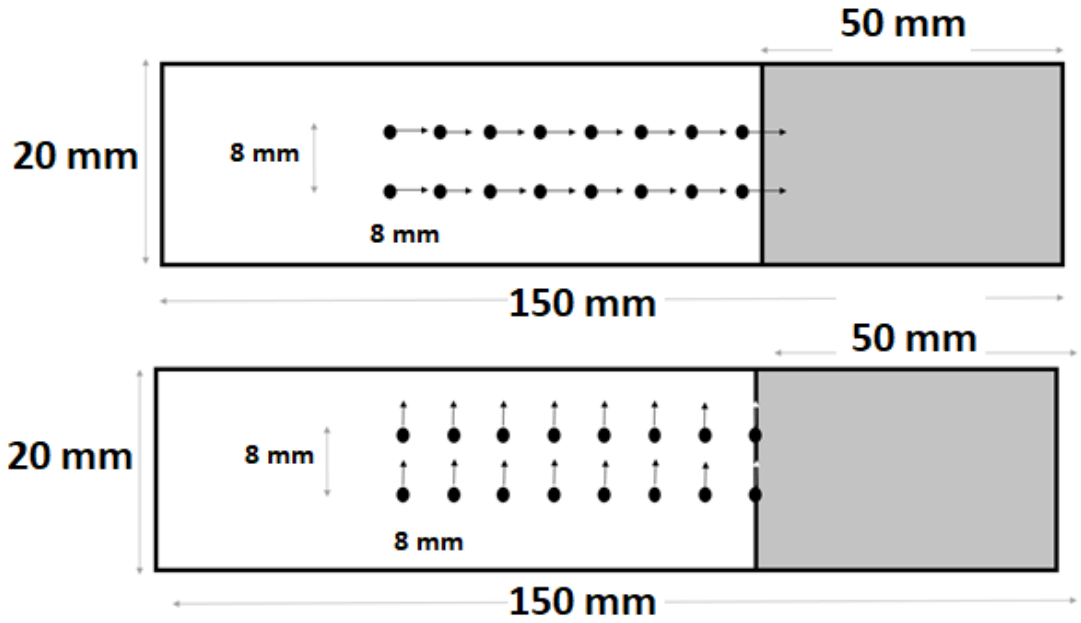

Figure 2.57: Top view of the laminate showing positions of pins on the top surface and the direction of pin insertions

To compare the effect of the pin orientation, finite element models are constructed for a single pin inserted into the laminate behind a crack tip as shown in Figure 2.58. One model has a pin in the x-direction, while the other has the pin in the y-direction. A unit displacement applied to the ends of the laminate shows in a 4% difference in the reaction forces with the pin in the x-direction providing higher stiffness. This indicates that the orientation of the pin may not cause a significant difference in delamination resistance of the laminate.

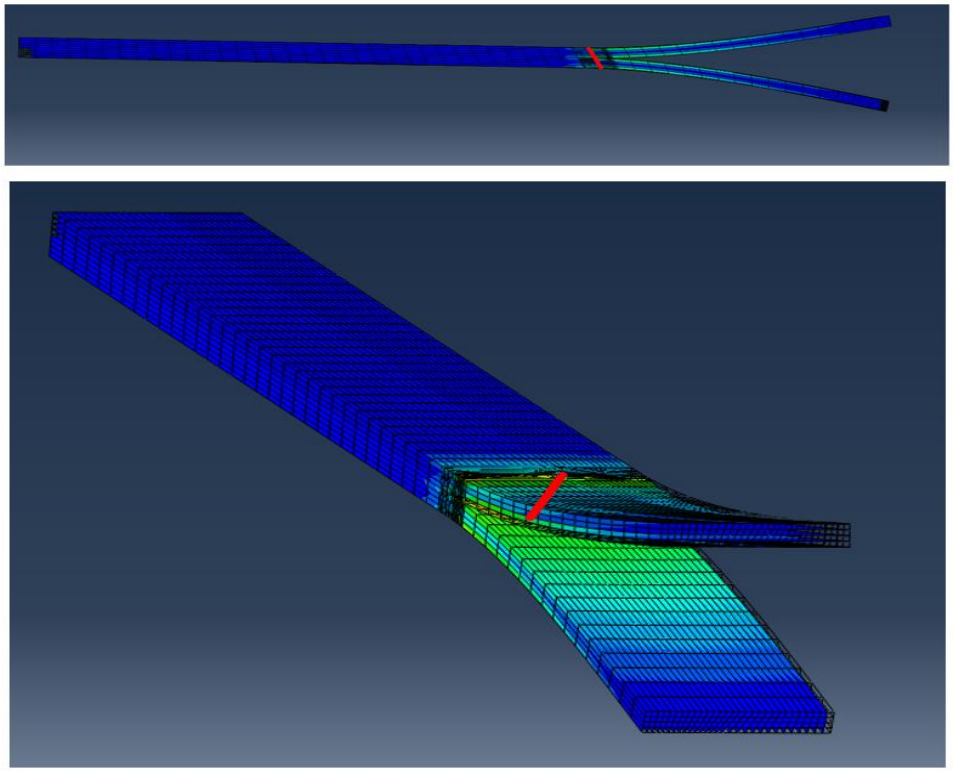

Figure 2.58: FE models created in ABAQUS for a single pin inserted at 30^{o} to the vertical in the x-direction (top) and y-direction (bottom)

Experimental results for these tests are provided in Figures. 2.59-2.60, where S2 pins are inserted at different angles according to the configurations shown in Figure 2.57. As expected, the plots show an increase in force at the onset of crack propagation and decrease in the rate of crack propagation with increase in pin angles. Figure 2.61 shows the crack propagation with applied displacement for specimens with pins of different orientations. These plots indicate negligible differences as a result of change in pin orientation.

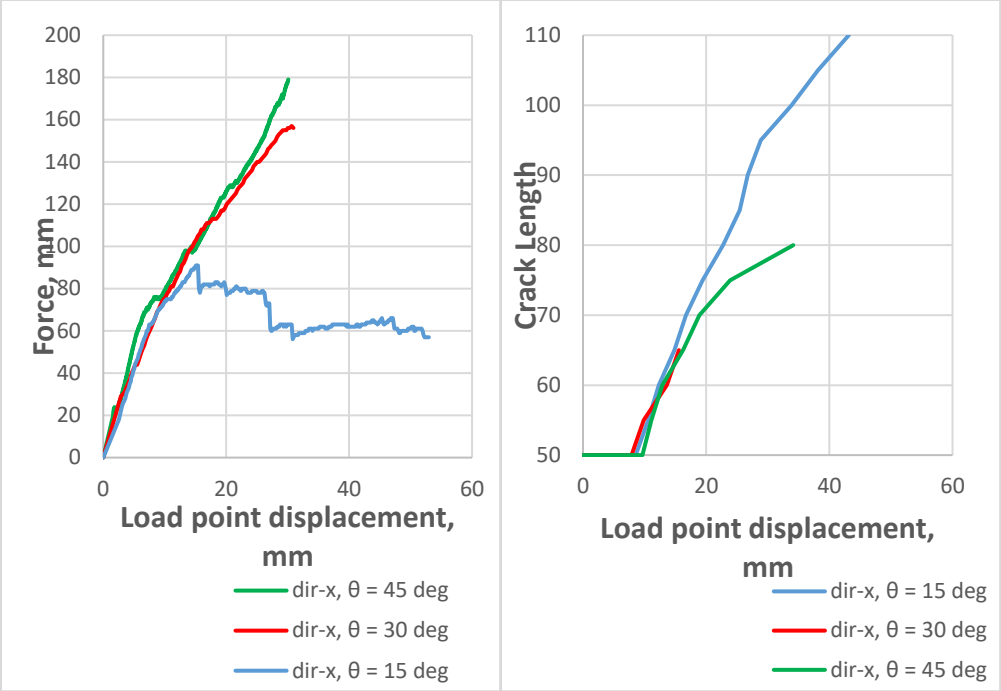

Figure 2.59: Force vs. displacement and progression of crack length in DCB specimens with pins inserted in the x-direction at different angles to the vertical

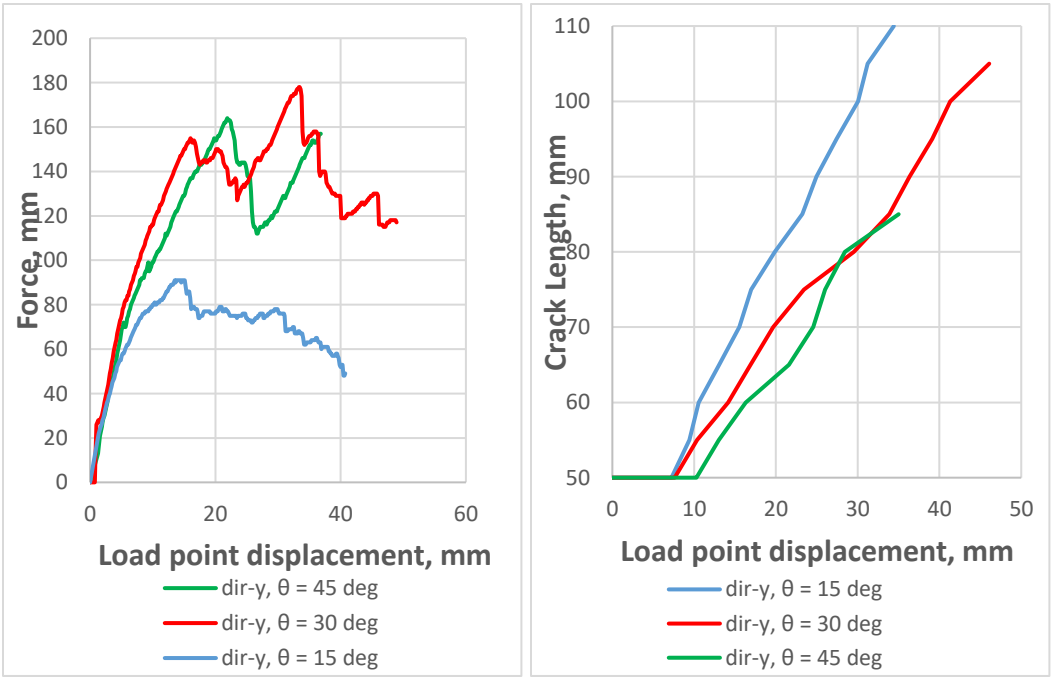

Figure 2.60: Force vs. displacement and progression of crack length in DCB specimens with pins inserted in the y-direction at different angles to the vertical

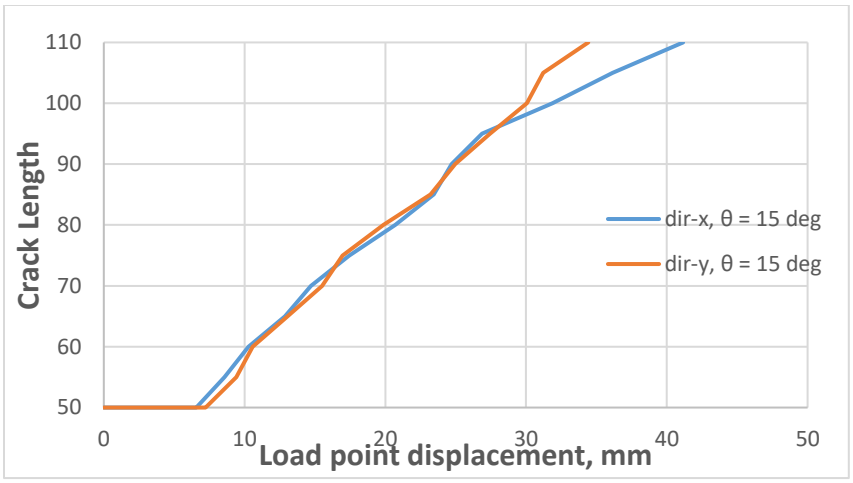

(a)

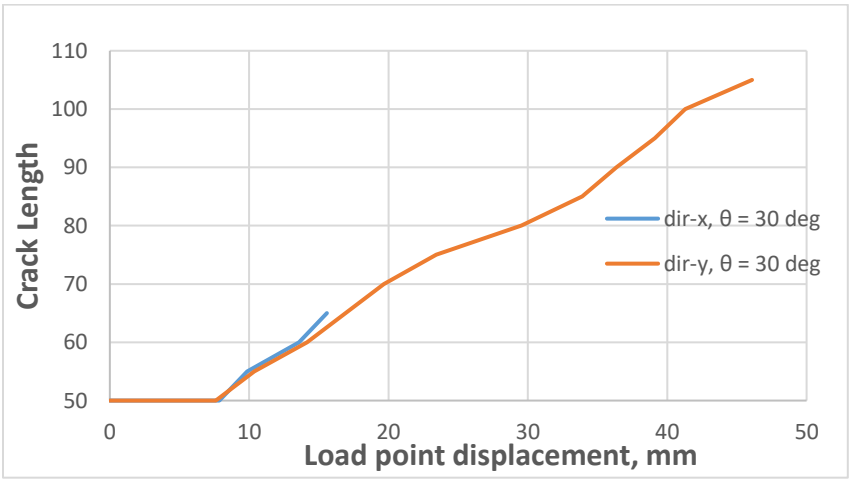

(b)

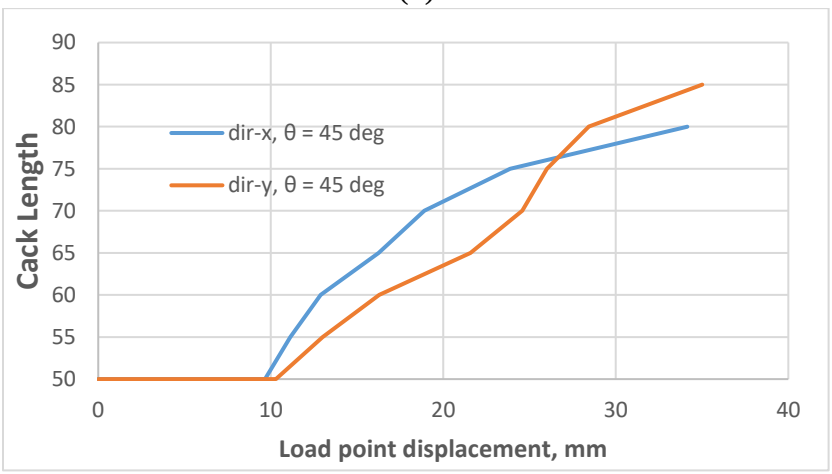

(c)

Figure 2.61: Plots showing progression of crack length in DCB specimens with pins inserted at the same angle to vertical but at different orientations

2.7 Galvanic Corrosion Tests

A concern that exists in using metal z-pins for reinforcement is galvanic corrosion. Galvanic corrosion is an electrochemical process in which one metal corrodes preferentially to another when both materials are in electrical contact, in the presence of an electrolyte. In this case, when steel pins and carbon are in contact, the more noble carbon decreases its corrosion potential at the expense of the more active aluminum. Potentially, galvanic corrosion may reduce the strength of the metal pins if a valid protection is not provided.

To test the impact of galvanic corrosion, test specimens according to the configuration given in Figure 2.62 were immersed in salt water with salinity of 3.5% NaCl solution which imitates sea-water conditions. Test specimens have ply configuration, $[0/90/90/0/0/90/90/0]_s$ with Teflon at mid layer and steel pins of 0.51mm diameter (S2 pins) are inserted vertically into the laminate. Specimens were then tested for pullout under tensile loading conditions.

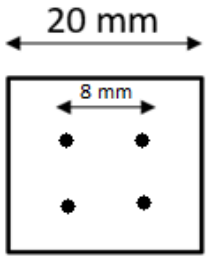

Figure 2.62: Top view of laminate geometry for specimens used to investigate the effect of galvanic corrosion

Specimens were tested and the mean pullout strengths obtained at different days of exposure to salinity are plotted in Figure2.63. The plot shows that there is no significant change in pullout strengths in SNN specimens immersed in saline solution up to 90 days. This alleviates concerns of galvanic corrosion effects on steel pin reinforced specimens

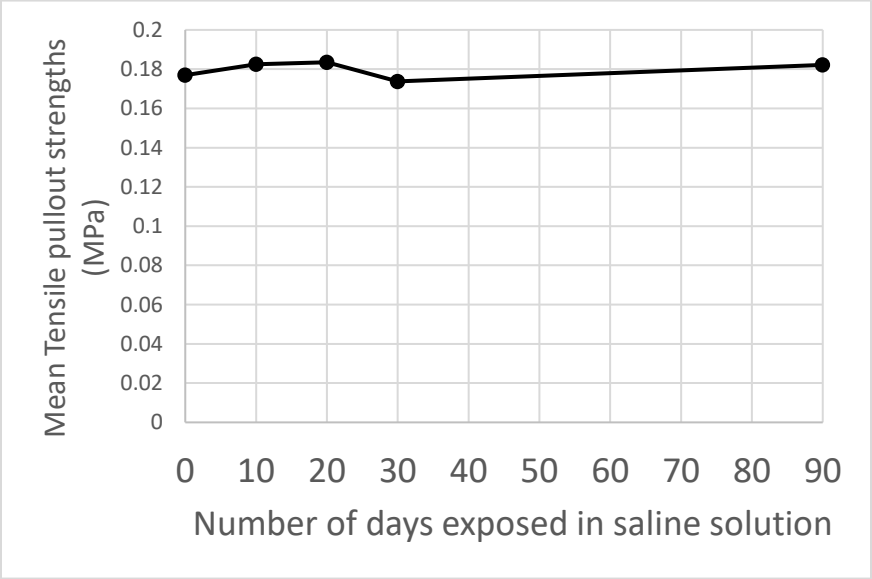

Figure 2.63: Mean tensile pullout strengths of specimens tested after various degrees of exposure to saline solution

2.8 Conclusions

This chapter summarizes novel z-pinning technologies developed to enhance delamination resistance for composite laminate structures through introduction of

various method for mechanical interlocking. Experiments were performed to test pullout strengths of laminates under tensile and shear loading with a pre-crack at the mid-layer of the laminate. Results obtained show an improvement in performance of the laminate when the pins were inserted at an angle, or had threaded exterior surface, or were anchored to the outer surface of the laminate. Similar improvement in delamination toughness was observed from crack propagation experiments on laminates with angled, threaded and anchored pin insertions. Non-linear FE models of the pin reinforced laminates constructed in ABAQUS verified experimental results of tensile pullout strengths of specimens reinforced with S2 pins. Galvanic corrosion was shown to have a minimal effect on the pin-reinforced laminates.

Chapter 3: Modeling of Z-pinning in X-Cor Sandwich Structures

3.1 Introduction

In this chapter, we focus on modeling the out-of-plane compressive and shear stiffness and strength of X-Cor sandwich structures where pins are aligned in a pyramidal geometry. First, we begin with a model based on the assumptions of a pin with perfect geometry and rigid connection to the facesheet. Comparing with known experimental results, we observe that this model is insufficient as it overestimates the stiffness and strength values of experimental specimens. Accordingly, the research presented in this chapter has been motivated in recognition of the need for a comprehensive analytical and computational model that incorporates the imperfections in the geometry and material properties of the structure. Towards this end, we develop models to understand the physics of the sandwich structure and estimate its performance with particular focus on individual components of the structure and the interaction between them. The approach is focused on developing appropriate macro-mechanical models that account for the meso-structural details unique to X-Cor composite sandwich panels. The model developed may then be used to estimate the out-of-plane compressive and shear stiffness and strength of the sandwich construction.

3.2 Sandwich Geometry, Nomenclature

3.2.1 Sandwich Geometry and Physics

The Z-pin reinforcements in an X-Cor sandwich core are arranged in a pyramidal geometry as shown in Figure 3.1. The figure shows a section of the sandwich structure in which four oblique pins are inclined at a constant angle to the vertical. Oblique pins 1 and 3 lie in the x-z plane while oblique pins 2 and 4 lie in the y-z plane. This pin geometry repeats on either sides at constant intervals until the sandwich boundaries are met. The top view of the corresponding four pins is shown in Figure 3.1(b).

Figure 3.2 shows a sketch of the side view of the sandwich panel illustrating the different core parameters. Parameters such as pin angle (θ), core thickness (h), specimen thickness (H), pin spacing (a), facesheet thickness (t_{fs}) are labeled in the figure. Pin radius is denoted by r and pin density ρ is inversely proportional to a^2. A unit cell of the sandwich is defined as a cross section of the sandwich with side-lengths equal to pin spacing.

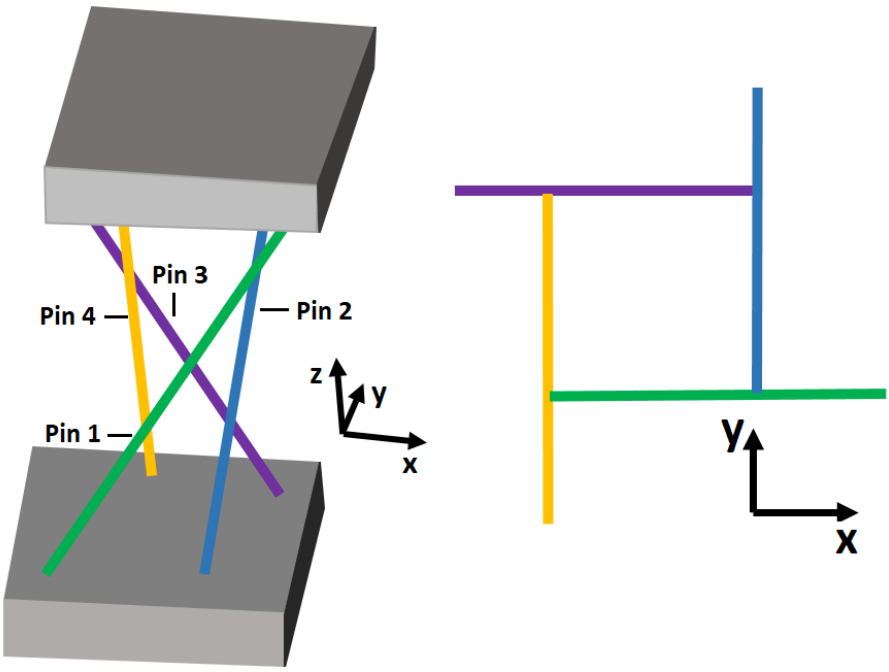

Figure 3.1(a) An isometric view of the pyramid geometry of the Z-pin reinforced sandwich structure (b) Top view of the arrangement

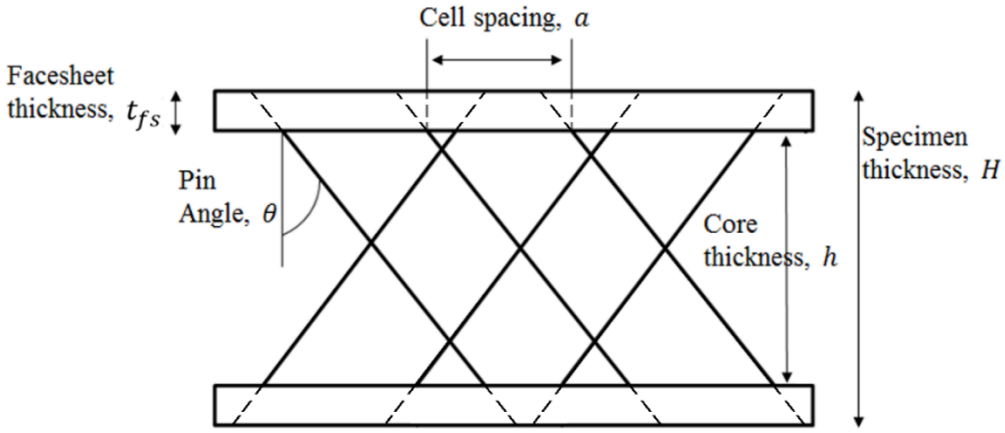

Figure 3.2 Sketch of the sandwich panel in its side view showing the geometric parameters

3.2.2 Experimental Specimen Samples at UMD

Our test samples for X-Cor sandwiches were received from Albany Engineering Composites (AEC). The specimens were composed of IM7 Carbon Fiber/ 8552 Epoxy Resin, while the pins were T300 composite fibers. The specimens had a pin density of 1 pcf (pound per cubic feet). The geometric and material properties of the facesheets, pin and the core are given in Tables 3.1 and 3.2 below.

The compressive and shear stiffness and strength values obtained for the specimens are given in Table 3.3. Shear stiffness values were not available due to constraints of

experimental setup. The experimental procedure for the tests are detailed further below in this chapter.

Table 3.1: Geometric properties of X-Cor sandwiches tested at UMD

Parameter	**Value**
Pin angle	30^o
Core thickness (mm)	12.7
Pin Spacing (mm)	5.3
Plate thickness (mm)	0.71
Pin diameter (mm)	0.28

Table 3.2: Material properties of pin, foam-core and facesheets of the X-Cor sandwiches tested at UMD

Material properties	**T300 (pin)**	**IM7 (facesheets)**	**Foam**
E_l	115 *GPa*	167.5 GPa	27.2 MPa
E_t	10 *GPa*	10.34 GPa	
G_{lt}	5 *GPa*	6.96 GPa	10.5 MPa
G_{tt}	3.7 *GPa*	4.3 GPa	
ν_{lt}	0.3	0.23	0.3
ν_{tt}	0.34	0.5	

Table 3.3: Experimental values for compressive and stiffness and strengths of UMD specimens

Compressive Stiffness (MPa)	**Compressive Strength (MPa)**	**Shear Strength (MPa)**
57	0.98	0.38

3.3 Preliminary Model of X-Cor sandwich

3.3.1 Pin Spring Constants

The pin truss forms the basis for the structural reinforcement of the Z-pin sandwich structure. Since the pins have moduli much greater than that of the foam core, the stiffness of the sandwich is mostly derived from the pins.

The performance of the z-pinned sandwich under out-of-plane compression loading and out-of-plane shear loading is directly related to the individual pin behavior under these loading conditions. For a sandwich under shear loading, only the pins in the direction of the loading, and the foam core contribute to the shear stiffness. Pins in the other direction have negligible resistance to shear loading. Among the pins that contribute to shear stiffness, half the pins are under compression (C-pins) and the other half under tension (T-pins). Under compressive loading of the sandwich, all the pins are under compression (C-pins). When a pin is under compression, the applied

displacements on the facesheets are transferred to the pin ends, but the rotation at the ends may be constrained. Figure 3.3 shows a single pin isolated from the structure under a vertical compressive load or a horizontal shear load.

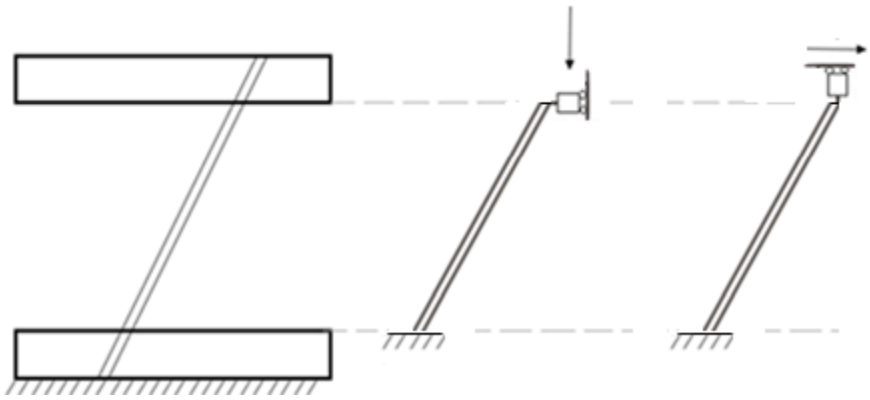

Figure 3.3: An oblique pin isolated from the sandwich structure under compression or shear loading represented as a slender body with guided boundary condition

The stiffness of the sandwich structure is directly dependent on the spring constant of the Z-pin. The compressive spring constant of the pin k_C is the vertical component of the force required to apply for a unit compressive displacement of one end while fixing the other end of the pin. The shear spring constant of the pin, k_S is the horizontal force component for a unit shear displacement. The compressive or shear spring constant of the pin is the sum of its axial and bending stiffness components in the corresponding loading direction.

For the pin under compression as shown in Figure 3.3, the compressive displacement. δ_c is related to axial displacement of the pin as $\delta_a = \delta_c \cos\theta$. The axial force required

for a unit axial displacement of the pin is given by $\frac{E\pi r^2}{L}$ where E is the longitudinal pin modulus. The component of force in the compressive direction is equal to $\frac{E\pi r^2}{L}\cos\theta = \frac{E\pi r^2}{h}\cos^2\theta$. Accordingly, the axial contribution to compressive spring constant is the compressive force per unit compressive displacement, and is given by

$$k_C = \frac{E\pi r^2}{h}\cos^3\theta$$

Alternatively, we may look at the strain energy of the pin acting as a bar under compression. Strain energy of the pin can be written as $U = \frac{1}{2}\frac{EA}{L}\delta_a{}^2$. Thus

$U = \frac{1}{2}\left(\frac{EA}{h}\cos^3\theta\right)\delta_c^2 = \frac{1}{2}k_c\delta_c^2$ where $k_c = \frac{EA}{h}\cos^3\theta$.

For a pin under shear as shown in Figure 3.3, the shear displacement, δ_s and axial displacement of the pin are related by $\delta_a = \delta_s \sin\theta$. The horizontal component of force for a unit shear displacement is then the axial contribution to shear spring constant of the pin and is given by $k_S = \frac{E\pi r^2}{h}\sin^2\theta\cos\theta$. The strain energy derivation of shear spring constant follows from the equation-

$U = \frac{1}{2}\frac{EA}{L}\delta_a{}^2 = \frac{1}{2}\left(\frac{EA}{h}\cos\theta\sin^2\theta\right)\delta_s^2 = \frac{1}{2}k_s\delta_s^2$ where $k_s = \frac{EA}{h}\sin^2\theta\cos\theta$.

The transverse displacement of a pin end under bending can be represented by an equivalent spring with a spring constant $k_b = \frac{3EI}{L^3}$ for a cantilever boundary condition. Under compressive loading, the transverse displacement of the pin, δ_b is related to the

compressive displacement as $\delta_b = \delta_c \cos\theta$. Additionally, the vertical component of the transverse force for a unit compressive displacement is equal to $\left(\frac{EI}{L^3}\sin\theta\right)\left(\frac{\delta_b}{\delta_c}\right) = \frac{3EI}{L^3}\sin^2\theta$. Hence, the contribution from bending stiffness towards compressive spring constant of the pin is equal to $\frac{3EI}{h^3}\sin^2\theta\cos^3\theta$.

Similarly, under shear loading of the sandwich, the transverse displacement relates to shear displacement as $\delta_b = \delta_c \sin\theta$ which then gives the bending contribution to shear spring constant as equal to $\frac{EI}{h^3}\cos^5\theta$. Summing up the bending and axial contributions, the compressive and shear spring constants of the pin are given by

$$k_C = \frac{E\pi r^2}{h}\left(1+3\xi^2\ \sin^2\theta\right)\cos^3\theta \tag{3.1}$$

$$k_S = \frac{E\pi r^2}{h}\left(\sin^2\theta+3\xi^2\ \cos^4\theta\right)\cos\theta \tag{3.2}$$

where $\xi = r/h$ is the ratio of the pin radius to core thickness. For typical sandwich geometries, $\xi << 1$ and hence the bending contribution to the spring constants may be neglected.

3.3.2 Model-1: A perfect-bonding model

If the pins of the sandwich are perfectly bonded to the facesheets, then the boundary conditions at the end of the pins can be assumed to be clamped. The compressive stiffness of the sandwich will be a sum of its contributions from the pins and the foam core. Let N_C be the number of pins and A_C the cross-sectional area of the specimen

used for compression testing, and the modulus of the foam be denoted by E_f. The compressive spring constant of the core, defined as the compressive force per unit compressive displacement is given by

$$K_c^{core} = N_c K_c + \frac{E_f A_C}{h} \tag{3.3}$$

Substituting for compressive spring constant of the pin from Equation (3.1), we obtain the compressive stiffness of the specimen as

$$E_C = \frac{K_c^{core} H}{A_C} = \frac{N_C H E \pi r^2}{A_C h}\left(1 + 3\xi^2 \sin^2\theta\right)\cos^3\theta + \frac{E_f H}{h} \tag{3.4}$$

Under shear loading, only the pins in the direction of loading resist the shear load, while the pins in the other direction have negligible shear stiffness. Let N_S be the total number of pins and A_S the cross-sectional area of the specimen used for shear testing, and G_f the shear modulus of the foam. The shear spring constant of the core defined as the shear force per unit shear displacement is given by

$$K_S^{core} = \frac{N_S K_S}{2} + \frac{G_f A_S}{h} \tag{3.5}$$

From Equations (3.2) and (3.5), we can obtain the shear stiffness of the specimen as

$$G_S = \frac{K_S^{core} H}{A_S} = \frac{N_S H}{2A_S}\frac{E\pi r^2}{h}\left(\sin^2\theta + 3\xi^2 \cos^4\theta\right)\cos\theta + \frac{G_f H}{h} \tag{3.6}$$

A clamped pin of length L has a Euler buckling load of $\frac{4EI\pi^2}{L^2}$. The pins under compression in the sandwich panel will buckle when the axial compression load carried by the pin reach this value. Ignoring the contribution of the foam core, we may calculate the compressive and shear strength of the sandwich based on the buckling load of the pins. Under compressive loading of the sandwich, the vertical component of the force

carried by the pins at buckling is equal to $\frac{4N_C EI\pi^2}{L^2}\cos(\theta)$. Accordingly, the buckling strength of the sandwich is given by

$$S_C = \frac{4N_C \pi^2 EI \cos^3\theta}{A_C h^2} \tag{3.7}$$

Under shear loading, the C-pins and the T-pins have the same spring constant. Accordingly, at the buckling of C-pins the shear load carried by the sandwich structure is equal to $\frac{2N_C EI\pi^2}{L^2}\sin(\theta)$ since only half the pins in the structure are in the direction of loading. Accordingly, the shear strength of the sandwich obtained from buckling load of the pins under compression as an indicator for failure is given by

$$S_S = \frac{2\pi^2 N_S EI}{A_S h^2}\cos^2\theta\sin\theta \tag{3.8}$$

For experimental specimens large in width, the number of pins per unit cross-sectional area of the panel can be approximated as $\frac{N_S}{A_S} = \frac{N_C}{A_C} = \frac{4}{a^2}$ where a is the pin spacing. The compressive and shear stiffness and strengths of UMD specimens are obtained from Equations (3.4)-(3.8) using this approximation for number of pins. The values obtained are compared with experimental values and are presented in Table 3.4. From Table 3.4, it can be gathered that the model grossly overestimates the compressive stiffness by nearly 10-fold in magnitude, but the compressive and shear strengths obtained from the model are underestimated by the model.

Table 3.4: Comparison of Experimental and Model-1 estimates for compressive stiffness and strengths of UMD specimens

Compressive Stiffness (MPa)		**Compressive Strength (MPa)**		**Shear Strength (MPa)**	
Experiment	**Model -1**	**Experiment**	**Model -1**	**Experiment**	**Model -1**
57	578	0.98	0.62	0.38	0.138

3.4 Improvements to X-Cor model

3.4.1 Motivation

The huge discrepancy in the preliminary model estimates for stiffness, especially in the case of compressive loading shows that the pin has to be remodeled taking into account its softening from material, bonding, and geometric defects. On the other hand, compressive and shear strength estimates are smaller than the experimental values since we have not taken into consideration the contribution of foam towards increasing strengths. In the following sections, we attempt to improve the model by considering various factors that affect the sandwich performance.

3.4.2 Bending-Axial Coupling

In the above derivation of pin spring constants, the coupling between axial and bending deformations of the pin was ignored. In this section, we investigate the effects of axial-bending coupling on the spring constants of the pin. Consider a single oblique pin under

compressive loading as shown in Figure 3.3. Let P and Q be the compressive and bending force acting on the pin boundaries. If we assume that the pin ends are constrained against rotation, then a moment M acts at the displacement end of the pin. The forces and moments on the pin under compressive loading are shown in Figure 3.4 below.

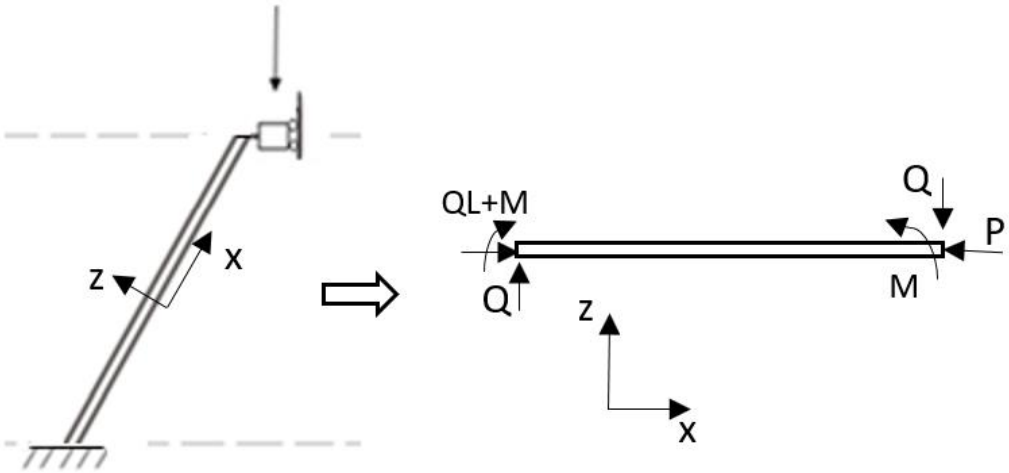

Figure 3.4: Oblique pin under compression isolated on the right showing boundary forces and moments acting

The governing equation for the axial-bending problem is given by

$$EI\frac{d^4w}{dx^4} + P\frac{d^2w}{dx^2} = M + Q(L-x) \tag{3.9}$$

where w is the transverse displacement of the pin. If u is the axial displacement of the pin, the boundary conditions of the pin with cantilever ends are given by

(3.10 a)

$$w_{x=0} = 0 \quad ; \left.\frac{dw}{dx}\right|_{x=0} = 0 \tag{3.10 b}$$

$$\left.\frac{dw}{dx}\right|_{x=L} = 0 \tag{3.10 c}$$

$$u_{x=L} = \frac{PL}{AE} + \frac{1}{2}\int_0^L \left(\frac{\partial w}{\partial x}\right)^2 dx$$
$$\frac{w_{x=L}}{u_{x=L}} = \tan\theta \tag{3.10 d}$$

The general solution for the governing equation in Equation (3.9) is given by

$$w(x) = C_1 \cos(\mu x) + C_2 \sin(\mu x) + \frac{M}{P} - \frac{Qx}{P} \tag{3.11}$$

where $\mu = \sqrt{\frac{P}{EI}}$. This gives

$$\frac{\partial w}{\partial x} = -C_1 \alpha \sin(\mu x) + C_2 \alpha \cos(\mu x) - \frac{Q}{P} \tag{3.12}$$

Substituting Equations (3.11) and (3.12) in Equation (3.10 a) gives $C_1 = -\frac{M}{P}$ and $C_2 = \frac{Q}{P\alpha}$. Substituting the values for these coefficients in Equations (3.12) and (3.10 b) gives $M = P\left(\frac{1-\cos(\mu L)}{\mu \sin(\mu L)}\right)$. Using this value for M in Equation (3.11) at $x = L$ provides the transverse displacement at the loading tip as

$$w(L) = \frac{Q}{S\mu}\left(\frac{2 - 2\cos(\mu L) - \alpha L \sin(\mu L)}{\sin(\mu L)}\right) \tag{3.13}$$

From the above values, Equations (3.12) and (3.10 c) give the tip axial displacement as

$$u(L) = \frac{PL}{AE} + \left(\frac{Q^2 \left(2\mu L + \mu L \cos(\mu L) - 3\sin(\mu L) \right)}{2P^2 \mu \left(1 + \cos(\mu L) \right)} \right) \tag{3.14}$$

Relating the transverse and axial displacements from Equations (3.13) and (3.14) by Equation (3.8 d) gives moment, Q in terms of P. Compressive spring constant may then be derived by the relationship

$$k_c = \frac{P\cos\theta + Q\sin\theta}{u(L)/\cos\theta} \tag{3.15}$$

The compressive force versus displacement is obtained computationally from Equation (3.15) for a sandwich with T300 pins of 0.28 mm diameter inclined at 30^o to the vertical with a core thickness equal to 12.7 mm. The Force-displacement plots for a pin under compression is shown in Figure 3.5. As can be seen the linear, uncoupled approximations for the F-d plots are nearly identical to the non-linear solution before buckling of the pin. In fact, for small displacements, the axial displacements can be approximated by including only the first term of the Taylor series expansion of the expression from Equation (3.14), and is given by

$$u(L) = \frac{PL}{AE} + \frac{Q^2 L^5}{240 E^2 I^2} \tag{3.16}$$

which when substituted in Equation (3.15) gives the compressive spring constant as

$$k_C = \frac{E\pi r^2}{h}\left(1 + 3\xi^2 \sin^2\theta\right)\cos^3\theta - \frac{2}{5}\frac{Qh}{r^2}\sin\theta \tag{3.17}$$

For a sandwich of typical dimensions, the bending term as well as the coupling terms are negligible compared to the axial stiffness and may simply be neglected.

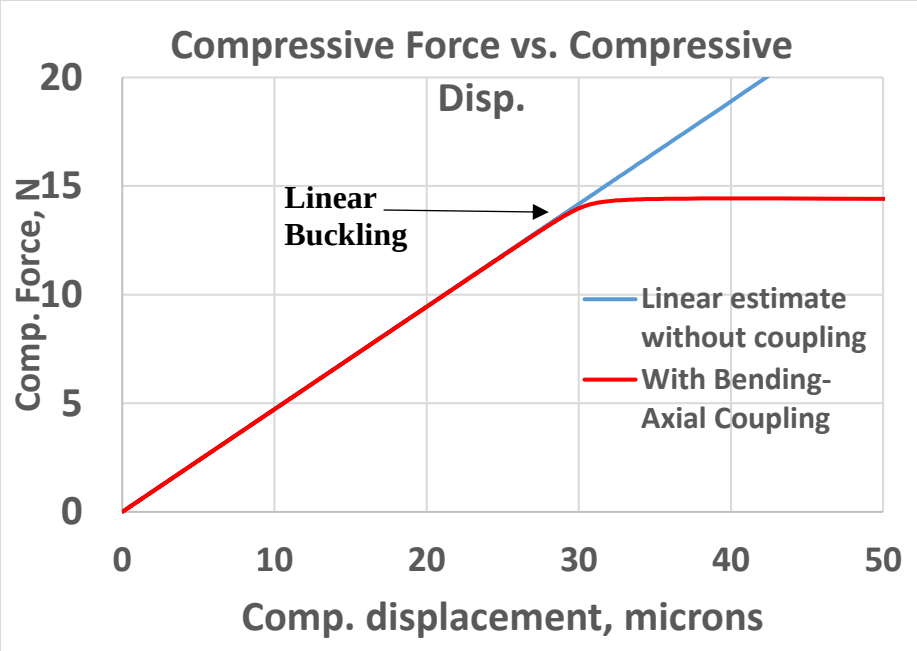

Figure 3.5: Compressive Force vs. displacement obtained by including bending-axial coupling compared with linear decoupled analysis

For a pin under shear loading, the bending and axial displacements are related by $\frac{w_{x=L}}{u_{x=L}} = \cot\theta$ for a pin under compression (C-pin) and $\frac{w_{x=L}}{u_{x=L}} = -\cot\theta$ for a pin under tension (T-pin). For a C-pin under shear, the shear force-displacement plot resembles that of compressive F-d plot as shown in Figure 3.5. Figure 3.6 shows the shear force vs shear displacement for a T-pin computed according to the non-linear analysis above. It can be seen that under shear loading the T-pin is hardening, i.e., its stiffness increases with displacement. This analysis assumes a rigid connection between the T-pin and the facesheet, i.e., the pin boundaries are assumed to be clamped. In the following section, we study the influence of flexible boundary conditions at the pin-facesheet interface.

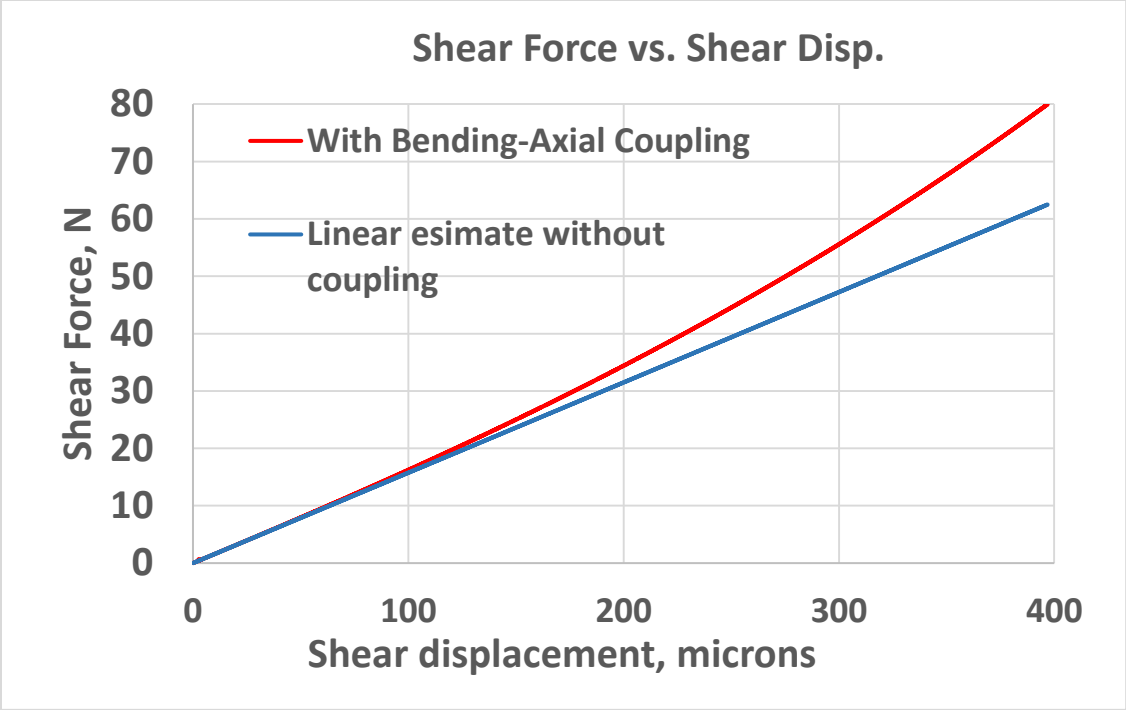

Figure 3.6: Shear Force vs. displacement obtained by including bending-axial coupling compared with linear decoupled analysis

3.4.3 Pin Boundary Conditions

For a pin embedded into the facesheet of an X-Cor specimen, the pin may be represented as a slender body with rotational springs with constant k_θ at its ends as shown in Figure 3.7. If the pin is embedded into a rigid plate, then $k_\theta \approx \infty$ and the pin can be assumed to have clamped boundary conditions at its ends. In X-Cor sandwich specimens, the pins embedded into the facesheets cause the formation of resin-rich zones around each pin. These zones are created from the voids formed between the composite fibers during pin insertion that are occupied by the resin during curing. This results in a pin-facesheet interface comprised of the compliant adhesive matrix. Thus, the rotation at the pin ends are only partially constrained resulting in softening of the

rotational spring constant and a boundary condition between hinged and clamped conditions, i.e. $0 < k_\theta < \infty$.

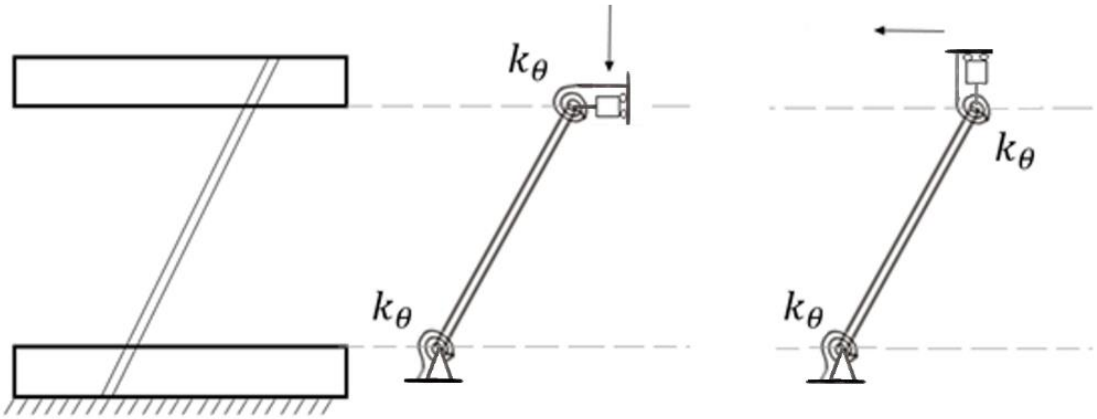

Figure 3.7: An oblique C-pin isolated from the sandwich structure under compression or shear loading represented as a slender body with rotational springs at its boundaries

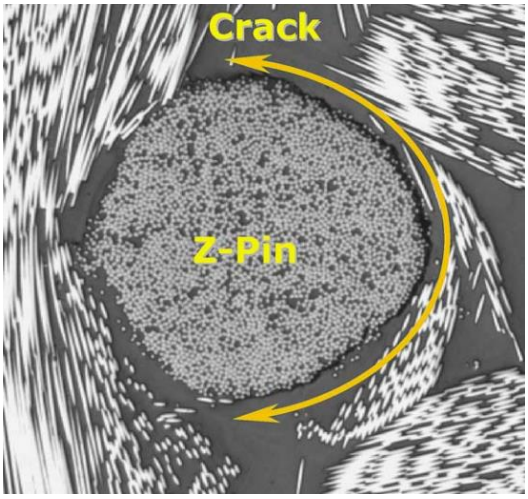

Figure 3.8: Resin rick area around a Z-pin inserted into aI composite laminate showing the crack around the z-pin, taken from [13]

The rotational spring constant k_θ at the boundary of the C-pin is dependent on the geometry and material properties of the pin-facesheet interface. Microscopic image of the resin-rich interface surrounding the pin inserted into a composite laminate is presented in [13] and shown in Figure 3.8. Based on the image, the interface layer thickness can be estimated to be about 17% of the pin radius. For this value of interface thickness, the rotational spring constant of the pin will depend on the interface modulus E_{int}. The equivalent rotational spring constant for the interface can then be obtained by an FE model of a single pin embedded in a facesheet and surrounded by a matrix interface of a fixed thickness as shown in Figure 3.9.

To obtain the rotational spring constant for a given interface modulus in the FE model, we may look at the response of the pin to a unit force applied perpendicular to the pin at its center while the external surfaces of the facesheets are fixed. The midpoint displacement may then be compared with an equivalent beam with rotational springs at its boundaries as shown in Figure 3.10. For a vertical central load Q applied on the beam shown in Figure 3.10, the midpoint displacement can be analytically obtained as

$$w_{mid} = \frac{Q\left(8EIL^3 + k_\theta L^4\right)}{192EI(2EI + Lk_\theta)} \tag{3.18}$$

From Equation (3.18), the non-dimensional rotational spring constant, κ is derived as

$$\kappa = \frac{k_\theta L}{EI} = \frac{8 - 384\beta}{192\beta - 1}; \qquad \beta = \frac{EIw_{mid}}{QL^3} \tag{3.19}$$

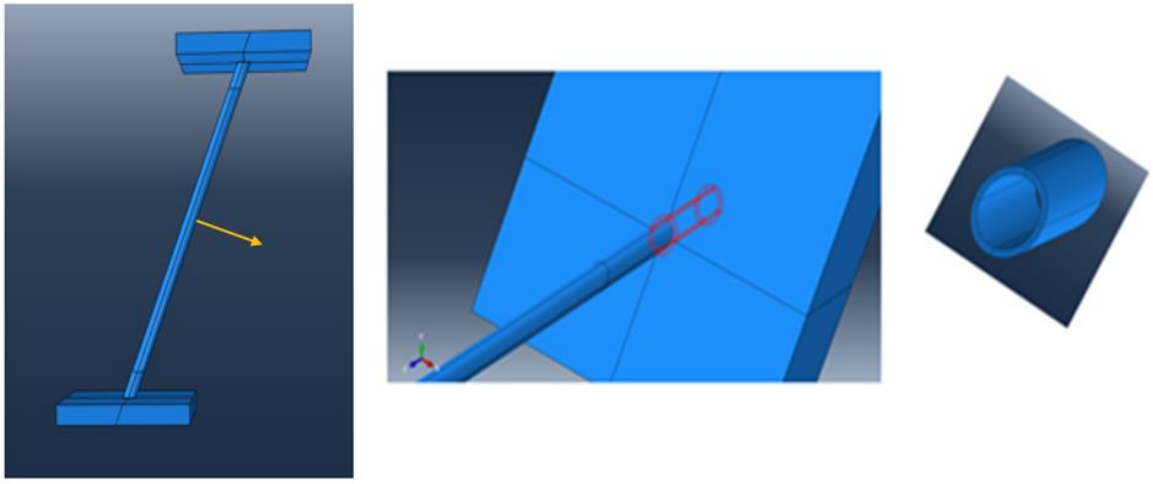

Figure 3.9 (a) FE model of a single pin embedded in a facesheet with a central load (b) Pin-facesheet interface showing adhesive layer surrounding the pin inside the facesheet (c) Interface layer isolated from rest of the model

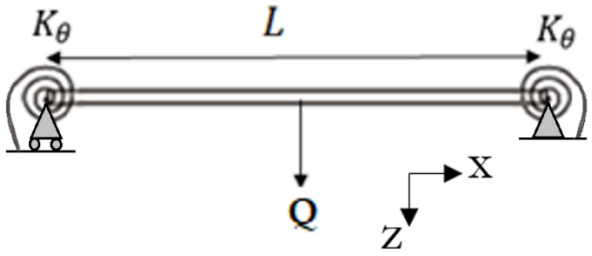

Figure 3.10: Z-pin represented with rotational spring constant at its ends

The governing equation for the pin in Figure 3.10 is given by

$$EI\frac{d^4w}{dx^4} + P\frac{d^2w}{dx^2} = 0 \qquad (3.20)$$

with

$$
\begin{aligned}
w_{x=0} &= 0, \qquad EI\left.\frac{d^2w}{dx^2}\right|_{x=0} - k_\theta \left.\frac{dw}{dx}\right|_{x=0} = 0 \\
w_{x=L} &= 0, \qquad EI\left.\frac{d^2w}{dx^2}\right|_{x=L} + k_\theta \left.\frac{dw}{dx}\right|_{x=L} = 0
\end{aligned}
\tag{3.21}
$$

The general solution to the equation is of the form

$$
w(x) = A\cos(\mu x) + B\sin(\mu x) + Cx + D \tag{3.22}
$$

where $\mu = \sqrt{\frac{P}{EI}}$. Substituting the boundary conditions from Equation (3.21) into Equation (3.22) gives

$$
\begin{bmatrix}
1 & 0 & 0 & 1 \\
\cos(\mu L) & \sin(\mu L) & L & 1 \\
-L\mu^2 & -\kappa\mu & -\kappa & 0 \\
-\kappa\mu\sin(\mu L) - \alpha^2 L\cos(\mu L) & \kappa\mu\sin(\mu L) - \mu^2 L\cos(\mu L) & \kappa & 0
\end{bmatrix}
\begin{Bmatrix} A \\ B \\ C \\ D \end{Bmatrix}
=
\begin{Bmatrix} 0 \\ 0 \\ 0 \\ 0 \end{Bmatrix}
\tag{3.23}
$$

To obtain the Euler buckling load for the pin, we must have the determinant of the matrix on the left hand side of Equation (3.23) equal to 0. Solving this gives the buckling load of the C-pin as $\frac{\alpha EI\pi^2}{L^2}$ where α is a coefficient dependent on κ by the equation-

$$
\begin{aligned}
&\kappa^2\left(2 - 2\cos\left(\sqrt{\alpha}\pi\right) - \alpha L\sin\left(\sqrt{\alpha}\pi\right)\right) + \\
&\kappa\left(2\sqrt{\alpha}\pi - 2\alpha\pi^2\cos\left(\sqrt{\alpha}\pi\right)\right) + \pi^3\sqrt{\alpha^3}\,\sin\left(\sqrt{\alpha}\pi\right) = 0
\end{aligned}
\tag{3.24}
$$

The relationship between α and κ is plotted in Figure 3.11.

Based on the analysis above, C-pins will buckle when the axial force in the pins reaches the Euler buckling load. The compressive force at which the pin in Figure 3.3 buckles is given by

$$F_C^b = \frac{\alpha EI\pi^2}{h^2}\cos^3\theta \tag{3.25}$$

Under shear loading, the shear force at which a C-pin will experience buckling is given by

$$F_S^b = \frac{\alpha EI\pi^2}{h^2}\cos^2\theta\sin\theta \tag{3.26}$$

Thus, the equivalent boundary condition for a given interface modulus can be obtained from the midpoint displacement of the pin in the FE model for a unit central force from Equation 3.19, while Equations 3.25 and 3.26 give corresponding pin buckling loads.

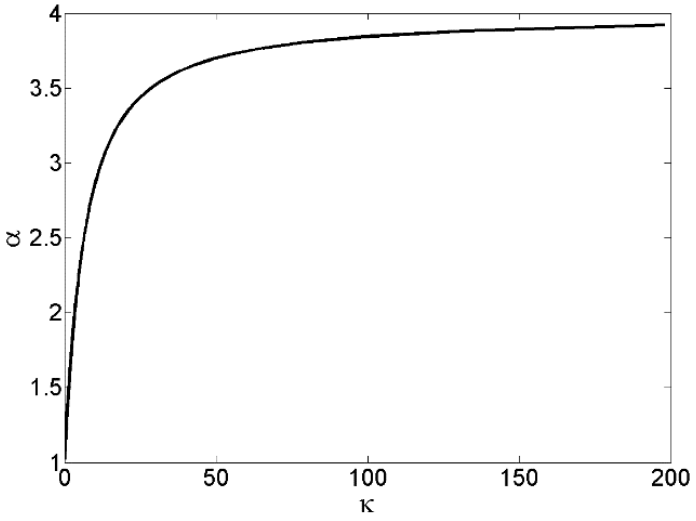

Figure 3.11: Plot showing relationship between α and non-dimensional spring constant κ

3.4.4 Eccentric Loading of sandwich under compression

When the sandwich is under compression, the displacement is applied to the facesheets which is transferred to the pin ends. Since the pin and the facesheet are not rigidly

connected, the effect of the eccentricity of the load point must be investigated. Towards this end, consider a single column under compression with a load acting at an offset distance, e from the center of the column as shown in Figure 3.12(a). The effect of eccentric load on the column is to create a bending moment at the pin ends causing further bending of the column. This results in reduction of axial stiffness of the pin through bending-axial coupling that may not be negligible. For the column shown in Figure 3.12(a), the governing equation is still given by Equation (3.18). Isolating the column as shown in Figure 3.12(b), we obtain the new boundary conditions as

$$\begin{aligned} w_{x=0} &= 0, \qquad EI\left.\frac{d^2w}{dx^2}\right|_{x=0} - k_\theta \left.\frac{dw}{dx}\right|_{x=0} = -Pe \\ w_{x=L} &= 0, \qquad EI\left.\frac{d^2w}{dx^2}\right|_{x=L} + k_\theta \left.\frac{dw}{dx}\right|_{x=L} = -Pe \end{aligned} \tag{3.27}$$

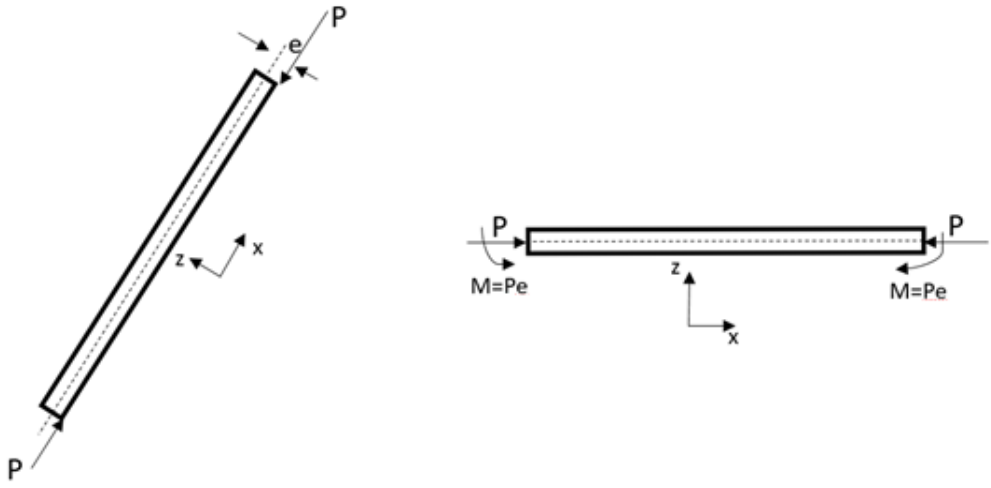

Figure 3.12 (a) An oblique pin subjected under axial loads at a distance away from the centroidal axis of the pin (b) Moments resulting at pin ends from eccentric loading

The effect of eccentric loading on a column is maximum for simply supported boundary conditions and null for clamped boundary conditions. Since, the pin-facesheet bonding is flexible, the effect of eccentric loading in a sandwich panel may not be neglected. For simply supported boundary conditions, we obtain the solution for transverse displacement as

$$w = e\left(\tan\left(\frac{\mu L}{2} \right) \sin\left(\mu x \right) + \cos\left(\mu x \right) - 1 \right) \tag{3.28}$$

where $\mu = \sqrt{\frac{P}{EI}}$. Using Equation (3.10 c) to obtain axial displacement, we get

$$u = \frac{PL}{AE} - \frac{\mu e^2 \left(\sin\left(L\mu \right) - L\mu \right)}{4\cos\left(\frac{L^2 \mu^2}{4} \right)} \tag{3.29}$$

Equation (3.29) is applied to plot compressive force versus displacement for a T300 pin of 0.28 mm diameter for various degrees of eccentricity in loading in Figure 3.13. As can be seen eccentricity in loading can significantly affect the axial modulus of the pin. The drop in axial stiffness of the pin increases with increase in the degree of eccentricity.

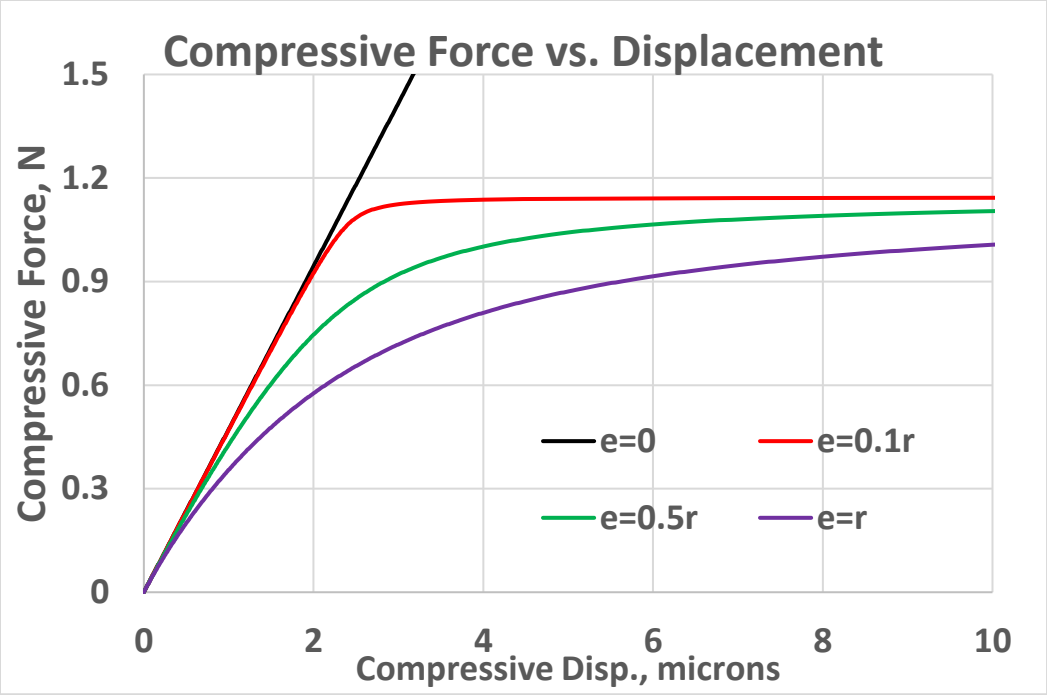

Figure 3.13: Compressive Force vs. displacement for an oblique T300 pin of 0.28 mm diameter with simply supported ends under eccentric axial loading with varying degrees of eccentricity

3.4.5 Effect of geometric imperfections of the pin

Sandwich panels have various geometric and material imperfections which affect their properties. The pins used to reinforce sandwich panels are slender and a small amount of eccentricity in its geometry including fiber misalignment can greatly reduce their effective stiffness under compression. Consider a pin as shown in Figure 3.14, with an initial imperfection $w_0(x)$ under a compressive load P. The governing equation and boundary conditions of the pin are given by

$$EI\frac{d^4w}{dx^4} + P\frac{d^2w}{dx^2} + P\frac{d^2w_0}{dx^2} = 0 \tag{3.30}$$

with

$$w_{x=0} = 0, \qquad EI \left.\frac{d^2 w}{dx^2}\right|_{x=0} - k_\theta \left.\frac{dw}{dx}\right|_{x=0} = 0$$
$$w_{x=L} = 0, \qquad EI \left.\frac{d^2 w}{dx^2}\right|_{x=L} + k_\theta \left.\frac{dw}{dx}\right|_{x=L} = 0 \tag{3.31}$$

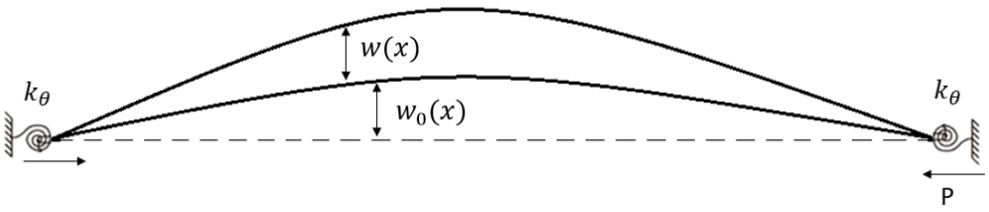

Figure 3.14: : A slender beam with geometric imperfections under compressive load

The imperfection, $w_0(x)$ may be represented in terms of a single parameter. For example, one may choose a pin imperfection expressed as

$$\frac{w_0(x)}{L} = \left(\frac{e}{L}\right)_{eff} \sin\left(\frac{\pi x}{L}\right) \tag{3.32}$$

For this pin imperfection, the exact solution for $w(x)$ can then be analytically derived in terms of axial load P. The axial deformation of the pin, Δ including the axial shortening due to pin bending is equal to

$$\Delta = \frac{PL}{AE} + \frac{1}{2}\int_0^L \left(\frac{dw}{dx}\right)^2 dx \tag{3.33}$$

The axial deformation may then be computed as a function of applied load P. For an imperfect pin, the slope of the force-displacement graph drops gradually with rate of decrease depending on the magnitude of effective imperfection. The slope of the axial force-displacement graph can be expressed in the following form

$$k_{axial} = \frac{1}{\partial\Delta/\partial P} = \frac{\lambda E \pi r^2}{L} \tag{3.34}$$

where λ is the stiffness reduction factor due to effective imperfection and varies with pin axial displacement. From Equations (3.1), (3.2), and (3.34), the compressive and shear spring constants of a single C-pin can be expressed as

$$k_C^{C-pin} = \frac{\lambda E \pi r^2}{h} \cos^3 \theta \tag{3.35}$$

$$k_S^{C-pin} = \frac{\lambda E \pi r^2}{h} \sin^2 \theta \cos \theta \tag{3.36}$$

Figure 3.15 shows the plot of a axial force vs. axial displacement of a T300 pin with 0.28 mm diameter with and without imperfections. For an imperfect pin, the slope of the force-displacement graph drops gradually with rate of decrease depending on the magnitude of effective imperfection. The decrease in slope or spring constant of the pin is captured in Figure 3.16 that shows a plot of the parameter, λ with pin axial displacement for various different degrees of geometric imperfection.

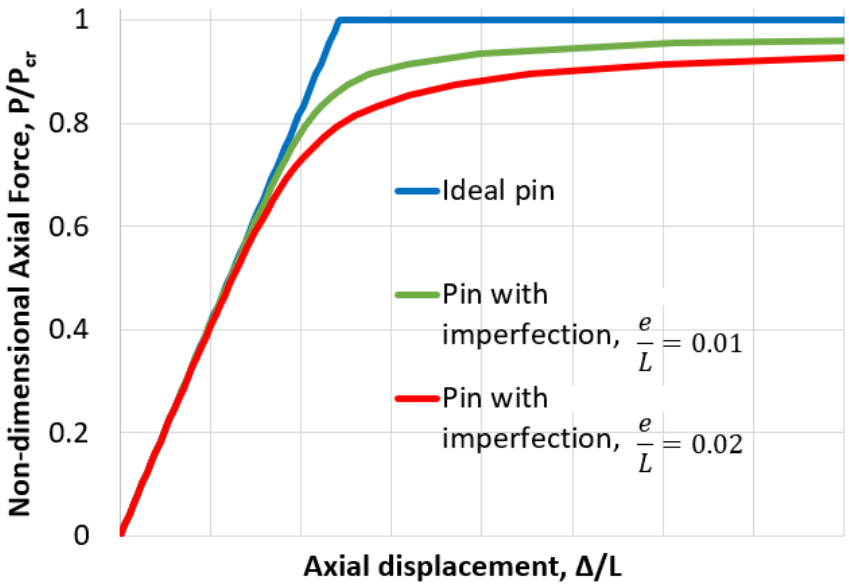

Figure 3.15: Axial force vs. displacement plots for a T300 pin with and without geometric imperfection

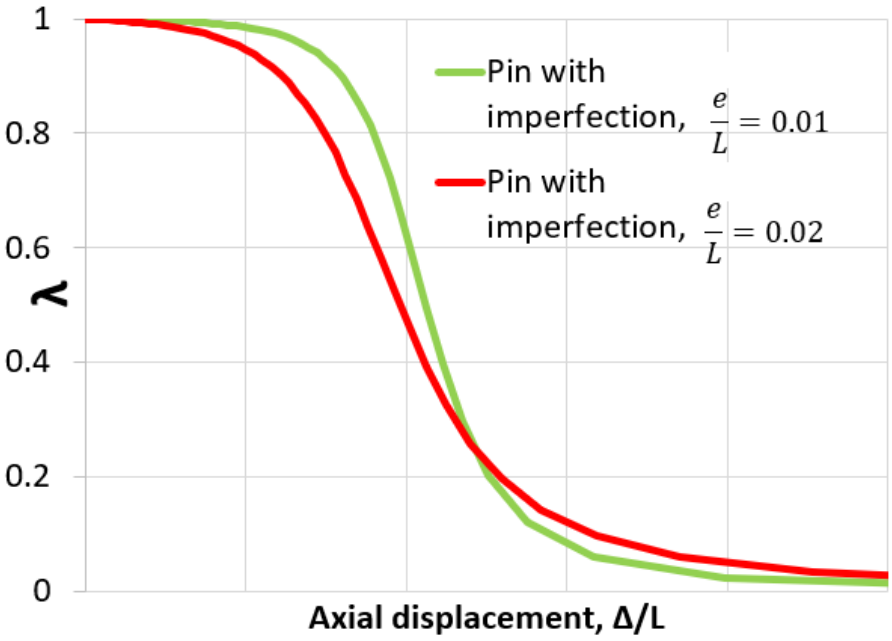

Figure 3.16: Variation of parameter, λ with pin axial displacement for a pin with geometric imperfections

3.4.6 Effective Imperfection and Effective Interface Modulus

The effect of geometric imperfection of the pin is identical to the effect of eccentric loading on the pin. In addition to geometric imperfections, composite fiber pins used to reinforce sandwich structures have been shown to contain voids in their interior caused from incomplete wetting of the fibers with resin matrix during their manufacture [8]. This results in loss of pin modulus with application of compressive stress in the pin. The bonding between the pin and the facesheet is also susceptible to imperfections. Accordingly, for the C-pins in the sandwich construction, the nonlinear behavior due to the combined effect of geometric and material imperfection, and eccentric loading can be represented by introducing two parameters: effective imperfection $\left(e/L\right)_{eff}$ and effective *in-situ* interface modulus E_{int}^{C-pin} different from the resin modulus. The effective imperfection $\left(e/L\right)_{eff}$ is an empirical parameter that captures the softening of the C-pin due to geometric and material defects. The effective *in-situ* interface modulus E_{int}^{C-pin} results in a modified boundary condition at the pin ends. Accordingly, the compressive and shear forces at which a pin buckles can be obtained from Equations (3.25) and (3.26) with the value of α corresponding to E_{int}^{C-pin}.

3.4.7 Stiffness and Strength of the T-pin under shear loading

The spring constant of the T-pin was earlier calculated by assuming rigid connection between pin and facesheet. In reality, the spring constant of the T-pin under shear

loading, k_s^{T-pin} will depend on the interface modulus as the pin is pulled through the compliant interface as shown in Figure 3.17. The spring constant can be obtained by simulating a shear loading condition on the FE model shown in Figure 3.9 to obtain the shear force required for a unit shear displacement on the facesheets.

While the C-pins fail by buckling, the T-pins fail by pullout through the facesheet. The shear strength of the sandwich would then not only depend on the buckling of the C-pins but also on the material properties of the pin-facesheet interface surrounding the T-pin. Failure of this interface layer will lead to total pullout of the T-pin. As the T-pin is pulled through the interface layer, the axial force on the T-pin is distributed on the lateral surfaces of the interface the pin is in contact with. Let σ_s denote the in-situ strength of the interface layer, namely the shear stress at which the interface layer fails, which depends on the pin and interface geometry and material. Then the shear force at which a single T-pin fails can be expressed as

$$F_S^{pullout} = 2\pi r \sigma_s t_{fs} \tan\theta \tag{3.37}$$

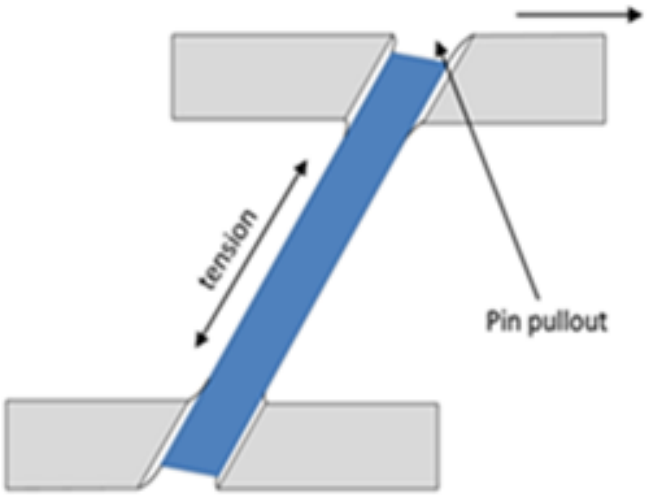

Figure 3.17: T-pin under shear loading being pulled though the pin-facesheet interface

3.4.8 Contribution from foam

In the preliminary model in the above section, the effect of foam in influencing the stiffness or the strength of the sandwich has been ignored. In reality, the foam core of the sandwich stabilizes the C-pin against buckling thus increasing the strength of the sandwich. The pin-foam interaction can be treated as a Winkler-type foundation on the pin obtained from superposition of horizontal springs between two pins separated by a unit cell distance, and vertical springs between the pin and the facesheet as shown in Figure 3.18. The combined effect of horizontal and vertical springs is then illustrated in Figure 3.19 with an equivalent foundation stiffness. Liu et. al [21] derived the foundation stiffness in terms of foam modulus, E_f, the as

$$k_f = 2E_f r\left(\frac{\sin\theta}{h}+\frac{\cos\theta}{a}\right) \tag{3.38}$$

In the above expression, the horizontal springs do not include the interaction between pins within the same unit cell, and also neglects the densification of foam at the point of failure. To account for the stiffening of the foam from the above factors, we modify the foundation modulus as below

$$k_f = 2\phi E_f r\left(\frac{\sin\theta}{h}+\frac{\cos\theta}{a}\right) \tag{3.39}$$

where ϕ is a modification factor that accounts for stiffening of the foundation.

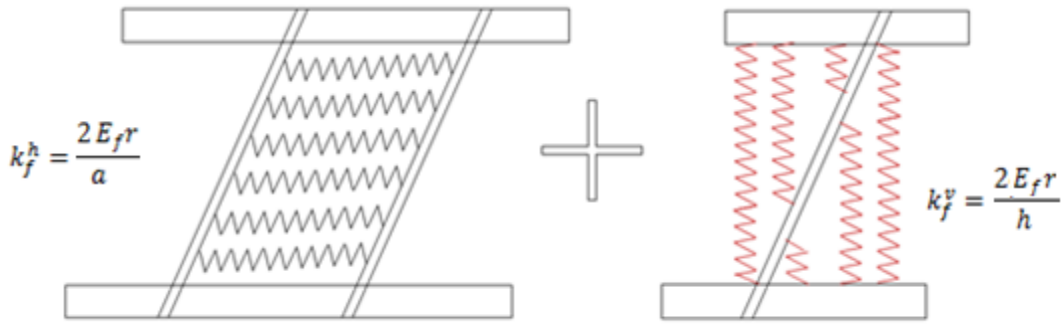

Figure 3.18: Vertical and horizontal springs on an X-cor pin (concept taken from [21])

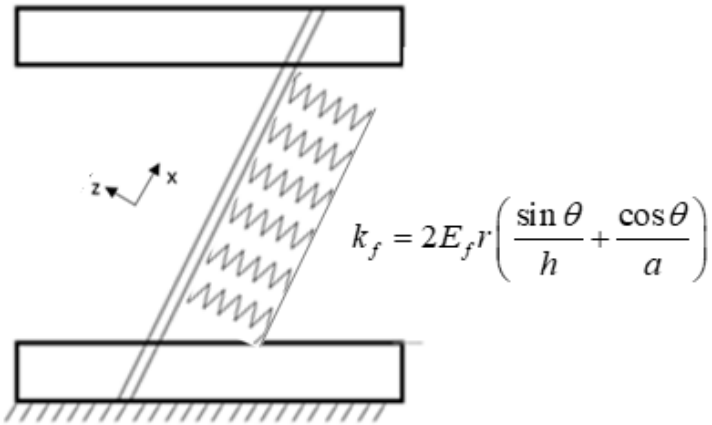

Figure 3.19: Foundation springs on pin due to foam with effective foundation modulus as a result of vertical and horizontal springs (concept taken from [21])

Due to the foundation on the pin, the pin will buckle at an axial load greater than the Euler buckling load. For a pin on a spring foundation as shown in Figure 3.19, the governing equation is given by

$$EI\frac{d^4w}{dx^4}+P\frac{d^2w}{dx^2}+k_f w=0 \tag{3.40}$$

with appropriate boundary conditions. The general solution to Equation (3.40) is given by [22]

$$w_0=Ae^{m_1x}+Be^{m_2x}+Ce^{m_3x}+De^{m_4x} \tag{3.41}$$

where

$$m_{1,2,3,4}=\pm\sqrt{\frac{P}{2EI}\pm i\sqrt{\frac{k_f}{EI}-\left(\frac{P}{2EI}\right)^2}} \tag{3.42}$$

For simply supported ends, substituting the boundary conditions in Equation (3.40) and solving for non-trivial solution gives the requisite condition for buckling of the pin as

$$\cos\left(L\sqrt{\frac{P}{4EI}-\sqrt{\frac{k_f}{4EI}}}\right)\pm\cos\left(L\sqrt{\frac{P}{4EI}+\sqrt{\frac{k_f}{4EI}}}\right)=0 \tag{3.43}$$

Equation (3.43) may be further simplified to

$$F_b=\frac{\pi^2EI}{L^2}+\frac{k_fL^2}{\pi^2} \tag{3.44}$$

where F_b is the axial force in the pin at buckling in the first mode.

For clamped supported ends, the transcendental equation in Equation (3.45) can be analytically obtained by substituting the boundary conditions in Equation (3.41) and solving for non-trivial solutions.

$$\frac{\sin\left(L\sqrt{\frac{P}{4EI}-\sqrt{\frac{k_f}{4EI}}}\right)}{L\sqrt{\frac{P}{4EI}-\sqrt{\frac{k_f}{4EI}}}}=\pm\frac{\sin\left(L\sqrt{\frac{P}{4EI}+\sqrt{\frac{k_f}{4EI}}}\right)}{L\sqrt{\frac{P}{4EI}+\sqrt{\frac{k_f}{4EI}}}} \tag{3.45}$$

The axial force in the pin at buckling under first mode, F_b which incorporates the stabilizing effect from a foundation with stiffness k_f for clamped boundary conditions may then be derived as

$$F_b=\frac{x\pi^2 EI}{L^2}\text{ for clamped BC} \tag{3.46}$$

where x is a solution of the equation shown below.

$$\frac{\sin\left(\frac{1}{2}\sqrt{\pi^2 x+2\sqrt{\frac{k_f L^4}{EI}}}\right)}{\sin\left(\frac{1}{2}\sqrt{\pi^2 x-2\sqrt{\frac{k_f L^4}{EI}}}\right)}=\pm\frac{\sqrt{\pi^2 x+2\sqrt{\frac{k_f L^4}{EI}}}}{\sqrt{\pi^2 x-2\sqrt{\frac{k_f L^4}{EI}}}} \tag{3.47}$$

Figure 3.20 shows the variation of buckling force with foundation stiffness for these two boundary conditions. Equation (3.35) can be linearized with respect to k_f as a very good approximation for the range of foundation stiffness shown in Figure 3.20. In

general, for a pin with rotational springs at its ends and supported by a foundation, the buckling force can be expressed as

$$F_b^k = \frac{\alpha\pi^2 EI}{L^2} + \mu k_f L^2 \tag{3.48}$$

where coefficient, μ is dependent on the rotational spring constant, k_θ and thus on α. Noting that $\mu = 1/\pi^4 = 0.0103$ for pinned ends while $\mu = 0.0075$ for clamped ends, one may use the following linear approximation for a pin with rotational spring at its ends,

$$\mu = 1.12\times10^{-2} - 9.33\times10^{-4}\alpha \tag{3.49}$$

to obtain the buckling load of the pin supported by a foundation.

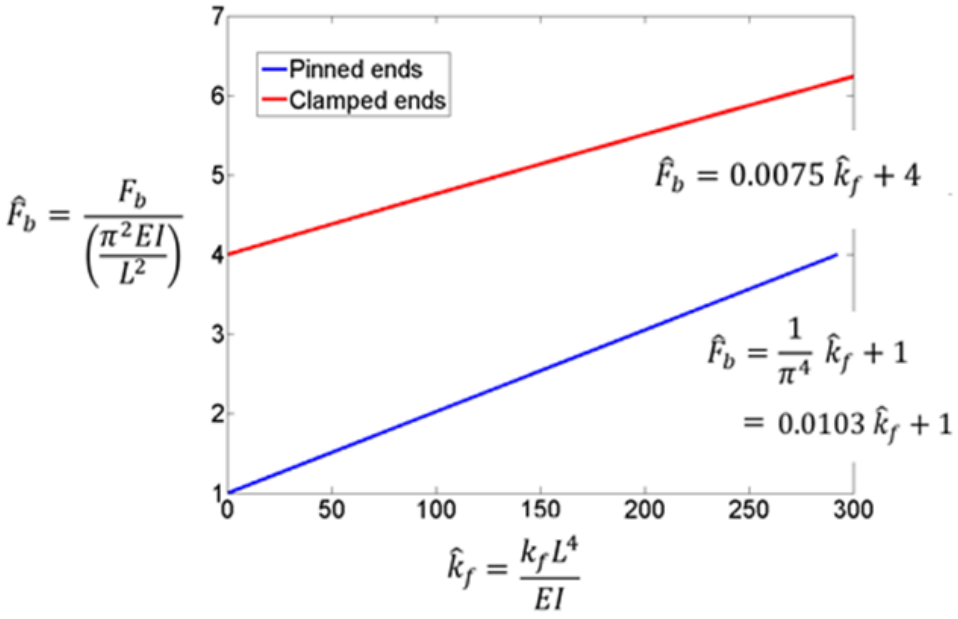

Figure 3.20: Variation of buckling force with foundation stiffness shown for a pin with pinned and clamped ends

In general, for the pin supported by a foundation owing to the foam, the bending rigidity of the pin is increased. To quantify the increase in bending rigidity due to foam support, one may consider a pin with clamped ends and a concentrated transverse load P at its center. For the pin supported by a foundation with modulus, k_f, the central displacement can be analytically obtained as [22]

$$\delta = \frac{PL^3}{\pi^4 EI} \sum_{n=1,3,5\ldots} \left(\frac{4}{n^4 + \frac{3k_f L^4}{\pi^4 EI}} \right) \tag{3.50}$$

We may then obtain the new bending rigidity of the pin, P/δ. However, for the typical properties of the Z-pinned sandwich, the increase in bending rigidity due to the foundation can be shown to be very small compared with the axial modulus and can be neglected. The foam can then be treated as an independent entity and its contribution towards stiffness is directly related to the foam modulus. Thus, while the foam in the sandwich construction plays an important role in increasing the pin buckling load, its contribution to pin spring constants is very small.

3.5 Model-2 for X-Cor Sandwich

In the sections above, we detailed the factors that influence the sandwich stiffness and strengths by studying the individual components of the sandwich and the interaction between them. In this section, we consolidate the parameters that are important in determining the sandwich properties and derive formulas for its stiffness and

strengths under compressive and shear loading using the results from the sections above.

3.5.1 Compressive Stiffness

For the sandwich under compressive loading, all pins contribute to the stiffness of the specimen. We have established that the effect of the foam on the spring constant of the pin is negligible. Hence, the compressive stiffness of the sandwich is just the sum of the contributions from the pins and that of the foam core. The spring constant of the pin is affected by geometric imperfections, material imperfections and eccentric loading of the pins. The combined effect of these factors may be combined into a single parameter namely the effective imperfection of the C-pin, $(e/L)_{eff}$. The effective imperfection of the pin then may be used to obtain the spring constant of the C-pin from Equation (3.35). N_C is the total number of pins and A_C the cross-sectional area of the specimen used for compressive testing. The compressive stiffness of the sandwich specimen may then be derived from Equation (3.3) and is given by

$$E_C = \frac{N_C \lambda E H \pi r^2 \cos^3\theta}{A_C h} + \frac{E_f H}{h} \tag{3.51}$$

3.5.2 Compressive Strength

Under compressive loading, we established that the foam acts as a foundation support to the pins and increases the buckling load of the pins. The compressive strength of the sandwich specimen based on pin buckling can be obtained from Equation (3.48). In this equation, the factor μ will be dependent on the boundary condition at the pin ends.

This boundary condition is in turn dependent on the rotational spring constant at the pin ends that is a function of the effective interface modulus E_{int}^{C-pin}. Additionally, the foundation modulus is dependent on the stiffening factor, ϕ.In other words, the parameters, effective interface modulus, E_{int}^{C-pin} and foam stiffening factor, ϕ determine the strength of the sandwich structure. The strength of the sandwich may be derived from Equation (3.48) as

$$S_C = \frac{N_C}{A_C}\left(\frac{\alpha\pi^2 EI\cos^3\theta}{h^2} + \frac{\mu k_f h^2}{\cos\theta}\right) \tag{3.52}$$

In this equation parameters, α and μ are dependent on E_{int} and may be obtained from Equations (3.24) and (3.49).

3.5.3 Shear Stiffness

Under shear loading, only the T-pins and the C-pins contribute towards the stiffness. The shear stiffness of the sandwich is the sum of the individual contributions from the T-pins, the C-pins and the foam core. The spring constant of the C-pin under shear loading will once again depend on the effective imperfection, $(e/L)_{eff}$ of the C-pin . The spring constant of the T-pin may be directly obtained from an FE model if we know the effective interface modulus, E_{int}^{C-pin}. N_S is the total number of pins and A_S the cross-sectional area of the specimen used for shear testing, and the shear stiffness is derived from Equations (3.6) and (3.36) as

$$G_S = \frac{N_S H}{4A_S}\frac{\lambda E \pi r^2}{h}\sin^2\theta\cos\theta + \frac{N_S H}{4A_S}k_S^{T-pin} + \frac{G_f H}{h} \qquad (3.53)$$

where k_S^{T-pin} is the shear spring constant of a single T-pin obtained from an FE model as shown in Figure 3.9.

3.5.4 Shear Strength

The shear strength of the sandwich will depend on the strength of the T-pin and the C-pin. The buckling load of the C-pin is obtained from Equation (3.35), and the strength of the T-pin is obtained from Equation (3.37). The T-pin strength will depend on the in-situ strength, σ_s. Consequently, the shear strength of the sandwich can be derived as

$$S_S = \frac{N_S}{4A_S}\left(\frac{\alpha\pi^2 EI}{h^2}\cos^2\theta\sin\theta + \frac{\mu k_f h^2 \sin\theta}{\cos^2\theta} + 2\pi r\sigma_s t_{fs}\tan\theta\right) \qquad (3.54)$$

The shear strength of the sandwich will depend of parameters, E_{int}^{C-pin} and ϕ.

3.5.5 Summary of parameters

Given the material and geometrical properties of the sandwich panel, the out-of-plane compressive and shear stiffness and strengths of the sandwich panel based on the model above can be expressed in terms of four independent parameters, $(e/L)_{eff}$, E_{int}^{C-pin}, ϕ and σ_s. Parameters, μ and α are directly dependent on E_{int}^{C-pin} and λ is a function of the effective pin imperfection, $(e/L)_{eff}$.

3.6 Experimental Correlations with UMD and CU specimens

To validate the modeling approach described in the previous sections without these simplifying assumptions, we conducted experiments at University of Maryland (UMD) on X-cor sandwich specimens to determine parameters, $(e/L)_{eff}$, E_{int}^{C-pin}, ϕ and σ_s of the model by matching stiffness and strength estimates from the model with experimental results. These parameter values were then used on X-Cor specimens tested at Cranfield University by Morasco et. al. [23] labeled CU in the following sections. The predictions from the model for these parameter values were then compared against experimental results for compressive and shear properties of CU specimens.

Both CU specimens and the specimens used for tests at UMD, labeled UMD specimens, have pins of T300 composite fibers and facesheets of IM7/8552 composite skins with 0.75 mm thickness. The sandwich core is 12.7 mm thick and is composed of Rohacell foam. Pin density for UMD specimens is equal to 1 pcf (pound per cubic feet) which corresponds to pin spacing of 5.3 mm. Tests for compressive and shear loading at UMD were performed on specimens with and without foam in the core of the sandwich. Hollow specimens were obtained by dissolving the foam core in a solution of sodium hydroxide.

3.6.1 Compressive stiffness and strength

The UMD specimens used for compression tests are 38.1 mm x 38.1 mm in size. The pin angle, diameter and number of pins in these specimens are given in Table 3.5. Three different CU specimen types are also listed in Table 3.5. The planar dimensions for CU specimens for compressive loading are 40 mm x 40 mm. Based on theoretical and effective pin density of CU specimens, the number of pins for each specimen is given in Table 3.5. Note that the pin diameter of CU specimens is substantially larger than that of UMD specimens.

Experiments to determine compressive stiffness and strengths were performed at UMD on an INSTRON 8841 machine as shown in Figure 3.21 in accordance with the ASTM C365 procedure. The compressive properties of the UMD specimens are given in Table 3.6. ASTM procedure requires the compressive stiffness to be measured between 0.1% and 0.3% strain. For this sandwich specimen, this amounts to displacements between 14 and 42 microns. The specimens were loaded at a slow rate of 0.5 mm/min to observe the behavior in this displacement range. Table 3.6 reports compressive stiffness values of UMD specimens measured at a strain value of 0.2%.

Table 3.5: Sandwich properties for X-Cor UMD and CU specimens tested for compression

Specimen	Pin Angle	Pin diameter (mm)	Foam	Number of pins in compression loading	Number of pins in shear loading
UMD-A	30º	0.28	No foam	138	102
UMD-B	30º	0.28	Rohacell	132	106
CU- A	22º	0.51	No foam	170	1124
CU- B	22º	0.51	Rohacell	170	1124
CU- C	30º	0.51	Rohacell	162	1124

Figure 3.21: Experimental setup for compression testing of sandwich specimens on INSTRON 8841 machine

Table 3.6: Mean values for compressive stiffness and strengths of UMD and CU specimens

Specimen	UMD-A	UMD-B	CU-A	CU-B	CU-C
Compressive Stiffness (MPa)	33	57	403	508	428
Compressive Strengths (MPa)	0.44	0.98	4.2	5	4.8

For the hollow UMD-A specimen, the compressive strength is entirely derived from the buckling of the pins since the foam is absent. Referring to Equation (3.52), this implies that the compressive strength of the specimen depends on a single parameter α. Equating the experimental result to the expression in Equation (3.52), we obtain $\alpha = 3.36$. FE models as shown in Figure 3.9 were constructed for a single pin embedded into the facesheet with interface thickness equal to 17% of pin radius for the UMD specimens. For the FE models, the pin, facesheet and the adhesive interface were modeled with 20-noded brick elements with a nominal mesh size equal to 0.05 mm. The pin had 32 elements along its circumference, and 140 elements along its length with a finer mesh closer to the pin-facesheet interface. For $\alpha = 3.36$ the effective interface modulus obtained from the FE model is $E_{\text{int}}^{C-pin} = 160\ MPa$. Using this value for effective interface modulus, the parameters, κ and α are obtained for CU specimens from their corresponding FE models and are reported in Table 3.7.

Compressive stiffness of UMD-A specimen as obtained from Equation (3.51) is dependent on parameter λ which is directly related to effective imperfection of the pin. Matching the experimental values for compressive stiffness of the UMD-A at 0.2% strain gives $(e/L)_{eff} = 0.024$. Substituting the experimental value for compressive strength of UMD-B specimen in Equation (3.52) for $\alpha = 3.36$ and using Equations (3.39) and (3.49) results in $\phi = 3.5$. Using the values for κ, α from Table 3.7 and $\phi = 3.5$, the compressive strengths for CU specimens are obtained from the model and are compared with experimental results in Figure 3.22. The plots show that the model is able to predict the strengths of the sandwich specimens within 6% of the mean experimental value. From the model, the compressive stiffness of the CU specimens

measured at 28 microns (0.2% strain) with $(e/L)_{eff} = 0.024$ is compared with experimental results in Figure 3.23. The plots show a good correlation between the model and experiments within a 10% difference from the mean experimental values.

Table 3.7: κ and α values for UMD and CU specimens

Specimen Type	κ	α
UMD- A, B	21.6	3.36
CU- A, B	4.71	2.25
CU- C	6.37	2.49

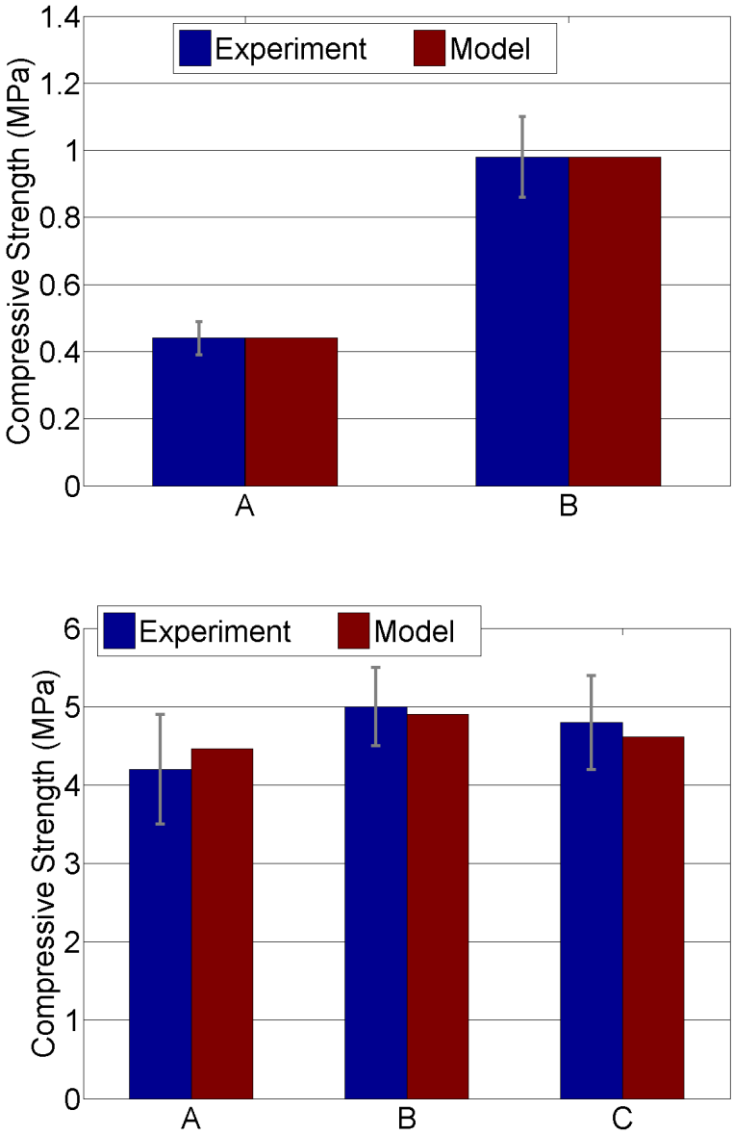

Figure 3.22: Comparison of experimental and model strengths for UMD specimens (top) and CU specimens (bottom) under compression loading

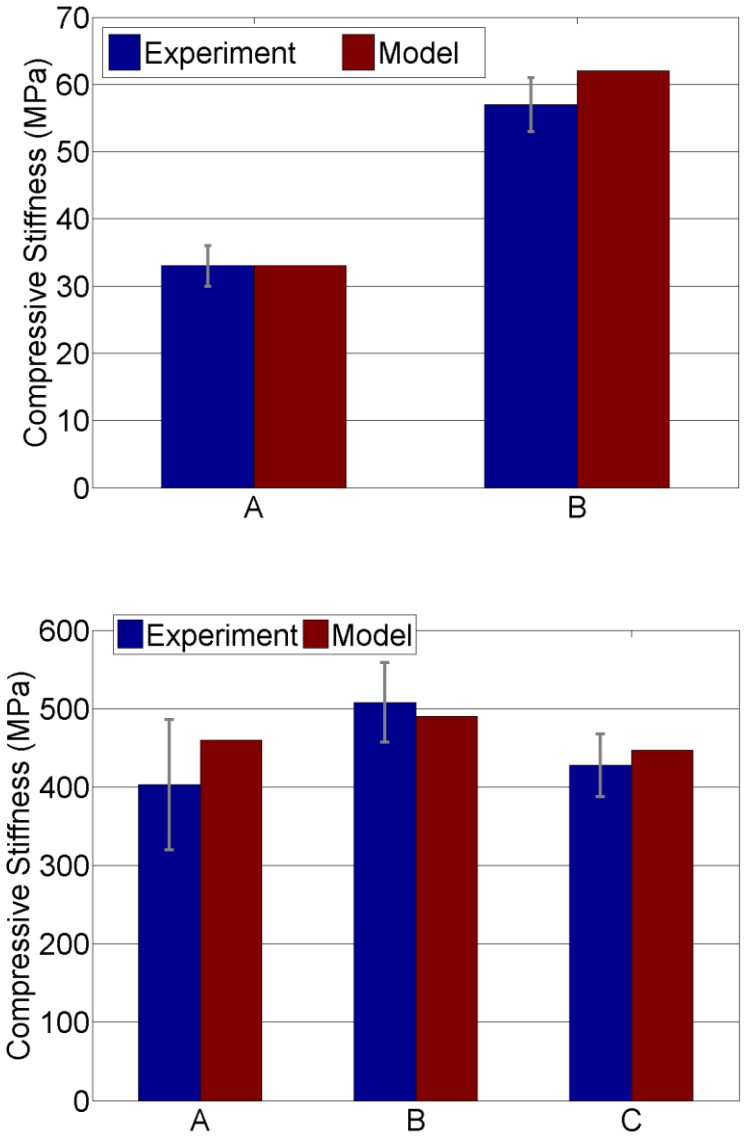

Figure 3.23: Comparison of experimental and model stiffness for UMD specimens (top) and CU specimens (bottom) under compression loading

3.6.2 Shear stiffness and strength

The specimens used for out-of-plane shear tests at UMD are 38.1 mm x 25.4 mm in size while CU specimens have dimensions of 188 mm x 50 mm. The loading in the specimens is along the length direction. The pin angle, diameter and number of pins of

both hollow and foam core specimens of UMD and CU are given in Table 3.5. The shear tests of UMD specimens were performed on IMADA machine as shown in Figure 3.24. Specimens were loaded at a rate 0.14 mm/s, which was the lowest setting for the machine. At this rate, the shear stiffness was not measurable, but these experiments were conducted to obtain shear strengths. Experimentally obtained shear strengths for UMD and CU specimens are given in Table 3.8.

From Equation (3.54), the experimental values for shear strength of UMD-A specimens are matched with the model for in-situ interface strength of $\sigma_s = 13.3\,MPa$. The shear strengths of UMD-B specimen, and CU specimens obtained by plugging this value of σ_s in Equation 3.54 are plotted in Figure 3.25. The shear strengths obtained from the model match with the experimental results within a 13% margin.

Since the shear stiffness is not available from the UMD test results, the shear stiffness of CU specimens was obtained from Equation (3.53) by using the same value of effective imperfection $(e/L)_{eff} = 0.024$, as obtained from compressive loading above. In this equation, the spring constant of the T-pin was obtained from the FE model. The shear stiffness of CU-B specimen obtained from Equation (3.53) matches with corresponding experimental result at 0.1% shear strain which lies in the range of ASTM standard for measurement. The shear stiffness values at this strain for all CU specimens are plotted in Figure 3.26 which show that the results from the model match with the experimental values within 10% accuracy. The reference for CU samples [23] does not report the shear strain value used to evaluate shear stiffness.

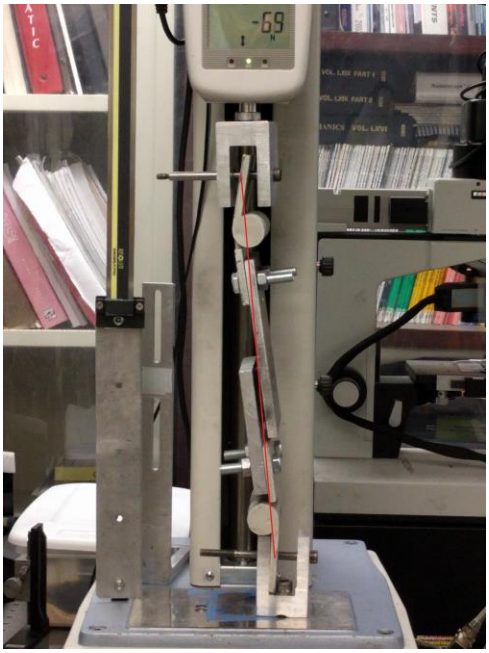

Figure 3.24: Experimental setup for shear testing of sandwich specimens on IMADA load frame

Table 3.8: Mean values for shear stiffness and strengths of specimens from UMD and CU

Specimen	UMD-A	UMD-B	CU-A	CU-B	CU-C
Shear Stiffness (MPa)	-	-	208	200	341
Shear Strengths (MPa)	0.21	0.38	0.7	0.8	1.0

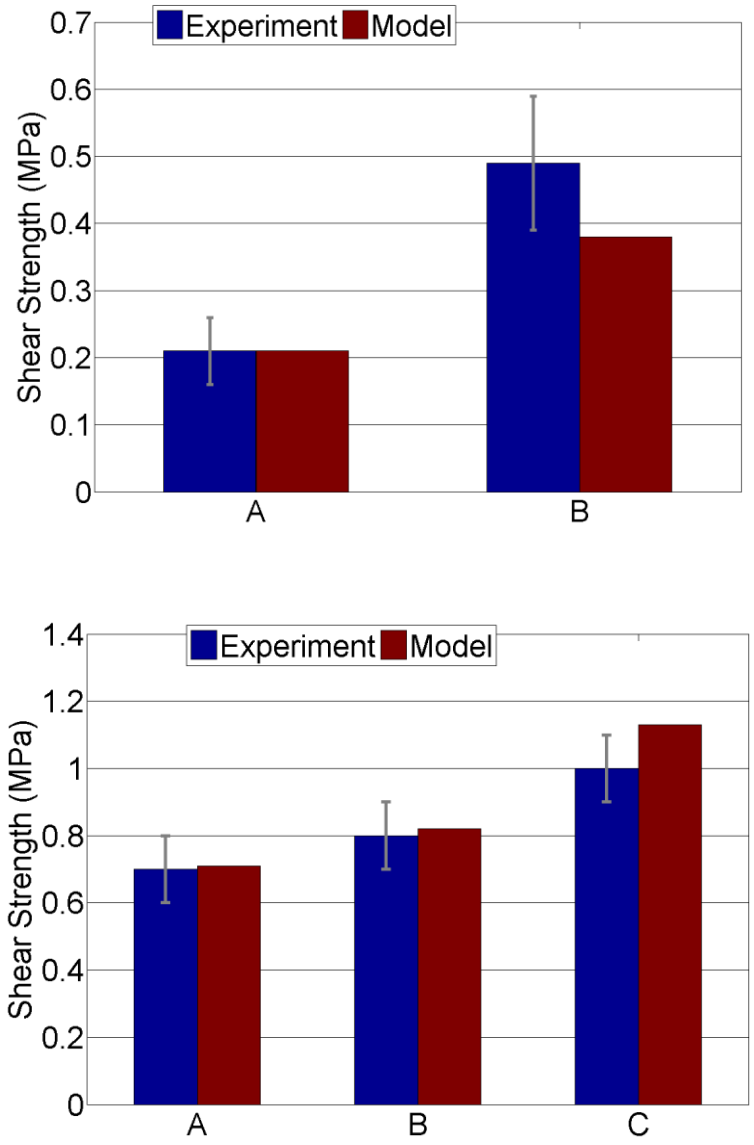

Figure 3.25: Comparison of experimental and model strengths for UMD specimens (top) and CU specimens (bottom) under shear loading

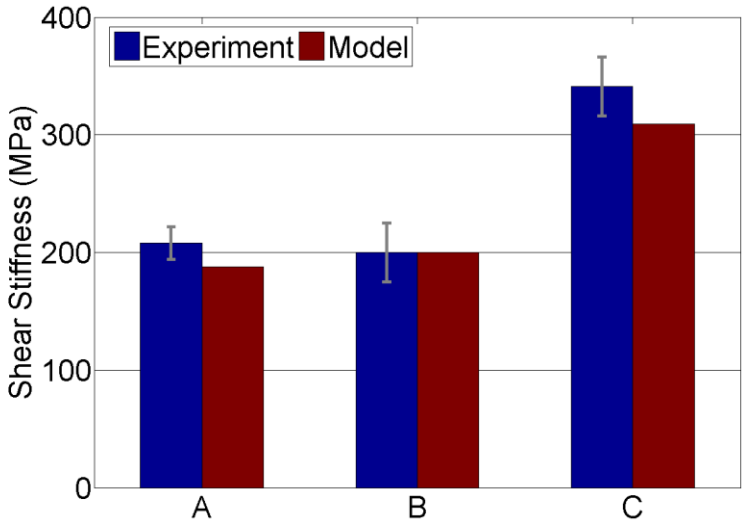

Figure 3.26: Comparison of experimental and model stiffness for CU specimens under shear loading

3.7 Conclusions

For X-Cor composite sandwich structures, a model based on the assumptions of a perfect pin geometry with rigid connection to the facesheet overestimates the out-of-plane compressive and shear stiffness and strength values. Accordingly, we outlined a computational-analytical model to incorporate the imperfections of the sandwich structures under compression and shear loading. Towards this end, parameters important in representing the behavior of the individual components of the sandwich were identified. These are empirical parameters that include effective imperfection, $(e/L)_{eff}$ of the C-pin, and E_{int}^{C-pin}, the in-situ pin-facesheet interface modulus which are essential in capturing the softening of the C-pins from geometric and material

imperfections. In addition, the model also incorporates densification of the foam to represent foundation support to the pins through parameter, ϕ and introduces in-situ pin-facesheet interface strength, σ_s as an indicator of pullout strength of the T-pins. The values of these parameters were extracted from compression and shear testing at UMD, and then used on the model for CU specimens reported in open literature. The results for compressive and shear properties of CU specimens from the model agree reasonably well with experimental results. From the correlation of the parameter values across different specimens, it appears that the model presented in this chapter is a viable representation of the physics of the sandwich components and the interaction between them. This provides a basis for developing a damage model via finite element analysis to represent pin-facesheet interface based on its nonlinear material properties. The interface properties may then be incorporated into a finite element model of a sandwich construction to determine its performance under compression and shear loading.

Chapter 4: Numerical tools to model composite delamination- Cohesive Zone Modeling

4.1 Introduction

Delamination is the most important mode of failure that occurs in laminated composites as it can be initiated at small loads if an initial crack is present in the structure. In Chapter 2, we studied novel techniques for Z-pinning in composite laminate structures that enhance the delamination resistance of the composite laminate. We utilized a numerical tool called cohesive zone modeling (CZM) in conjunction with FEM to analyze the performance of a Z-pinned laminate under various loads. In this chapter, we provide the background for CZM and the numerical techniques used to model FE models with cohesive elements.

The CZM technique is a unique combination of the concept of strain energy release rate as a criterion used in fracture mechanics for crack propagation and the damage mechanics of a non-linear process zone ahead of the crack tip described in terms of stiffness degradation [16]. In a cohesive zone model (CZM), cohesive elements are placed in the path of potential crack path and they are governed by a prescribed traction-separation displacement law to simulate delamination. The damage parameter is CZM can be integrated into a fatigue-law to simulate delamination of composites under fatigue loading conditions. For the scope of this research, we intend to understand, and

expand the CZM capabilities as it pertains to delamination or contact separation in a FE model.

4.2 Cohesive separation law and modeling

4.2.1 Constitutive law for cohesive zone

Cohesive zone modeling involves defining a cohesive zone near the crack front in a region where the crack is expected to propagate. In a composite delamination problem, cohesive elements are inserted between two plies. In a Z-pinned composite laminate, the cohesive elements are inserted between the pin and the laminate. A CZM model relates surface tractions to separation displacements at the interface of the two surfaces where the cohesive zone is introduced. ABAQUS has in-built capabilities to model CZM with a bi-linear traction separation law (besides exponential and user-specified softening laws) as shown in Figure 4.1. The graph shown is for a pure mode I scenario, with the normal tractions plotted against normal separation displacements. The graph consists of a linear elastic region of a high stiffness followed by a linear softening region. σ_0 is the interfacial strength attained at a separation displacement of Δ_0. The area under the curve is equal to the delamination toughness, G_{IC}. Damage mechanics of the cracked laminate is linked to the traction-separation response through the parameters labeled in the graph. A dimensionless damage coefficient, D is associated to the cohesive region when the contact stresses reach a critical value of σ_0. At this point, D is equal to 0 and damage is initiated. The value of the damage coefficient linearly increases to a value of 1 at the maximum separation displacement. The

interface strength at an intermediate point, when the damage coefficient has reached a value of D is given by $\sigma_0(1\text{-}D)$.

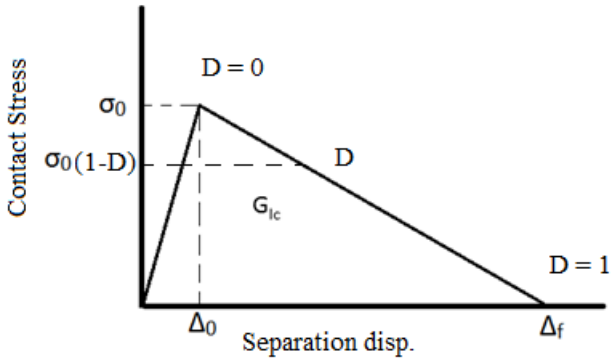

Figure. 4.1: Bi-linear traction separation law for a CZM

Application of a CZM for problems in single mode is fairly straightforward, but for mixed-mode problems, the interaction between two modes must be taken into account. In such cases, a single damage parameter in these models is introduced in the interfacial constitutive relationship. In our FE models, we simple use a linear failure criterion under mix-mode loading as given below where a combination of properties for different modes are used. The condition for onset of damage is given by

$$\max\left\{\frac{\sigma^1}{\sigma_0^1},\frac{\sigma^2}{\sigma_0^2}\right\}=1 \tag{4.1}$$

The interfacial stresses are defined by the cohesive law

$$\begin{aligned}\sigma^1 &= (1-D)\sigma_0^1\\ \sigma^2 &= (1-D)\sigma_0^2\end{aligned} \tag{4.2}$$

The damage evolution is governed by the relation between traction energies, G_{IC} and G_{IIC} in mode-I and mode-II respectively, as

$$\frac{G_I}{G_{IC}} + \frac{G_{II}}{G_{IIC}} = 1 \tag{4.3}$$

4.2.2 Development of user-based cohesive element

The UEL subroutine in ABAQUS allows for development of user based subroutines with user defined characterization for the element. A cohesive element was developed in the UEL subroutine of ABAQUS to be used in conjunction with finite element models. The three-dimensional cohesive element has 8 nodes with each node consisting of three degrees of freedom. A representative cohesive element connecting two arms of a composite laminate is shown in Figure 4.2 with the general node numbering. The crack plane separates nodes 1 to 4 from nodes 5 to 8. The cohesive element is isolated in Figure 4.3 in which the degrees of freedom of the element are also shown. The degrees of freedom of the cohesive element, u_j: j=1, 2, 3… 24 are the displacements of the nodes in the global coordinate system and are numbered in the sequence as shown in the figure.

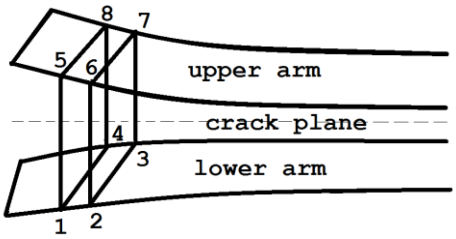

Figure 4.2: A representative cohesive element connecting the two arms of a laminate

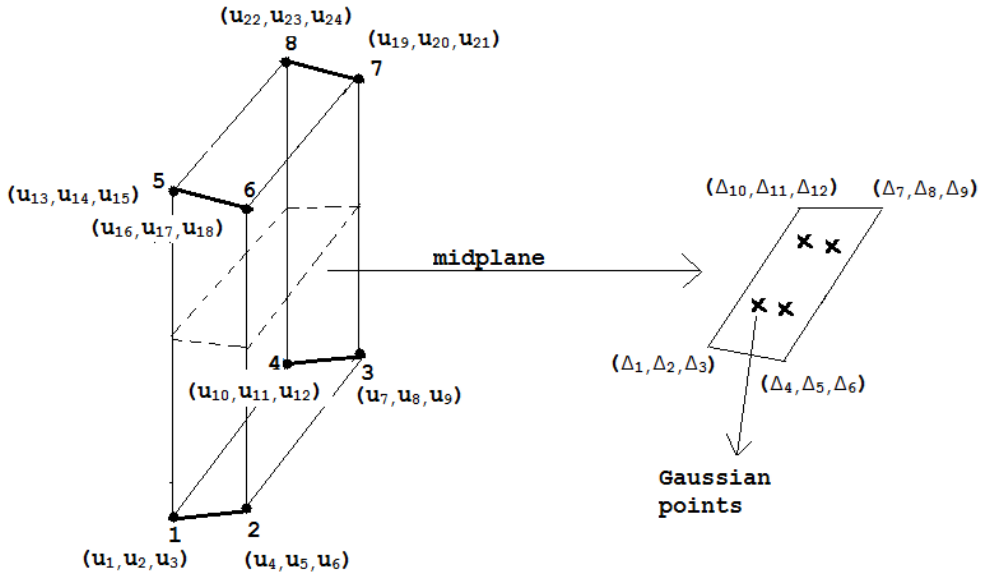

Fig 4.3: Cohesive element and its degrees of freedom. The midplane of the cohesive element is isolated on the right.

A simple bilinear traction-separation law for the cohesive elements shown in Figure 4.1. The graph in Figure 4.1 is shown for a pure mode 1 case, with normal tractions plotted against normal separation displacements. A similar constitutive law for tangential stresses and tangential displacements of the cohesive interface can be defined. The stiffness properties of the cohesive element differ in the tangential and normal direction which are local to that cohesive element. The properties of the cohesive element in a mixed mode are obtained from those in the normal and tangential direction which are local to the cohesive element. The global displacements of the cohesive element are related to the local displacements as

$$\{\hat{u}\}_{24\times1} = [R]_{24\times24}\{u\}_{24\times1} \tag{4.4}$$

where **[R]** is the rotational matrix and $\hat{u}_j$: j=1,2,3… 24 are the nodal displacements in the local coordinate system. The separation displacements, Δ_j are defined at the four corners of the midplane of the cohesive element as shown in Figure 4.3. They can be obtained as

$$\Delta_j = \hat{u}_{12+j} - \hat{u}_j \tag{4.5}$$

or as

$$\{\Delta\}_{12\times1} = [S]_{12\times24}\{\hat{u}\}_{24\times1} \tag{4.6}$$

where the elements of the matrix **[S]** are 0, 1, or -1.

The separation displacements at each Gaussian point are obtained from the nodal separation displacements and the shape functions as follows.

$$\begin{Bmatrix}\Delta_x\\ \Delta_y\\ \Delta_z\end{Bmatrix} = \begin{bmatrix} N_1 & 0 & 0 & N_2 & 0 & 0 & N_3 & 0 & 0 & N_4 & 0 & 0\\ 0 & N_1 & 0 & 0 & N_2 & 0 & 0 & N_3 & 0 & 0 & N_4 & 0\\ 0 & 0 & N_1 & 0 & 0 & N_2 & 0 & 0 & N_3 & 0 & 0 & N_4 \end{bmatrix}\{\Delta\}_{12\times1} = [N]_{3\times12}\{\Delta\}_{12\times1} \tag{4.7}$$

where $N_{1,2,3,4} = (1\pm\xi)(1\pm\eta)$, with ξ, η being the parametric coordinates of the Gaussian point. The cohesive forces at the Gaussian points are related to the corresponding separation displacements according to the following equation.

$$\begin{Bmatrix}F_x\\ F_y\\ F_z\end{Bmatrix} = \begin{bmatrix} K_n & 0 & 0\\ 0 & K_t & 0\\ 0 & 0 & K_t \end{bmatrix}\begin{Bmatrix}\Delta_x\\ \Delta_y\\ \Delta_z\end{Bmatrix} = [K_c]\begin{Bmatrix}\Delta_x\\ \Delta_y\\ \Delta_z\end{Bmatrix} \tag{4.8}$$

where K_n and K_t are defined according to the bi-linear traction separation law as given in Figure 4.1. Substituting Eqs. (4.4), (4.6) and (4.7) in Eq. (4.8), we obtain

$$\begin{Bmatrix} F_x \\ F_y \\ F_z \end{Bmatrix} = [K_c][B_c]\{u\} \tag{4.9}$$

where $[\mathbf{B_c}] = [\mathbf{N}][\mathbf{S}][\mathbf{R}]$. The stiffness matrix of the cohesive element can then be obtained as

$$[K]_{24\times 24} = \iint [B_c]^T [K_c][B_c]\, dxdy \tag{4.9}$$

where the integration is carried over the mid-plane of the cohesive element by summation over Gaussian points.

4.2.3 Verification of Cohesive Zone Model

To validate the results generated by ABAQUS with a CZM application, an FEA model of a double cantilever beam (DCB) is obtained from prior work by *Landry and Laplante* [24] on a carbon-fiber/epoxy specimen as shown in Figure 4.4. An FEA model similar to the one used in the paper was constructed in ABAQUS as shown in Figure 4.5. The elements used were 8 noded brick, of size 0.25 mm in the length direction. Only one element was used in the width direction and each leg of the beam had two elements in the direction of the thickness. A plane strain formulation was enforced by constraining the displacement of the beam in the width direction. A bilinear traction separation law was used for the CZM model as detailed in Figure 4.1. The cohesive and laminate parameters were obtained from the paper and are tabulated in Table 4.1. Results obtained for load-displacement curve and delamination growth are shown in Figures 4.6 and 4.7. The static linear line in Figure 4.6 was obtained for the model without any cohesive zone, to compare the initial (pre-crack opening) slope of the plots with the

static linear slope. The correlation between the ABAQUS models and experiments from the paper is very good for the mesh size used in the paper. The user developed cohesive element developed in the previous section was also verified with identical results.

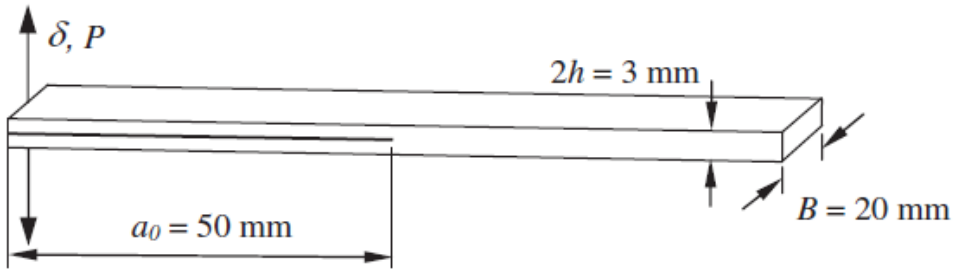

Figure 4.4: Double cantilever beam (DCB) configuration for crack opening of a composite laminate. a_0 is the initial crack length. P is the loading force, and δ is the loading point opening displacement. Total length of the beam is 150 mm.

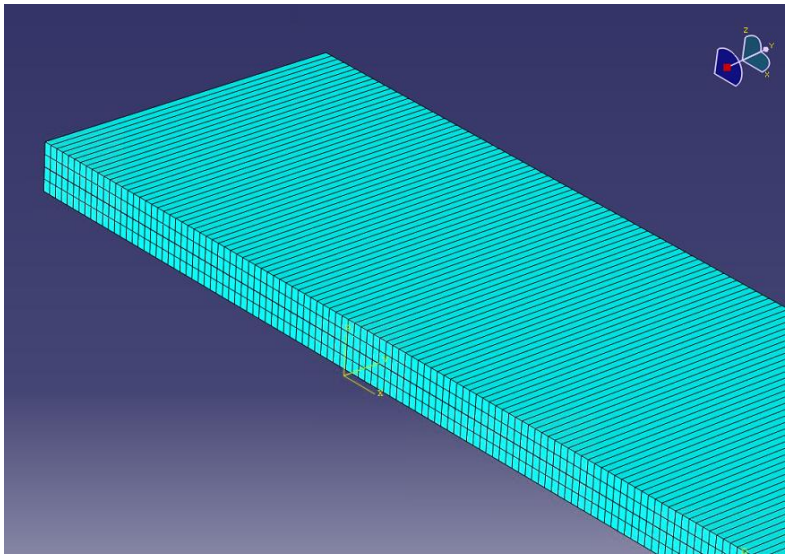

Figure 4.5: Meshing used for the FE model of composite beam in ABAQUS

Table 4.1: Lamina and cohesive properties used in the model, obtained from the paper by Landry and Laplante

Lamina properties		**Cohesive properties**	
E_{11}	155 GPa	Δ_0	5×10^{-6} m
$E_{22} = E_{33}$	10.5 GPa	σ_0	7 MPa
$G_{12} = G_{23}$	4.83 GPa	G_{Ic}	422 J/m^2
G_{23}	3.37 GPa	$K = \sigma_0 / \Delta_0$	1.4×10^{12} N/m^3
υ_{12}	0.3	$\Delta_f = 2\, G_{Ic} / \sigma_0$	1.21×10^{-4} m

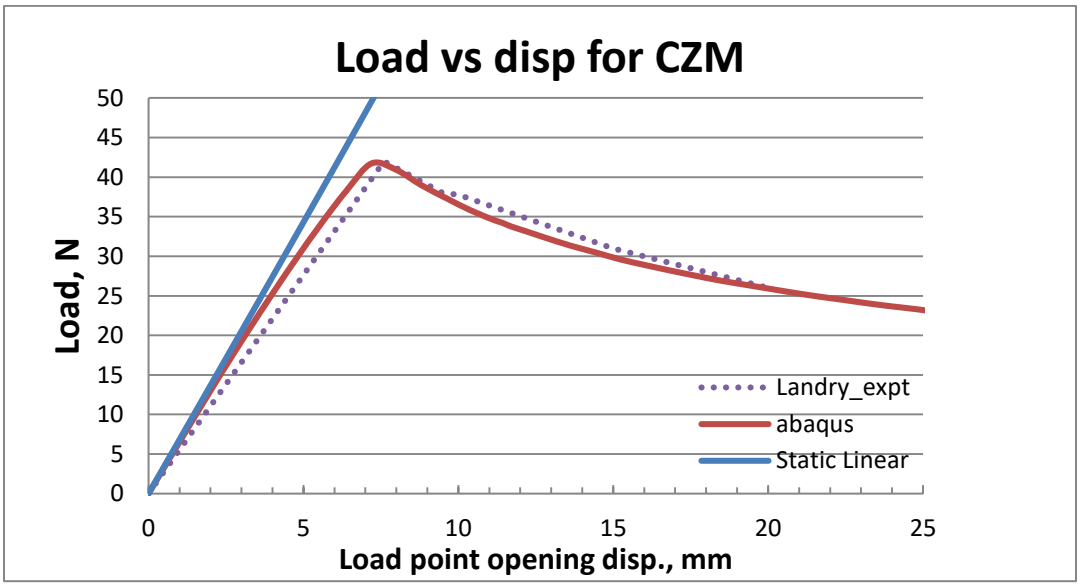

Figure 4.6: Comparing force-displacement curves between experiment and ABAQUS' computational model

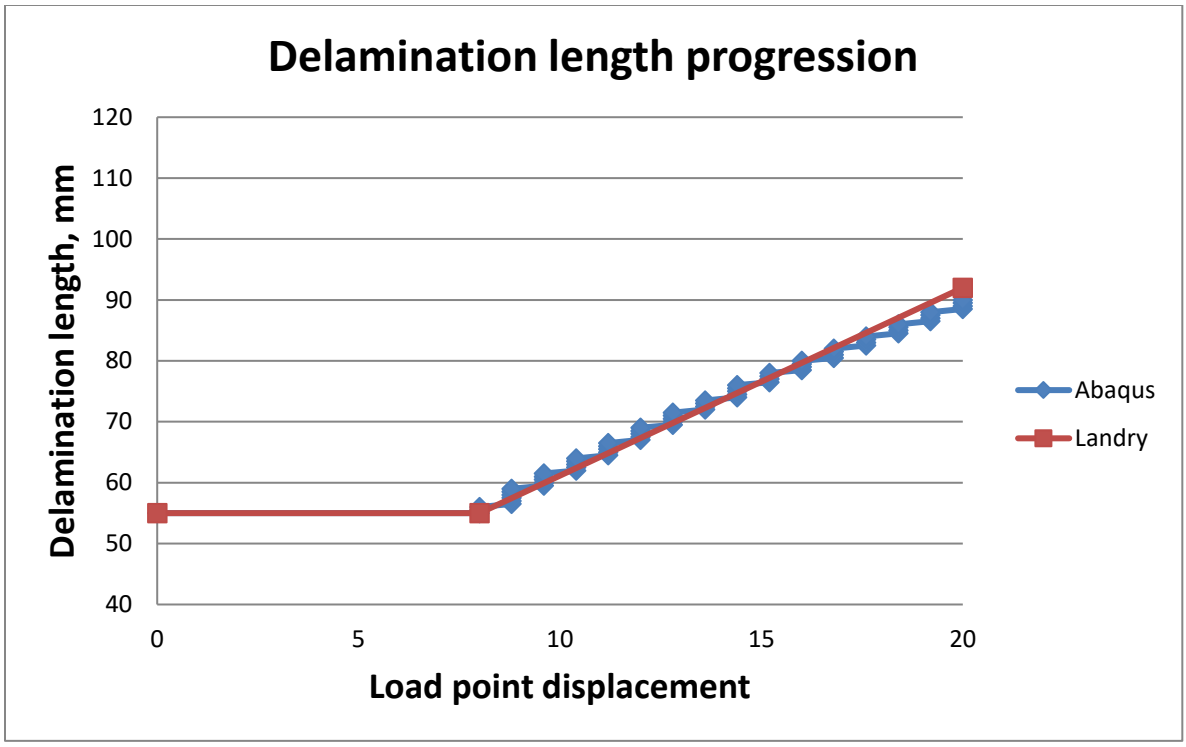

Figure 4.7: Delamination length versus load point displacement

4.3 Convergence Issues in CZM

4.3.1 Viscous Regularization

The delamination problem above in ABAQUS failed to converge upon using smaller mesh sizes in the model in the length direction in conjunction with cohesive elements. In ABAQUS, models exhibiting a softening behavior and stiffness degradation can often lead to severe convergence difficulties in implicit finite element analysis. Accordingly, the software has an in-built capability called viscous regularization to overcome some of these convergence difficulties. Using this approach, the traction-separation laws can be regularized using viscosity by permitting stresses to be outside the limits set by the traction-separation law. Viscous regularization causes the tangent

stiffness matrix that defines the contact stresses to be positive for sufficiently small time increments. In this formulation, a viscous stiffness degradation variable, D_v, is defined by the evolution equation-

$$\frac{\partial}{\partial t} D_v = \frac{1}{\mu}\left(D - D_v\right) \tag{4.10}$$

or,

$$\frac{\partial}{\partial t} D_v + \frac{1}{\mu} D_v = D \tag{4.11}$$

The constitutive equations of damage mechanics are then written in terms of the variable D_v. Using viscous regularization with a small value of the viscosity parameter helps improve the rate of convergence. The basic idea is that the solution of the 'viscous' system relaxes to that of the 'inviscid' case as $\mu \rightarrow 0$.

For the DCB specimen above, we obtained the load-displacement results for different values of viscous regularization coefficient, μ ranging from 10^{-5} to 0.001. The corresponding results are plotted below in Figure 4.8. The force-displacement curves obtained thus are observed to be dependent on the value of the viscous coefficient, μ. The response of the 'viscous' system is closer to that of the inviscid case for small values of the viscosity coefficient $\mu \leq 10^{-4}$.

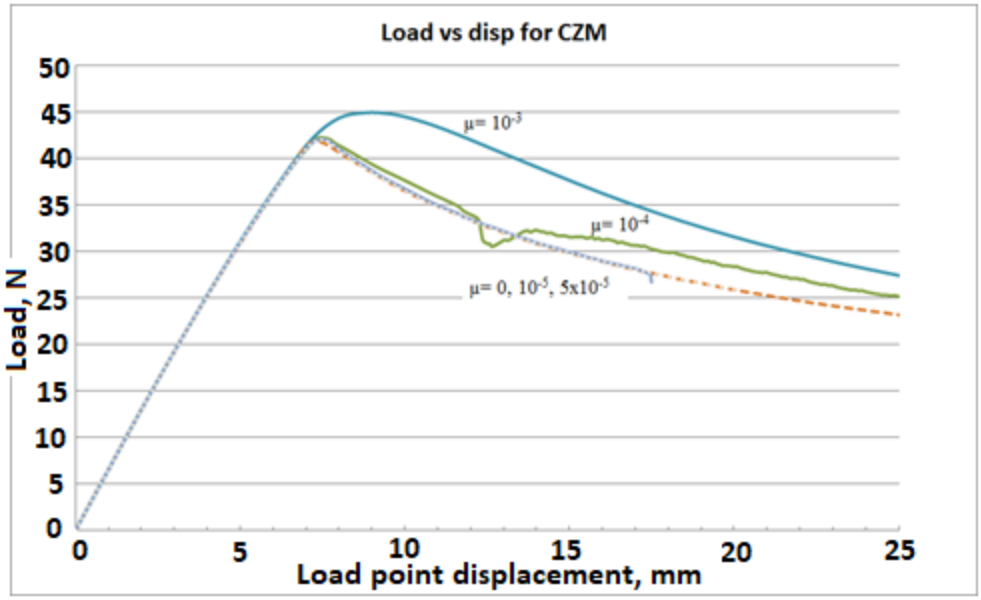

Figure 4.8: Load displacement curves obtained from computational models with different values of viscous regularization coefficients.

4.3.2 Single Degree of Freedom model attached to a softening spring

To understand the convergence difficulties for systems exhibiting a softening behavior, we first studied a single degree of freedom (SDOF) system as shown as in Figure 4.9. A mass *m* is attached to a linear spring of constant *k* on one side and to a non-linear spring on the other side along with a damper with a damping coefficient *c*. The model incorporates a bi-linear stiffness to the non-linear spring as shown in Figure 4.10, similar to that of the cohesive model above. The magnitude of slopes of the bi-linear plot are equal to k_1 and k_2 respectively.

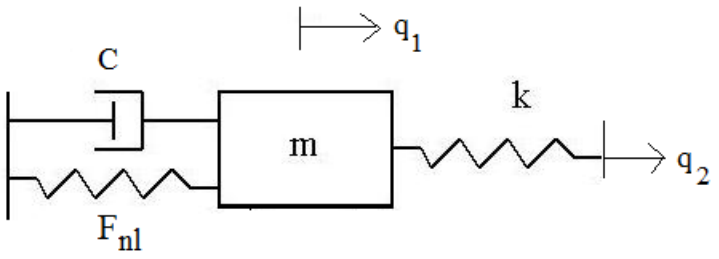

Figure 4.9: SDOF system with a non-linear (softening) spring

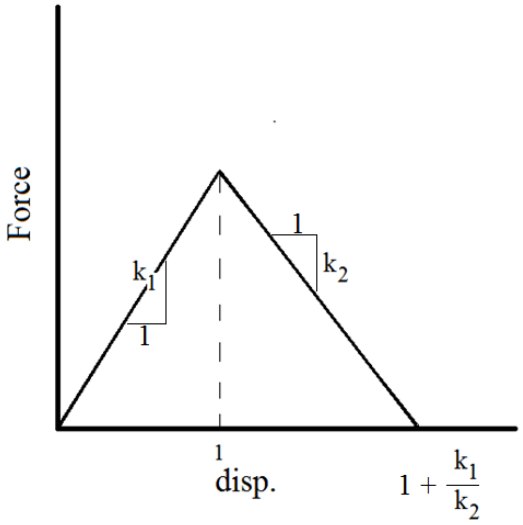

Figure 4.10: Force-displacement relationship for the non-linear spring.

The governing equation of the single body system is given by

$$m\ddot{q}_1 + c\dot{q}_1 + kq_1 + F_{nl} = kq_2 \tag{4.12}$$

where q_2 is the applied displacement as a function of time. For simplicity, we choose $m = 1 \text{ and } k = 1$. The non-linear force F_{nl} can be written as

$$F_{nl} = \begin{cases} k_1 q_1, & 0 < q_1 \leq 1. \\ k_1.1 - k_2(q_1 - 1), & 1 < q_1 \leq 1 + \dfrac{k_1}{k_2} \\ 0, & q_1 > 1 + \dfrac{k_1}{k_2} \end{cases} \tag{4.13}$$

The static equilibrium positions of the system are obtained by solving the static equation

$$k\widetilde{q_1} + F_{nl} = k\widetilde{q_2} \tag{4.14}$$

where $\widetilde{q_1}$ and $\widetilde{q_2}$ are steady state values of the displacements. The value of $\widetilde{q_1}$ depends on the applied displacement $\widetilde{q_2}$. The dependence is plotted in Figure 4.11, for $k_1 = k_2 = 2$. There are three equilibrium positions, $\widetilde{q_1}$ for the values of $2 \leq \widetilde{q_2} \leq 3$. The existence of multiple solutions for $\widetilde{q_1}$ in this range causes failure of solution process via Newton-Raphson method. This is further illustrated by the example of a cantilever beam below.

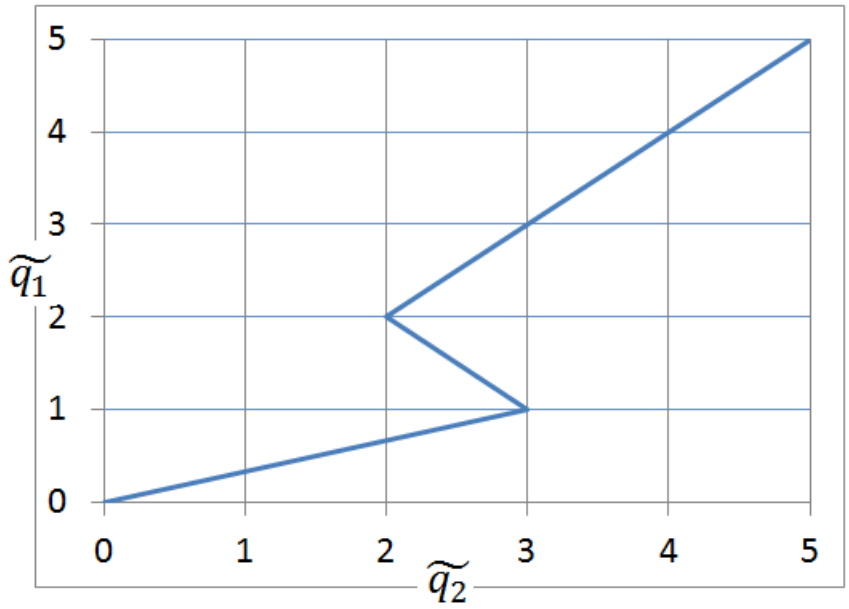

Figure 4.11: Solution for equilibrium positions as a function of the steady state values of applied displacements, for a system with m = k = 1, k_1

4.3.3 Cantilever beam on a softening non-linear spring

Consider a uniform beam of mass *m*, length *L*, inertia, *I*, with a non-linear spring and a damper with a damping coefficient *c* attached at its midpoint as shown in Figure 4.12. Let the Young's modulus of the beam material be denoted by *E*. The spring constant of the non-linear spring is defined by a bi-linear stiffness model as shown in Figure 4.13, similar to that of a cohesive element with bi-linear traction-separation law. The non-linear spring force is given by

$$F_{nl} = \begin{cases} k_1 w_2 \; if \; w_2 \leq \alpha \\ (k_1 + k_2)\alpha - k_2 w_2 if \; \alpha < w_2 < \left(1 + \frac{k_1}{k_2}\right)\alpha \\ k_2 w_2 \; if \; w_2 \geq \left(1 + \frac{k_1}{k_2}\right)\alpha \end{cases} \tag{4.15}$$

where w_2 is the vertical displacement at the center of the beam. Let $\tilde{k}_1$ and $\tilde{k}_2$ be the non-dimensional spring constants defined as

$$\tilde{k}_{1,2} = \frac{k_{1,2}}{EI} \tag{4.16}$$

The spring at the center of the beam fails if the beam displacement at this point is greater than a fixed value, imitating the behavior of a cohesive zone element.

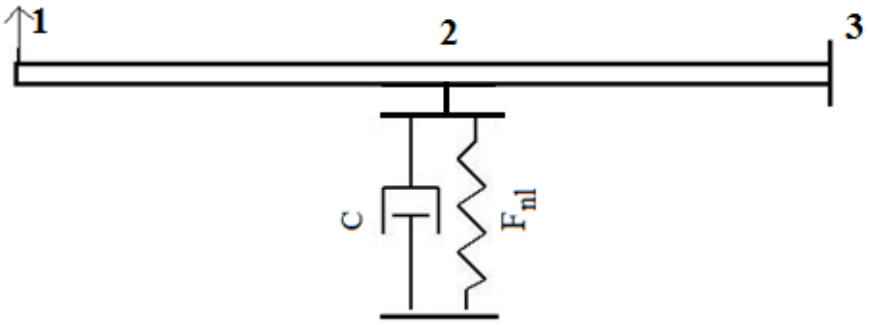

Figure 4.12: A cantilever beam on a spring model

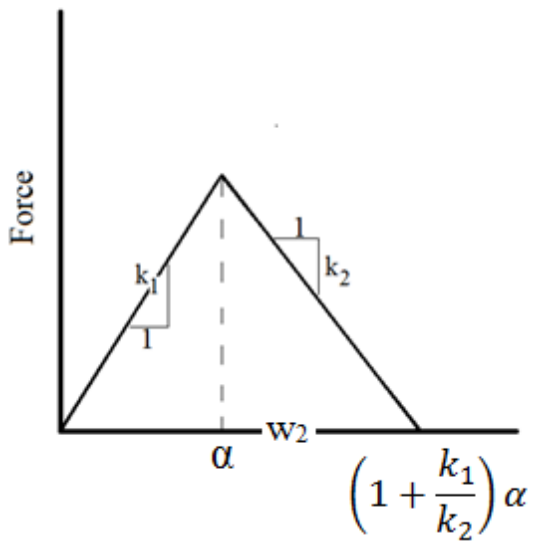

Figure 4.13: Force-displacement relationship for the non-linear spring.

First, consider the beam without a damper in the system, i.e, for c = 0 with an applied at the free end of the beam. We are interested in the response of the beam for different values of the applied displacement. Accordingly, a finite element analysis of the beam is performed with two elements along its length with nodes labeled 1, 2 and 3 as shown in Figure 4.12. Let the vertical displacements and the rotation angles at these nodes be denoted by w_1, w_2, w_3 and $\theta_1, \theta_2, \theta_3$ respectively.

The solutions for w_2 can be obtained analytically for a given w_1. The displacement, w_2 and the load, F_1 (reaction force at the tip) obtained thus are plotted for two different cases in Figures 4.14 and 4.15. If $k_2 < \frac{768}{7} EI$ or equivalently, $\tilde{k}_2 < \frac{768}{7}$, then there is a unique solution w_2 for every value of the applied displacement w_1. If $\tilde{k}_2 > \frac{768}{7}$, then there exist multiple solutions (equilibrium positions) for w_2 in the range $\frac{16(k_1+k_2)}{k_2}\alpha < w_1 < \frac{768+7\tilde{k}_1}{240}\alpha$. The standard Newton-Raphson method may be used to

extract these solutions statically when unique solutions exist. However, this method is not adequate when multiple solutions exist as the solution method becomes unstable. For instance, Figure 4.16 illustrates how the Newton-Raphson iterates for w_2 bounce between points A and B for a given value of w_1.

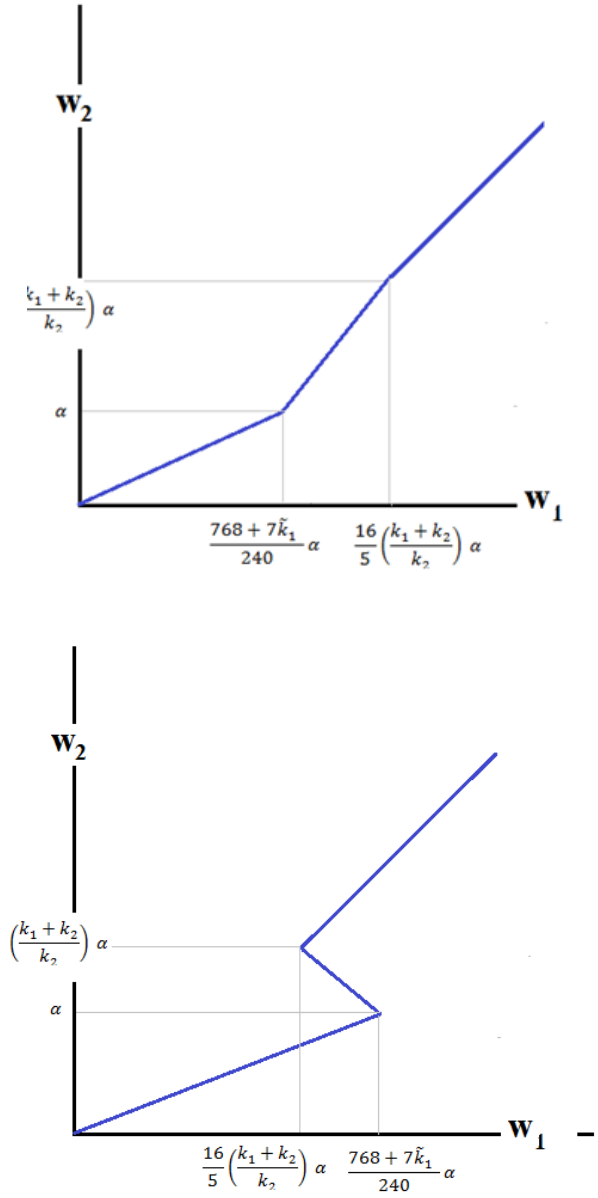

Figure 4.14: Analytical solution for w_2 as a function of w_1 when $\tilde{k}_2 < \frac{768}{7}$(left) and $\tilde{k}_2 > \frac{768}{7}$(right)

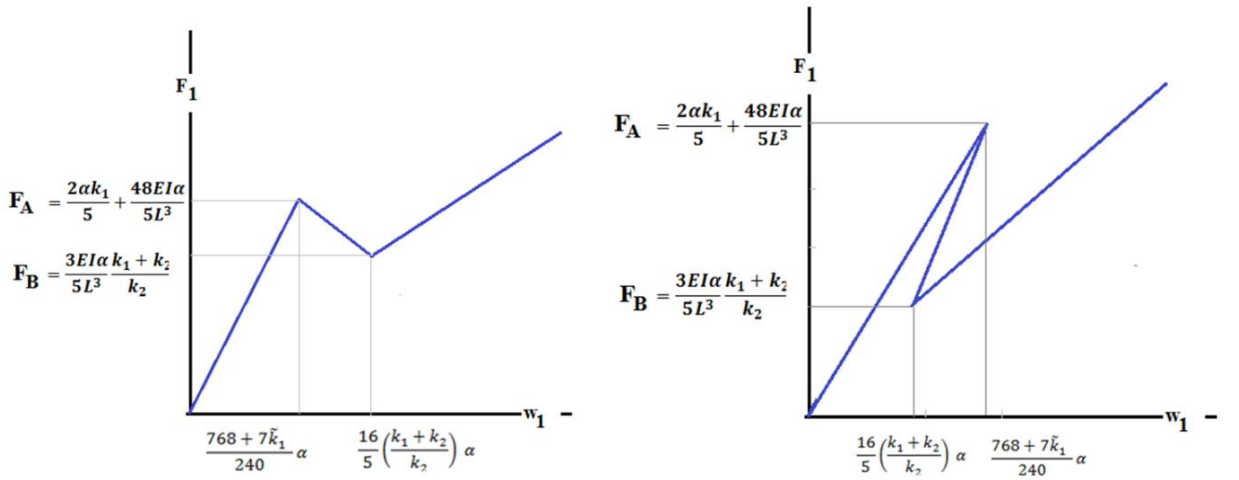

Figure 4.15: Analytical solution for load F_1 as a function of w_1 when $\tilde{k}_2 < \frac{768}{7}$(left) and when $\tilde{k}_2 > \frac{768}{7}$(right)

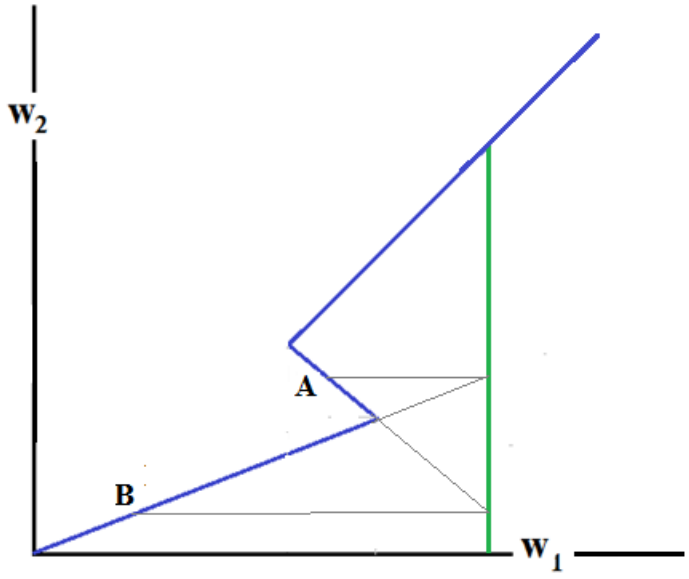

Figure 4.16: Newton-Raphson method fails for this case. With a starting point at the origin, the solution iterates bounce back and forth between points A and B.

The instability of Newton-Raphson method for this case is the source for convergence issues for a softening model in ABAQUS. To obtain solutions for the unstable range, the above system can be treated as a time-dependent problem with a damper attached to the midpoint of the beam as shown in Figure 4.10. Neglecting the inertia of the beam, the equation for the two-element FEA is of the form-

$$\boldsymbol{K}\begin{Bmatrix}\theta_1\\ w_2\\ \theta_2\end{Bmatrix}+\begin{bmatrix}0 & 0 & 0\\ 0 & c & 0\\ 0 & 0 & 0\end{bmatrix}\begin{Bmatrix}\dot{\theta}_1\\ \dot{w}_2\\ \dot{\theta}_2\end{Bmatrix}=\boldsymbol{F_{w_1}}+\begin{Bmatrix}0\\ F_{nl}\\ 0\end{Bmatrix} \tag{4.17}$$

where **K** is the stiffness matrix of the beam and $\boldsymbol{F_{w_1}}$ is the force vector at node 1, as a result of applied displacement w_1. The variables θ_1 and θ_2 can be solved statically, while w_2 must be determined from the above equation by numerical integration in time. Towards this end, we introduce a time-dependent input for the applied displacement. For this problem we allow w_1 to be increased at a constant rate until it reaches a fixed value, i.e,

$$w_1(t)=\begin{cases}\widehat{w}_1\frac{t}{T}\ if\ \ 0\le t\le T\\ \widehat{w}_1\ if\ \ t>T\end{cases} \tag{4.18}$$

and the steady state solution for w_2 is obtained. This is repeated for multiple values of $\widehat{w}_1$. The plot of w_2^{steady} vs. $\widehat{w}_1$ is shown in Figure 4.17(a). The corresponding load (F_1) versus $\widehat{w}_1$ plot is also shown in the figure. Note that the steady state solution w_2^{steady} is independent of the value of the damping coefficient c. It is observed that by introducing a damping coefficient to the system, the non-linear spring on the beam problem can be solved for all scenarios. Also note the jump in the solution of w_2 for an unstable problem as seen in Figure 4.17(a). This manifests as a sudden load drop at the critical value evident in Figure 4.17(b).

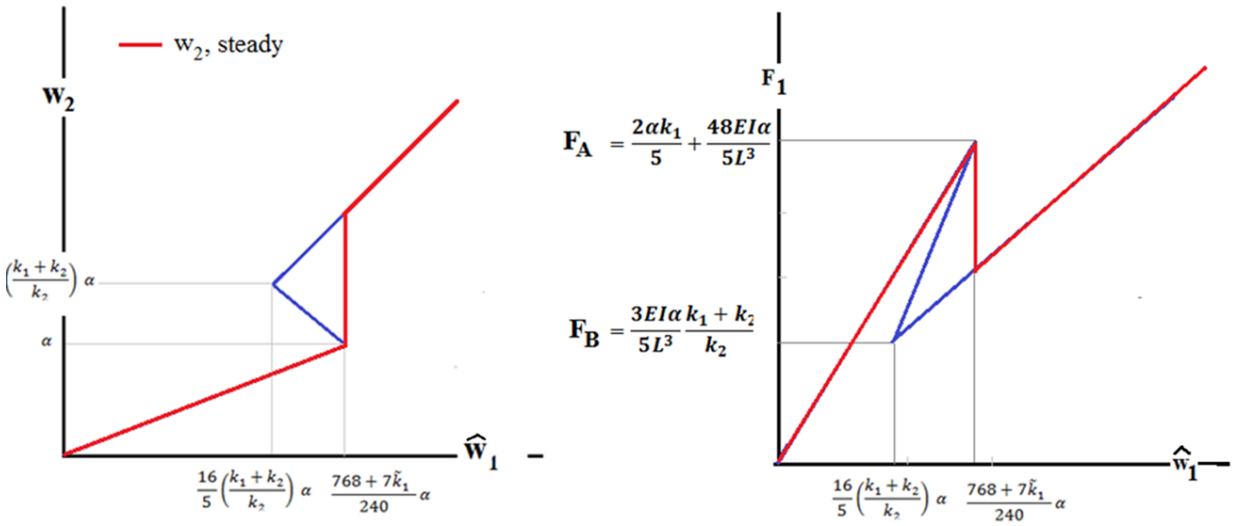

Figure 4.17 a) Steady solutions for w_2 obtained as a function of applied displacement, w_1 b) Corresponding load vs. displacement plot

4.3.4 Effect of beam inertia and transient response of the beam

In the solution process for the time-dependent problem above, we neglected the inertia of the beam in obtaining the steady state response of the beam. If we include the beam inertia effect, the governing equation becomes

$$\boldsymbol{M}\begin{Bmatrix}\ddot{\theta}_1\\ \ddot{w}_2\\ \ddot{\theta}_2\end{Bmatrix} + \boldsymbol{K}\begin{Bmatrix}\theta_1\\ w_2\\ \theta_2\end{Bmatrix} + \begin{bmatrix}0 & 0 & 0\\ 0 & c & 0\\ 0 & 0 & 0\end{bmatrix}\begin{Bmatrix}\dot{\theta}_1\\ \dot{w}_2\\ \dot{\theta}_2\end{Bmatrix} = \boldsymbol{F}_{w_1} + \begin{Bmatrix}0\\ F_{nl}\\ 0\end{Bmatrix} \qquad (4.19)$$

where $\boldsymbol{M}$ is the mass matrix of the beam. The variables θ_1, θ_2, w_2 must be solved dynamically from the above equation. We are interested in solving the problem for the case $\tilde{k}_2 > \frac{768}{7}$. The time dependent input for w_1 is still given by Equation (4.12). Figure 4.18(a) shows the steady state solutions obtained for w_2, for two different rates of increase of the applied displacement w_1. Note that if w_1 changes at a very small rate (T is large), then the inertia forces become negligible and the steady state solution

obtained is same as that obtained without inertia above. For higher rates of increase of w_1, the solution jump in w_2 happens earlier as shown in Figure 4.18(b). The corresponding load drop also occurs earlier for this case.

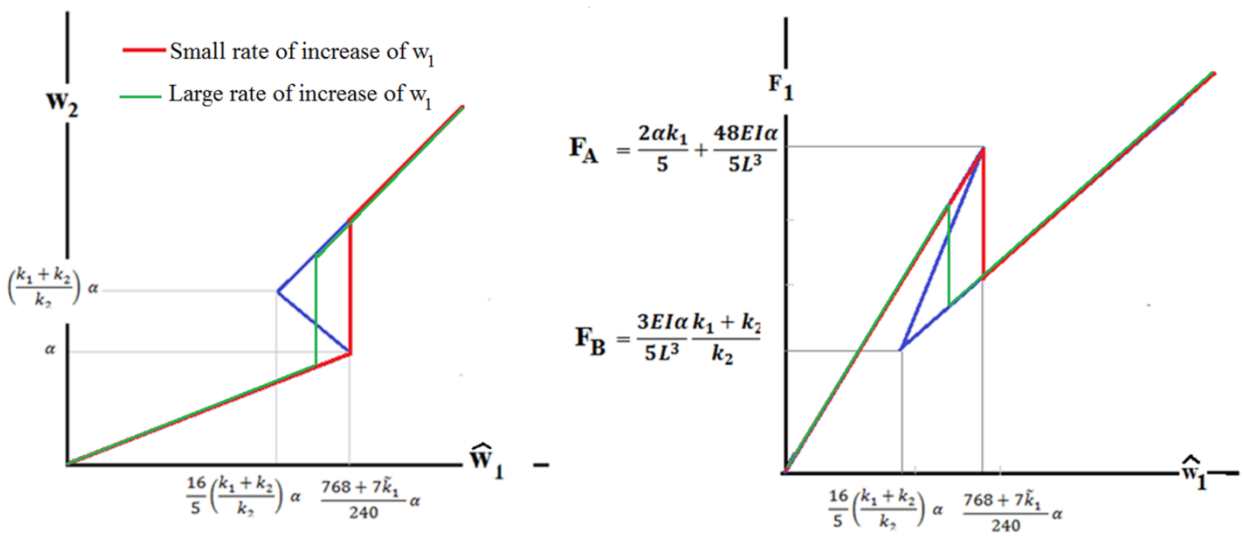

Figure 4.18 a) Steady solutions for w_2 obtained dynamically with inertia included, for two different rates of increase of applied displacement, w_1 b) Corresponding load vs. displacement plot

Up to this point, we focused on obtaining the steady state response of the beam. Allowing w_1 to increase at a very slow rate, i.e, $w_1 = \mu t$, where μ is a small constant, we obtain the transient response of the beam plotted in Figure 4.19. We have neglected the inertia of the beam in obtaining these plots. The transient response of the beam, as seen in Figure 4.19, depends on the coefficient of damping. To solve this problem, we may we introduce the smallest value of damping coefficient, just enough to obtain convergence of the solution. To avoid such a trial-error based approach, we can obtain

the steady-state response of the system that is independent of the viscous parameter. The steady state solution for different values of applied displacement gives the load-displacement curve.

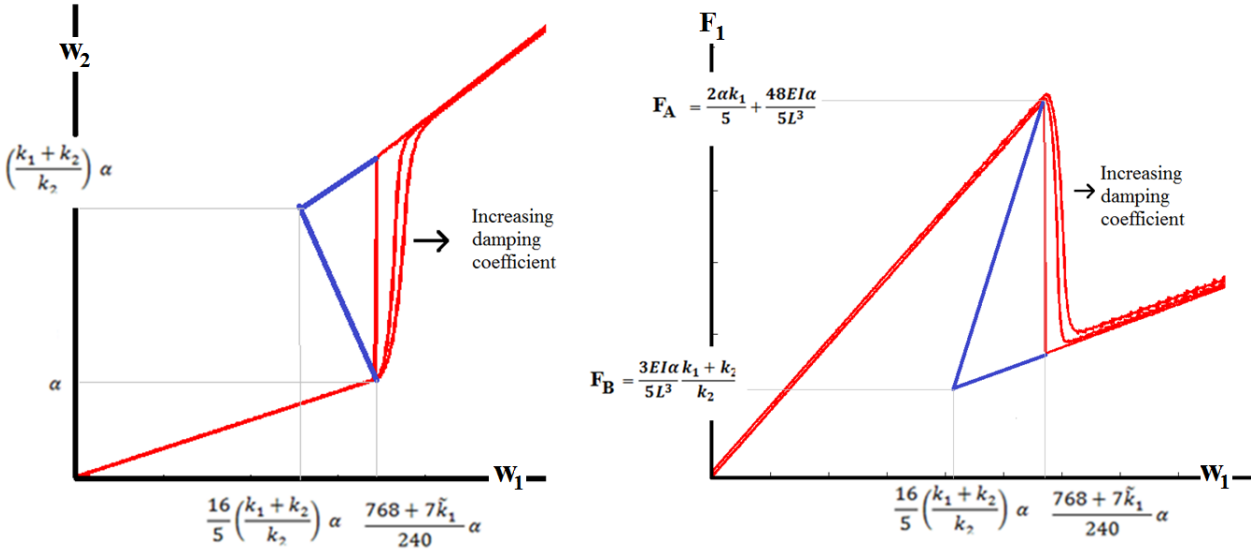

Figure 4.19 a) Transient solutions for w_2 obtained for different values of damping coefficient and neglecting the inertia of the beam b) Corresponding load vs. displacement plot

4.3.5 Material damping and quasi-static solutions

Newton-Raphson method for static analysis of a model with softening spring is inadequate to obtain the response of a beam on a non-linear softening spring. This is the primary reason for convergence issues of FE models with cohesive zone elements. One way around this problem is to solve static crack opening as a dynamic problem. Introducing a damping parameter in the system of equations allows us to solve the

problem for all scenarios. In fact, at the point of crack propagation when the cohesive element fails, the elastic energy contained in the adjacent elements before separation is converted into kinetic energy resulting in oscillations of the separated elements. Experimentally, crack opening in a quasi-static loading results in smaller amplitude of the oscillations that decay quickly. Hence, a quasi-static process is necessary in the numerical analysis and this may be simulated by introducing damping in the composite material. A proportional damping model may then be used such that the damping matrix for the structure is given by $[C] = \alpha[M] + \beta[K]$ where parameters, α and β are numerical constants that may be adjusted for the problem. Using a value of $\alpha = 10$ and $\beta = 5$, the delamination problem of Landry and Laplante was solved for small mesh sizes. In the following section, we verify the structural damping model for a new set of composite delamination experiments performed at UMD.

4.4 UMD experiments for mixed-mode crack propagation

The cohesive element model with a proportional damping was verified for delamination of carbon-fiber/epoxy by comparing with experiments set up at UMD by Puishys and Bruck under mixed-mode loading conditions. The experimental setup for mixed-mode crack propagation called the Wyoming test fixture is shown in Figure 4.20. The schematic for the test apparatus is shown in Figure 4.21. Loading forces are applied to the composite laminate via tabs that are attached to one end of the composite laminate with a pre-crack in that section. The lever roller acts as a fulcrum between the lever arm where the load is applied and the tabs attached to the composite specimen. The

length of the level arm can be changed to vary the mode-mix ratio of the delamination. Experiments were performed according to ASTM D6671 manual and the corresponding FE model are shown in Figure 4.22. In the FE model, the fixture is modeled using brick and wedge elements. A line contact is imposed on the top surface of the test specimen at the center and the right end. At the center line of contact, the vertical displacements of the laminate are constrained simulating the boundary conditions of a roller. At the right end, all degrees of freedom are fixed at both bottom and top of the plate. At the bottom of the composite laminate on the left side, only vertical displacements are constrained. While modeling the fixture, particular attention was given to modeling the arm lengths and the loading height precisely. Elastic properties of steel were used for the fixture.

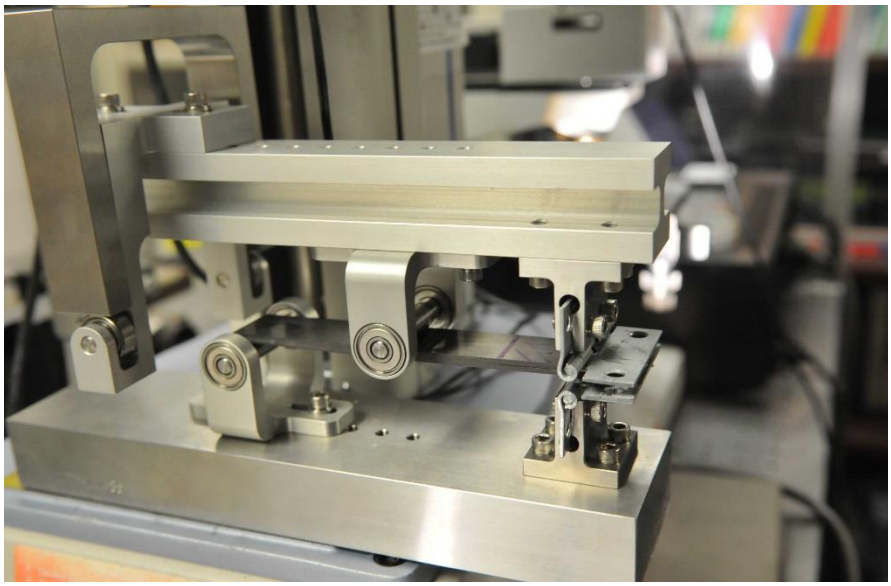

Figure 4.20: Wyoming Test Fixture used at FGM Lab, UMD [25] to perform mix-mode crack propagation test on composite laminate

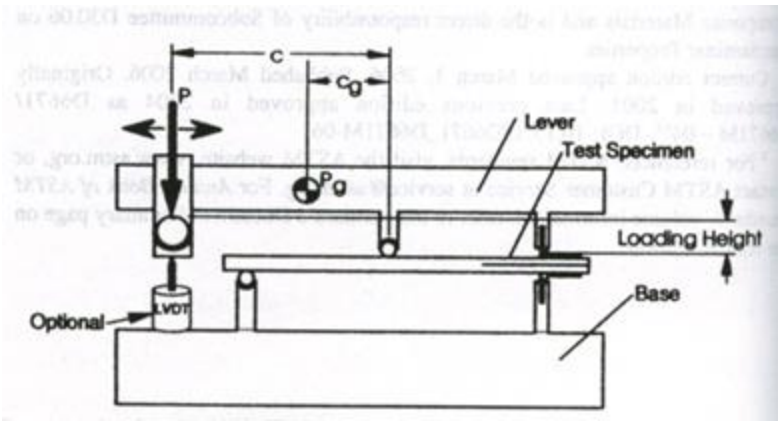

Figure 4.21: Mixed-mode bending test schematic [26]

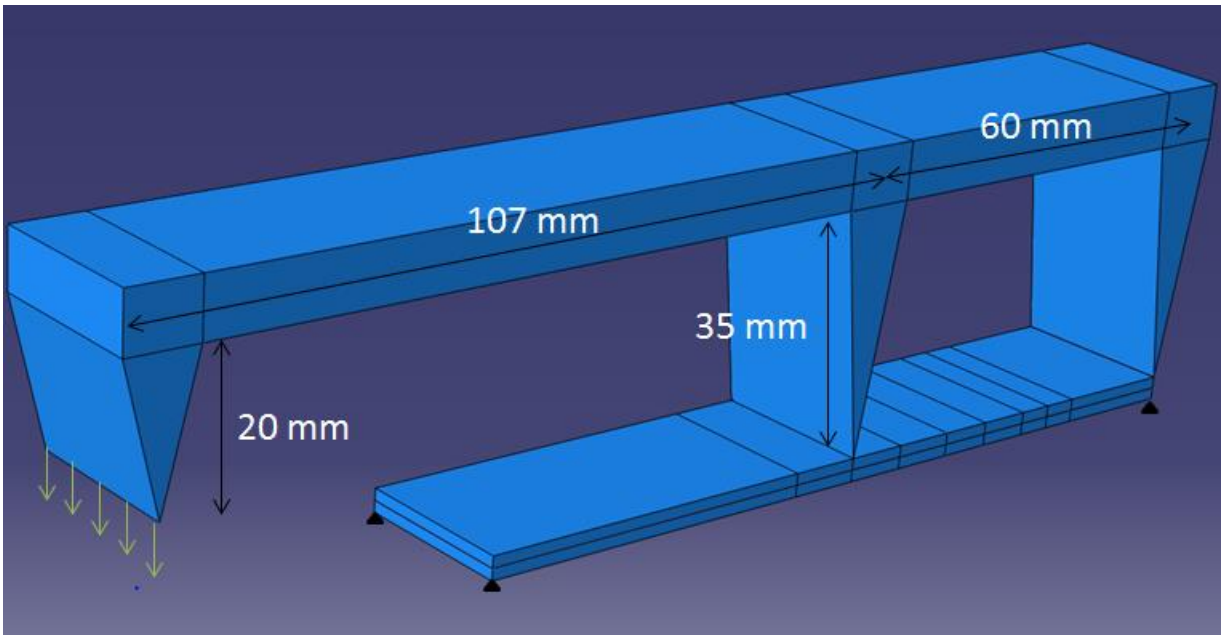

Figure 4.22: Illustration of the model constructed in Abaqus

The composite laminate is meshed non-uniformly as shown in Figure 4.23. The plate is meshed coarsely using 20 node brick elements away from the crack tip. Closer to the crack tip, the plate is meshed finely using 15 node wedge elements. Only one element is used in the width direction everywhere. The number of elements in the thickness

direction varies from 4, in the coarser region, to 48 in the crack tip region. A close-up of the mesh near the crack tip is shown in Figure 4.24. A very coarse mesh is used for the fixture owing to its high stiffness. Only three wedge elements and 5 brick elements are present on the fixture as shown in Figure 4.22.

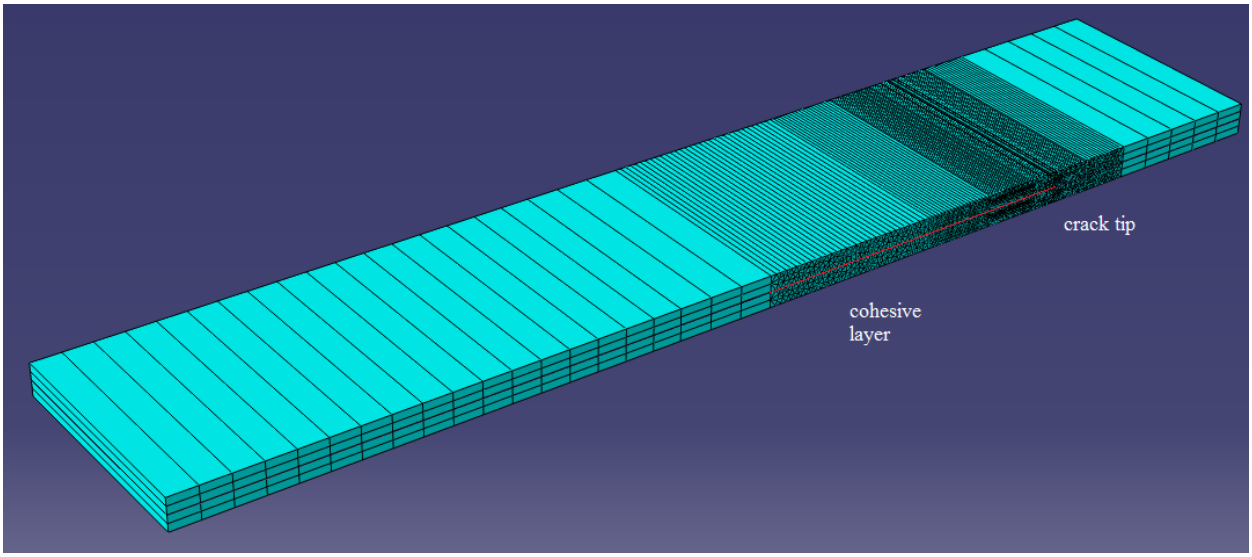

Figure 4.23: The test specimen model with meshing.

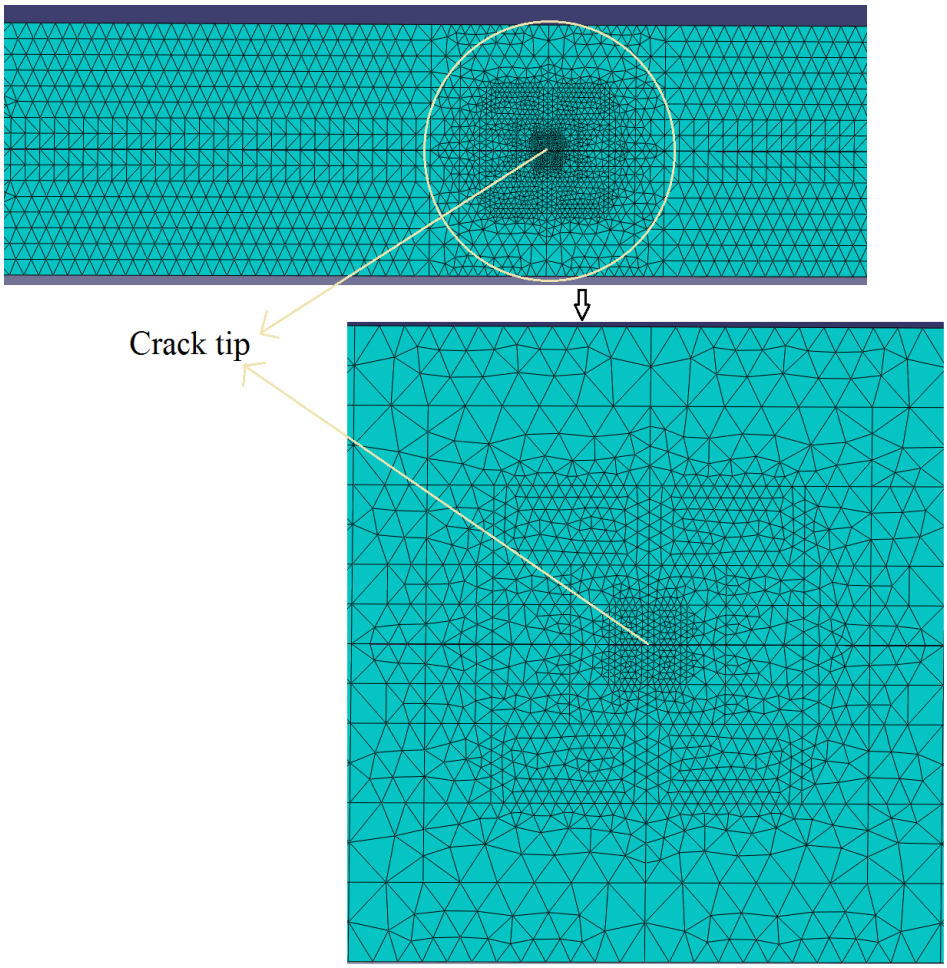

Figure 4.24: Close up of meshing of composite laminate around the crack-tip.

A cohesive layer was inserted in the mid-plane between the two legs of the composite laminate. This cohesive layer extends from the crack-tip to the center of the plate as shown in Figure 4.23. The material properties used for the plate were experimentally determined and are listed in Table 4.2. The value of G_{IC} was obtained from ASTM calculations and is equal to 371.2 J/m^2. A high value of 1.4 x 10^{12} N/m^3 is used for the initial slope of the traction-separation response curve (K), which is the same value as used in the DCB beam of Landry-Laplante. The force-displacement response was obtained for mode-I, mode-II and 22% mode-mixture bending for interfacial strength

$\sigma_0 = 9MPa$. Figure 4.25 shows the deformed states of the FE model corresponding to mode-I and 22% mode mixture. The force-displacement plots obtained from the FE models are plotted in Figures 4.26-4.28 along with experimental results. The results from FE models correlate with experiments fairly well. The methodology using material damping for cohesive zone was used for analysis of Z-pinned laminates as presented in Chapter 2.

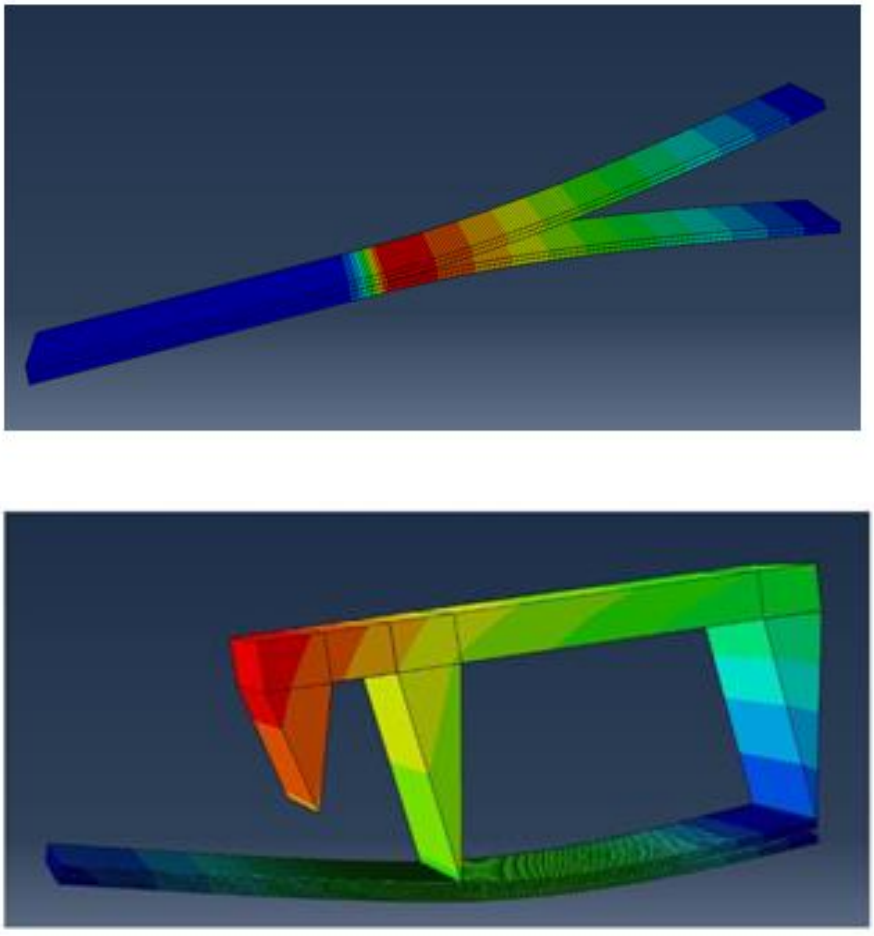

Figure 4.25: Deformed state of FE models corresponding to mode-I and 22% mode-mix bending conditions

Table 4.2: Lamina properties of the composite used as the test specimen, obtained experimentally

Lamina properties	
E_{11}	138GPa
$E_{22} = E_{33}$	10.3 GPa
$G_{12} = G_{23}$	5.9 GPa
G_{23}	3.41 GPa
υ_{12}	0.3

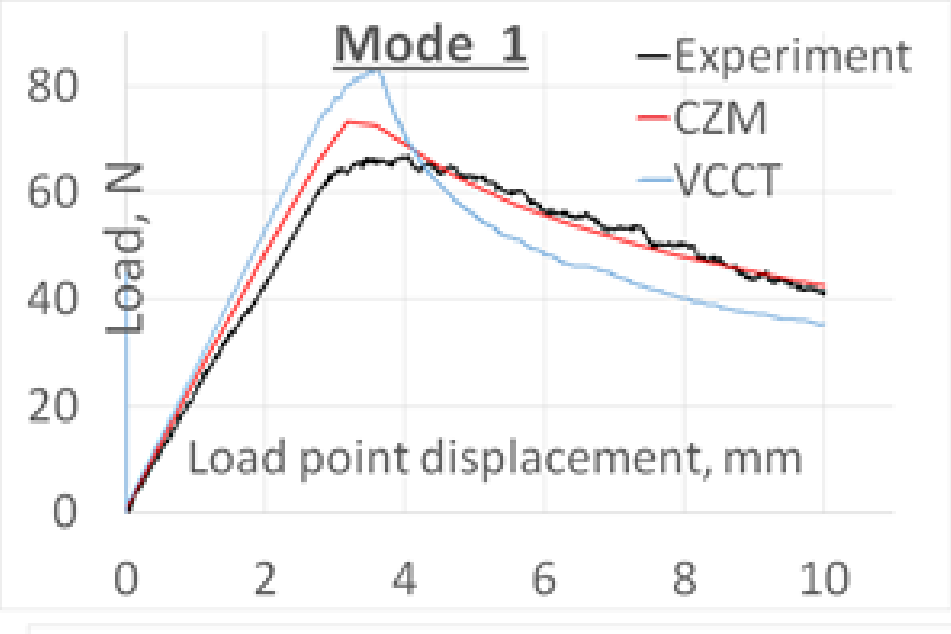

Figure 4.26: Global load displacement results for delamination of a carbon-fiber/epoxy laminate under mode-I loading

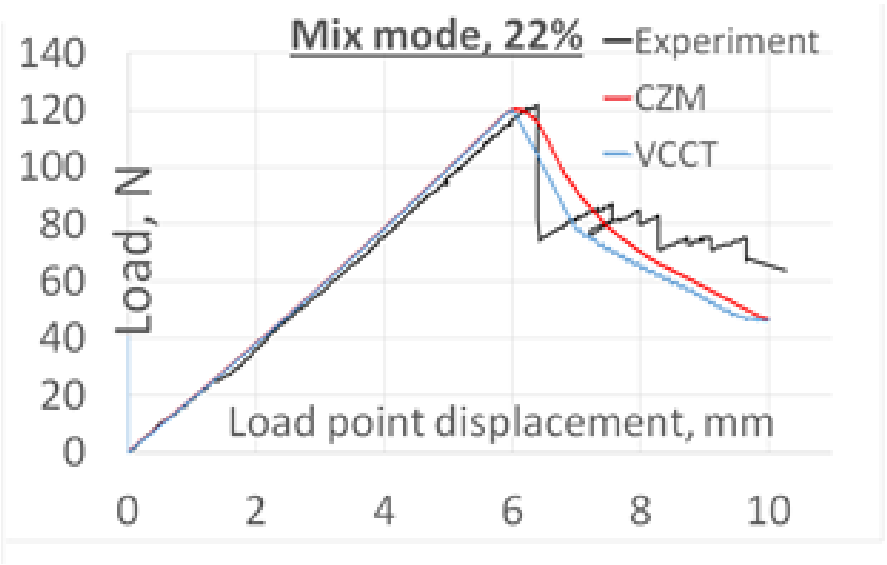

Figure 4.27: Global load displacement results for delamination of a carbon-fiber/epoxy laminate under 22% mode-mix conditions

Figure 4.28: Global load displacement results for delamination of a carbon-fiber/epoxy laminate under mode-II loading

Chapter 5: Conclusions and Future Work

5.1 Summary and contributions of this research

This research summarizes novel Z-pinning technologies developed to enhance delamination resistance for composite laminate structures through introduction of various method for mechanical interlocking. Since the performance of a Z-pinned laminate is dependent on the mechanical interlocking of the pin and the laminate, we proposed methods to increase the interlocking via three novel techniques- a) Angled pin insertion where pins are inserted at an angle to the vertical b) threaded pin insertion where threaded pins with grooves on the outer surface are used for Z-pins, and c) Anchored pin insertion, where the pins inserted are anchored to the outer surfaces of the laminate. Experiments were performed to test pullout strengths of laminates under tensile and shear loading with a pre-crack at the mid-layer of the laminate. Results obtained show an improvement in performance of the laminate when the pins were inserted at an angle, or had threaded exterior surface, or were anchored to the outer surface of the laminate. Similar improvement in delamination toughness was observed from crack propagation experiments on laminates with angled, threaded and anchored pin insertions. Non-linear FE models of the pin reinforced laminates constructed in ABAQUS verify with experimental results of pullout strengths. Galvanic corrosion has been shown to have a minimal effect on the pin-reinforced laminates.

For X-Cor composite sandwich structures, a model based on the assumptions of a perfect pin geometry with rigid connection to the facesheet overestimates the out-of-

plane compressive and shear stiffness and strength values. Accordingly, our research outlined a computational-analytical model to incorporate the imperfections of the sandwich structures under compression and shear loading. Towards this end, parameters important in representing the behavior of the individual components of the sandwich were identified. These are empirical parameters that include effective imperfection, $(e/L)_{eff}$ of the C-pin, and E_{int}^{C-pin}, the in-situ pin-facesheet interface modulus which are essential in capturing the softening of the C-pins from geometric and material imperfections. In addition, the model also incorporates densification of the foam to represent foundation support to the pins through parameter, ϕ and introduces in-situ pin-facesheet interface strength, σ_s as an indicator of pullout strength of the T-pins.

The values of these parameters were extracted from compression and shear testing at UMD and then used on the model for CU specimens reported in open literature. The results for compressive and shear properties of CU specimens from the model agree reasonably well with experimental results. From the correlation of the parameter values across different specimens, it appears that the model presented in this paper is a viable representation of the physics of the sandwich components and the interaction between them. This provides a basis for developing a damage model via finite element analysis to represent pin-facesheet interface based on its nonlinear material properties. The interface properties may then be incorporated into a finite element model of a sandwich construction to determine its performance under compression and shear loading.

Finally, we have made some strides in the numerical technique of cohesive zone modeling which is used to analyze delamination of composites in conjunction with FE models. To combat the convergence issues encountered by CZM, we proposed trreting the problem dynamically with a material damping included in the structure. Proportional damping was assigned to the structures and was shown to successfully tackle convergence issues. This method was then validated by experiments available in open literature as well as experiments performed at UMD for mixed-mode bending of laminates. The CZM method with damping model was then used to validate tensile pullout tests of Z-pinned laminates presented in Chapter 1.

The findings from this research work has been published in the Journal of Composite Structures titled “A viable model for out-of-plane compressive and shear properties of Z-pin reinforced composite sandwich panels”. A second journal paper presenting the work of Z-pinned laminates is under review.

5.2 Applications of this research and recommendations for future work

5.2.1 Optimally Contoured Pins

The threaded pin used in the experiments show significant improvement in enhancing the pullout strengths of the laminate but are limited by the breaking of the pins at the locations of its minimum diameter where the sharp edges cause stress concentrations. A Finite element based study on the optimal contouring of the pins to delay delamination by increasing mechanical interlocking as well as the stress concentration can be studied as a part of future work.

5.2.2 Application to tapered and curved tapered laminates

Ply drop-off locations in composite laminates are ripe sites for stress concentration and hence are, typically, the locations for onset of delamination in a laminate. Z-pinning may be judiciously used at these specific sites to prevent or delay delamination with intention of reducing the weight increase from Z-pinning. In a composite laminate with multiple ply-drop locations, FE modeling may be used to predict the exact location for the onset of delamination and the direction in which the delamination crack is expected to propagate. [See Appendix for more work on this topic]

5.2.3 Application to T-joints

T-joints occur in common engineering structures where two segments of a composite laminate are joined together at right angles. Delamination between two skins of the T-joints is a big concern since they are location for stress concentrations. Z-pinning technologies developed in this research can be tested on T-joints as shown in the crude sketch presented in Figure 5.1 as a part of future work.

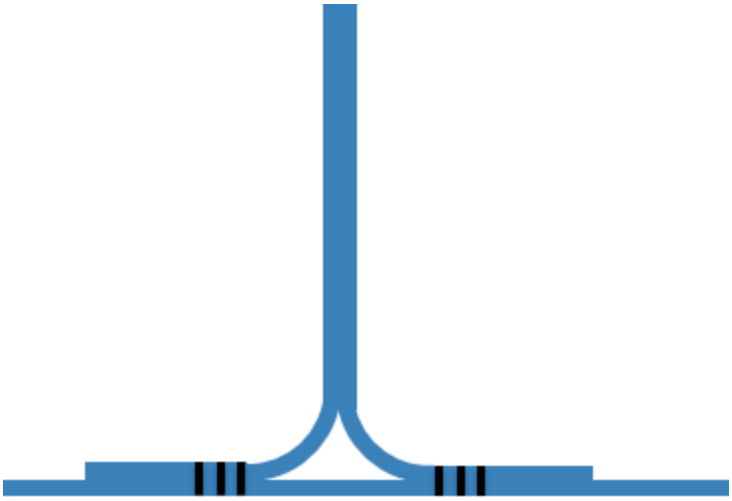

Figure 5.1: Z-pinning in T-joints to increase delamination resistance

5.2.4 Modeling of DCB beams with cohesive springs

In this research, we verified experimental results for tensile pullout strengths of Z-pinned specimens via a CZM model used in an FE analysis. This may be extended to a DCB specimen where the Z-pins can be replaced by cohesive layer between the layers as shown in Figure 5.2. Cohesive layers between the arms of the laminate must have appropriately chosen parameters or the CZM based on the type of reinforcement. Research in this regard is left for future work.

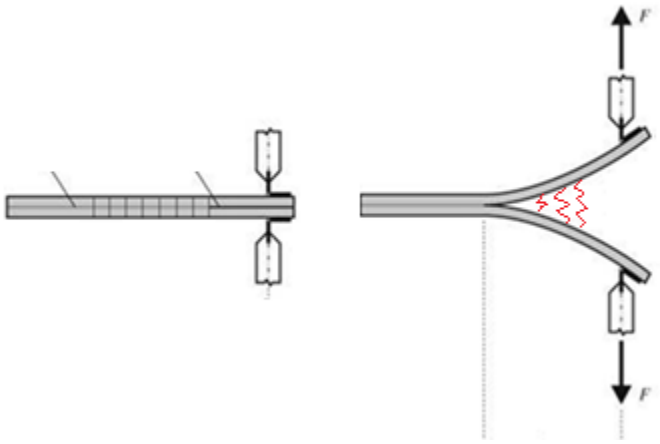

Figure 5.2: DCB specimens of Z-pinned laminates modeled with cohesive layers acting as spring between two arms of the laminate

5.2.5 Anchored pin for sandwich panels

We showed that the Z-pin bonding defects and material imperfections are a big reason for stiffness reduction in sandwich structures. Fiber-resin bonding defects and fiber

crimping are significantly higher for composite fiber Z-pins than metal Z-pins. In addition, we showed that anchoring of Z-pins to the outer surface of the laminate significantly increases pullout strengths and fracture toughness under mode-I loading od DCB specimens. In this light, we would also expect that sandwich panels designed with anchored pins as shown in Figure 5.3 will have improved properties. Manufacture and testing of anchored pin sandwich panels is left for future work.

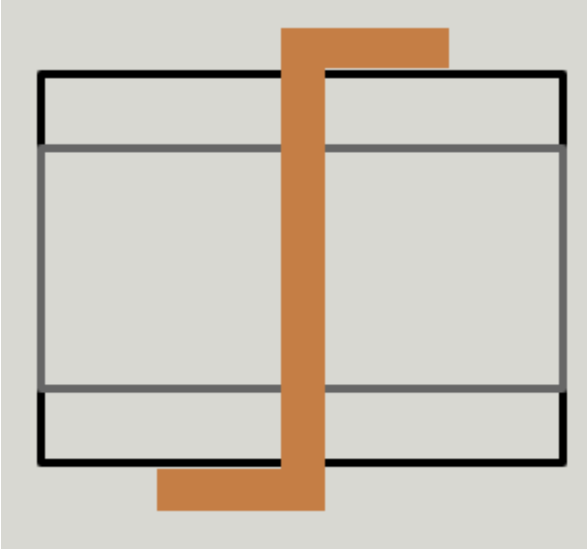

Figure 5.3: Sketch of an anchored Z-pin in a sandwich panel

Appendix

In this section, we present a study on how the curvature of the laminate affects the interlaminar stresses and the location of maximum stresses in a laminate. To study the influence of curvature on interlaminar stresses, a flat laminate is chosen from the research of Fish and Lee [27] and modified to construct a curved tapered laminate with similar properties. The flat tapered laminate is shown with ply numbering in Figure A1 and has a thin section with 8 plies, thick section with 14 plies and a taper region. Plies 5-10 are dropped from the thick section to the thin section two at a time successively over one-third the length of the tapered region. Two different laminate configurations are considered for this study- A: $[\pm 45_5, 0_4]$ and B: $[0_4, \pm 45_5]$. For the curved laminate, the plies of same width as that of the flat laminate are laid on a cylinder of fixed radius to obtain curved tapered laminates as shown in Figure A2. Four different radii are chosen for the cylinder so that width of the curved laminate extends along angles of $\theta = 15^o, 30^o, 45^o$ and 60^o.

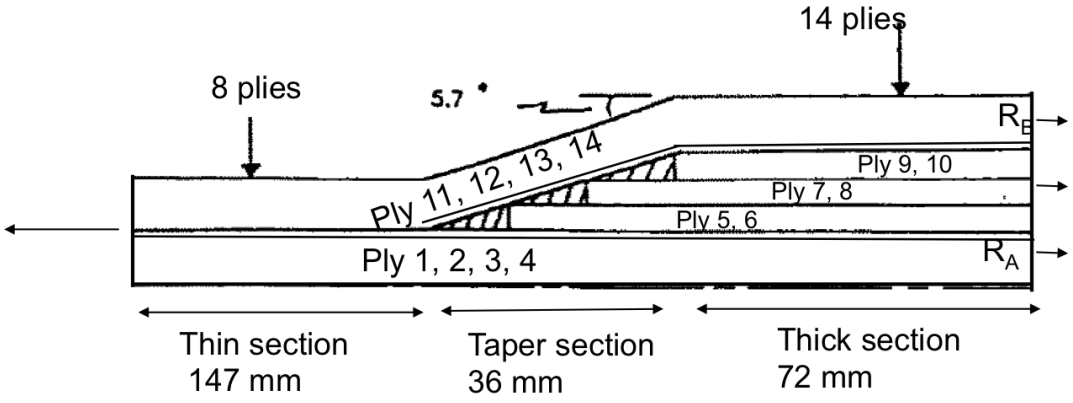

Fig A1: Ply layup and geometry for flat tapered laminate taken from [27]

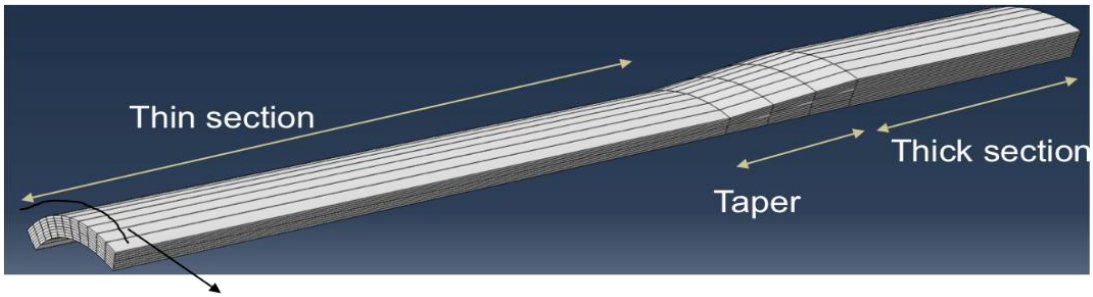

Fig A2: Curved tapered laminate with same layup and ply-dimensions as the flat laminate

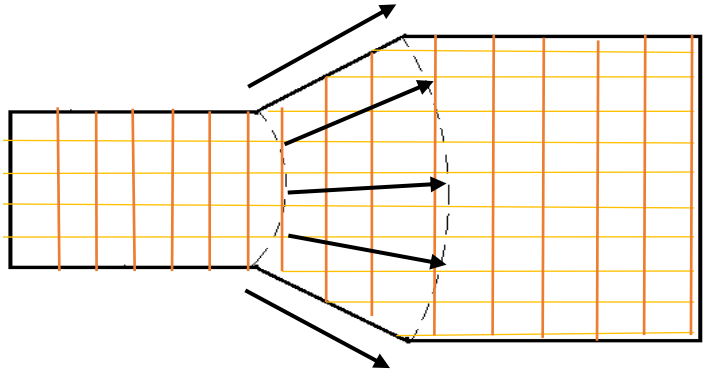

Figure A3: Planform view of plies 11-14 for curved laminate showing the fiber angles different from longitudinal direction

The geometry of the curved specimen forces the laminate to have non-uniform fiber angles in the taper region. Figure A3 represents the planform views of plies 11-14 with a trapezoidal portion at the center of the plies to wrap around the taper region. In the process, the 0^o fibers are deviated away from the longitudinal direction of the laminate. Accordingly, the curved specimes with $\theta = 15^o, 30^o, 45^o$ and 60^o will have a maximum angle of deviation equal to 0.75^o, 1.5^o, 2.25^o and 3^o respectively. The change in

material properties due to this small angle deviation is negligible and is not accounted for in the analyses below.

The response of the flat and curved specimens subjected to axial loading are analyzed here. One end of the laminate at the thick section is fixed and a uniform unit displacement is applied to the cross-section at the other end as shown in Figure A4. Due to asymmetry in the geometry, the laminate will also undergo bending deformations. Loading is quasi-statically applied such that axial force per unit cross-section area was the same across all specimens. The laminates are computationally analyzed by non-linear finite element modeling in ABAQUS. For the models, the resin-rich layers above ply 4 and below ply 11 were also modeled. The thickness of the resin-rich layer was assumed to be 10% of the ply thickness. The resin rich layers are illustrated in Figure A4(b) and (c). Quadratic 20 noded brick elements (C3D20) were used for the models with one element in the thickness direction of the plies. The resin-rich region is modeled by as many as 4 elements through the thickness. Five elements were used in the width of the flat laminate and for the curved laminate, the width of the element spanned no more than 5^o angle. The material properties of the SP-25-S29 Glass Epoxy composite used are given as: E_L = 48.26 GPa, E_T = 14.48 GPa, ν_{LT} = 0.26, G_{LT} = 5.52 GPa and for the resin: E = 3.93 GPa, ν_{LT} = 0.26.

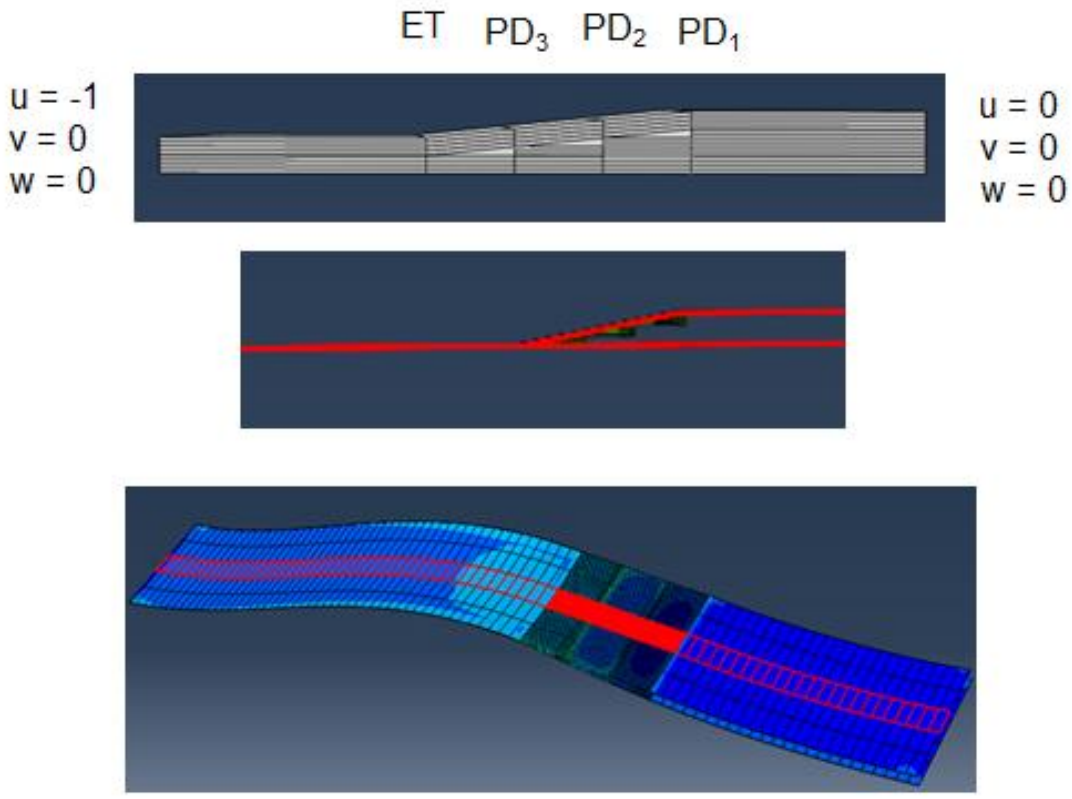

Figure A4 (a) Sketch of the tapered laminate with appropriate boundary conditions at its ends. (b) Location of resin-rich layers above ply 4 and below ply 11 extending across the length of the laminate. (c) Resin-rich layers shown on cross-sectional view

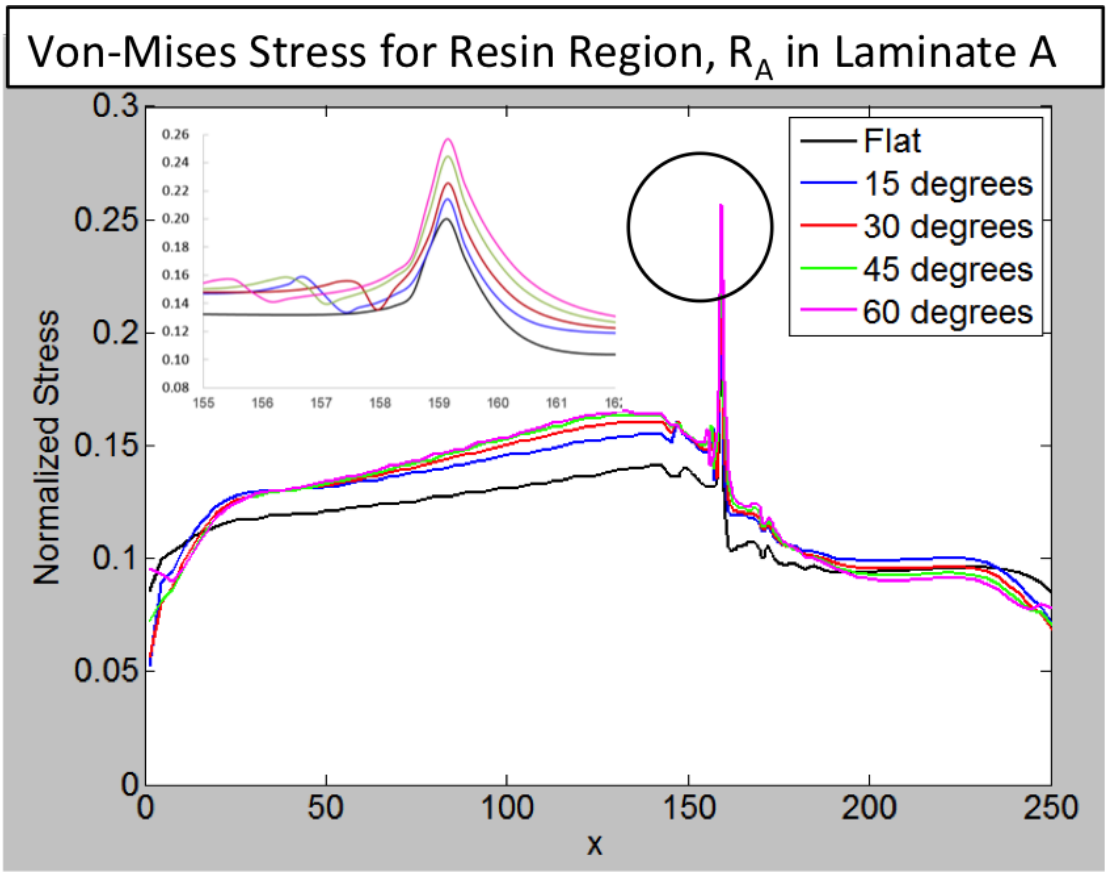

Figure A5: Von-Mises stresses along the length of the laminate in regions R_A for curved and flat specimens of ply configuration A

Von-Mises stresses in the inter-ply resin regions above the 4th ply (R_A) and below the 11th ply (R_B) was used as an indicator for resin failure and onset of delamination in the composite. For the flat specimen, the stresses were maximum in the region R_B ahead of the last ply-drop step. This is consistent with the observation made from experiments in [27] for a symmetric laminate. For the curved laminates, the von-Mises stresses are plotted in Figures 5.5-5.8. The region around which the stress was observed to be maximum is enlarged to show the trend. It is observed that for laminate A, the stresses in region, R_A was maximum at the last ply-drop step and they increased with increase

in curvature. The stresses in region R_B was also maximum at the last ply-drop step, but the opposite trend was observed with changes in curvature. This changes the location of the onset of delamination from region, R_B to R_A for curvature angles, 30^o , 45^o and 60^o. For the 15^o laminate, the maximum stress is still at location, R_B. For laminate B, the maximum stresses were consistently observed to occur in region R_B of the laminate ahead of the last ply drop step. The maximum stresses for region, R_A occured at the junction between the thin section and taper section of the laminate, but were smaller compared to that in region, R_B. Accordingly, the location of onset of delamination does not change in this case with curvature.

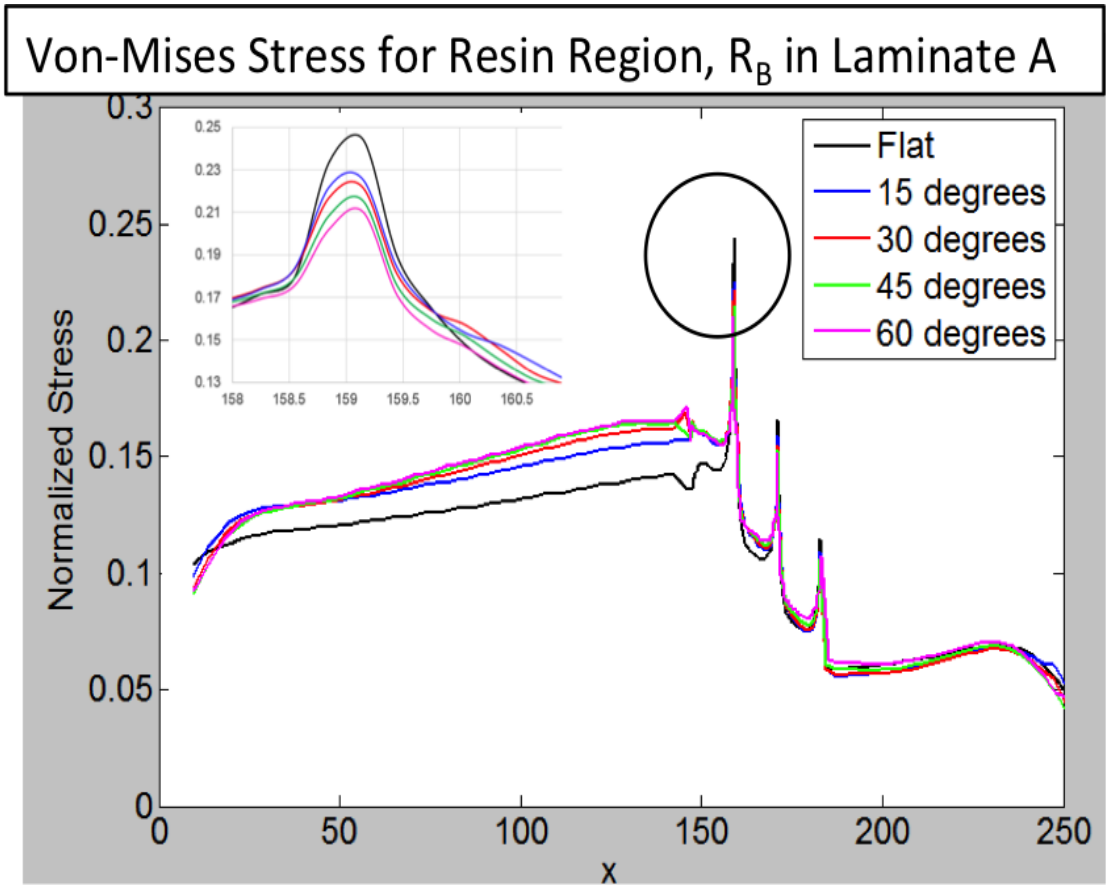

Figure A6: Von-Mises stresses along the length of the laminate in regions R_B for curved and flat specimens of ply configuration A

The most significant observation from the results is that the location of onset of delamination may change with changes in curvature of the laminate depending on the ply configuration and the degree of curvature. This can be important when trying to prevent the delamination through targetted application of reinforcements. In addition, an optimum ply configuration may be chosen so as to obtain the same stiffness properties, but still delay the delamination.

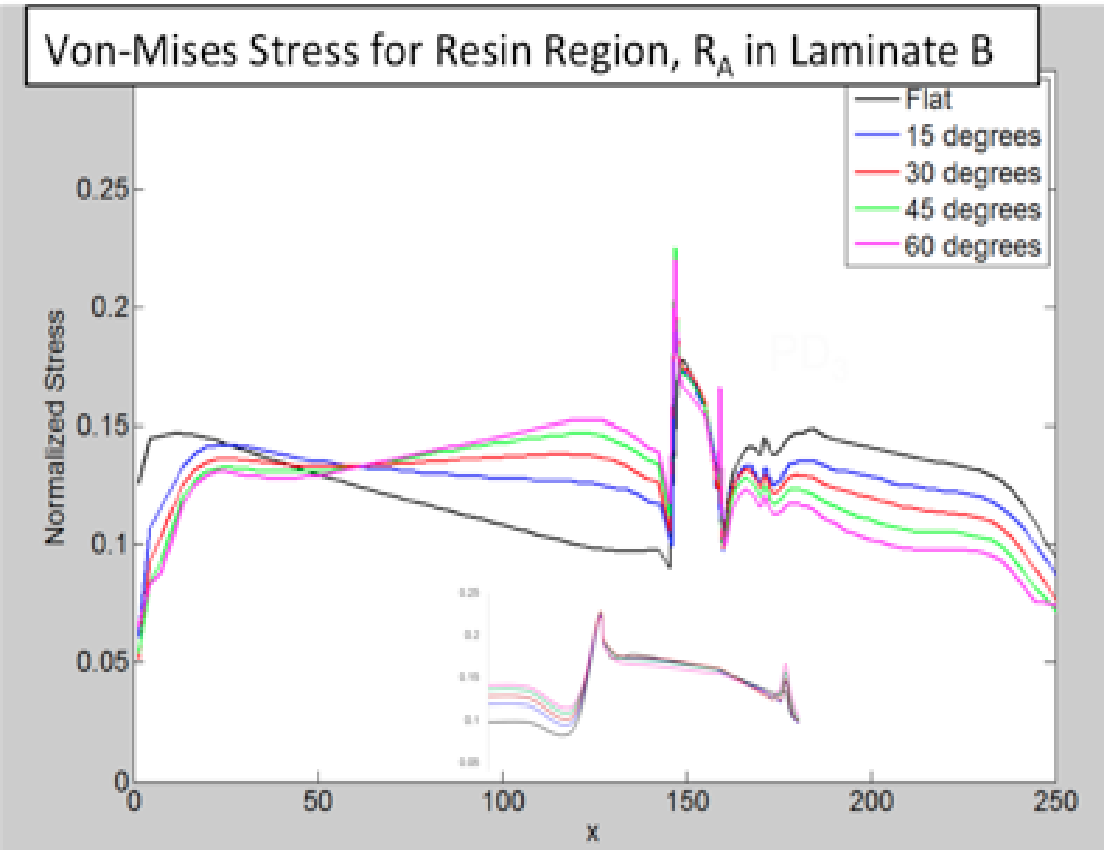

Figure A7: Von-Mises stresses along the length of the laminate in regions R_A for curved and flat specimens of ply configuration B

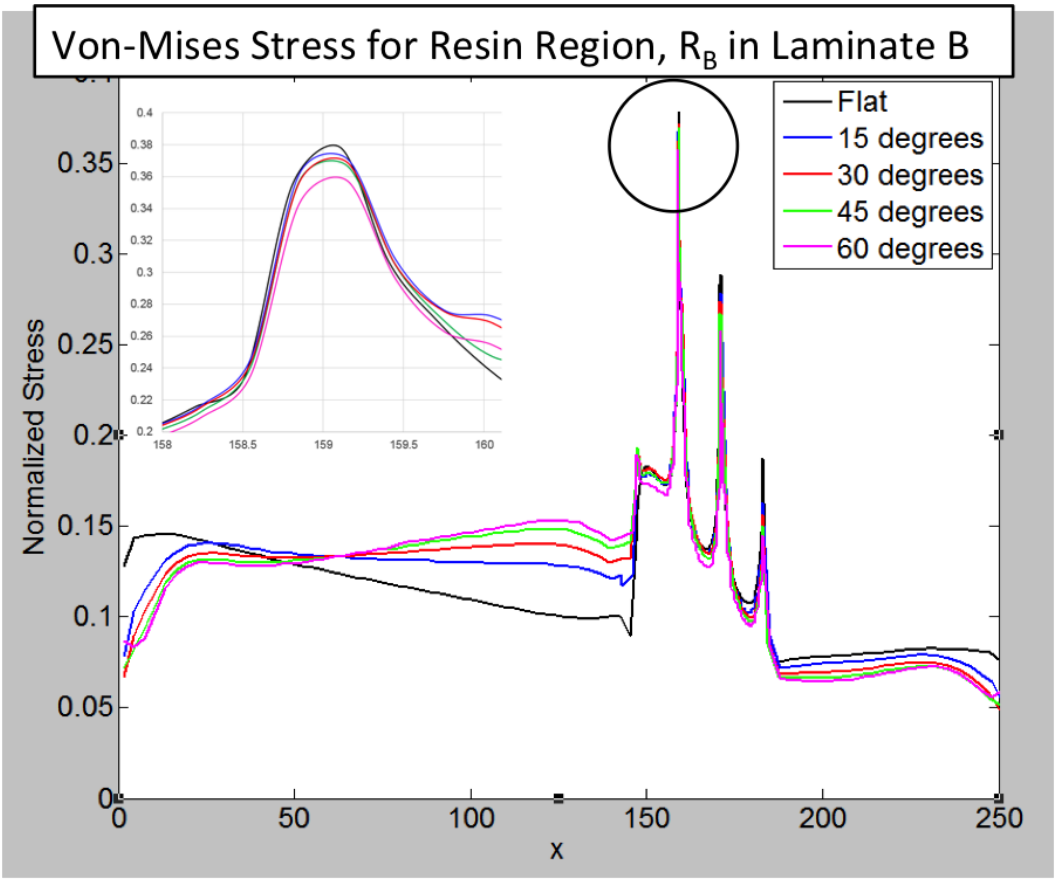

Figure A8: Von-Mises stresses along the length of the laminate in regions R_B for curved and flat specimens of ply configuration B

Bibliography

[1] Mouritz, A.p., et al. “Review of Applications for Advanced Three-Dimensional Fibre Textile Composites.” *Composites Part A: Applied Science and Manufacturing*, vol. 30, no. 12, 1999, pp. 1445–1461., doi:10.1016/s1359-835x(99)00034-2.

[2] Dransfield, Kimberley, et al. “Improving the Delamination Resistance of CFRP by Stitching- a Review.” *Composites Science and Technology*, vol. 50, no. 3, 1994, pp. 305–317., doi:10.1016/0266-3538(94)90019-1.

[3] Dellâ Anno, G., et al. “Manufacturing of Composite Parts Reinforced through-Thickness by Tufting.” *Robotics and Computer-Integrated Manufacturing*, vol. 37, 2016, pp. 262–272., doi:10.1016/j.rcim.2015.04.004.

[4] Pearson, Raymond A, and Albert F Yee. “Toughening Mechanisms in Thermoplastic-Modified Epoxies: 1. Modification Using Poly(Phenylene Oxide).” *Polymer*, vol. 34, no. 17, 1993, pp. 3658–3670., doi:10.1016/0032-3861(93)90051-b.

[5] Shivakumar, Kunigal N., et al. “Interleaved Polymer Matrix Composites - A Review.” *54th AIAA/ASME/ASCE/AHS/ASC Structures, Structural Dynamics, and Materials Conference*, 2013, doi:10.2514/6.2013-1903.

[6] Chen, S.F., and B.Z. Jang. “Fracture Behaviour of Interleaved Fiber-Resin Composites.”*Composites Science and Technology*, vol. 41, no. 1, 1991, pp. 77–97., doi:10.1016/0266-3538(91)90054-s.

[7] Fusco, T. M., Magee, C. and Freitas, G., Foster-Miller Inc, Waltham, MA, U.S. Patent Application for a “Method and System for Inserting Reinforcing Elements in a Composite Structure,” U.S. Patent No. 5,589,015, filed 31 Dec. 1996

[8] Mouritz, A.P. “Compression Properties of z-Pinned Composite Laminates.” *Composites Science and Technology*, vol. 67, no. 15-16, 2007, pp. 3110–3120., doi:10.1016/j.compscitech.2007.04.017.

[9] Choi, Ik-Hyeon, et al. “New Manufacturing Method of Z-Pinned Composite Laminates.” 51st AIAA/ASME/ASCE/AHS/ASC Structures, Structural Dynamics, and Materials Conference 18th AIAA/ASME/AHS Adaptive Structures Conference 12th, 2010, doi:10.2514/6.2010-3133.

[10] Song, Qinghua, et al. “Study on an Automatic Multi-Pin Insertion System for Preparing Z-Pin Composite Laminates.” *Chinese Journal of Aeronautics*, vol. 27, no. 2, 2014, pp. 413–419., doi:10.1016/j.cja.2014.02.012.

[11] Pingkarawat, K., and A.p. Mouritz. “Comparative Study of Metal and Composite z-Pins for Delamination Fracture and Fatigue Strengthening of Composites.” *Engineering Fracture Mechanics*, vol. 154, 2016, pp. 180–190., doi:10.1016/j.engfracmech.2016.01.003.

[12] Cartie, D.D.R., et al. “Mechanisms of Crack Bridging by Composite and Metallic Rods. ”*Composites Part A: Applied Science and Manufacturing*, vol. 35, no. 11, 2004, pp. 1325–1336., doi:10.1016/j.compositesa.2004.03.006.

[13] Sweeting, Roderick D., and Rodney S. Thomson. “The Effect of Thermal Mismatch on Z-Pinned Laminated Composite Structures.” *Composite Structures*, vol. 66, no. 1-4, 2004, pp. 189–195., doi:10.1016/j.compstruct.2004.04.037.

[14] Steeves, Craig A., and Norman A. Fleck. “In-Plane Properties of Composite Laminates with through-Thickness Pin Reinforcement.” *International Journal of Solids and Structures*, vol. 43, no. 10, 2006, pp. 3197–3212., doi:10.1016/j.ijsolstr.2005.05.017.

[15] Hermann F. Seibert, Applications for PMI foams in aerospace sandwich structures” *Reinforced Plastics*, 50(1) (2006): 44-48

[16] “The Cohesive Zone Model: Advantages, Limitations and Challenges.” *Engineering Fracture Mechanics*, Pergamon, 28 Nov. 2001

[17] Planas, Jaime, and Manuel Elices. “Nonlinear Fracture of Cohesive Materials.” *SpringerLink*, Kluwer Academic Publishers, link.springer.com/article/10.1007/BF00033975.

[18] Park, Kyoungsoo, and Glaucio H. Paulino. “Cohesive Zone Models: A Critical Review of Traction-Separation Relationships Across Fracture Surfaces.” *Applied Mechanics Reviews*, vol. 64, no. 6, 2013, p. 060802., doi:10.1115/1.4023110.

[19] Cartie DDR. “Effect of z-fibre_ on the delamination behavior carbon fibre/epoxy laminates”. *PhD thesis*, Cranfield University, 2000.

[20] Denis D. Cartie, Norman A. Fleck. The effect of pin reinforcement upon the through-thickness compressive strength of foam-cored sandwich panels, *Composites Science and Technology* 63 (2003): 2401–2409

[21] Tao Liu, Zi Chen Deng, Tian Jian Lu., Analytical modeling and finite element simulation of the plastic collapse of sandwich beams with pin-reinforced foam cores, *International Journal of Solids and Structures* 45 (2008): 5127–5151

[22] M. Hetenyi, *Beams on Elastic foundation*, University of Michigan Press, 1946

[23] Andrea I. Marasco, Denis D.R. Cartie, Ivana K. Partridge, Amir Reza., Mechanical properties balance in novel Z-pinned sandwich panels: Out-of-plane properties, *Journal of Composites*: Part A 37 (2006): 295–302

[24] Landry, Benoit, and Gabriel Laplante. “Modeling Delamination Growth in Composites under Fatigue Loadings of Varying Amplitudes.” *Composites Part B: Engineering*, vol. 43, no. 2, 2012, pp. 533–541., doi:10.1016/j.compositesb.2011.08.020.

[25] Prakhar Singh, “ Characterization of fatigue crack growth in unidirectional carbon fiber epoxy composites using digital image correlation”, Master’s Thesis, 2014 University of Maryland

[26] ASTM Standard D6671-13, "Test Method for Mixed Mode I-Mode II Interlaminar Fracture Toughness of Unidirectional Fiber Reinforced Polymer Matrix Composites," American Society for Testing and Materials, West Conshohocken, Pennsylvania (first published in 2001).

[27] Fish, John C., and Sung W. Lee. "Delamination of Tapered Composite Structures." *Engineering Fracture Mechanics*, vol. 34, no. 1, 1989, pp. 43–54., doi:10.1016/0013-7944(89)90241-5.

[28] Hamed E, Rabinovitch O, Modeling and Dynamics of Sandwich Beams with a Viscoelastic Soft Core, *AIAA Journal*, 47-9 (2009): 2194-2211

[29] Kardomateas GA, Frostig, Y , Phan, CN, Dynamic Elasticity Solution for the Transient Blast Response of Sandwich Beams/Wide Plates, *AIAA Journal*, 51-2 (2013): 485-491

[30] Rakow, JF , Waas AM, Response of actively cooled metal foam sandwich panels exposed to thermal loading, *AIAA Journal*, 45-2 (2007): 329-336

[31] Basu S, Waas AM, Ambur DR, Computational modeling of damage growth in composite laminates, *AIAA Journal* 41-6 (2003): 1158-1166

[32] Bulent Murat Icten, Onur Sayman., Failure analysis of pin-loaded aluminum–glass–epoxy sandwich composite plates, *Composites Science and Technology* 63 (2003): 727–737

[33] David W. Sleight and John T. Wang., Buckling Analysis of Debonded Sandwich Panel Under Compression, NASA Technical Memorandum 4701

[34] Marc R. Schultz, Leonard Oremont, J. Carlos Guzman, Douglas McCarville, Cheryl A. Rose, Mark W. Hilburger, Compression Response of Fluted-Core Composite Panels, *AIAA Journal* 50 (2012) 2546-2557

[35] Nanayakkara, S. Feih, A.P. Mouritz, Experimental analysis of the through-thickness compression properties of Z-pinned sandwich composites, *Composites* Part A 42 (2011): 1673–1680

[36] P. Chang, A.P. Mouritz, B.N. Cox., Flexural properties of Z-pinned laminates, *Journal of Composites:* Part A 38 (2007): 244–251

[37] Du Long, Jiao Guiqiong., Indentation study of Z-pin reinforced polymer foam core sandwich structures, *Journal of Composites:* Part A 40 (2009): 822–829

[38] A. P. Mouritz., Compression properties of Z-pinned sandwich composites, *Journal of Materials Science* (2006) 41: 5771–5774

[39] Brian. T. Wallace, Bhavani V. Sankar and Peter G. Ifju., Pin Reinforcement of Delaminated Sandwich Beams under Axial Compression, *Journal of Sandwich Structures and Materials*, Vol. 3—April 2001 117 1530-7972/01/02 0117–13

[40] Xia Fan, Wu Xiao-qing., Study on impact properties of through-thickness stitched foam sandwich composites, *Journal of Composite Structures* 92 (2010): 412–421

[41] F.W. Zok, S.A. Waltner, Z. Wei, H.J. Rathbun, R.M. McMeeking, A.G. Evans., A protocol for characterizing the structural performance of metallic sandwich panels: application to pyramidal truss cores, *International Journal of Solids and Structures* 41 (2004): 6249–6271

[42] *Fatigue Life Prediction and Strength Degradation of Wind Turbine Rotor Blade Composites, R.P.L. Nijssen*, Dissertation publicly defended on November 27th, 2006 at Delft University of Technology

[43] *Fatigue Degradation and Failure of Rotating Composite Structures –Materials Characterisation and Underlying Mechanisms, E. Kristofer Gamstedt and Svend Ib Andersen*, Riso National Laboratory, Roskilde, Denmark, March 2001

[43] *Development of a Composite Delamination Fatigue Life Prediction Methodology, T. Kevin O'Brien,* Durability, Damage Tolerance and Reliability Branch NASA Langley Research

[45] *Fatigue life prediction of laminated polymer matrix composites, N. Himmel*, International Journal of Fatigue 24 (2002) 349–360

[46] *Environmental fatigue behavior and life prediction of unidirectional glass–carbon/epoxy hybrid composites, Ying Shan, Kin liao*, International Journal of Fatigue 24 (2002) 847–859

[47] *Fatigue life prediction and load cycle elimination during spectrum loading of composites Joakim Schoria, Anders Blom*, International Journal of Fatigue 24 (2002) 361–367
[48] *Probabilistic fatigue life prediction of multidirectional composite laminates, Yongming Liu, Sankaran Mahadevan*, Composite Structures 69 (2005) 11–19

[49] *Fatigue life prediction of composite laminates by FEA simulation method, Wei Lian, Weixing Yao*, International Journal of Fatigue 32 (2010) 123–133

[50] *Prediction of the fatigue life of unidirectional glass giber/epoxy composite laminae using different neural network paradigms, Hany El Kadi, Yousef Al-Assaf,* Journal of Composite Structures 55 (2002) 239-246

[51] *A damage mechanics model for fatigue life prediction of fiber reinforced polymer composite laminate Wenjing Shi Weiping, Hu Miao Zhang*, Qingchun Meng, Acta Mechanica Solida Sinica, Vol. 24, No. 5, October, 2011

[52] *Prediction of fatigue damage and life for composite laminates under service loading spectra, L. J. Lee, K. E. Fu & J. N. Yang*, Composites Science and Technology 56 (1996) 635-648

[53] *Influence of the constant life diagram formulation on the fatigue life prediction of composite materials Anastasios P. Vassilopoulos, Behzad D. Manshadi, Thomas Keller*, International Journal of Fatigue 32 (2010) 659–669

[54*] A two-stage theory on fatigue damage and life prediction of composites J.J. Xiong, R.A. Shenoi,* Composites Science and Technology 64 (2004) 1331–1343

[55] *Fatigue life predictions in polymer particle composites F.V. Antunes, J.M. Ferreira, J.D. Costa, C. Capela* , International Journal of Fatigue 24 (2002) 1095–1105

[56] *Fatigue-life prediction of sic aluminum composite using a Weibull model D. Shan, H. Nayeb-Hashemi*, NDT&E International 32 (1999) 265–274

[57] *Evaluation of the residual strength degradation in composite laminates under fatigue loading H.A. Whitworth*, Composite Structures 48 (2000) 261-264

[58] *Fatigue behaviour and life assessment of composite laminates under multiaxial loadings Marino Quaresimin Luca Susmel, Ramesh Talreja*, International Journal of Fatigue 32 (2010) 2–16

[59] *Damage and fatigue in composites – A personal account Ramesh Talreja*, Composites Science and Technology 68 (2008) 2585–2591

[60] *Micromechanical modeling of fatigue strength of unidirectional fibrous composites Zheng-Ming Huang,* International Journal of Fatigue 24 (2002) 659–670

[61] *Observations on damage development in fibre reinforced polymer laminates under cyclic loading A.W. Wharmby, F. Ellyin, J.D. Wolodko,* International Journal of Fatigue 25 (2003) 437–446

[62] *An empirical model for fatigue behavior prediction of glass fibre-reinforced plastic composites for various stress ratios and test frequencies Jayantha A. Epaarachchi, Philip D. Clausen*, Composites: Part A 34 (2003) 313–326
[63] *Spectrum fatigue lifetime and residual strength for fiberglass laminates in tension, Neil Wahl,* AIAA-2001-0025

[64] *Cumulative damage leading to fatigue and creep failure for General materials, Richard M. Christensen*, October 18th 2008, Failurecriteria.com

[65] *Life Prediction Methodologies for Composite Materials*, National Materials Advisory Board Commission on Engineering and Technical Systems National Research Council with Max E. Waddoups as Chairman

[66] *An appropriate stiffness degradation parameter to monitor fatigue damage evolution in composites Rui Tang, Ya-Jun Guo 1, Y.J. Weitsman*, International Journal of Fatigue 26 (2004) 421–427

[67] *Modeling the variable amplitude fatigue of composite materials: A review and evaluation of the state of the art for spectrum loading N.L. Post, S.W. Case, J.J. Lesko,* International Journal of Fatigue 30 (2008) 2064–2086

[68] Experimental analysis of the through-thickness compression properties of z-pinned sandwich composites, A. Nanayakkara, S. Feih, A.P. Mouritz, *Composites Part A 42 (2011) 1673–1680*

[69]. Failure analysis of pin-loaded aluminum–glass–epoxy sandwich composite plates, Bulent Murat Icten, Onur Sayman, *Composites Science and Technology 63 (2003) 727–737*

[70]. Flexural properties of z-pinned laminates, P. Chang, A.P. Mouritz, B.N. Cox, *Composites: Part A 38 (2007) 244–251*
[71]. Study on impact properties of through-thickness stitched foam sandwich composites, Xia Fan, Wu Xiao-qing, *Composite Structures 92 (2010) 412–421*

[72]. Indentation study of Z-pin reinforced polymer foam core sandwich structures, Du Long, Jiao Guiqiong, *Composites: Part A 40 (2009) 822–829*

[73]. Mechanical properties balance in novel Z-pinned sandwich panels: Out-of-plane properties, Andrea I. Marasco, Denis D.R. Cartie, Ivana K. Partridge, Amir Reza, *Composites: Part A 37 (2006) 295–302*

[74]. The effect of pin reinforcement upon the through-thickness compressive strength of foam-cored sandwich panels, Denis D. Cartie , Norman A. Fleck, *Composites Science and Technology 63 (2003) 2401–2409*

[75] Pin Reinforcement of Delaminated Sandwich Beams under Axial Compression, Brian. T. Wallace, Bhavani V. Sankar and Peter G. Ifju, *Journal of Sandwich Structures and Materials, Vol. 3—April 2001 117 1530-7972/01/02 0117–13*

[76] Analytical modeling and finite element simulation of the plastic collapse of sandwich beams with pin-reinforced foam cores, Tao Liu a, Zi Chen Deng a,b, Tian Jian Lu c, *International Journal of Solids and Structures 45 (2008) 5127–5151*

[77] A protocol for characterizing the structural performance of metallic sandwich panels: application to pyramidal truss cores, F.W. Zok *, S.A. Waltner, Z. Wei, H.J. Rathbun, R.M. McMeeking, A.G. Evans, *International Journal of Solids and Structures 41 (2004) 6249–6271*

[78] Compression properties of z-pinned sandwich composites A. P. Mouritz, *J Mater Sci (2006) 41:5771–5774*

[79] Buckling Analysis of Debonded Sandwich Panel Under Compression, David W. Sleight and John T. Wang, *NASA Technical Memorandum 4701*

[80] Vaziri, A., Xue, Z., Hutchinson, J.W., 2006. Metal sandwich plates with polymer foam-filled cores. *Journal of Mechanics of Material and Structures 1, 95–125.*

[81] Mouritz A.P.,Gellert E., Burchill P., Challis K. (2001) Review of advanced composite structures for naval ships and submarines, Composite Structures, 53: 21-41

[82] Haldar S., Bruck H.A. (2014) Mechanics of Composite Sandwich Structures with Bioinspired Core, Composites Science and Technology, 95:67-74

[83] Puishys J., Bruck H.A. (2012) Determination of Mixed Mode Energy Release Rates in Laminated Carbon Fiber Composite Structures using Digital Image Correlation, University of Maryland

[84] Rotem A., Nelson H.G. (1989) Failure of a Laminated Composite Under Tension-Compression Fatigue Loading, Composites Science and Technology 36:45-62

[85] Pascoe J.A., Alderliesten R.C., Benedictus R. (2013) Methods for the Prediction of Fatigue Delamination Growth in Composites and Adhesives Bonds- A Critical Review, Engineering Fracture Mechanics, 112-113: 72-96

[86] Blanco N., Gamstedt E.K., Asp L.E. (2004) Mixed Mode Delamination Growth in Carbon-fiber Composite Laminates under Cyclic Loading, International Journal of Solids and Structures, 41: 4219-4235

[87] ASTM Standard D6115-97 (2011) Standard Test Method for Mode I Fatigue Delamination Growth Onset of Unidirectional Fiber-Reinforced Polymer Matrix Composites

[88] ASTM Standard D6671/D6671M (2006) Standard Test Method for Mixed Mode I- Mode-II Interlaminar Fracture Toughness of Unidirectional Fiber Reinforced Polymer Matrix Composites

[89] Baral N., Guezenoc H. (2008) High modulus carbon fiber composites: Correlation between transverse tensile and mode I interlaminar fracture properties, Materials Letters, 62, 6-7:1096-1099

[90] Pinho S.T., Robinson P. (2006) Fracture toughness of the tensile and compressive fiber failure modes in laminated composites, Composites Science and Technology, 66: 2069-2079

[91] Nikbakht M., Choupani N. (2008) Fracture Toughness Characterization of Carbon- Epoxy Composite Using Arcan Specimen, World Academy of Science, Engineering and Technology, 41: 738-744

[92] Miyajima T., Sakai M. (1991) Fiber Bridging of a Carbon Fiber-Reinforced Carbon Matrix Lamina Composite, Journal of Materials, Materials research Society, 6: 539-547

[93] Mogadpalli G.P., Parameswaran V. (2008) Determination of Stress Intensity Factor for Cracks in Orthotropic Composite Materials using Digital Image Correlation, Strain, 44: 446-452

[94] Kinloch A.J., Wang Y., Williams J.G. (1993) The Mixed Mode Delamination of Fiber Composite Materials, Composites Science and Technology, 47(3): 225-237

[95] Liu C., Rosakis A.J., Ellis R.W. Stout M.G. (1998) A Study of the Fracture Behavior of Unidirectional Fiber –Reinforced Composites Using Coherent Gradient Sensing(CGS) interferometry, International journal of Fracture, 90: 355- 382